The 3D Characterisation Of Microscale Indentations On Silicon Nitride

Adam Benjamin Baggott

Department of Materials Science and Engineering

University of Sheffield

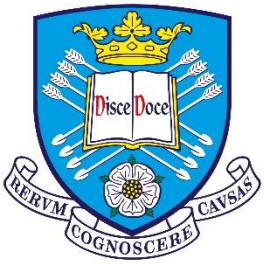

The University Of Sheffield.

This thesis is submitted as a requirement for the degree of Doctor of Philosophy

Submitted April 2020

Abstract

Silicon nitride is a high hardness structural ceramic that is often used for the production of ball-bearing components due to its good mechanical properties. However, during manufacturing, microscale pits (called “star features”) can form on the surface of ball components. In this project, microscale pits, on silicon nitride balls are characterised in three-dimensions using a combination of surface and sub-surface characterisation techniques. Investigations into low load (0.5 kg and 1 kg) Vickers micro-indentations on silicon nitride are first carried out to ascertain which techniques are most applicable to evaluation of star features. This includes the determination of key microstructural parameters including microstructure, cracking distribution and residual stress. High resolution SEM imaging and Raman spectroscopy of indentations reveal a primarily intergranular fracture mode for cracking, with surface tensile stresses of ~ 1 GPa at radial crack tips for 1 kg indentations.

Micro-XCT resolves sub-surface half-penny, lateral, and radial cracking present after high load 5 kg Vickers indentation into silicon nitride. Focused ion beam (FIB) tomography revealed the presence of half-penny and lateral cracking in low load (0.5 kg and 1 kg) indentations with c/a ratios < 2. The initiation depth of half-penny and lateral cracking has been used to approximate the volume of the compressive stress region that exists beneath the indentation impression.

FIB tomography of star features on silicon nitride balls reveals half-penny cracking that has not observed using UV fluorescence microscopy. The lateral extension of lateral cracking from the centre of star features observed via FIB tomography has been found to correlate well with UV fluorescence imaging. In addition, lateral cracking is found to be located at the same depth as adjacent regions of missing material, implying that material removal initiates from lateral cracking. Uplifted zones of up to ~ 0.8 μm vertical displacement were also found to exist surrounding star features.

Overall it is found that 3D characterisation methodologies, including FIB tomography, optical profilometry and micro-XCT, are highly effective in the quantification of tribological surface damage in silicon nitride, giving new insights into the distribution and role of surface deformation and fracture.

Acknowledgments

First of all, I would like to thank Prof. Beverley Inkson for all of her excellent advice, encouragement and support throughout my Ph.D. I am extremely grateful to have had such an accomplished and revered supervisor who continually provided me with opportunities not only to better my research understanding, but also to better myself. I would also like to thank my industrial supervisors Mehdi Mazaheri and Charlotte Vieillard for their patience and expertise.

I would like to thank the NanoLab group members, past and present, for all the guidance, suggestions, and most importantly – friendships. I would also like to thank the various staff members who have assisted in my research in the form of equipment training and usage. In particular, Dr Le Ma and Dr Cheryl Shaw of the Sorby Centre facility, who always acted with humour and grace whenever the Helios was being difficult.

I would like to thank all of my friends and family. Especially my parents, for loving and supporting me in every single moment of my life, and throughout this Ph.D journey. I could not ask for better parents and I would not be who I am today without you both. You are amazing. I would like to thank Katie, my marvel of a fiancée, for bringing me joy, happiness and companionship – I am a blessed man indeed. I would also like to show much gratitude to my church family who have continually prayed for me and shown unconditional kindness.

Finally, I would like to honour my God who is the foundation and cornerstone of all that I am. His love and guidance has been unrelenting and always good. I give this thesis as an act of worship, for as it says in Proverbs 3: 5 – 6: "Trust in the Lord with all your heart and lean not on your own understanding. In all of your ways submit to Him and He will make your paths straight.".

Nomenclature List

BF	– *Bright Field*
BSE	– *Backscattered Secondary Electron*
CCD	– *Charge-Coupled Device*
CT	– *Computed Tomography*
DF	– *Dark Field*
DVC	– *Digital Volume Correlation*
EDX	– *Energy-Dispersive X-ray*
ETD	– *Everhart-Thornley Detector*
FEG	– *Field Emission Gun*
FEM	– *Finite Element Modelling*
FIB	– *Focused Ion Beam*
FIB-SEM	– *Focused Ion Beam – Scanning Electron Microscope*
FWHM	– *Full Width at Half Maximum*
GFIS	– *Gas Field Ion Source*
HIM	– *Helium Ion Microscopy*
HPC	– *Half-Penny Crack*
HV	– *Vickers Hardness*
IMOD	– *Image Modelling Software*
ISE	– *Ion-Induced Secondary Electrons*
LC	– *Lateral Crack*
LMIS	– *Liquid Metal Ion Source*
M1	– *Morphology 1*
M2	– *Morphology 2*
PC	– *Palmqvist Crack*
SAM	– *Scanning Acoustic Microscopy*
SE	– *Secondary Electron*
SEM	– *Scanning Electron Microscopy*
SIMS	– *Secondary Ion Mass Spectroscopy*

TEM – *Transmission Electron Microscopy*

UV – Ultraviolet

VSWLI – *Vertical Scanning White Light Interferometry*

XCT – *X-ray Computed Tomography*

Figures and Tables

Chapter 2

Chapter 3

Chapter 4

Chapter 5

Chapter 6

Chapter 7

Table of Contents

Chapter 1: Introduction

1.1. Background

The use of ball-bearings for reducing rotational friction whilst being able to support an applied external load has a wide variety of applications in many industries; from hard drives and exercise equipment, to skateboards and space shuttles [1], [2]. Conventional ball-bearings are typically made out of steel because of its relatively low cost, ease to manufacture, and good mechanical properties. However, steel ball-bearings do have disadvantages in the form of limited corrosion resistance, reduced durability at high temperature and a risk of magnetic interference (e.g. in medical applications) [3], [4]. In the last few decades, ceramic ball-bearings have come to prominence as an alternative to steel because of their advantageous mechanical properties; one such commonly used ceramic is silicon nitride. Silicon nitride (Si_3N_4) is structural ceramic which offers solutions to the drawbacks of steel, i.e. chemical resistance, good high temperature properties and, is non-magnetic in nature [4]–[7]. In addition to this, it also possesses a range of other desirable properties for bearings such high hardness, low density, electrical resistance and a smoother surface finish; all of which result in reduced wear [8].

The high hardness of silicon nitride bearings means that they undergo differing damage mechanisms to steel bearings. For example, during processing (via diamond lapping) and service, loose material under high load can indent the surface of the rotating ball causing microscale pits and indentations (often referred to as “star features” [7], [9]) with associated cracking due to the intrinsic brittleness of silicon nitride [10]. Under further applied pressure, such as in operational use, cracking can propagate further leading to material removal in the form of spalling and flaking [11], [12]. Therefore, it is important that these star features are well characterised so that their evolution in operation conditions can be better understood.

1.2. Aims and Objectives

The primary aim of this project is to characterise both the surface and sub-surface nature of microscale star features and cracking on commercial grade silicon nitride ball-bearings in order to gain an insight into how they may evolve. For the surface characterisation of

indents there are many techniques available with sufficient resolution, e.g. optical and electron microscopy. However, revealing the sub-surface nature of indents and cracking, which are not observable from the surface, is less trivial as there are limited methods with the required nano/microscale resolution. Therefore, the secondary aim of this project is to find the most suitable methods for the sub-surface characterisation of microscale indents in silicon nitride.

One of the techniques used in this work is known as Focused Ion Beam (FIB) tomography. It involves using a beam of positively charged ions, usually gallium, (via a gallium-FIB microscope) to serial section the sample by sputtering away material to reveal a sub-surface cross-section. In conjunction with this, a high resolution scanning electron microscope (SEM) oriented in the direction of the cross-section can be used to image the sub-surface plane. By incrementally sectioning with the FIB and imaging with the SEM, a 3D reconstruction of the sub-surface can be created [13]–[15]. The advantage of this technique is that the FIB has nanoscale spatial resolution and sputtering of material for sub-surface analysis is highly localised. In addition, FIB tomography has previously proved successful for the 3D analysis of cracking beneath Vickers indentations on ceramics, albeit of smaller dimensions than will be analysed in this project [16]–[19].

Another, and more well known, technique used for sub-surface characterisation will be microscale X-ray Computed Tomography (micro-XCT). The application of this technology is primarily within the medical industry for 3D images of the body, i.e. a CT scan [20]–[22], however it has found many applications in materials science for viewing the internal structure of materials. Micro-XCT does not possess the same resolution as FIB tomography, although unlike FIB tomography, it is a non-destructive technique meaning samples are available undamaged for further analysis. The final technique for exploring the sub-surface nature of indentations is incremental manual grinding of the indentations from the top down, in conjunction with optical imaging. It is a simple but effective technique that has been frequently used to observe sub-surface cracking surrounding indentations, although it does have limitations in the form low spatial resolution as well as sample destruction [23]–[26].

The silicon nitride ball star features investigated in this project have differing morphologies due to the range of processing and service conditions the balls have been subjected to [27]–[29]. Microindentation of a material surface with a Vickers indentation is often used as a representative morphology for compression defects because of their similar characteristic features, i.e. a central impression and associated surrounding

cracking [30], [31]. The applied indentation load can also be adjusted to change the size of the damage zone and residual indentation impression produced. Therefore, in this study Vickers microindentation has been used to create artificial star features in a controlled and reproducible way. This has been done for two reasons: firstly, it allows the trialling of the sub-surface characterisation methods before using them on the silicon nitride ball samples that possess star features – this is necessary as the ball samples are of limited supply. Secondly, the effect that the applied load and material composition have on the cracking present beneath indentations can be investigated. Since Vickers indentation is widely used to obtain a variety of material mechanical properties (e.g. hardness, fracture toughness, elastic modulus), it is important that indentations are well characterised [32], [33].

The surface characterisation of star features is of equal importance to the sub-surface investigations. As previously mentioned, star features (and Vickers indentations) have been examined under high resolution SEM and optical microscopy so that their surface morphology can be observed. These techniques reveal details about the surface nature of features such as how cracking interacts with the surface microstructure (often material dependent) and the geometry of the central indentation impression. However, despite certain types of microscopy (e.g. secondary electron SEM imaging) offering topographical contrast which may give an insight into vertical dimensions of star features, quantifiable measurements of surface topography are more desirable, particularly for rotating balls, where low surface roughness is paramount to good performance. Therefore, an optical surface profilometry technique has been employed here that uses white light interferometry to measure changes in the surface height of a sample. It is a methodology that is commonly used within the ball-bearings industry and should provide information about the star features and Vickers indentations not attainable through the other techniques [34], [35]. In addition to topography, the magnitude and location of residual stresses present surrounding star features is also an important factor for how they may behave under applied external pressure. Methods of localised stress measurement with microscale resolution are limited, but in Raman spectroscopy, a technique conventionally used for surface chemical analysis, changes in spectra peak position can be used to determine changes in stress; in this work, Raman has been utilised for stress analysis in the region surrounding indentations and their associated cracking [36]–[38].

The SEM imaging of samples provides high resolution detail about their morphology, however, because silicon nitride is an insulator, samples imaged under an electron beam

are usually coated with a conductive surface layer of either gold or carbon to alleviate surface charge build-up [39]. This can occasionally inhibit further surface analysis as the conductive layer is difficult to remove. Recently, a new type of FIB instrument (that differs from the conventional liquid gallium source FIB) has been developed that uses a helium or neon gas field ion source (GFIS) to produce the positively charged ion beam [40], [41]. The helium ion beam is particular good for imaging because of the deep penetration depth and small probe size offered which allow for higher resolution imaging than even SEM [42], although the problem of surface charge when imaging an insulator still exists; it is just positive charge build-up instead of negative. However, GFIS FIB instruments now typically have an attached electron flood gun which is incident on the sample at the same time as the ion beam and acts to neutralise the positive charge hence eliminating surface charge build-up and therefore improving image quality without the need for a conductive coating [43], [44]. This technique has not previously been applied to imaging of ceramics, and more specifically, microscale surface damage on ceramics, so its suitability for such applications has been investigated here on indentations in silicon nitride.

The use of silicon nitride ball-bearings in a variety of applications and industries means that understanding the factors that affect their performance and lifetime is of high importance. One such factor, as has been discussed, is the presence of microscale star features on the surface of the rotating balls and their evolution in operational conditions which is dependent on their constitution. Using the techniques and methodologies introduced in this Chapter, this project has sought to characterise the surface and sub-surface nature of artificial and lapping-induced indentations on silicon nitride balls whilst also identifying the most effective tools and operating parameters for achieving this.

To summarise, the main **Aims** of this project are as follows:

- To characterise the surface and sub-surface nature of microscale star features on silicon nitride bearings.
- To characterise the surface and sub-surface nature of Vickers indentations of different load.
- To decide upon the most suitable characterisation techniques for the above aims, particularly the sub-surface characterisation.

In attempt to accomplish these aims, the following **Objective** tasks will be performed:

- Use Vickers indentation of varying loads to emulate the microscale star features.

- Perform surface characterisation on Vickers indentations using SEM imaging, 3D optical profilometry, optical imaging and GFIS imaging.
- Conduct stress analysis on Vickers indentations using Raman spectroscopy.
- Utilise XCT, FIB tomography, and manual polishing to characterise the sub-surface features of Vickers indentations.
- Apply the most successful surface and sub-surface analysis techniques to characterise the star features on the ball-bearing samples.

1.3. Thesis Outline

This thesis comprises eight Chapters, including this introduction, and the outline is as follows:

Chapter 2 introduces the theory behind the primary methodologies used in this project, as well as an in-depth review of the previously published literature concerning the investigations carried out here.

Chapter 3 describes in detail the experimental equipment and methodologies utilised in these investigations. This includes sample preparation, stress analysis, and surface and sub-surface characterisation.

Chapter 4 covers the surface characterisation of Vickers indentations on silicon nitride using high resolution SEM, Raman spectroscopy and surface profilometry. It also includes the non-destructive 3D characterisation of indentations by micro-XCT.

Chapter 5 presents an investigation into the sub-surface morphology of Vickers indentations on silicon nitride using FIB tomography and a top-down manual polishing technique.

Chapter 6 uses the FIB tomography method, in addition to surface profilometry and other microscopy methods, to characterise the surface and sub-surface of various star features on silicon nitride balls to predict how they may evolve.

Chapter 7 investigates the applicability of the recently developed He/Ne GFIS microscopy for characterisation of non-conductive ceramic material such as silicon nitride. This includes a comparison of helium and neon beam imaging as well as the influence of surface conductive coating on imaging resolution.

Chapter 8 brings this thesis to a conclusion and offers ideas for future investigations.

1.4. Publications

The publications associated with the research conducted in this Ph.D. thesis are as follows:

- A. Baggott, M. Mazaheri, and B. J. Inkson, "3D characterisation of indentation induced sub-surface cracking in silicon nitride using FIB tomography," *J. Eur. Ceram. Soc.*, vol. 39, no. 13, pp. 3620–3626, 2019.

- A. Baggott, M. Mazaheri, Y. Zhou, H. Zhang, and B. J. Inkson, "A comparison of He and Ne FIB imaging of cracks in microindented silicon nitride," *Mater. Charact.*, vol. 141, pp. 362–369, 2018.

1.5. References

[1] L. Wang, R. Snidle, and L. Gu, "Rolling Contact Silicon Nitride Bearing Technology: a Review of Recent Research," *Wear*, vol. 246, no. 1–2, pp. 159–173, 2000.

[2] N. Kawashima, N. Hiraoka, and Y. Yoshii, "Space tribology in Japan," *Proc. Inst. Mech. Eng. Part J J. Eng. Tribol.*, vol. 210, no. 3, pp. 173–178, 1996.

[3] F. J. Ebert, "Performance of Silicon Nitride (Si 3N4) Components in Aerospace Bearing Applications," in *ASME 1990 International Gas Turbine and Aeroengine Congress and Exposition*, 1990, vol. 5, pp. 1–8.

[4] B. S. Bal and M. N. Rahaman, "Orthopedic applications of silicon nitride ceramics," *Acta Biomater.*, vol. 8, no. 8, pp. 2889–2898, 2012.

[5] H. Klemm, "Silicon nitride for high-temperature applications," *J. Am. Ceram. Soc.*, vol. 93, no. 6, pp. 1501–1522, 2010.

[6] Z. Krstic and V. D. Krstic, "Silicon nitride: The engineering material of the future," *J. Mater. Sci.*, vol. 47, no. 2, pp. 535–552, 2012.

[7] W. Wang, M. Hadfield, and A. A. Wereszczak, "Surface strength of silicon nitride in relation to rolling contact performance measured on ball-on-rod and modified four-ball tests," *Tribol. Int.*, vol. 43, no. 1–2, pp. 423–432, 2010.

[8] S. Hampshire, "Silicon nitride ceramics - review of structure, processing and properties," *J. Achiev. Mater. Manuf. Eng.*, vol. 24, no. 1, pp. 43–50, 2007.

[9] J. Lai, Y. Kadin, and C. Vieillard, "Characterization and modelling of the degradation of silicon nitride balls with surface missing-material defects under lubricated rolling contact conditions," *Wear*, vol. 398–399, no. March, pp. 146–157, 2018.

[10] L. Wang, R. J. K. Wood, T. J. Harvey, S. Morris, H. E. G. Powrie, and I. Care, "Wear performance of oil lubricated silicon nitride sliding against various bearing steels," vol. 255, pp. 657–668, 2003.

[11] Y. Wang and M. Hadfield, "A mechanism for nucleating secondary fractures near a

pre-existing flaw subjected to contact loading," *Wear*, vol. 254, no. 7–8, pp. 597–605, 2003.

[12] P. Zhao, M. Hadfield, Y. Wang, and C. Vieillard, "Subsurface propagation of partial ring cracks under rolling contact. Part I. Fracture mechanics analysis," *Wear*, vol. 261, no. 3–4, pp. 390–397, 2006.

[13] P. R. Munroe, "The application of focused ion beam microscopy in the material sciences," *Mater. Charact.*, vol. 60, no. 1, pp. 2–13, 2009.

[14] B. J. Inkson and Günter Möbus, "Nanoscale tomography in materials science," *Mater. Today*, vol. 10, no. 12, pp. 18–25, 2007.

[15] L. A. Giannuzzi and F. A. Stevie, *Introduction to Focused Ion Beams: Intrumentation, Theory, Techniques and Practice*. Springer Science & Business Media, 2006.

[16] H. Z. Wu, S. G. Roberts, G. Möbus, and B. J. Inkson, "Subsurface damage analysis by TEM and 3D FIB crack mapping in alumina and alumina/5vol.%SiC nanocomposites," *Acta Mater.*, vol. 51, no. 1, pp. 149–163, 2003.

[17] Z. H. Xie, P. R. Munroe, R. J. Moon, and M. Hoffman, "Characterization of surface contact-induced fracture in ceramics using a focused ion beam miller," *Wear*, vol. 255, no. 1–6, pp. 651–656, 2003.

[18] N. Payraudeau, D. McGrouther, and K. U. O'Kelly, "Quantification of subsurface damage in a brittle insulating ceramic by three-dimensional focused ion beam tomography.," *Microsc. Microanal.*, vol. 17, no. 2, pp. 240–5, 2011.

[19] F. Elfallagh and B. J. Inkson, "Evolution of residual stress and crack morphologies during 3D FIB tomographic analysis of alumina.," *J. Microsc.*, vol. 230, no. Pt 2, pp. 240–51, 2008.

[20] V. Cnudde and M. N. Boone, "High-resolution X-ray computed tomography in geosciences: A review of the current technology and applications," *Earth-Science Rev.*, vol. 123, pp. 1–17, 2013.

[21] E. N. Landis and D. T. Keane, "X-ray microtomography," *Mater. Charact.*, vol. 61, no. 12, pp. 1305–1316, 2010.

[22] L. Salvo, P. Cloetens, E. Maire, S. Zabler, J. J. Blandin, J. Y. Buffière, W. Ludwig, E. Boller, D. Bellet, and C. Josserond, "X-ray micro-tomography an attractive characterisation technique in materials science," *Nucl. Instruments Methods Phys. Res. Sect. B Beam Interact. with Mater. Atoms*, vol. 200, pp. 273–286, 2003.

[23] T. Lube, "Indentation crack profiles in silicon nitride," *J. Eur. Ceram. Soc.*, vol. 21, pp. 211–218, 2001.

[24] H. Miyazaki, H. Hyuga, Y. I. Yoshizawa, K. Hirao, and T. Ohji, "Crack profiles under a Vickers indent in silicon nitride ceramics with various microstructures," *Ceram. Int.*, vol. 36, no. 1, pp. 173–179, 2010.

[25] R. Cook and G. Pharr, "Direct observation and analysis of indentation cracking in glasses and ceramics," *J. Am. Ceram. Soc.*, vol. 73, no. 4, pp. 787–817, 1990.

[26] Y. Vertyagina, M. Mostafavi, C. Reinhard, R. Atwood, and T. J. Marrow, "In situ quantitative three-dimensional characterisation of sub-indentation cracking in polycrystalline alumina," *J. Eur. Ceram. Soc.*, vol. 34, no. 12, pp. 3127–3132, 2014.

[27] K. Kida, T. Honda, and E. C. Santos, "Semi-circular surface cracks and flaking failures in silicon nitride bearings," *Adv. Mater. Lett.*, vol. 2, no. 5, pp. 336–340, 2011.

[28] G. Levesque and N. K. Arakere, "Critical Flaw Size in Silicon Nitride Ball Bearings," *Tribol. Trans.*, vol. 53, no. July 2010, pp. 511–519, 2010.

[29] K. Kida, M. Saito, and K. Kitamura, "Flaking failure originating from a single surface crack in silicon nitride under rolling contact fatigue," *Fatigue Fract. Eng. Mater. Struct.*, vol. 28, no. 12, pp. 1087–1097, 2005.

[30] M. Hadfield and T. A. Stolarski, "Observations of delamination fatigue on pre-cracked ceramic elements in rolling contact," *Ceram. Int.*, vol. 21, no. 2, pp. 125–130, 1995.

[31] K. Kida, T. Urakami, T. Yamazaki, and K. Kitamura, "Surface crack growth of silicon nitride bearings under rolling contact fatigue," *Fatigue Fract. Eng. Mater. Struct.*, vol. 27, pp. 657–668, 2004.

[32] G. D. Quinn and R. C. Bradt, "On the vickers indentation fracture toughness Test," *J. Am. Ceram. Soc.*, vol. 90, no. 3, pp. 673–680, 2007.

[33] A. E. Giannakopoulos, P. L. Larsson, and R. Vestergaard, "Analysis of Vickers indentation," *Int. J. Solids Struct.*, vol. 31, no. 19, pp. 2679–2708, 1994.

[34] C. Vieillard, "Observation of subsurface rolling contact fatigue cracks in silicon nitride and comparison of their location to Hertzian contact subsurface stresses," *Int. J. Fatigue*, vol. 96, pp. 283–292, 2017.

[35] C. Vieillard, Y. Kadin, G. E. Morales-Espejel, and A. Gabelli, "An experimental and theoretical study of surface rolling contact fatigue damage progression in hybrid bearings with artificial dents," *Wear*, vol. 364–365, pp. 211–223, 2016.

[36] N. Muraki, G. Katagiri, V. Sergo, and G. Pezzotti, "Mapping of residual stresses around an indentation in beta-Si3N4 using Raman spectroscopy," *J. Mater. Sci.*, vol. 32, no. 2, pp. 5419–5423, 1997.

[37] S. Tochino and G. Pezzotti, "Micromechanical analysis of silicon nitride: A comparative study by fracture mechanics and Raman microprobe spectroscopy," *J. Raman Spectrosc.*, vol. 33, no. 9, pp. 709–714, 2002.

[38] U. Schmidt, W. Ibach, J. Muller, K. Weishaupt, and O. Hollricher, "Raman spectral imaging-A nondestructive, high resolution analysis technique for local stress measurements in silicon," *Vib. Spectrosc.*, vol. 42, no. 1, pp. 93–97, 2006.

[39] K. H. Kim, Z. Akase, T. Suzuki, and D. Shindo, "Charging Effects on SEM/SIM Contrast of Metal/Insulator System in Various Metallic Coating Conditions," *Mater. Trans.*, vol. 51, no. 6, pp. 1080–1083, 2010.

[40] G. Hlawacek, V. Veligura, R. Van Gastel, B. Poelsema, G. Hlawacek, V. Veligura, R. Van Gastel, and B. Poelsema, "Helium ion microscopy," *J. Vac. Sci. Technol. B*, vol. 32, 2014.

[41] F. H. M. Rahman, S. McVey, L. Farkas, J. A. Notte, S. Tan, and R. H. Livengood, "The prospects of a subnanometer focused neon ion beam," *Scanning*, vol. 34, no. 2, pp. 129–134, 2012.

[42] J. Notte, B. Ward, N. Economou, R. Hill, R. Percival, L. Farkas, and S. McVey, "An

introduction to the helium ion microscope," *AIP Conf. Proc.*, vol. 931, no. 2007, pp. 489–496, 2007.

[43] G. Hlawacek, V. Veligura, R. van Gastel, and B. Poelsema, "Helium Ion Microscopy," pp. 1–16, 2013.

[44] R. Hill and F. H. M. Rahman, "Advances in helium ion microscopy," *Nucl. Instrum. Methods Phys. Res., Sect. A*, vol. 645, no. 1, pp. 96–101, 2011.

Chapter 2: Literature Review and Theory

2.1. Introduction

The characterisation of micro-pits in silicon nitride balls and their associated cracking, both surface and sub-surface, is of great importance in predicting how they will evolve under operational conditions and what effect this will have on hybrid bearing performance. A good starting point for this is to gain an in-depth understanding of the properties and fracture behaviour of silicon nitride. In addition, it is also beneficial to have a good knowledge of the available tools that may assist in characterisation of such fracture. In this chapter, an overview of previous investigations in to silicon nitride fracture is given, as well as a review of the techniques that have been, and that could potentially be, used to further the understanding of micro-cracking in silicon nitride balls for hybrid bearings.

2.2. Silicon Nitride for Bearings Applications

2.2.1. Silicon Nitride

Silicon nitride (Si_3N_4) is a widely used structural ceramic by virtue of its high hardness, good thermal stability, low density, and low wear properties, making it desirable for use in applications such as high performance bearings, cutting tools and rotor blades [1], [2]. There are two primary crystallographic forms of silicon nitride, an α and a ß phase, both of which possess a hexagonal structure; the variation in the two is a consequence of their different atomic stacking sequences [3]. A distorted tetrahedron comprising of a central silicon atom surrounded by 4 nitrogen atoms is the principal component of these two forms, and it is the high strength covalent bond between the silicon and nitrogen that gives silicon nitride its good mechanical properties. Bulk α-silicon nitride was originally produced using the reaction bonding process in which compressed silicon powder is heated at temperatures of 1100-1450°C in nitrogen atmosphere with the advantage being that there is little reduction in size of the starting silicon compact. However, this method causes high micro-porosity and hence a decrease in strength [4], [5]. The level of micro-porosity could be decreased with sintering techniques, but a barrier to this is that the

temperature at which the diffusivity is sufficient for densification is also the temperature at which silicon nitride breaks down (~ 1800°C). Therefore, in the sintering of silicon nitride, oxide sintering additives are added such as yttria (Y_2O_3), alumina (Al_2O_3) and magnesia (MgO) [6]. In the sintering process, the thin silica layer on the outside of the starting α-silicon nitride powder particles reacts with the additive and nitride at sintering temperatures to form an oxynitride solution. Within this solution the α phase dissolves and undergoes a lattice transformation, precipitating out as the more stable ß phase and in doing so achieves greater densification. The remaining oxynitride liquid solidifies as an intergranular glassy phase promoting further densification [7]. An example of a typical silicon nitride microstructure is given in Fig. 2.1.

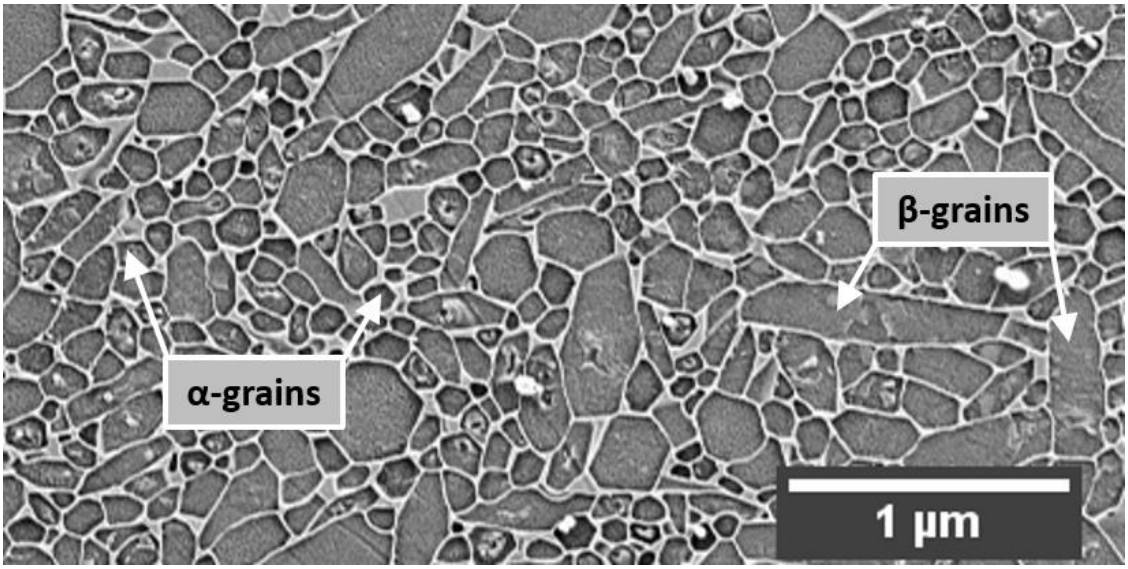

Figure 2.1: An SEM image of a plasma etched silicon nitride surface revealing the grain microstructure. Examples of α and β grains have been labelled. The lighter contrast region surrounding the grains is the intergranular glassy phase.

2.2.2. Fracture in Silicon Nitride

An additional advantage of the α to ß transformation is that the ß grains typically undergo preferential growth in one direction leading to elongated rod-like grains with a high aspect ratio [8]. A lot of research has been focused on microstructural control of the growth of the ß grains as they have been attributed to an increase in fracture toughness of silicon nitride via mechanisms such as crack deflection/bridging [9]–[11]. Kawaoka et al [12] varied the α/ß ratio (wt%) of pulse electric current sintered silicon nitride by changing the sintering temperature and duration. It was observed that fracture toughness increased linearly with an increased presence of ß grains and subsequent electron micrographs showed the

cause of this to be crack bridging and pull-out. However, hardness was shown to decrease due to the decrease in presence of α grains which were shown, via micro-Vickers indentation tests on single crystals, to have a higher hardness than ß grains. The authors of [12] therefore determined that a composition of 60-80-wt% ß-phase is desirable for applications of silicon nitride that require good fracture toughness and strength. Of course, it is not solely the presence of ß grains that have an influence on fracture toughness but also their morphology i.e. diameter and aspect ratio, as this determines the toughening mechanism. This was investigated by Sajgalik et al [13] who observed that ß grains with a diameter > 1 μm exhibited crack deflection more frequently than those with diameter < 1 μm where grain pull-out and elastic bridging is the primary mechanism for toughening. This is because during the grain growth process, larger diameter grains intersect with each other to cause a mechanical lock and hence inhibit grain pull-out.

The fracture pathways within silicon nitride are largely determined by whether crack propagation is intergranular or transgranular in nature, i.e. through the intergranular glassy phase or through the silicon nitride grains themselves. This is an important aspect of fracture to investigate because of its direct influence on fracture toughness, namely because if cracks propagate transgranularly then the mechanisms already discussed for increasing toughness (crack deflection, bridging) do not initiate [14]. The grain shape and size do have an influence on the propagation pathway of cracks, however, they may have a greater influence in the presence of some compositions of the amorphous intergranular phase [15]. For instance, in high purity silicon nitride with minimal sintering additives transgranular crack propagation is dominant [16] whereas for silicon nitride with additives, intergranular fracture is dominant (although not exclusive).

Wei et al [11] modelled the influence of grain boundary/grain toughness ratio and found that as it increased so did the proportion of transgranular cracking present, fitting with the frequently-held assumption that cracks propagate along the direction of maximum energy release. Studies of the effect of additive type on cracking carried out by Dusza et al [17] found that scandium-doped intergranular phase material produced more intergranular fracturing and a higher fracture toughness as a result, whereas alumina and zirconia-doped material showed higher transgranular fracture despite possessing similar microstructures. This conflict in fracture types was explained to be a result of the differing residual stresses present in the intergranular phase of the doped materials as well as difference in atomic structure at grain interfaces owing to their differing chemistries.

High resolution transmission electron microscopy (TEM) investigations by Ii et al [10], [18] revealed the exact pathway of both transgranular and intergranular cracking within silicon nitride. It was originally put forth that intergranular cracking could occur either within the intergranular glassy phase itself or along the grain/glassy phase interface with the latter crack pathway being the one experimentally observed [18]. The proposed hypothesis by Ii et al, supported by molecular dynamic simulations, behind the cause of this is that at the grain/glassy phase interface there exists a number of free dangling bonds that produce a higher localised energy state than at the silicon nitride grains or intergranular glassy phase, leading to preferential crack propagation. For transgranular cracking it was found that the crack walls were completely atomically flat and further simulations combined with TEM imaging showed that the cleavage occurred on the $(1\bar{1}00)$ plane where the minimal amount of silicon-nitrogen bonds are required to be broken. It is generally a combination of both transgranular and intergranular cracking that occurs within silicon nitride so it leads that there must be factors that determine the transition from one mode to another. Modelling by Mousavi [19] et al of strain rates found that lower strain rates are conducive to intergranular cracking, but as higher strain rates are approached there is a switch to transgranular cracking due to an increase in crack velocity allowing propagation through grains. The increased rate of energy dissipation associated with transgranular cracking causes a stress decrease which subsequently induces a switch back to intergranular fracture.

The direction at which the crack tip approaches a grain also affects the likelihood of inter/transgranular propagation. Kadin et al [20] observed, via scanning electron microscopy (SEM), the angle of cracks within grains and intergranular phase of silicon nitride with the aim of quantifying the angle θ at which the crack tip needs to contact a grain in order for transgranular fracture occur. This was calculated to be $> 77°$ (where $90°$ is the crack tip being perpendicular to the grain face); beneath this value intergranular fracture occurs. They equate their findings to Hutchinson and Suo's energy criterion [21] that aims to predict θ from the ratio of energy release rate and fracture toughness within the two phases (granular and intergranular phase). A reasonable agreement was found, with discrepancies attributed to the limited view of crack paths available from just viewing the surface plane, as well as the change in crack velocity which had been neglected from Hutchinson and Suo's criterion [20].

2.3. Indentation Testing

2.3.1. Indentation Theory and Applications

Indentation testing has been in use for a number of decades as a standard method for determining a range of material properties such as fracture toughness and hardness. The basic premise for hardness testing involves the indenter tip, composed of a high hardness material (e.g. diamond), coming in to contact with the surface of a softer material for a specified time under a specified applied load. This creates an impression on the softer material of a certain morphology from which material properties can be acquired. Of course, the shape of the indenter tip is the largest determiner of the residual indentation impression morphology remaining on the material surface, and therefore there are a variety of tip shapes that have been used. The schematic below shows (Fig. 2.2) the tip shapes of some of the more commonly used indenters as well as the residual impression they form on the soft material surface: The Vickers, Berkovich and Knoop tips are modelled on pyramids with a square, triangular, and rhomboid base respectively, with the conical and spherical tip shapes being self-explanatory. Indentation testing as a method of determining material properties is often favoured over other methods because of several key advantages: simple sample preparation - just a flat surface is required, small samples can be tested, indentation is quick, and the resulting impression can more often than not be measured optically. Additionally, indentation testing only creates localised damage which means the bulk material is still useable unlike in notch testing.

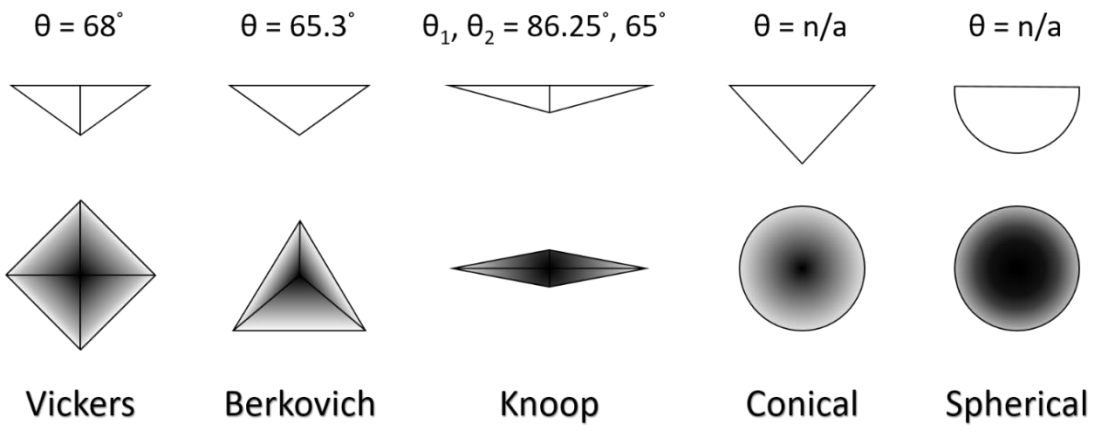

Figure 2.2: The different types of indenter tip geometries (top) as well as the residual indentation impression left by each (bottom). The angle θ is the centreline-to-face angle for each geometry.

The most common of the indenter tip shapes used to determine hardness is the Vickers tip. This is due to its symmetric, square geometry being easy to measure in comparison to the impressions formed by conical and spherical tips. Conventionally hardness values gained from indentation are defined as the ratio between the load applied and the projected contact area between the indenter tip and the material [22]. For Vickers indentation the hardness, or 'Vickers hardness' (HV), is calculated by the equation (Eq. 2.1) [23]:

$$HV = \frac{F}{A} = \frac{2 \cdot F \cdot \sin\theta}{d^2} = 1.8544 \cdot \frac{F}{d^2}$$

Equation 2.1: The relationship between Vickers hardness (HV), applied load, and diagonal length (d) of an indentation.

where F is the applied force in Newtons, A is indent contact area, and d is the average of the two diagonal measurements from the indentation corner tips (in millimetres). The angle θ is generally 68° and is the semi-apex angle for a pyramid with a four-sided base. The Vickers hardness of some common materials is shown in Table 2.1:

Material	Vickers Hardness, HV ($kg \cdot mm^{-2}$)
diamond	10,000
silicon carbide	2700
alumina	2160
silicon nitride	1600
zirconia	1100
hardened steel	900
iron	150

Table 2.1: A table giving Vickers Hardness (HV) values for commonly used industrial materials [22], [24]–[26].

Although widely used in industry to gauge hardness, there are problems associated with the reliability of values gained from using Vickers indentation, mainly from the indentation size effect. The indentation size effect is an increase in the Vickers hardness value obtained for a material as a function of decreasing applied load [27], particularly where the indentation depth approaches a few microns [28]. Whilst it is not fully

understood, it is thought the indentation size effect occurs due to phenomena such as work hardening, tip geometry influences at small scales, and the elastic response of the material to indentation; with the primary cause of the indentation size effect often being material dependent (e.g. work hardening for metals but not ceramics). The effects on the surrounding area after indentation are also strongly dependent on material, for instance, metals will plastically deform because of the high mobility of dislocations whereas in ceramics the mobility of dislocations is very low due to reduced slip systems and higher activation energies. Therefore, in ceramics stresses may build up until release in the form of the creation of a new surface via fracture, and for Vickers indention this fracture is typically initiated at the four corners of the indentation impression where stresses are highest. It is this predictability in cracking that has led Vickers indentation to be used in the study of ceramics for understanding crack propagation pathways and fracture toughness (as in much of the literature already discussed).

2.3.2. Vickers Indentation Cracking Regimes

The surface morphology of cracks in brittle materials induced by Vickers indentation does not change significantly with applied load (except at very low loads), and consists of four 'radial' cracks emanating outward from the four corners [29]; a schematic diagram of which is shown in Fig. 2.3. Occasionally there may also be secondary corner radial cracks as well as micro-cracking that follow the edge of the residual indentation impression, the cause of which is associated with pile up of material at edges due to volume displacement on loading [30]. Sub-surface cracks have a variety of morphologies and are harder to characterise. There has been a number of research studies on the characterisation of cracking around Vickers indentations on translucent brittle materials, which enable the observation of the sub-surface crack morphologies using optical microscopy [31]–[33]. For the radial cracks visible on the surface (emanating from the indentation corners), the sub-surface nature of these cracks can be one of either two morphologies: 'Palmqvist' cracks (PC) or 'half-penny' cracks (HPC) [34] (Fig. 2.3). PCs have a semi-circular depth profile and follow the path of the surface radial crack, i.e. they extend from the indentation corner to the tip of the radial crack (labelled PC in Fig. 2.3(b)). HPCs also possess a semi-circular depth profile but the crack extends from the tip of one radial crack, propagating underneath the plastically deformed zone beneath the residual indentation impression

and connecting to the tip of the radial crack on the opposing side of the indentation (labelled HPC in Fig. 2.3(c)).

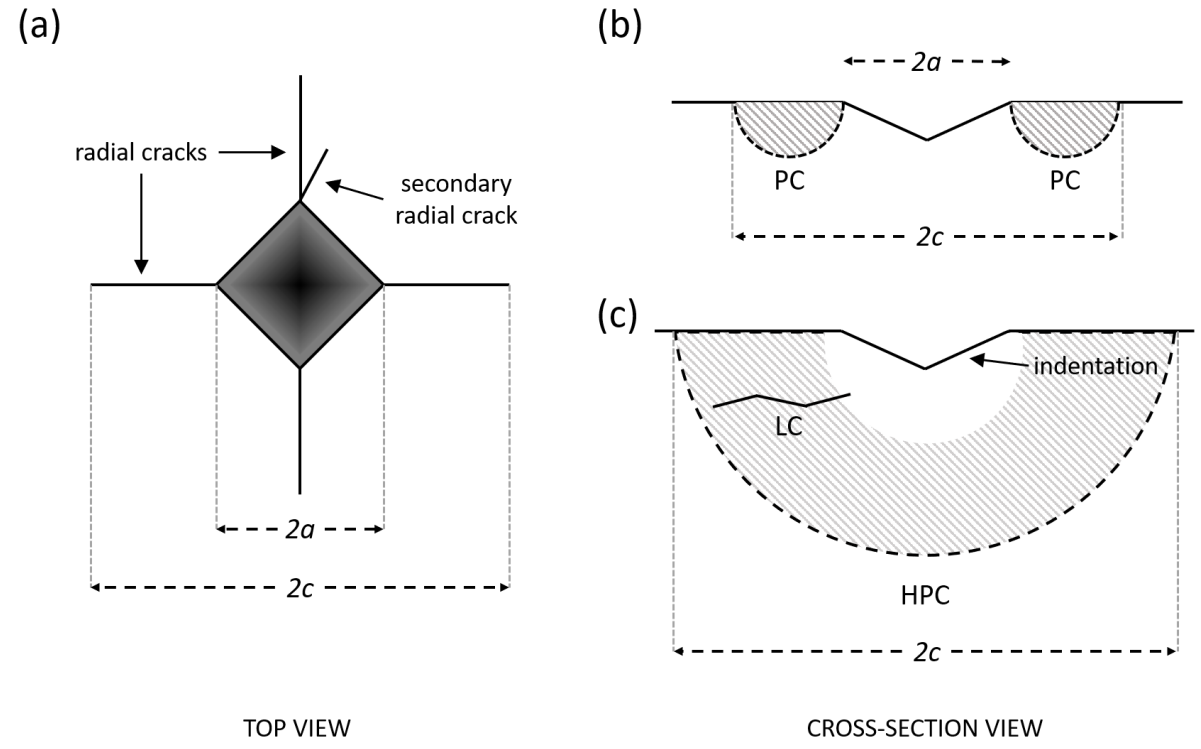

Figure 2.3: Vickers indentation crack profiles: (a) Top-down view of a Vickers indentation residual impression showing locations of radial cracks and the measurements represented by the tip to tip crack length, *2c*, and the indentation diagonal length, *2a*. (b) Cross-sectional view of the indentation and associated cracking in the Palmqvist crack (PC) regime. (c) Cross-sectional view of the indentation and associated cracking in the half-penny crack (HPC) regime. A lateral crack (LC) is also labelled. PC and HPC cracks are highlighted with the dashed line.

In addition to HPCs and PCs, occasionally 'lateral' cracks (LC) may be present that run approximately parallel to the surface and extend from the indentation edges. LCs are either located at a similar depth to the plastically deformed zone or closer to the surface. Cook and Pharr [30] investigated the sub-surface cracking of glasses and optically transparent crystalline materials using a Vickers indentation setup that enable crack morphologies to be viewed on loading and unloading by placing the optical objective lens beneath the materials focused upward. Their observations identified a transition at which the cracking regime changes from PC to HPC at higher loads (the load being material dependent) but that these cracking systems are independent (in the sense that PCs do not evolve in to HPCs), and that both crack types reach full extension upon unloading [30]. Interestingly for the crystalline materials, PCs formed on loading whereas for the glasses they formed on unloading; this was also observed for LCs. They also suggested that when

there is chipping near the residual indentation impression it is caused by material removal due to the presence of shallow lateral cracks near the surface. Although a useful starting point, it is clear that there will be differences in the crack profiles between the glasses and crystalline materials investigated by Cook and Pharr and other brittle materials, such as polycrystalline ceramics.

To determine the sub-surface crack profiles of opaque materials Niihara et al [34] suggested that the cracking regime present beneath the surface in brittle materials could be inferred by the ratio of the surface radial tip to tip crack length, $2c$, to the indentation diagonal length, $2a$ (Fig. 2.3). It was originally proposed that at a threshold c/a ratio, independent of material composition, the regime would change from PC to HPC [34], although further investigations have found that it is not only material dependent but also dependent on the hardness and fracture toughness of materials of slightly differing composition [35], [36]. The radial crack length, c, is also a commonly used parameter in determining the fracture toughness of ceramics but it has been found to be unreliable, particularly in the lower load regime where the cracking morphology is primarily PC [34], [37]. Therefore, to truly understand the sub-surface cracking profiles beneath indentations in opaque brittle materials, and the effect they have on the approaches used to ascertain specific mechanical properties, methods in which these sub-surface cracks can actually be observed must be employed.

Two of the early techniques for observing cracking profiles underneath Vickers indentations were first employed by Lankford [38] on soda-lime glass to determine the applied load threshold at which sub-surface cracking occurred. One method involved cleaving the indentations in half along the radial crack plane to reveal a single cross-section directly beneath the centre of the indentation, which were subsequently observed by SEM. The other technique was carried out on polycrystalline alumina in which material was incrementally removed using diamond paste grinding, parallel to the surface of the specimen – this is known as serial sectioning. Each grinding increment allows for the observation, at different depths, of the cross-section of the cracks surrounding the Vickers indentation. There are advantages and disadvantages to both methods: cleaving is very quick and allows for the exact depth measurement of sub-surface cracking, however, only cracks along the cleaved plane are visible. Whereas for serial sectioning, all major cracks surrounding the indentation are visible in cross-section but the process of continual polishing then imaging (especially when SEM is used) is time consuming.

Cleaving and serial sectioning techniques have been used for the investigations of Vickers indentations on silicon nitride; the material of interest in this project. Lube [39] utilised both methods, although with slight modifications, on Vickers indented silicon nitride (with loads ranging from 3 kg – 100 kg) to observe the change in sub-surface crack profiles as a function of applied load. Serial sectioning via polishing was carried out perpendicular to the surface plane, thus ensuring that material removal rate could be precisely measured, lateral cracks were not chipped away by polishing, and crack depth was more easily measured in comparison to the conventional parallel plane sectioning [39]. Optical images of the revealed cross-sections at various locations through the indentations showed that the crack profiles were PC in nature for the 3 kg indentations only, and loads greater than this exhibited HPC. Shallow lateral cracking was observed for indentations > 3kg extending out to the tips of the surface radial cracks. Cleaving of the indentations was also carried out as in Lankford's investigations [38], however, Lube used lead acetate solution to penetrate the cracking formed during Vickers indentation to increase the crack contrast when viewed under SEM using a backscattered electron (BSE) detector (the contrast caused by BSEs is determined by a material's atomic number). Electron micrographs showed that the lead acetate solution had penetrated the cracks, and good contrast HPCs were seen for loads > 5 kg. A discrepancy in the cracking profile between the serial-sectioning method, and cleaving method was observed for 5 kg indentations, with apparent PC observation in the cleaved sample being attributed to incomplete penetration of the lead acetate into the cracks. hence making them appear to be PCs. In addition, both cleaving and serial sectioning revealed a volume of material directly beneath the residual indentation impression around which HPCs and PCs bordered but did not propagate into. This was a plastically deformed zone which exhibited material breakout when polished through, thought to be because of high levels of compressive stress, which would also explain the lack of crack propagation within it. Lube's studies have been extended by Miyazaki et al [40] who not only sought to investigate the applied load-crack profile relationship in silicon nitride, but also the effect that different microstructures may have. Twenty different silicon nitride samples with various microstructures, some of bearings grade standard, were Vickers indented with decreasing load from 10 kg to 1 kg with their crack morphology being determined via surface parallel serial sectioning and cleaving. Microstructure was found to influence the load at which the transition from HPC to PC occurred [40]. In coarse microstructures this was at < 5 kg but for fine microstructures PCs only existed at loads of 1 kg although some compositions

showed HPC even at that load. When the c/a ratio was > 2, HPC was observed regardless of the microstructure [40].

2.3.3. Silicon Nitride Bearings and Star Feature Formation

Investigating the fracture mechanisms of silicon nitride is of great importance in understanding how the material will behave in its applications, in particular for those where fracture can have very undesirable consequences. One such prominent application, and the research basis of much of this project, is the use of silicon nitride in hybrid ball-bearings. The advantage of silicon nitride bearings, over the more conventional steel ball-bearings, is their good high temperature properties, higher hardness, and the lower surface roughness that can be achieved [41]. This makes them ideal for applications where the operating environments are more extreme e.g. wind turbines, space vehicles [42]. However, there are also disadvantages compared to steel in the form of lower fracture toughness and higher manufacturing costs, attributed to long processing times and expensive processing materials [43].

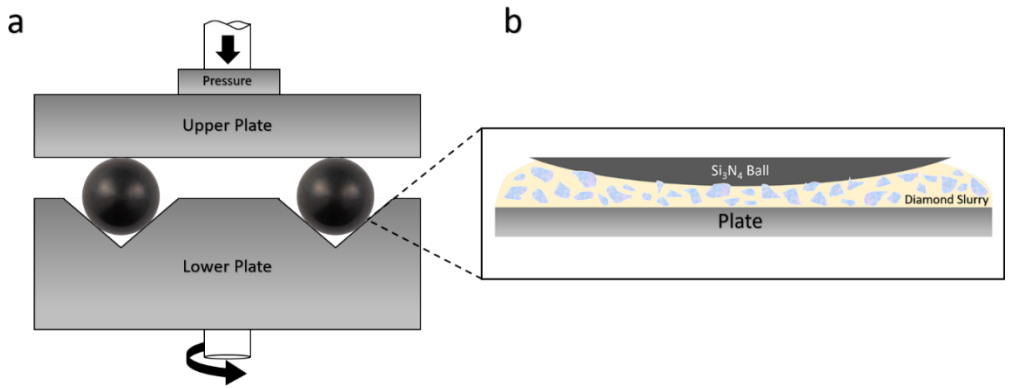

Figure 2.4: A schematic of the silicon nitride ball bearing lapping process: (a) The lapping equipment set-up. (b) A close-up of the bearing surface in contact with the diamond lapping paste.

Silicon nitride ball-bearings are generally manufactured using diamond lapping under load (Fig. 2.4) as the high hardness of silicon nitride requires an even higher hardness material for effective material removal. The primary material removal mechanisms within the lapping process are brittle fracture as a consequence of lateral cracks located parallel to the surface as well as radial cracks, and ductile cutting of surface material [44].

The contact of the diamonds under load with the ball surface can be considered like that of a sharp sliding indenter with the removal rate being determined by the load applied and the sliding speed. Typical loads and speeds used in the lapping process are of the order of 10 N and 50 rpm respectively [45]; the slow lapping speed is another contributor to the higher cost.

Under these high load lapping conditions undesired damage to the surface can occur in the form of micro-cracking, deep pits (Fig. 2.5(a)), and plastically deformed zones which can remain even after further polishing with lower loads [46], [47]; this process is shown in Fig. 2.5. One study found that 96% of ball-bearings observed contained surface pitting [48]. There are several reasons why these lapping induced phenomena are detrimental to the performance of the bearing: the change in surface microstructure causes changes in the localised fracture toughness and hardness of the material leading to weakened areas more prone to further damage [49]. Changes in surface roughness due to grain breakout from compressed zones after further polishing (as observed by Lube [39]) will inevitably change the tribological properties of the ball bearings in rolling contact i.e. when in contact with adjacent ball-bearings. In addition to this, the residual pits are susceptible to being sites of spalling and flaking on rolling contact as a result of the propagation of associated sub-surface cracking up to the ball-bearing surface causing material removal as seen in Fig. 2.5(c). The stress intensity at crack tips is already high in silicon nitride because of its hardness but there is further stress applied in Hertzian rolling contact leading to crack propagation [42], [50]. The stress levels reached by sub-surface cracks are higher when their distance from the surface is smaller, therefore it is the near surface lateral cracks that are the likeliest candidates for spalling [51].

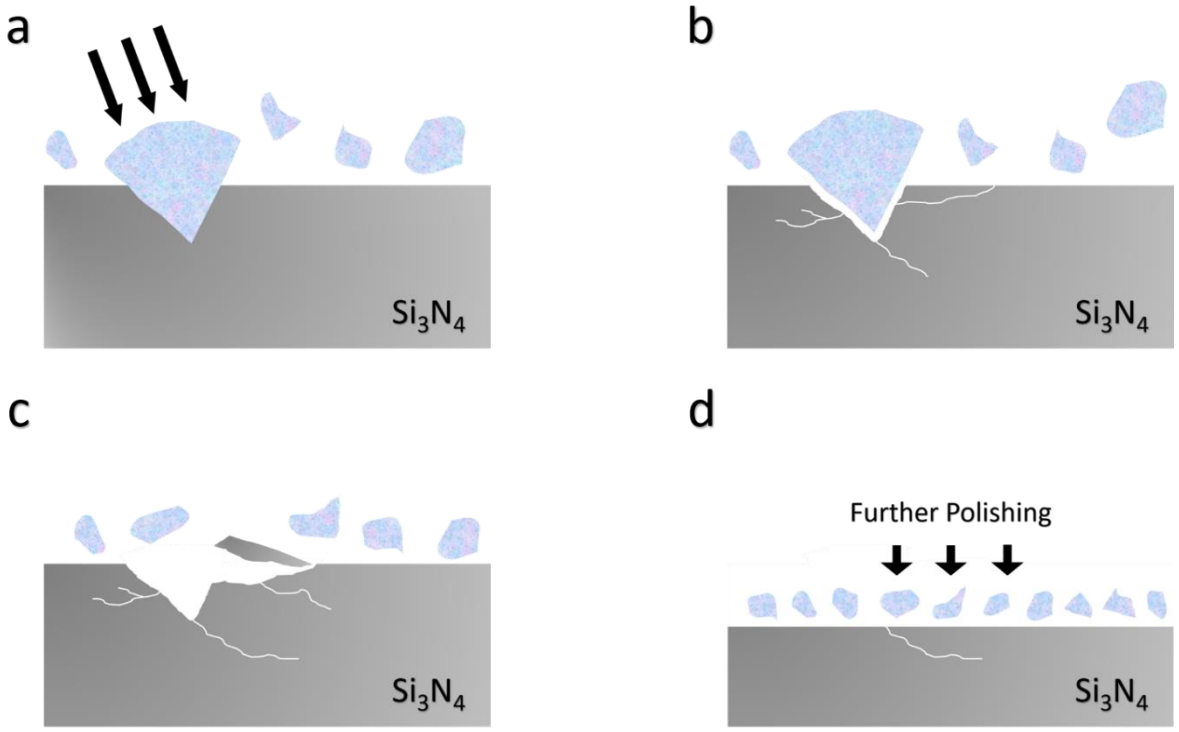

Figure 2.5: An illustration of the formation of star features on silicon nitride ball bearings during diamond lapping under load: (a) A diamond under load impacts the surface of the bearing. (b) This causes an indentation with associated surface and sub-surface cracking. (c) Under pressure cracks can propagate leading to chipping and flaking. (d) Continued polishing can remove the residual indentation impression leaving behind just cracking.

The size of residual pit-like features, often referred to as "stars" because of their physical appearance [52], [53], from which the spalling/flaking initiates, is a function of the size of the diamonds used for lapping and the load applied to these diamonds. This typically leads to a feature size of the order of ~ 100 μm from crack tip to tip. The size of these stars means that they are unlikely to lead to catastrophic failure of the balls, however, their presence, effect on ball performance, and evolution in working conditions means that they warrant investigation. Vickers indentation with diamond indenter tips can be used to replicate star features because of the similar morphology they generate, i.e. a central pit with associated cracking, both radial and lateral. Hadfield and Stolarski [54] Vickers indented silicon nitride ball-bearings with an applied load of 5 kg to see the effect that lubricated rolling contact would have on the indentations and the surrounding region. The ball-bearings were cycled 14 million times at a speed of 5000 rpm under a Hertzian contact pressure of 6.4 GPa (noted to be greater than normal operating pressure) in a four-ball machine. Subsequent SEM imaging revealed that radial cracks had propagated, lateral cracks had undergone spalling and one indentation revealed failure via

delamination of the material from the surface, as well as a region primed for further delamination.

Since the sub-surface nature of crack damage cannot be observed using SEM, dye penetrant that fluoresces under ultraviolet light can be used in conjunction with optical microscopy [51], [54]. The use of fluorescent dyes is effective in silicon nitride because it is slightly translucent meaning light emission from the dye that has penetrated the sub-surface can reach the surface. In the ball-bearing investigations by Hadfield and Stolarksi [54], the localised fluorescence gave further detail of the sub-surface damage, in particular the extent of the damage beneath the region where further delamination seemed likely. To verify the results of the dye penetrant, scanning acoustic microscopy (SAM) – a technique that uses focused sound waves to form an image [55], was successfully used to map the sub-surface damage at different depths. It was concluded that sub-surface damage may extend some distance (~ 35 μm) from observed surface radial cracking, and that the delamination failure is accelerated by lubricant under pressure entering the surface cracks leading to crack opening.

The observed morphology of a star feature in a new ball is dependent on any further polishing that occurs after its initial formation because the affected ball-bearing will continue being processed regardless [56]. For instance, a star which has just been formed will have the characteristic central pit and surrounding cracking (Fig. 2.5(a)) whereas a star which has undergone subsequent polishing may just be left with cracks and a flat polished central zone (Fig. 2.5(b)), or potentially just cracking if the compressed zone has been polished through (Fig. 2.5(c)). The lack of a pit reduces the potential contact area but even the remnant cracks can serve as further crack nucleation point under contact loading as investigated by Wang and Hadfield [48], [57]. To investigate this, line features (i.e. single radial cracks) on silicon nitride ball-bearings were cycled in a four-ball machine and viewed under SEM to track crack evolution [48]. Both spalling and fatigue crack growth were observed, with additional secondary surface cracks forming around the original line defect because of the increase in surrounding tensile stress as the line defect crack opening widens because of local plastic deformation. It is these secondary surface cracks that are thought to be the cause of spalling when they propagate downwards from the surface and intersect with the line defect that has itself undergone sub-surface propagation perpendicular to the surface. These predictions of sub-surface propagation in silicon nitride have been observed by Zhao et al [58] by sectioning and then incrementally polishing through cracks post rolling contact fatigue testing. Cross-sections of cracks with

and without spalling, as well as those that exhibited partial spalling, were viewed optically with ultraviolet illumination: a non-spalled sample showed an increase in crack depth as the mid-point of the crack was approached as well as crack propagation laterally. A spalled sample revealed that spalling had not arisen from the initial crack and was most likely initiated from branching of secondary surface cracks. Polishing through the partially spalled crack gave good insight in to the spalling mechanisms; a section which had not yet flaked off showed that the initial crack had propagated parallel to the surface and subsequent crack branching along this crack had started extending upwards but without intersecting the surface. Secondary surface cracks were also viewed to have propagated down in to the ball-bearing and connected with the branches from the initial crack leading to the formation of a crack network and resultant flaking. These investigations, along with complimentary computational analysis also by Zhao et al [59], lead to a mechanism of spalling from pre-existing cracks in silicon nitride bearings when put under rolling contact: Hertzian pressure in combination with bending pressure from the initial crack induce tensile stress in the surrounding region that causes the opening of secondary surface cracks which propagate downwards. Subsequent intersection with the primary crack, and its branching, that has extended laterally beneath the surface causes material removal via spalling [53]. Serial sectioning via incremental polishing can reveal useful information about sub-surface cracking; however it is a destructive method, meaning that samples investigated in this way are changed in the process. Therefore, investigation techniques with the ability to observe sub-surface cracking without inducing mechanical damage are highly desirable.

2.4. Micro X-ray Computed Tomography (Micro-XCT)

2.4.1. XCT Theory

X-ray computed tomography (XCT) is a non-destructive technique used for obtaining images and material property information from the interior of a sample. The most well-known application of XCT is in medical industry where it is commonly utilised to evaluate human bodily structures e.g. bone fracture [60]. In the area of material science, XCT is now widely used to view material microstructures for correlation with their macroscale properties. The basic principle, shown in Fig. 2.6, involves an x-ray source emitting high energy photons towards a sample which are then detected by a scintillator on the opposing

side and used to form a grayscale image. The contrast in the image is a function of the x-ray attenuation: the decrease in intensity of the x-rays as they traverse the material. This is determined by the photon scattering and absorption mechanisms, which in turn are dependent on the materials density and composition [61], [62]. Therefore, materials with a high density will generally have higher x-ray attenuation and hence appear darker in a grayscale image. The intensity of radiation incident on the detector is related to Beer's Law given in Eq. 2.2:

$$I = I_0 e^{-x\mu}$$

Equation 2.2: The relationship between x-ray intensity (I) at the detector, initial intensity (I_0), and the material of interest.

where I_0 and I are the initial and final intensity respectively, x is the x-ray path length and μ a material dependent attenuation coefficient [63]. This is a simplified situation for the actual intensity detected in practice because samples often contain more than one material as well as variations in density. In addition to this, Eq. 2.2 assumes a monochromatic x-ray source when for most devices the source emits across a range of energies meaning an integral over this range must be taken.

The usefulness of a single 2D plane image, called a radiograph, is limited because it only gives an average of x-ray absorption meaning that gauging three-dimensional positional information of features is not possible. For instance, if a porous region with low absorption was located behind a dense region of high absorption there would be no way of distinguishing these microstructures. In XCT scans this problem is overcome by rotating the sample (or rotating the source and detector combination whilst the sample remains static) around a single axis whilst taking images at set angle increments. These images are then used in conjunction with tomography algorithms to create a 3D reconstruction of the sample where each voxel (the equivalent of a pixel but in 3D space) is representative of the x-ray absorption and hence material density at any given location; allowing for the advanced 3D visualisation of the internal structure. The 3D reconstruction can then be digitally sectioned along any plane and converted to a stack of 2D images for further analysis. A schematic of this whole process is shown in Fig. 2.6 [60].

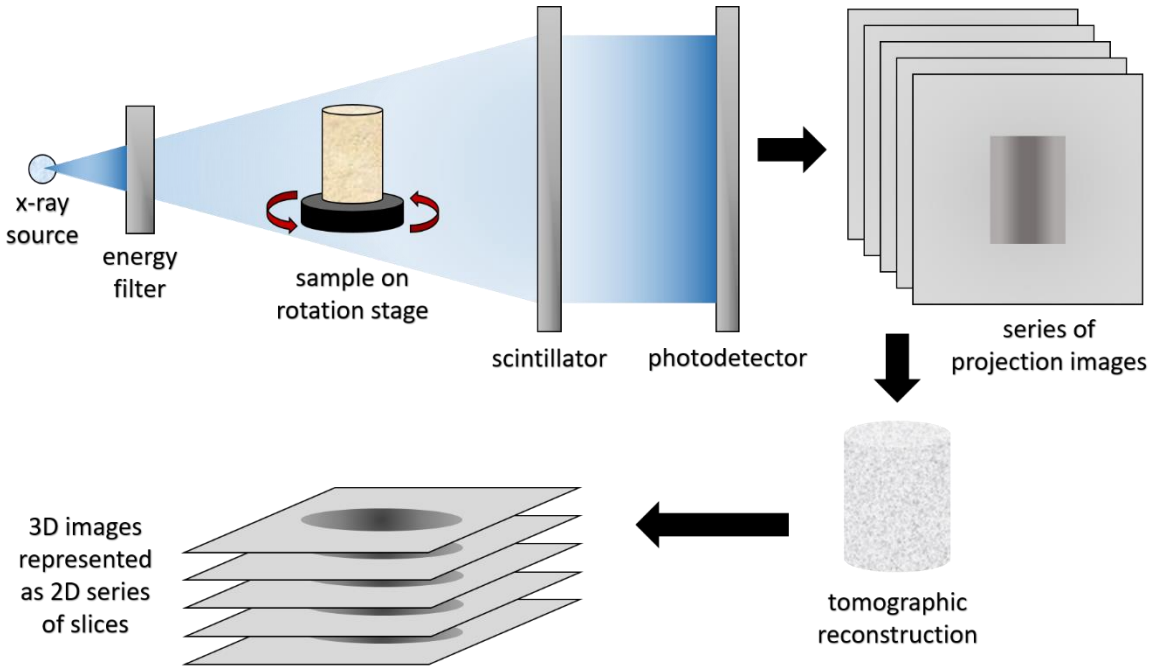

Figure 2.6: A schematic showing the x-ray tomography process from the initial sample imaging to the tomographic reconstruction.

2.4.2. XCT for Fracture Investigations

The spatial resolution of an X-ray Computed Tomography (XCT) device is determined primarily by the x-ray source spot size, sample-detector position, and the detector attributes. The development of these devices over recent years has led to the emergence of microscale-XCT, and even nanoscale-XCT [60]. The increase in resolution has been key to XCT use in materials science as it has allowed for non-destructive internal investigations of materials approaching resolutions (~ 50 nm) previously only reserved for surface characterisation techniques (although nano-XCT is limited to samples < 15 μm in size) [64]. Typical lab-quality devices have a spatial resolution of ~ 0.5 μm. It is therefore clear to see why XCT is desirable in the study of sub-surface fracture, particularly at scales where other non-destructive methods become difficult to apply.

Even with the higher x-ray CT resolutions available, observing microscale cracks is not trivial because they must be within a block of material that encases the whole crack with representative stress state, and they also must be open, in order to be visible in a tomography scan. However, a crack with width less than the pixel size can still potentially be detected by the change in contrast of the pixel in comparison to an adjacent pixel due to the presence of the crack; cracks with opening displacements of < 1.8 μm have even

been detected using this method where the crack width was one tenth of the pixel size (2 μm pixel size) [64]. It has been found that an alternative type of x-ray contrast, called phase contrast, is more suited to detecting cracks than the conventional absorption contrast dictated by Beer's Law (Eq. 2.2) [65]–[67]. Absorption contrast is determined by the change in intensity of the x-rays as they permeate through different materials whereas phase contrast is a product of small changes in refractive index typically between low attenuation volumes that causes local changes in the x-ray path length causing a phase change. Phase contrast is particularly prominent for cracking where diffraction fringes increase the edge contrast, hence making them more detectable. A disadvantage of phase contrast is that it requires a coherent x-ray source, i.e. a source with a single x-ray wavelength and constant phase difference. This is only possible using advanced lab tomography devices or a synchrotron source in which the x-ray radiation is emitted from radially accelerated charged particles. Synchrotron sources are advantageous to lab sources in many ways: they offer significantly increased flux (<1000x that of lab tomography), a smaller source, and a parallel beam geometry allowing for higher resolution and faster scan times. However, the number of synchrotron facilities is limited as a particle accelerator is required for the x-ray emission [68].

Synchrotron x-ray tomography in conjunction with phase contrast imaging has been used to study sub-surface Vickers indentation damage in polycrystalline alumina [69]. Vertyagina et al [69], [70] performed in-situ indentation to measure crack opening displacement on loading and unloading for an applied load of 34 kg. Tomography scans were taken before, during, and after loading, with pores within the alumina being used as reference points in order to correlate the material displacement in a technique known as Digital Volume Correlation (DVC). Although not directly observed in the images, lateral cracking beneath the indentation was inferred by the upward displacement (~ 1 μm) of material on unloading, extending out to the radial crack tips. Radial cracks were visible via the phase contrast exhibited but not from attenuation contrast, and the cracks had an estimated width less than that of the voxel size (0.9 μm).

Although useful for the detection of cracks, phase contrast does have its limitations, for instance, when applied in lab-based tomography (i.e. not synchrotron) long acquisition times (> few hours) are required to get sufficient contrast [67]. In some cases, it may be beneficial to instead find ways of increasing crack visibility when using a lab x-ray source. Such a study comparing various methods of crack imaging in XCT was carried out by Wu et al [71], [72] on glass-fibre composites. The three methods in addition to phase contrast

investigated by Wu et al were: increasing image resolution (by decreasing the pixel size), using an applied load to open up the cracks hence making them more visible, and penetrating the cracks with a high attenuation dye to increase their contrast. Both increasing the resolution and crack opening via loading (although this can change the crack geometry) were found to be effective, in essence because they increase the pixel count associated with a crack. The most effective method was the use of zinc iodide penetrant as a contrast agent with cracks being detectable down to $1/10^{th}$ of the spatial resolution (~ 0.2 μm) although the success of this method is based on the full saturation of cracks with the penetrant as well as the cracks intersecting with the surface in order for the penetrant to enter in the first place. It is also noted that crack opening is clearly not determinable when the width of the crack is less than that of the spatial resolution. It is therefore apparent that a higher resolution method is required for observing sub-surface features on the micro and nanoscale.

2.5. Focused Ion Beam – Scanning Electron Microscope (FIB-SEM) Tomography

2.5.1. FIB-SEM Theory

The focused ion beam (FIB) is a technique that was originally developed in the late 1960's and became commercially available from the 1990's. Initially it was primarily used for the machining of integrated circuits within the semi-conductor industry [73]–[75]. More recently it has found widespread applications in materials science as a method of imaging and sputtering away material from samples in order to reveal the sub-surface microstructure, as well as for the precision preparation of transmission electron microscope (TEM) samples [76], [77].

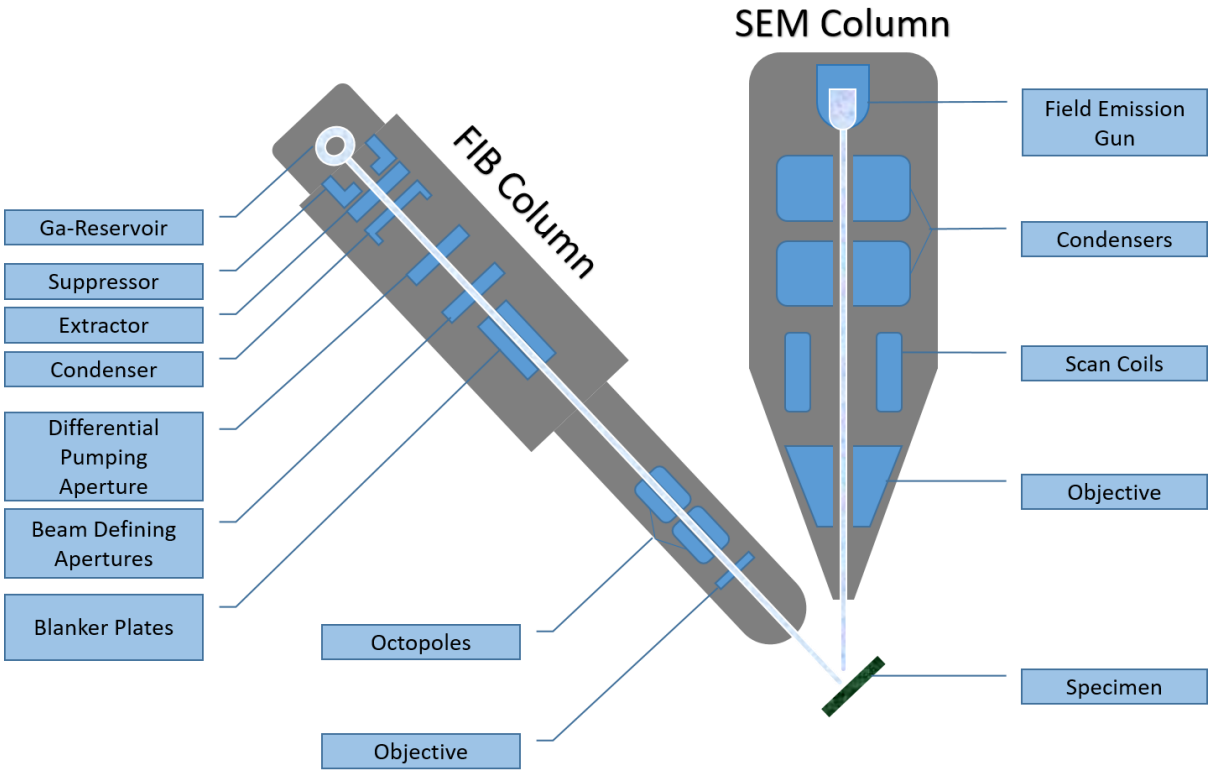

Figure 2.7: A diagram showing the key components of a Focused Ion Beam (FIB) and a Scanning Electron Microscope (SEM), setup in a FIB-SEM configuration.

The ion beam is emitted from a liquid metal ion source (LMIS) that is formed in to a Taylor cone (a cone that emits charged particles formed from electrically conductive fluid in the presence of an electric field) by a strong electric field (of the order of ~ 10^{10} Vm^{-1}) at the tip of a tungsten needle. The needle itself is typically 10 µm in radius and is wetted with the liquid metal which in most cases is gallium [74]. Conventional FIB devices use gallium as their LMIS because of its low melting temperature, low vapour pressure and low volatility which allow for easy manipulation and good stability [78]. The now ionised gallium at the Taylor cone tip (which generally has a radius ~ 5 nm but this is dependent on emission current) is extracted down towards the suppressor (Fig. 2.7) where the current is subsequently stabilised to between 1-4 µA [76]. Thereafter, a combination of the objective and condenser lens are used for definition and focusing of the beam onto the sample with the beam diameter and current being determined by further beam defining apertures. Deflection and blanker plates manoeuvre the beam across the sample surface, and stop it, respectively (the blanker plate does not so much stop the beam but more acts to deflect it away from the sample). In addition, octopoles are used to keep the beam profile circular as it is not just optical lenses that are subject to astigmatism; non-uniformity of fields produced by the electrostatic components within a FIB device produce a similar

effect. Once incident on the surface, the beam energy is typically set between ~ 5-50 keV with a current range of ~ 1 pA-65 nA depending on the beam requirements (imaging, sputtering, deposition etc.) [79].

The spatial resolution of a FIB device (for both imaging and milling purposes), unlike in scanning electron microscopy (SEM), is only partially determined by the beam spot size. The limiting factor for this is a combination of spherical aberration from the electrostatic lenses, and the chromatic aberration that arises from the energy distribution of the ion beam. This results in an achievable resolution of ~ 5 -10 nm (with a Gaussian profile). However, the primary determining factor actually comes from the signal to noise ratio caused by the sputtering away of the sample surface by the incident Ga^+ ions [80], [81]. This not only has the effect of modifying the features that are being imaged but it also limits the beam dwell time which is directly related to the signal produced. Therefore, the resolution for FIB often depends on the sample that is being imaged as the sputtering rate is material specific.

It is the plethora of interactions with the sample surface that makes FIB such a versatile technique. The transfer of kinetic energy as incident ions contact the surface induces a range of phenomena: sputtering of surface atoms/ions, electron and electromagnetic radiation emission, atomic displacement, ion reflection, sample heating, chemical reactions via bond breaking, as well as Ga^+ implantation [74], [75]. For imaging, it is primarily the ion-induced secondary electrons (ISEs) emitted from near the surface of the sample via inelastic ion collisions that are detected. However, secondary ion emission can also be utilised for techniques such as secondary ion mass spectroscopy (SIMS) [79]. When viewing crystalline materials, channelling contrast is observed as incident ions are directed along certain crystal lattice orientations, and as the ISE emission is a function of ion penetration depth, different crystal orientations produce different contrasts [82]. This in turn means that channelling contrast varies with the ion beam angle of incidence. Due to the implantation of Ga^+ ions into the surface of the material, FIB is occasionally used to image insulating samples as it inhibits negative charge build up that would often be associated with SEM imaging at comparable voltages [74]. In addition, any positive ion build up can be removed with an electron flood gun [83].

The main advantage of FIB in comparison to SEM is its ability to mill and modify a sample via the sputtering away of atoms. There is always a certain degree of sputtering when the ion beam is incident upon the sample surface; however, for milling, deliberately higher currents are used to increase the sputtering rate. Since atoms are removed from the

surface via inelastic collisions with the Ga^+ ions, the sputtering rate is dependent on the material being milled. For example, silicon has a sputtering yield (atoms removed/ions incident) of 1.98 at 30 keV whereas aluminium has a yield of 2.91 [75]. It is important to note though that net sputtering yields calculated through simulations are often overestimates, as they do not take in to account the redeposition of sputtered atoms onto the area they were originally sputtered from. The incident angle of the ion beam also has an effect on the sputter yield and, although it may seem intuitive that the highest yield comes at an angle of 90° (in relation to the surface), the optimum angle is actually ~ 80° due to the proportion of incident Ga^+ ions that are backscattered when the incident ion beam is perpendicular to the surface [74].

One of the common applications of sputtering using a FIB is to reveal the sub-surface structure of the sample that has been milled. For instance, it can allow for the observation of grain microstructure in materials and highlight sub-surface phase transitions. This is quite a slow process with solely a FIB device as simultaneous milling and imaging is not possible; imaging can only be undertaken once the milling has been completed as the same beam is used for both purposes. Even at the level of current used for imaging (~ 50 pA), material sputtering still occurs, and in addition to this the angle of the incident beam in relation to the surface also has to be adjusted for viewing the sub-surface cross-section that has been revealed; a time-consuming process, particularly when incremental milling and subsequent imaging is required. It is these reasons, amongst others, that led to the development of a "dual beam" system incorporating both FIB and SEM columns [82].

SEM theory will not be discussed in great depth here, but the basic premise is similar to that of a FIB device in that charged particles emitted from a source are focused on the surface of a sample using lenses. The main differences being that electrons are negatively charged, SEM's have a higher resolution than Ga^+-FIBs, and the lenses used within an SEM can be electromagnetic due to their low mass in comparison to ions [84], [85]. But it is not just the makeup of the instrument components that differ from FIB, the greatest advantage of a dual FIB-SEM system is that electrons incident on the sample surface have different interactions to the Ga^+ ions from the FIB meaning alternative information can be obtained. Similar to incident ions, incident electrons produce secondary electron (SE) emission via inelastic collisions, however they also produce backscattered electrons (BSE) in elastic or inelastic collisions, or BSEs with an additional x-ray emission if the interaction is inelastic [86]. SEs are generally lower energy than BSEs and therefore can only escape from the top surface layer (< 20 nm). This allows them to be used for obtaining

topographical information as well as higher resolution imaging than BSE images which have a larger escape volume and hence provide lower resolution images. Because their scattering probability is dependent on the mass of the atomic nuclei they collide with, BSEs are often used to determine differences in material composition across a sample [87], [88]; so-called "Z-contrast", where areas of higher average atomic number appear brighter when imaged from BSEs.

With the advantages of both SEM and FIB being combined, as well as some additional advantages as a result of the combination (in-situ imaging whilst milling etc…), it is clear to see why a dual-beam FIB-SEM system is favourable. The first iteration of the FIB-SEM was developed by Sakamoto et al [89] as a proof of concept for creating 3D elemental maps using Auger spectroscopy. The experimental set-up consisted of a Ga^+ FIB and an electron beam angled at 90° to each other both incident on an aluminium wire. The FIB was used to incrementally mill away slices of the wire whilst after each slice the electron beam was used to image the newly revealed cross-section via SE detection. The SE images of the successive cross-sections were subsequently collated giving a 3D representation of the wire. Progression to 3D elemental mapping would simply require the addition of an Auger electron detector. Modern FIB-SEMs often use the incremental slicing and imaging via FIB and SEM respectively for the creation 3D structural reconstructions and elemental mapping in what has been termed FIB tomography. This has been particularly useful in the area of materials science where high resolution, sub-surface grain and composition analysis is highly desirable. Konrad et al [90] were the first to pair FIB-SEM with electron backscattered diffraction (EBSD) to observe orientation gradients surrounding a specific phase within an Fe_3Al-based alloy by imaging sliced cross-sections using conventional 2D-EBSD and then using these slices to successfully form a 3D-EBSD map. EBSD mapping does require stage tilting in order that the serial-sectioned surface is orientated towards the detector and this can cause misalignment of the area of interest when the stage is returned to the milling position. A solution to this problem was developed by Groeber et al [91] when creating a 3D-EBSD map of the grain structure in a Ni-based polycrystalline super alloy. They used milled fiducials in conjunction with image recognition software to correct for rotation misalignment and stage drift which allows for a constant thickness and location for FIB-milled slices. This is greatly advantageous in producing an accurate 3D reconstruction of the grain microstructure that is not possible with manual re-alignment. In addition, the image recognition and stage adjustments were automated allowing for a less time-consuming process.

FIB tomography was originally undertaken with just a FIB device (prior to the addition of a SEM column) used for both milling slices and imaging after a subsequent change of angle to observed the revealed cross-section [92]. However, the constant movement of the stage required for the FIB-only methodology brings in mechanical drift which puts a lower limit on the spacing of slices that is significantly larger than that of the FIB resolution [93]. This mechanical drift is all but eradicated with the use of a dual-beam FIB-SEM system as there is no stage adjustment necessary for successive slice milling and imaging.

2.5.2. FIB-SEM Tomography for Indentation and Fracture Investigations

Interestingly for this project, some of the first FIB tomography work was conducted on indentation sites in an alumina-silicon carbide composite with the aim of mapping the sub-surface crack morphology. Inkson et al [94] used solely a FIB to both image and mill cross-sections through a 1 N Vickers indentation with the cracking being successfully mapped in three dimensions. They did however note that some of the very finest cracks may not have been observed due to sputtering of material into them by the milling process or lack of imaging resolution. Similar investigations were carried out by Elfallagh and Inkson [95] of 0.5 N, 1 N and 2 N indentations on alumina with a view to critically analysing FIB tomography methodology for sub-surface crack mapping. The ion beam was used to serial section the indentations with a trench depth of 10 μm, slice thickness = 0.25 μm and a SEM imaging angle of 55°. Similar crack morphologies were observed under each load with radial cracks from indentation corners being linked by deep laterals. As well as observing the presence of fewer cracks beneath the residual indentation impression, the crack density and maximum length was measured to be reduced in the second half of the indentation in comparison to the first. This is put down to the destructive nature of FIB in that the opening of a new free surface via milling will inevitably change the local residual stress and hence influence the length, width and morphology of nearby residual cracks.

Xie et al [96] used FIB to observe the sub-surface cracking induced by indentation, scratch tests, and grinding on silicon nitride-based SiAlONs with differing grain morphologies (fine equiaxed and large elongated morphologies). The FIB cross-section through a 1 kg (10 N) Vickers indentation showed the presence of interconnecting radial and lateral cracking with the lateral cracks propagating progressively deeper and their morphology being dependent on that of the radial cracks present. FIB milling through ground down

areas revealed that lateral cracking that had intersected with the surface was the main cause of material removal on the equiaxed grain sample, whereas for the elongated grain sample material removal was minimal in comparison and only micro-cracking was observed. This led to the conclusion that elongated grains can reduce crack propagation and hence material removal. Cracking directly beneath and along the sides of the scratch track were lateral and radial in nature respectively, leading to a difference in material removal mechanisms.

Consecutive FIB milling and imaging of a sample with the aim of 3D mapping is a time-consuming process that requires periodic adjustment of beam and stage parameters. Therefore, the automation of this process is an area which has invited a lot of interest [97]–[99], particularly for FIB device manufacturers. Schaffer et al [97] were the first to develop such system in order to carry out 3D elemental analysis using energy dispersive x-ray spectroscopy (EDXS) on a large area ($15 \times 15 \times 15$ μm^3) of a non-conductive ceramic (Ca)$MgTiO_x$ without the requirement for a microscope operator to be present during long acquisition times (> day). Automation of the milling and imaging (with EDX mapping) was achieved by scripting routines in the microscopy software programming language. A non-conductive sample was chosen as they have additional complications associated with them in comparison to conductive samples (a successful automated milling process of an insulating sample is directly transferable to conductive samples). For instance, there can be variations in brightness across the milled cross-section when imaging with SEM due to localised charge build-up on the surface. The ion and electron beams also experience drift as a result of local changes in electric and magnetic fields; for the electron beam this means scans to be used for a 3D reconstruction have to be aligned in post-analysis, and for the ion beam, the accuracy of the location and thickness of successive FIB-milled slices is affected. General problems associated with FIB milling are also cited: a decrease in detected electron signal as a function of depth causes a brightness gradient on the cross-section. In addition, there is a shadowing effect caused by the presence of the trench side walls. For larger volumes, milled material redeposited on to the trench walls can obstruct the view of the cross-section with the area obstructed increasing with each milled slice. It was noted by Schaffer et al [97] that the viewable area of their sample cross-section was reduced by a third from that of the original setup due to redeposition. They showed that the amount of redeposited material was directly dependent on the number of slices, the slice depth and thickness, but not their width. Redeposition and shadowing effects were removed by milling two side trenches around the area of interest in addition to the conventional front trench to create a “U-pattern”. The width of one side trench was set to

a third of the planned milled slice height to decrease redeposition whereas the front and remaining trench size were determined by the EDX detector and electron beam. The depth of the side trenches was set a few microns deeper than the desired cross-section height so as to decrease shadowing and charging effects. Ion beam drift was calculated by comparing successive BSE images of the milled area in order to measure slice thickness. Any slice thickness differences were then taken in to account during 3D reconstruction. For the electron beam drift correction an overview BSE image was taken after each slice that contained both the cross-section and the sample surface. Since the FIB was only incident on the area to be sliced during milling, the rest of the sample surface remained unchanged and was thus used to align the stack of BSE overview images. The alignment data from the overview images could then be used to align more detailed BSE images of just the cross-section and hence also the EDX maps of the same area allowing for a well aligned 3D elemental reconstruction. This data correction process was automated via the creation of scripts within image analysis software.

A similar automation process was used by Payraudeau et al [99] for the FIB tomography of a 2 N Vickers indentation on a highly insulating ß-SiAlON, with the aim of producing a sub-surface map of the indent-induced cracking. However, they did not use the "U-pattern" trench shape to reduce shadowing and redeposition citing Elfallagh and Inkson's observation [95], [100] that opening new free surfaces will change the localised residual stress and may induce crack propagation or closure. To correct for ion beam drift, x-shaped fiducial markers were FIB milled into the sample surface away from the region of interest. These markers were imaged after each slice and subsequent re-alignment applied. The 2D SEM images of the cross-sections were collated together and cracks traced using software in order to interpolate the crack pathways and create a 3D map of the cracking underneath the indentation.

The latest automated commercial systems utilise X-shaped fiducial markers as standard to counteract ion beam drift, as well as software for automated milling and imaging [101]. However, there still remains problems in the methodology of FIB tomography for 3D reconstructions. Although slice thickness can accurately be measured and the ion beam adjusted to ensure milling position is precise, the consistency of slice thickness is still not guaranteed with variations of ± 50% recorded [102], [103]. Again, this is more prevalent on ceramic samples where charging effects at the surface can affect the ion beam. Even using a fiducial can not necessarily ensure a correct milling location as at high ion beam currents the fiducial itself undergoes significant sputtering when being imaged for drift

correction [93]. Therefore, variations in slice thickness should be taken into account when viewing 3D reconstructions as they may not provide an accurate representation if not corrected for during reconstruction processing.

2.6. Gas Field Ion Source (GFIS) Microscopy

2.6.1. GFIS Theory

Within the last decade a new development in FIB technology has arisen with microscopes that use a gas field ion source (GFIS) instead of the LMIS (gallium) used in conventional devices. The two currently favoured sources used with GFIS microscopy are the noble gases helium and neon. The first attempts at creating a working GFIS microscope involved applying a voltage to a tungsten spherical-shaped needle tip with diameter ~ 100 nm in order to give it a positive bias and induce a large electric field up to 40 V/nm [104]. The gas atoms are then drawn towards the needle due to the large electric field and positively ionised, causing them to subsequently accelerate away from the needle. The problem with this method is that the gas ions are ionised across the whole diameter of the needle tip and in effect this produces multiple ion beams. The solution to this was to manipulate the spherical tip into a three-sided pyramid with the apex consisting of just three atoms; known as a trimer tip (Fig. 2.8). This means that the ionisation of the gas atoms occurs just at the trimer tip allowing for the emission of the ionised gas atoms per tip atom to increase by orders of magnitude. A single atom from the three at the trimer tip is then chosen as the beam, hence allowing for a monochromatic, high brightness ion source (the beams from the other two tip atoms are directed elsewhere) [105]–[107]. The main requirement when choosing a gas source for GFIS microscopy is that the ionisation energy of the source is higher than that of any contaminants (e.g. nitrogen, carbons dioxide, oxygen) that may be present within the emission vicinity. This ensures that the contaminants are ionised before reaching the trimer tip. The high ionisation energy of nitrogen (15.6 eV) limits the gas sources that can be used, but fortunately helium and neon have sufficiently high energies (24.5 eV and 21.6 eV respectively) [108]. In practice, GFIS devices have both helium and neon sources as it is easy to simply switch the gas being released near the needle. A schematic of a GFIS device is given in Fig. 2.8 below:

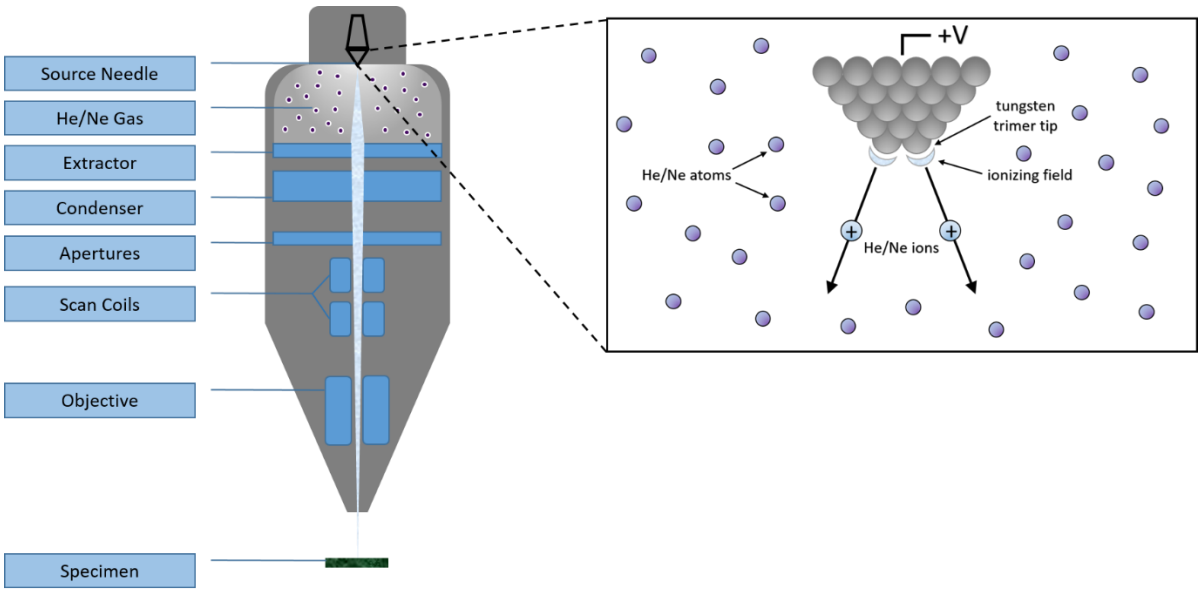

Figure 2.8: A schematic of a Gas Field Ion Source (GFIS) microscope. Inset is an illustration of the interactions at the trimer tip.

The use of the helium GFIS for imaging purposes, sometime referred to as helium ion microscopy (HIM), has many advantages in comparison to imaging with a gallium source or an electron beam. For instance, helium has a smaller sample interaction volume, has a higher secondary electron yield, and is a source of greater brightness which leads to spatial resolutions of < 0.25 nm [106], [109]–[111]. Fig. 2.9 shows the results from Monte Carlo simulations undertaken by Cohen-Tanugi and Yao [112] as to the interaction of 30 keV gallium, helium, and electron beams down to a depth of 20 nm in a silicon sample. It can be seen that at the electron escape depth (~10 nm), the helium beam width is only 1 nm in diameter in comparison to 15 nm for gallium and 2 nm for SEM. The reason for this smaller interaction volume relates to the energy loss interaction of the helium ions: for helium ions, which possess a low Z number, energy loss is initially dominated by the electronic stopping power until < 5 keV where the nuclear stopping power takes over. These electronically dominant interactions allow for decreasing interaction radii at high energies in addition to greater penetration depth than that of gallium ions and SEM. The lower mass of helium ions also means there will be less sputtering damage to the sample surface which is a concern when imaging with gallium [113].

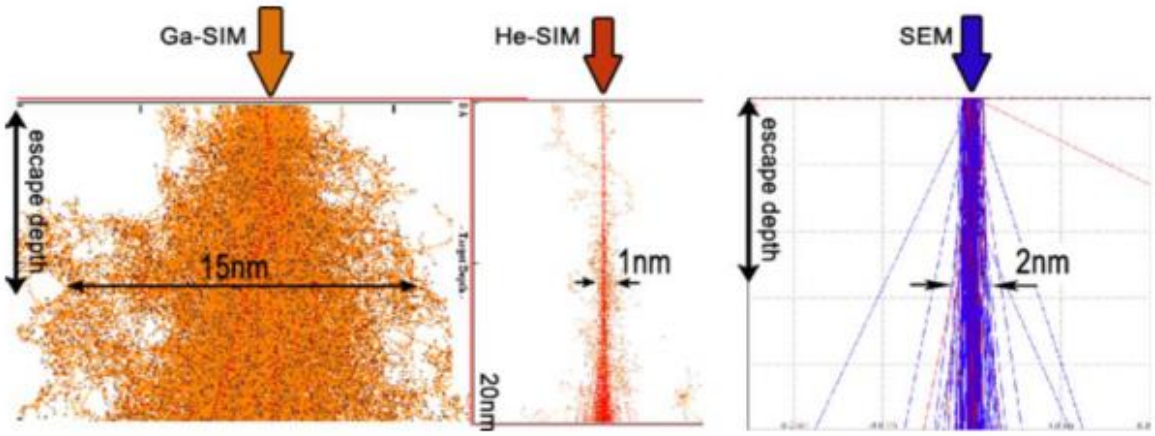

Figure 2.9: A Monte Carlo simulation of the interaction volume for gallium-source microscopy, helium source microscopy, and SEM. Taken from Cohen-Tanugi and Yao [112]**.**

2.6.2. Applications for Imaging Insulating Samples

The interactions of helium ions with a sample surface offer advantages in the imaging of non-conductive materials, e.g. biological specimens, ceramics, polymers [114]. Generally, when imaging insulating samples with ion/electron beams, a thin conductive coating of gold or carbon is applied to inhibit the build-up of charged particles, however, this can obstruct the view of surface features and make surface chemical analysis more difficult. Gallium ion-induced secondary electrons (ISEs) have been used for imaging insulating materials as the metallic gallium can implant at the surface creating a conductive layer [74], although a more conventional charge neutralisation method when ion imaging without a pre-applied conductive coating is to use an electron flood gun. This uses an electron beam incident on the area being imaged and allows for localised charge neutralisation as well as control of the magnitude of neutralisation via current and dwell time control. The charging associated with HIM is primarily positive and has contributions from a number of phenomena: the incident helium ions themselves are positive, and the high ISE yield from helium-sample interactions (as high as ten ISEs per incident helium ion in some materials [104]) leaves a positively charged surface layer. In addition to this, beam currents used with HIM (<0.25 pA) are generally lower than those of SEM (typically 1-2 nA current) so charge build-up is a more gradual process making neutralisation of the surface positive charge with a flood gun straightforward [114]. To date, imaging of non-conductive samples has mainly been in the area of biological research where the use of HIM in conjunction with a flood gun has proved particularly successful [115], [116]. Boden et al's [117] imaging of butterfly wings revealed that HIM provides

higher resolution and less localised charging than low voltage SEM, as well as offering a greater depth of field at higher magnifications allowing for features at different heights to be in focus simultaneously. A comparison between HIM and SEM imaging of a highly insulating tooth enamel sample by Bidlack et al [118] pointed to the same advantages of HIM but also noted that its high surface sensitivity means samples have to thoroughly cleansed of contamination to avoid unwanted imaging of a thin hydrocarbon surface layer. The lack of available chemical characterisation using HIM is also listed as a current shortcoming in contrast to SEM, but research is currently being conducted in the area of He-SIMS and SE spectroscopy [106], [119].

2.6.3. Neon Source GFIS Microscopy

Most GFIS microscopes have a neon source attached which can be used for imaging and may offer alternative imaging contrast to helium due to differing surface interactions (e.g. higher electron yield, greater nuclear stopping power). Neon ions do have a greater Z number than helium though resolutions higher than ~1.5 nm are hard to achieved because of the increased nuclear stopping power [120] However, one area where a neon source may be more beneficial than helium is in milling applications. Helium has been used for high resolution nanoscale milling e.g. for graphene device editing [121], but the increased sputter yield of neon (100x greater than helium at the same voltage [120]) as a consequence of heavier ion mass and increased current make it more suitable for milling larger volumes. The sputter yield is only 50% less than that of gallium ions yet neon offers advantages in the form of a smaller probe size, or situations where gallium implantation is not desirable (such as the formation of alloys when milling metals) [122].

2.7. Raman Spectroscopy for Stress Analysis

The previously discussed techniques for surface and sub-surface characterisation of fracture/indents on polycrystalline ceramics can provide good data about morphology and structure, but limited information is gained about the stress in and around such regions. One method for determining localised stress down to a spatial resolution of ~ 1 μm is Raman spectroscopy. The underlying principle of this technique is the inelastic scattering of monochromatic light at a surface of a material caused by interactions with vibrating

molecules [123]. The incident light (from a monochromatic source such as a laser) is absorbed by the vibrating molecules causing excitation and subsequent photon re-emission at a differing energy level. The energy of the emitted photon is characteristic of the material under incidence, hence making Raman spectroscopy a useful tool for chemical composition analysis; on a Raman spectrum the light intensity against wavenumber is plotted leading to peaks at certain wavenumbers. The energy of the vibrational modes can be changed by the residual stress of a material leading to a subsequent change in the position of peaks on the Raman spectrum as the energy of re-emitted photons changes; this is called the piezospectroscopic effect [124], [125]. The direction and magnitude of the peak shift determines whether the localised stress is compressive or tensile. A quantified stress value can then be obtained using Eq. 2.3:

$$\sigma = \frac{\Delta\nu}{\Pi}$$

Equation 2.3: Piezospectroscopic relationship between residual stress and shift in peak position.

where σ is the uniaxial stress, $\Delta\nu$ is the change in wave frequency, and Π is a material dependent property known as the piezospectroscopic coefficient which is determined by plotting the change in wave frequency of a specified Raman peak as a function of applied stress (usually using a bending bar in conjunction with a four-point bend jig).

The Raman spectrum of silicon nitride has multiple peaks ranging from ~180 – 1050 cm^{-1}, however not all of these peaks show a linear stress relationship that can be used to calculate the piezospectroscopic coefficient. The peaks which do show a strong linear dependence include the 730, 862, 927 and 937 (a doublet), and the 1045 cm^{-1} peaks [126], [127]. The 862 cm^{-1} shows the strongest linear dependence of all silicon nitride Raman peaks and has been used by Muraki et al [126] to map the stress around a Berkovich indentation with side lengths ~ 20 μm. Two line scans were taken from the indentation centre: one outwards in the direction of an indentation corner, and the other one outwards passing through the side of the indentation. The stress was found to be compressive around the indentation centre with a maximum at 10 μm away with both lines exhibiting similar stress profiles out to 25 μm implying an isotropic region of surface stress surrounding the indentation. However, the line scan passing through the indentation corner showed tensile stress from 25 – 45 μm outward which is present as a response to the compressive stress formed perpendicular to the indentation in order to maintain

equilibrium. It is this long range tensile stress that is responsible for radial cracks that sometimes emanate from indentation corners. At the indention centre, the Raman peaks were found to be broader; it is proposed that this is due to the compression from the indenter tip causing plastic deformation to occur at the centre and hence changing the lattice structure [126]. As an expansion on this work, Pezzotti et al [128]–[130] used Raman spectroscopy to compare bridging stresses behind the tips of notch-induced cracks for equiaxed and acicular (needle-shaped) grained silicon nitride. High levels of tensile stress were present in the wake of the crack tip for the acicular, but not for the equiaxed microstructure. This was attributed to the needle-like silicon nitride grains in the acicular sample undergoing crack bridging, and subsequent SEM images of these localised regions of high tensile stress revealed this to be true leading to the conclusion that crack bridging is a primary method of increasing fracture toughness in acicular silicon nitride. Further to this work, Tochino and Pezzotti [131] conducted Raman mapping surrounding a notched induced crack firstly with zero applied external load and then with the critical load for crack propagation. Again, high levels of tensile stress were observed at various locations behind the crack tip as a consequence of bridging stresses (more so closer to the tip). There was also significant tensile stress ahead of the crack tip which increased upon loading, as did the bridging stress due to traction of the bridging grains [131].

2.8. Summary

In this chapter, a review of the previous research into indentations on silicon nitride has been undertaken, as well as a review of the literature and theory of characterisation techniques used in this project. Investigations into indentation features on silicon nitride have rarely focused on actual ball star features, with artificial indentation (e.g. Vickers, Berkovich) being used instead because of its controllability. Observations of sub-surface cracking has primarily been carried out using serial sectioning via grinding or cleaving, in conjunction with optical and electron microscopy [39], [40], [57]. This has revealed valuable information about the nature and evolution of micro-pits, for instance that the application of pressure leads to secondary crack formation and sub-surface crack propagation to the surface resulting in material removal [48], [57]. These methods have also provided information on how the applied load influences the cracking regime beneath indentations. However, optical microscopy provides limited spatial resolution when viewing features < 1 μm in size, and although it offers higher resolution, electron

microscopy is insufficient for observing multiple manually ground serial-sectioned cross-sections within a reasonable timescale. An alternative to this is the use of a FIB-SEM microscope that allows for in-situ serial sectioning using the FIB whilst simultaneously imaging with the SEM at high resolution. This technique has previously been used successfully to observe sub-surface features on indented polycrystalline ceramics and create 3D reconstructions of crack maps [95], [99]. Another promising technique, with the advantage of being non-destructive, is micro-XCT. Although not having the resolution of SEM, crack contrast can be increased using propagation phase contrast imaging and crack penetration with high absorption dye [71], [72]. For high resolution surface characterisation, GFIS microscopy with an electron flood gun has been cited as new technology for imaging insulating materials removing the need for conductive coatings that can obstruct features, although to date only polymer and biological samples, not ceramics, have been investigated [115], [117], [118]. Raman spectroscopy for localised stress analysis has also been shown to be a useful technique in gauging stress levels surrounding cracks in silicon nitride [126], [131]. Separately the techniques reviewed in this chapter can offer different information, each with their own advantages and disadvantages. However, if combined, there is the potential for a more complete picture of the morphology and characteristics of star features on silicon nitride balls to be constructed.

2.9. References

[1] Z. Krstic and V. D. Krstic, "Silicon nitride: The engineering material of the future," *J. Mater. Sci.*, vol. 47, no. 2, pp. 535–552, 2012.

[2] S. Hampshire, "Silicon nitride ceramics - review of structure, processing and properties," *J. Achiev. Mater. Manuf. Eng.*, vol. 24, no. 1, pp. 43–50, 2007.

[3] C.-M. Wang, X. Pan, M. Rühle, F. L. Riley, and M. Mitomo, "Silicon nitride crystal structure and observations of lattice defects," *J. Mater. Sci.*, vol. 31, pp. 5281–5298, 1996.

[4] A. J. Moulson, "Reaction-bonded silicon nitride: its formation and properties," *J. Mater. Sci.*, vol. 14, no. 5, pp. 1017–1051, 1979.

[5] H. M. Jennings and M. H. Richman, "Structure, formation mechanisms and kinetics of reaction-bonded silicon nitride," *J. Mater. Sci.*, vol. 11, no. 11, pp. 2087–2098, 1976.

[6] F. I. Riley, "Silicon Nitride and Related Materials," *J. Am. Ceram. Soc.*, vol. 83, no. 2, pp. 245–265, 2000.

[7] H. Suematsu, M. Mitomo, T. E. Mitchell, J. J. Petrovic, O. Fukunaga, and N.

Ohashi, “The α-ß transformation in silicon nitride single crystals,” *J. Am. Ceram. Soc.*, vol. 80, no. 191860, pp. 615–620, 1997.

[8] M. J. Hoffmann and G. Petzow, “Tailored microstructures of silicon nitride ceramics,” *Pure Appl. Chem.*, vol. 66, no. 9, pp. 1807–1814, 1994.

[9] B. T. Lee, B. D. Han, and H. D. Kim, “Comparison of fracture characteristic of silicon nitride ceramics with and without second crystalline phase,” *Mater. Lett.*, vol. 58, no. 1–2, pp. 74–79, 2004.

[10] S. Ii, C. Iwamoto, K. Matsunaga, T. Yamamoto, and Y. Ikuhara, “TEM in situ observation of fracture behavior in ceramic materials,” *Appl. Surf. Sci.*, vol. 241, no. 1–2 SPEC. ISS., pp. 68–74, 2005.

[11] S. Wei, L.W. Porz, Z. Xie, B. Liu, J. Chen, W. Xue, “Crack propagation in silicon nitride ceramics under various temperatures and grain boundary toughness,” *Mater. Sci. Eng. A*, vol. 632, no. April, pp. 58–61, 2015.

[12] H. Kawaoka, T. Adachi, T. Sekino, Y.-H. Choa, L. Gao, and K. Niihara, “Effect of α/ß phase ratio on microstructure and mechanical properties of silicon nitride ceramics,” *J. Mater. Res.*, vol. 16, no. 08, pp. 2264–2270, 2011.

[13] Pavol Sajgalik, “Relationship between Microstructure, Toughening Mechanisms, and Fracture Toughness of Reinforced Silicon Nitride Ceramics.” pp. 2619–24, 1995.

[14] M. Döblinger, G.B. Winkelman, C. Dwyer, C. Marsh, “Structural and compositional comparison of Si3N4 ceramics with different fracture modes,” *Acta Mater.*, vol. 54, no. 7, pp. 1949–1956, 2006.

[15] P. F. Becher, E.Y. Sun, K.P. Plucknett, “Microstructural Design of Silicon Nitride with Improved Fracture Toughness: I, Effects of Grain Shape and Size,” *J. Am. Ceram. Soc.*, vol. 81, no. 11, pp. 2821–2830, 1998.

[16] R. Van Weeren, “The Effect of the Thermo Mechanical Properties of the Grain Boundary Phase on the Fracture Toughness of Laser-Derived Silicon Nitride,” The State University of New Jersey, 1995.

[17] J. Dusza J. Morgiel, A. Duszová, L. Kvetková, “Microstructure and fracture toughness of Si 3 N 4 + graphene platelet composites,” *J. Eur. Ceram. Soc.*, vol. 32, pp. 3389–3397, 1999.

[18] S. Ii, C. Iwamoto, K. Matsunaga, T. Yamamoto, and Y. Ikuhara, “Identification of crack path of inter- and transgranular fractures in sintered silicon nitride by in situ TEM,” *J. Electron Microsc. (Tokyo).*, vol. 53, no. 2, pp. 121–127, 2004.

[19] S. M. Taheri Mousavi, B. Hosseinkhani, C. Vieillard, M. Chambart, P. J. J. Kok, and J. F. Molinari, “On the influence of transgranular and intergranular failure mechanisms during dynamic loading of silicon nitride,” *Acta Mater.*, vol. 67, pp. 239–251, 2014.

[20] Y. Kadin, S. Strobl, C. Vieillard, P. Wijnbergen, and V. Ocelik, “In-situ observation of crack propagation in silicon nitride ceramics,” *Procedia Struct. Integr.*, vol. 7, pp. 307–314, 2017.

[21] J.W. Hutchinson, Z. Suo, “Mixed Mode Cracking in Layered Materials,” *Adv. Appl. Mech.*, vol. 29, pp. 63–191, 1992.

[22] G. Ben, A. Tricoteaux, A. Thuault, and G. Louis, "Comparison of conventional Knoop and Vickers hardness of ceramic materials," *J. Eur. Ceram. Soc.*, vol. 37, no. 6, pp. 2531–2535, 2017.

[23] J. Gong, J. Wang, and Z. Guan, "A comparison between Knoop and Vickers hardness of silicon nitride ceramics," vol. 56, no. November, pp. 941–944, 2002.

[24] D. Chicot, D. Mercier, F. Roudet, K. Silva, M. H. Staia, and J. Lesage, "Comparison of instrumented Knoop and Vickers hardness measurements on various soft materials and hard ceramics," *J. Eur. Ceram. Soc.*, vol. 27, no. 4, pp. 1905–1911, 2007.

[25] A. R. Oganov and A. O. Lyakhov, "Towards the theory of hardness of materials," *J. Superhard Mater.*, vol. 32, no. 3, pp. 143–147, 2010.

[26] R. B. Ross, *Metallic Materials Specification Handbook*, Fourth. Chapman & Hall, 1992.

[27] J. Gong, J. Wu, and Z. Guan, "Examination of the indentation size effect in low-load vickers hardness testing of ceramics," *J. Eur. Ceram. Soc.*, vol. 19, no. 15, pp. 2625–2631, 1999.

[28] G. M. Pharr, E. G. Herbert, and Y. Gao, "The Indentation Size Effect: A Critical Examination of Experimental Observations and Mechanistic Interpretations," *Annu. Rev. Mater. Res.*, vol. 40, no. 1, pp. 271–292, 2010.

[29] Y. Tang, A. Yonezu, N. Ogasawara, N. Chiba, and X. Chen, "On radial crack and half-penny crack induced by Vickers indentation," *Proc. R. Soc. A Math. Phys. Eng. Sci.*, vol. 464, no. May, pp. 2967–2984, 2008.

[30] R. Cook and G. Pharr, "Direct observation and analysis of indentation cracking in glasses and ceramics," *J. Am. Ceram. Soc.*, vol. 73, no. 4, pp. 787–817, 1990.

[31] E. Apel, J. Deubener, A. Bernard, M. Höland, "Phenomena and mechanisms of crack propagation in glass-ceramics," *J. Mech. Behav. Biomed. Mater.*, vol. 1, no. 4, pp. 313–325, 2008.

[32] R. F. Cook and E. G. Liniger, "Kinetics of Indentation Cracking in Glass," *J. Am. Ceram. Soc.*, vol. 76, no. 5, pp. 1096–1105, 1993.

[33] S. M. Smith and R. O. Scattergood, "Crack-Shape Effects for Indentation Fracture-Toughness Measurements," *J. Am. Ceram. Soc.*, vol. 75, no. 2, pp. 305–315, 1992.

[34] K. Niihara, R. Morena, and D. P. . Hasselman, "Evaluation of Klc of Brittle Solids By the Indentation Method With Low Crack To Indent Ratios," *J. Mater. Sci. Lett.*, vol. 1, pp. 13–16, 1982.

[35] X. Yang, X. Liu, Z. Huang, X. Yao, and G. Liu, "Vickers indentation crack analysis of solid-phase-sintered silicon carbide ceramics," *Ceram. Int.*, vol. 39, no. 1, pp. 841–845, 2013.

[36] A. Pajares, F. Guiberteau, F. L. Cumbrera, R. W. Steinbrech, and A. Dominguez-Rodriguez, "Analysis of kidney-shaped indentation cracks in 4Y-PSZ," *Acta Mater.*, vol. 44, no. 11, pp. 4387–4394, 1996.

[37] G. D. Quinn and R. C. Bradt, "On the vickers indentation fracture toughness Test," *J. Am. Ceram. Soc.*, vol. 90, no. 3, pp. 673–680, 2007.

[38] J. Lankford, "Threshold microfracture during elastic-plastic indentation of

ceramics," *J. Mater. Sci.*, vol. 16, no. 5, pp. 1177–1182, 1981.

[39] T. Lube, "Indentation crack profiles in silicon nitride," *J. Eur. Ceram. Soc.*, vol. 21, pp. 211–218, 2001.

[40] H. Miyazaki, H. Hyuga, Y. I. Yoshizawa, K. Hirao, and T. Ohji, "Crack profiles under a Vickers indent in silicon nitride ceramics with various microstructures," *Ceram. Int.*, vol. 36, no. 1, pp. 173–179, 2010.

[41] E. Jisheng, T. A. Stolarski, and D. T. Gawne, "Mechanical and Tribochemical Effects During Accelerated Wear of Silicon Nitride in Diamond Slurries Mechanical and Tribochemical Effects During Accelerated Wear of Silicon Nitride in Diamond Slurries," *Tribol. Trans.*, vol. 40, no. 4, pp. 597–604, 1997.

[42] L. Wang, R. Snidle, and L. Gu, "Rolling Contact Silicon Nitride Bearing Technology: a Review of Recent Research," *Wear*, vol. 246, no. 1–2, pp. 159–173, 2000.

[43] M. Jiang and R. Komanduri, "On the finishing of Si3N4 balls for bearing applications," *Wear*, vol. 215, pp. 267–278, 1998.

[44] S. Chandrasekar and T. N. Farris, "Machining and surface finishing of brittle solids," *Sadhana - Acad. Proc. Eng. Sci.*, vol. 22, no. pt 3, pp. 473–481, 1997.

[45] R. Komanduri *et al.*, "A 'gentle' method for finishing Si3N4balls for hybrid bearing applications," *Tribol. Lett.*, vol. 7, no. 1, pp. 39–49, 1999.

[46] W. Maw, F. Stevens, S. C. Langford, and J. T. Dickinson, "Single asperity tribochemical wear of silicon nitride studied by atomic force microscopy," *J. Appl. Phys.*, vol. 92, no. 9, pp. 5103–5109, 2002.

[47] S. R. Hah, C. B. Burk, and T. E. Fischer, "Surface Quality of Tribochemically Polished Silicon Nitride," *J. Electrochem. Soc.*, vol. 146, no. 4, pp. 1505–1509, 1999.

[48] Y. Wang and M. Hadfield, "A study of line defect fatigue failure of ceramic rolling elements in rolling contact," *Wear*, vol. 253, no. 9–10, pp. 975–985, 2002.

[49] S. R. Hah and T. E. Fischer, "Tribochemical Polishing of Silicon Nitride," *J. Electrochem. Soc.*, vol. 145, no. 5, pp. 1708–1714, 1998.

[50] N. K. Arakere, S. Pattabhiraman, G. Levesque, and N. H. Kim, "Uncertainty analysis for rolling contact fatigue failure probability of silicon nitride ball bearings," *Int. J. Solids Struct.*, vol. 47, no. 18–19, pp. 2543–2553, 2010.

[51] C. Vieillard, "Observation of subsurface rolling contact fatigue cracks in silicon nitride and comparison of their location to Hertzian contact subsurface stresses," *Int. J. Fatigue*, vol. 96, pp. 283–292, 2017.

[52] J. Lai, Y. Kadin, and C. Vieillard, "Characterization and modelling of the degradation of silicon nitride balls with surface missing-material defects under lubricated rolling contact conditions," *Wear*, vol. 398–399, no. March, pp. 146–157, 2018.

[53] W. Wang, M. Hadfield, and A. A. Wereszczak, "Surface strength of silicon nitride in relation to rolling contact performance measured on ball-on-rod and modified four-ball tests," *Tribol. Int.*, vol. 43, no. 1–2, pp. 423–432, 2010.

[54] M. Hadfield and T. A. Stolarski, "Observations of delamination fatigue on pre-cracked ceramic elements in rolling contact," *Ceram. Int.*, vol. 21, no. 2, pp. 125–130, 1995.

[55] Z. Yu and S. Boseck, "Scanning Acoustic Microscopy and Its Applications to Material Characterization," *Rev. Mod. Phys.*, vol. 67, no. 4, pp. 863–891, 1995.

[56] J. Kang and M. Hadfield, "Examination of the material removal mechanisms during the lapping process of advanced ceramic rolling elements," 2005.

[57] Y. Wang and M. Hadfield, "A mechanism for nucleating secondary fractures near a pre-existing flaw subjected to contact loading," *Wear*, vol. 254, no. 7–8, pp. 597–605, 2003.

[58] P. Zhao, M. Hadfield, Y. Wang, and C. Vieillard, "Subsurface propagation of partial ring cracks under rolling contact. Part I. Fracture mechanics analysis," *Wear*, vol. 261, no. 3–4, pp. 390–397, 2006.

[59] P. Zhao, M. Hadfield, Y. Wang, and C. Vieillard, "Subsurface propagation of partial ring cracks under rolling contact. Part II. Fracture mechanics analysis," *Wear*, vol. 261, no. 3–4, pp. 390–397, 2006.

[60] E. N. Landis and D. T. Keane, "X-ray microtomography," *Mater. Charact.*, vol. 61, no. 12, pp. 1305–1316, 2010.

[61] L. Salvo, M. Suéry, A. Marmottant, N. Limodin, and D. Bernard, "3D imaging in material science: Application of X-ray tomography," *Comptes Rendus Phys.*, vol. 11, no. 9–10, pp. 641–649, 2010.

[62] L. Salvo P. Cloetens, E. Maire, S. Zabler, "X-ray micro-tomography an attractive characterisation technique in materials science," *Nucl. Instruments Methods Phys. Res. Sect. B Beam Interact. with Mater. Atoms*, vol. 200, pp. 273–286, 2003.

[63] V. Cnudde and M. N. Boone, "High-resolution X-ray computed tomography in geosciences: A review of the current technology and applications," *Earth-Science Rev.*, vol. 123, pp. 1–17, 2013.

[64] E. Maire and P. J. Withers, "Quantitative X-ray tomography," *Int. Mater. Rev.*, vol. 59, no. 1, pp. 1–43, 2014.

[65] S. R. Stock, K. Ignatiev, G. Davis, J. Elliot, "Fatigue Cracks in Aluminum Samples Studied With X-Ray Phase Contrast Imaging and With Absorption," *Int. Cent. Diffration Dataernational Cent. Diffration Data*, vol. 45, no. c, pp. 123–127, 2002.

[66] P. Cloetens, M. Pateyron-Salomé, J. Y. Buffiere, G. Peix, J. Baruchel, F. Peyrin, M. Schlenker, "Observation of microstructure and damage in materials by phase sensitive radiography and tomography," *J. Appl. Phys.*, vol. 81, no. 9, pp. 5878–5886, 1997.

[67] S. C. Mayo, A. W. Stevenson, and S. W. Wilkins, "In-Line Phase-Contrast X-ray Imaging and Tomography for Materials Science," *Materials (Basel).*, vol. 5, no. 5, pp. 937–965, 2012.

[68] J. Baruchel, JY. Buffiere, P. Cloetens, M. Di Michie, "Advances in synchrotron radiation microtomography," *Scr. Mater.*, vol. 55, no. 1 SPEC. ISS., pp. 41–46, 2006.

[69] Y. Vertyagina, M. Mostafavi, C. Reinhard, R. Atwood, and T. J. Marrow, "In situ quantitative three-dimensional characterisation of sub-indentation cracking in polycrystalline alumina," *J. Eur. Ceram. Soc.*, vol. 34, no. 12, pp. 3127–3132, 2014.

[70] J. Marrow, C. Reinhard, Y. Vertyagina, L. Saucedo-Mora, D. Collins, and M. Mostafavi, "3D Studies of Damage by Combined X-ray Tomography and Digital

Volume Correlation," *Procedia Mater. Sci.*, vol. 3, pp. 1554–1559, 2014.

[71] B. Yu, R. S. Bradley, C. Soutis, P. J. Hogg, and P. J. Withers, "2D and 3D imaging of fatigue failure mechanisms of 3D woven composites," *Compos. Part A Appl. Sci. Manuf.*, vol. 77, pp. 37–49, 2015.

[72] B. Yu, R. S. Bradley, C. Soutis, and P. J. Withers, "A comparison of different approaches for imaging cracks in composites by X-ray microtomography," *Philos. Trans. R. Soc. A Math. Phys. Eng. Sci.*, vol. 374, no. 2071, p. 20160037, 2016.

[73] V. E. Krohn and G. R. Ringo, "Ion source of high brightness using liquid metal," *Appl. Phys. Lett.*, vol. 27, no. 9, pp. 479–481, 1975.

[74] C. A. Volkert and A. M. Minor, "Focused Ion Beam Microscopy and Micromachining," *MRS Bull.*, vol. 32, no. 05, pp. 389–399, 2007.

[75] S. Reyntjens and R. Puers, "A review of focused ion beam applications in microsystem technology," *J. Micromechanics Microengineering*, vol. 11, no. 4, pp. 287–300, 2001.

[76] M. Y. Ali, W. Hung, and Y. Q. Fu, "A Review of Focused Ion Beam Sputtering," *Int. J. Precis. Eng. Manuf.*, vol. 11, no. 1, pp. 157–170, 2010.

[77] J. Mayer, L. a Giannuzzi, T. Kamino, and J. Michael, "T EM Sample Preparation and Damage," *MRS Bull.*, vol. 32, no. 5, pp. 400–407, 2007.

[78] M. Sezen, "Focused Ion Beams (FIB) — Novel Methodologies and Recent Applications for Multidisciplinary Sciences," in *Modern Electron Microscopy in Physical and Life Sciences*, 2016, pp. 121–140.

[79] L. A. Giannuzzi and F. A. Stevie, *Introduction to Focused Ion Beams: Intrumentation, Theory, Techniques and Practice*. Springer Science & Business Media, 2006.

[80] V. Castaldo, C. W. Hagen, and P. Kruit, "Simulation of ion imaging: Sputtering, contrast, noise," *Ultramicroscopy*, vol. 111, no. 8, pp. 982–994, 2011.

[81] J. Orloff, "Fundamental limits to imaging resolution for focused ion beams," *J. Vac. Sci. Technol. B Microelectron. Nanom. Struct.*, vol. 14, no. 6, p. 3759, 1996.

[82] P. R. Munroe, "The application of focused ion beam microscopy in the material sciences," *Mater. Charact.*, vol. 60, no. 1, pp. 2–13, 2009.

[83] D. J. Stokes, T. Vystavel, and F. Morrissey, "Focused ion beam (FIB) milling of electrically insulating specimens using simultaneous primary electron and ion beam irradiation," *J. Phys. D. Appl. Phys.*, vol. 40, no. 3, pp. 874–877, 2007.

[84] K. D. Vernon-Parry, "Scanning electron microscopy: an introduction," *III-Vs Rev.*, vol. 13, no. 4, pp. 40–44, 2000.

[85] H. Ma, K.-J. Shieh, and T. X. Qiao, "Study of Transmission Electron Microscopy (TEM) and Scanning Electron Microscopy (SEM)," *Nat. Sci.*, vol. 4, no. 3, pp. 14–22, 2006.

[86] R. Shimizu and D. Ze-Jun, "Monte Carlo modelling of electron-solid interactions," *Reports Prog. Phys.*, vol. 55, no. 4, pp. 487–531, 1992.

[87] G. E. Lloyd, "Atomic Number and Crystallographic Contrast Images with the SEM: A Review of Backscattered Electron Techniques," *Mineral. Mag.*, vol. 51, no. 359,

pp. 3–19, 1987.

[88] J. I. Goldstein, D. E. Newbury, J. R. Michael, N. W. Ritchie, J. H. J. Scott, and D. C. Joy, *Scanning electron microscopy and X-ray microanalysis*. Springer, 2017.

[89] Y. N. Tetsuo Sakamoto, Zhaohui Cheng, Masanori Takahashi, Masanori Owari, "Development of an Ion and Electron Dual Focused Beam Apparatus Microanalysis for Three-Dimensional," *Jpn. J. Appl. Phys.*, vol. 37, 1998.

[90] J. Konrad, S. Zaefferer, and D. Raabe, "Investigation of orientation gradients around a hard Laves particle in a warm-rolled Fe3Al-based alloy using a 3D EBSD-FIB technique," *Acta Mater.*, vol. 54, no. 5, pp. 1369–1380, 2006.

[91] M. A. Groeber, B. K. Haley, M. D. Uchic, D. M. Dimiduk, and S. Ghosh, "3D reconstruction and characterization of polycrystalline microstructures using a FIB-SEM system," *Mater. Charact.*, vol. 57, no. 4–5, pp. 259–273, 2006.

[92] B. . Inkson, M. Mulvihill, and G. Möbus, "3D determination of grain shape in a FeAl-based nanocomposite by 3D FIB tomography," *Scr. Mater.*, vol. 45, no. 7, pp. 753–758, 2001.

[93] L. Holzer, F. Indutnyi, P. Gasser, B. Munch, and M. Wegmann, "Three-dimensional analysis of porous BaTiO3 ceramics using FIB nanotomography," *J. Microsc.*, vol. 216, no. 1, pp. 84–95, 2004.

[94] B. J. Inkson, T. Steer, H. Z. Wu, and G. Mobus, "3D mapping of subsurface cracks in alumina using FIB," *Mater. Res. Soc. Symp. - Proc.*, vol. 649, p. Q7.7.1-Q7.7.6, 2001.

[95] F. Elfallagh and B. J. Inkson, "Evolution of residual stress and crack morphologies during 3D FIB tomographic analysis of alumina.," *J. Microsc.*, vol. 230, no. Pt 2, pp. 240–51, 2008.

[96] Z. H. Xie, P. R. Munroe, R. J. Moon, and M. Hoffman, "Characterization of surface contact-induced fracture in ceramics using a focused ion beam miller," *Wear*, vol. 255, no. 1–6, pp. 651–656, 2003.

[97] M. Schaffer, J. Wagner, B. Schaffer, M. Schmied, and H. Mulders, "Automated three-dimensional X-ray analysis using a dual-beam FIB," *Ultramicroscopy*, vol. 107, no. 8, pp. 587–597, 2007.

[98] D. A. M. De Winter, C.T.W.M. Schneijdenberg, M.N. Lebbink, B. Lich, A.J . Verkleij, M.R. Drury, "Tomography of insulating biological and geological materials using focused ion beam (FIB) sectioning and low-kV BSE imaging," *J. Microsc.*, vol. 233, no. 3, pp. 372–383, 2009.

[99] N. Payraudeau, D. McGrouther, and K. U. O'Kelly, "Quantification of subsurface damage in a brittle insulating ceramic by three-dimensional focused ion beam tomography.," *Microsc. Microanal.*, vol. 17, no. 2, pp. 240–5, 2011.

[100] B. J. Inkson, D. Leclere, F. Elfallagh, and B. Derby, "The effect of focused ion beam machining on residual stress and crack morphologies in alumina," *J. Phys. Conf. Ser.*, vol. 26, no. 1, pp. 219–222, 2006.

[101] K. P. Mingard, H. G. Jones, and M. G. Gee, "Metrological challenges for reconstruction of 3-D microstructures by focused ion beam tomography methods," *J. Microsc.*, vol. 253, no. 2, pp. 93–108, 2014.

[102] S. Korte, M. Ritter, C. Jiao, P. A. Midgley, and W. J. Clegg, "Three-dimensional electron backscattered diffraction analysis of deformation in MgO micropillars," *Acta Mater.*, vol. 59, no. 19, pp. 7241–7254, 2011.

[103] M. D. Uchic, "Serial sectioning methods for generating 3D characterization data of grain-and precipitate-scale microstructures," *Comput. Methods Microstruct. Relationships*, pp. 31–52, 2011.

[104] B. W. Ward, J. A. Notte, and N. P. Economou, "Helium ion microscope: A new tool for nanoscale microscopy and metrology," *J. Vac. Sci. Technol. B Microelectron. Nanom. Struct.*, vol. 24, no. 6, p. 2871, 2006.

[105] G. Hlawacek, V. Veligura, R. van Gastel, and B. Poelsema, "Helium Ion Microscopy," pp. 1–16, 2013.

[106] N. Stehling, R Masters, Y Zhou, R O'Connell, "New perspectives on nano-engineering by secondary electron spectroscopy in the helium ion and scanning electron microscope," *MRS Commun.*, vol. 8, no. 2, pp. 226–240, 2018.

[107] J. Notte *et al.*, "An introduction to the helium ion microscope," *AIP Conf. Proc.*, vol. 931, no. 2007, pp. 489–496, 2007.

[108] F. H. M. Rahman, S. McVey, L. Farkas, J. A. Notte, S. Tan, and R. H. Livengood, "The prospects of a subnanometer focused neon ion beam," *Scanning*, vol. 34, no. 2, pp. 129–134, 2012.

[109] G. Hlawacek, V Veligura, R van Gastel, "Helium ion microscopy," *J. Vac. Sci. Technol. B*, vol. 32, 2014.

[110] D. Bell, "Contrast Performance: Low Voltage Electrons vs. Helium Ions," *Microsc. Microanal.*, vol. 17, no. S2, pp. 660–661, 2011.

[111] D. C. Bell, "Contrast mechanisms and image formation in helium ion microscopy.," *Microsc. Microanal.*, vol. 15, no. 2, pp. 147–153, 2009.

[112] D. Cohen-tanugi and N. Yao, "Superior imaging resolution in scanning helium-ion microscopy : A look at beam- sample interactions Superior imaging resolution in scanning helium-ion microscopy : A look at beam-sample interactions," *J. Appl. Phys.*, vol. 104, no. 6, pp. 063504-063504-7, 2008.

[113] K. Ohya, T. Yamanaka, K. Inai, and T. Ishitani, "Comparison of secondary electron emission in helium ion microscope with gallium ion and electron microscopes," *Nucl. Instruments Methods Phys. Res. Sect. B Beam Interact. with Mater. Atoms*, vol. 267, no. 4, pp. 584–589, 2009.

[114] R. Hill and F. H. M. Rahman, "Advances in helium ion microscopy," *Nucl. Instrum. Methods Phys. Res., Sect. A*, vol. 645, no. 1, pp. 96–101, 2011.

[115] W. L. Rice, A. N. Van Hoek, T.G. Păunescu, C. Huynh, "High Resolution Helium Ion Scanning Microscopy of the Rat Kidney," *PLoS One*, vol. 8, no. 3, 2013.

[116] T. G. Păunescu, W.W.C. Shum, C. Huynh, "High-resolution helium ion microscopy of epididymal epithelial cells and their interaction with spermatozoa," *Mol. Hum. Reprod.*, vol. 20, no. 10, pp. 929–937, 2014.

[117] S. A. Boden, A. Asadollahbaik, H. N. Rutt, and D. M. Bagnall, "Helium ion microscopy of Lepidoptera scales," *Scanning*, vol. 34, no. 2, pp. 107–120, 2012.

[118] F. B. Bidlack, C. Huynh, J. Marshman, and B. Goetze, "Helium ion microscopy of

enamel crystallites and extracellular tooth enamel matrix," *Front. Physiol.*, vol. 5, no. OCT, pp. 1–10, 2014.

[119] T. Wirtz, N. Vanhove, L. Pillatsch, D. Dowsett, S. Sijbrandij, and J. Notte, "Towards secondary ion mass spectrometry on the helium ion microscope: An experimental and simulation based feasibility study with He+ and Ne+ bombardment," *Appl. Phys. Lett.*, vol. 101, no. 4, p. 041601, 2012.

[120] R. H. Livengood, S. Tan, R. Hallstein, J. Notte, S. McVey, and F. H. M. Faridur Rahman, "The neon gas field ion source - A first characterization of neon nanomachining properties," *Nucl. Instrum. Methods Phys. Res., Sect. A*, vol. 645, no. 1, pp. 136–140, 2011.

[121] Y. Zhou, P. Maguire, J. Jadwiszczak, M. Muruganathan, H. Mizuta, and H. Zhang, "Precise milling of nano-gap chains in graphene with a focused helium ion beam," *Nanotechnology*, vol. 27, no. 32, 2016.

[122] T. C. Pekin, F. I. Allen, and A. M. Minor, "Evaluation of neon focused ion beam milling for TEM sample preparation," *J. Microsc.*, vol. 264, no. 1, pp. 59–63, 2016.

[123] G. S. Bumbrah and R. M. Sharma, "Raman spectroscopy – Basic principle, instrumentation and selected applications for the characterization of drugs of abuse," *Egypt. J. Forensic Sci.*, vol. 6, no. 3, pp. 209–215, 2016.

[124] Q. Ma and D. R. Clarke, "Piezospectroscopic Determination of Residual Stresses in Polycrystahe Alumina," no. 3, pp. 298–302, 1993.

[125] Q. Ma and D. R. Clarke, "Stress Measurement in Single-Crystal and Polycrystalline Ceramics Using Their Optical Fluorescence," *J. Am. Ceram. Soc.*, vol. 76, no. 6, pp. 1433–1440, 1993.

[126] N. Muraki, G. Katagiri, V. Sergo, and G. Pezzotti, "Mapping of residual stresses around an indentation in beta-Si3N4 using Raman spectroscopy," *J. Mater. Sci.*, vol. 32, no. 2, pp. 5419–5423, 1997.

[127] V. Sergo, G. Pezzotti, G. Katagiri, N. Muraki, and T. Nishida, "Stress Dependence of the Raman Spectrum of ß-Silicon Nitride," *Journal of the American Ceramic Society*, vol. 79, no. 3. pp. 781–784, 1996.

[128] G. Pezzotti, "Microprobe piezo-spectroscopy for the micromechanical analysis of fracture and deformation phenomena in polycrystalline ceramics," *Compos. Sci. Technol.*, vol. 59, no. 6, pp. 821–831, 1999.

[129] G. Pezzotti, "In situ Study of Fracture Mechanisms in Advanced Ceramics using Fluorescence and Raman Microprobe Spectroscopy," *J. Ra*, vol. 875, no. May, pp. 867–875, 1999.

[130] G. Pezzotti, H. Ichimaru, and L. P. Ferroni, "Raman Microprobe Evaluation of Bridging Stresses in Highly Anisotropic Silicon Nitride," *J. Am. Ceram. Soc.*, vol. 90, pp. 1785–1790, 2001.

[131] S. Tochino and G. Pezzotti, "Micromechanical analysis of silicon nitride: A comparative study by fracture mechanics and Raman microprobe spectroscopy," *J. Raman Spectrosc.*, vol. 33, no. 9, pp. 709–714, 2002.

Chapter 3: Materials and Methodology

3.1. Introduction

This chapter will describe in detail the experimental methods that have been used in this thesis, from materials preparation to characterisation techniques. These include (but are not limited to) micro-indentation, SEM investigations, FIB tomography and micro-XCT. All techniques here have been applied to silicon nitride of a range of compositions.

3.2. Materials

The material of interest in this research project, and hence the material used throughout, is silicon nitride (Si_3N_4). Four different compositions of sintered and hot-isostatically pressed silicon nitride are used (supplied by the industrial sponsor of this project), each meeting ASTM F2094 certification grade for use in rolling elements in rolling bearings. These will be referred to as SNA, SNB (the two primary compositions used in this thesis), SNC and SND. Mechanical properties and sintering additives of the different compositions provided by the supplier are given below in Table 3.1:

	SNA	SNB	SNC	SND
Hardness (GPa)	16	15.5	14.5	15
Hardness (HV)	1630	1580	1480	1530
Fracture Toughness (Mpa·$m^{1/2}$)	6.6	6.5	5.6	5.5
Additives	Ti, Al	Ca, Y	Fe, Al, Y	Hf, Mo, Y, Al

Table 3.1: Mechanical properties of the four different compositions of silicon nitride: Hardness, Vickers hardness (HV) and fracture toughness. Also given is sintering additives for each composition. Values were provided by the project industrial sponsor.

3.3. Micro-indentation of Silicon Nitride

3.3.1. Surface Preparation

Before micro-indentation, all silicon nitride samples were required to have a flat, polished surface so as not to damage the diamond indenter tip on indentation, and to improve

image clarity. Samples were first ground down using a diamond grinding disc to achieve a flat surface, and subsequently polished with 30 µm, 15 µm, 6 µm and finally 1 µm diamond lapping paper using a Buehler Minimet 1000 Grinder-Polisher. Diamond lapping paper (instead of alternatives, e.g. silicon carbide) was used due to the high hardness of silicon nitride (~ 1700 HV).

3.3.2. Vickers Micro-indentation

Micro-indentation of the silicon nitride samples was undertaken using a Struers Durascan Hardness Tester. Samples were indented with a Vickers-type diamond tip under a range of applied loads from 0.5 kg – 5 kg depending on the subsequent investigation requirement. The indentation dwell time was always 15 s and carried out at room temperature and pressure conditions. Examples of indentations on the SNA composition are given in Fig. 3.1.

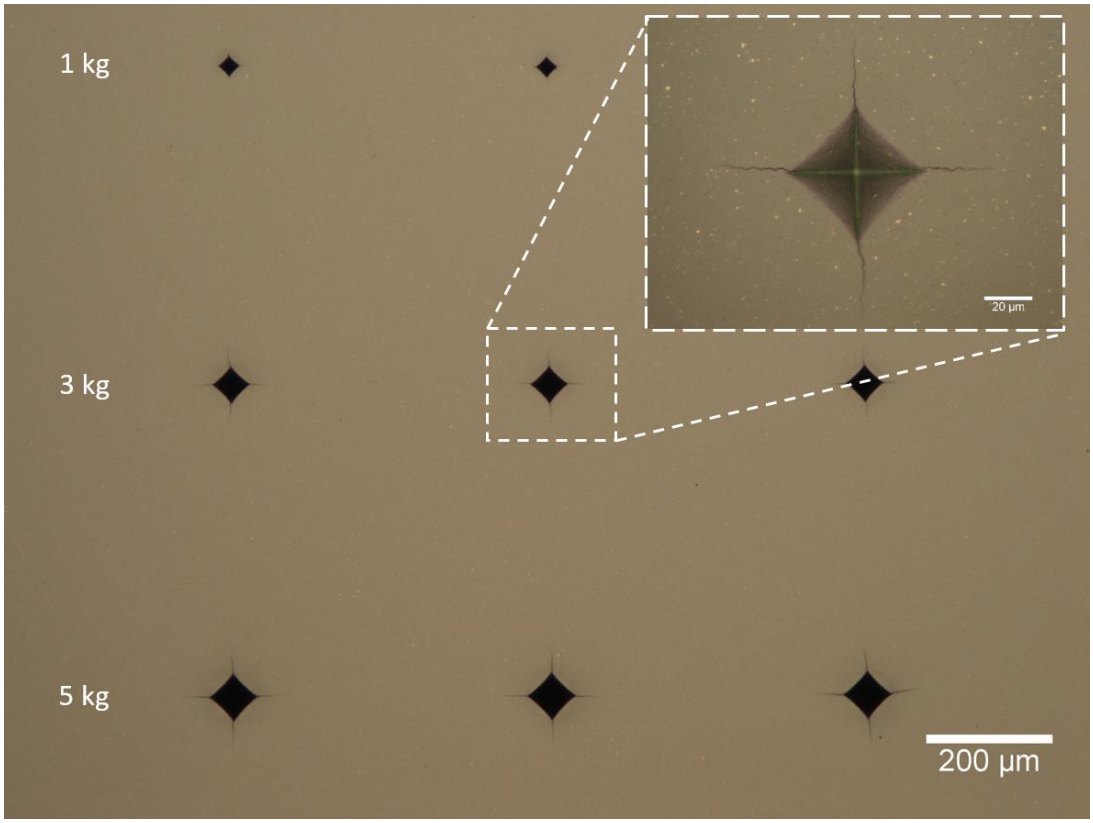

Figure 3.1: An optical image of a 3×3 array of Vickers indentations on the SNA composition carried out under loads of 1 kg, 3 kg and 5 kg.

3.4. Incremental Polishing of SNA

A 3×3 array of 1 kg, 3 kg, and 5 kg indentations on an SNA sample was incrementally polished and imaged in order to reveal the change in crack morphology with depth. Polishing was carried out using 1 μm diamond lapping paper so that surface damage was kept to a minimum. For each polishing increment the force, polishing time, and speed were set at 8 N, 10 minutes, and 25 rpm respectively; these parameters were chosen as they removed material at a desired rate (~ 400 nm per increment). The depth of polishing was estimated using a surface profilometer (Bruker ContourGT) to measure the depth and geometry of the residual indentation impression of a reference 5 kg indentation prior to polishing. The decrease in diagonal length of the residual indentation with each polishing increment was then used to approximate how much material was removed [1].

Optical imaging of samples was carried out using an optical microscope (Nikon Eclipse LV100). Imaging for all samples was taken using the 50× objective lens. In addition, further 20× magnification images were taken for the 5 kg indentation which did not fit in the field of view at 50× magnification. Two optical imaging modes were used because of the differing contrast offered: bright field (BF) and dark field (DF). In BF images, cracking appears dark and the surrounding material light, whereas in DF images the cracking is lighter and the surrounding material dark. This is because DF images exclude unscattered light from the incident beam.

3.5. Raman Spectroscopy

Raman spectroscopy for residual stress analysis was carried out on, and in the surrounding region of, 1 kg Vickers indentations. Two Raman microscopes were used for investigations, a Renishaw InVia and a Horiba XPlora Plus; both devices are similar in specification and setup procedures but the Horiba has better area mapping capabilities. The set-up of the Raman spectroscopy is shown in Fig. 3.2.

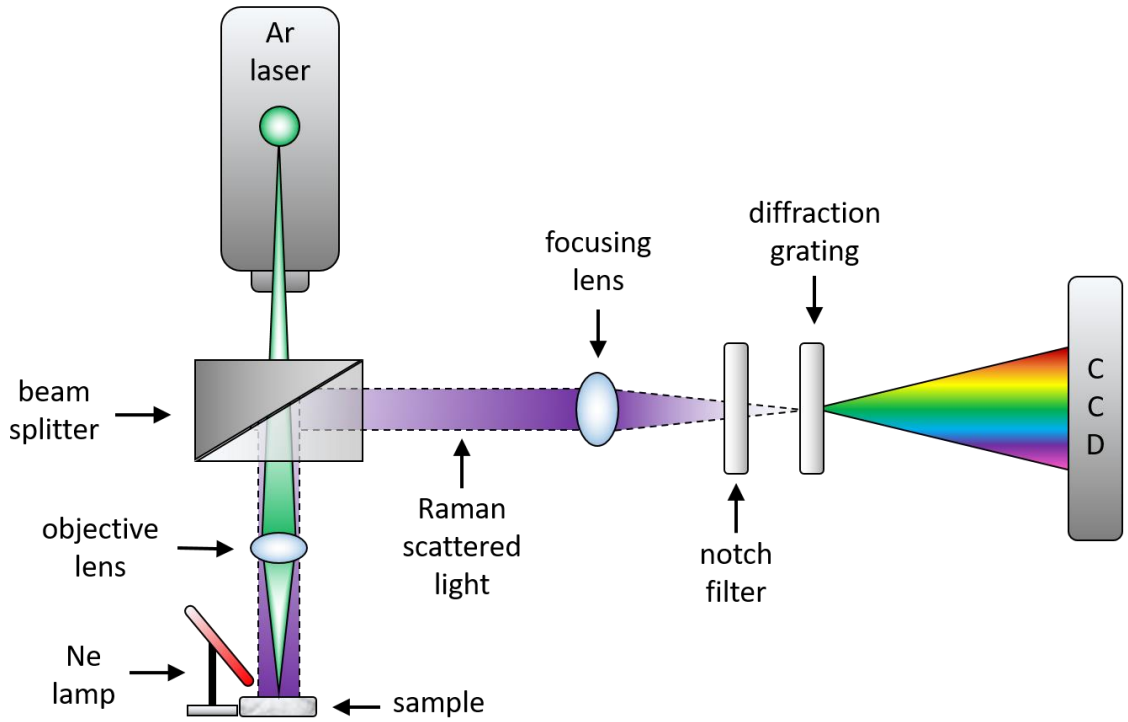

Figure 3.2: A schematic of the Raman spectroscopy set-up showing the primary components.

Prior to use with a silicon nitride sample, the Raman device was first calibrated using a reference standard silicon sample (with known Raman peaks) and an argon green light laser with a power of 25 mA and wavelength of 514.5 nm. The surface of the silicon was brought into focus at 50× magnification and then the laser shutter was opened and the laser spot incident on the surface adjusted to the smallest size achievable (~ 1 μm in diameter). The laser was then centred and a scan of the reference silicon taken to complete the calibration. For indented samples, the area of interest i.e. the indentation, was focused at 50× magnification and the laser shutter opened. An initial Raman spectrum was then acquired with three 20 seconds acquisitions being taken at the minimum laser spot size of 1 μm – this was done to check that the Raman device was producing an acceptable spectrum. Three 20 seconds acquisitions were taken instead of a single 60 second acquisition because it reduces the signal-to-noise ratio. A minimum stress (parent material) spectrum needed to be taken as a reference to compare with subsequent stress-affected spectra. This was done by acquiring a spectrum far away from any indentation (as to avoid any indentation induced residual stresses) with an increased spot size of 10 μm to average the spectrum over a larger area. An example of a reference Raman spectrum is given in Fig. 3.3.

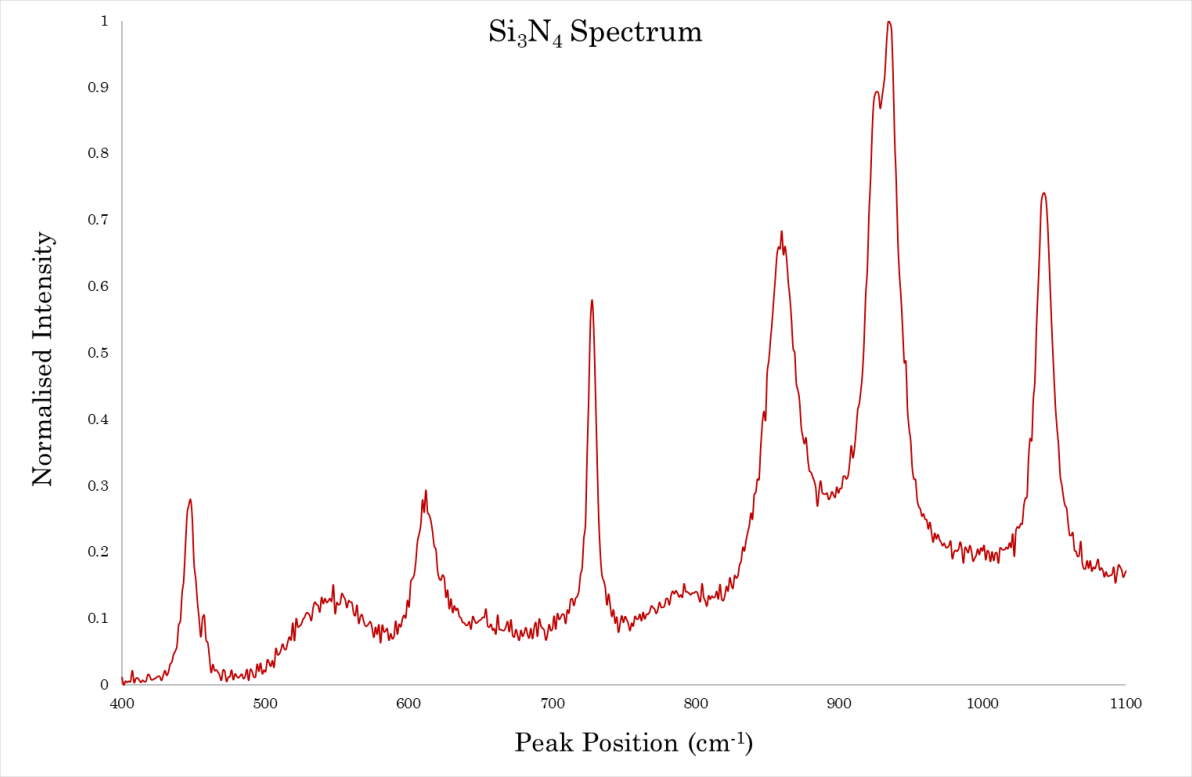

Figure 3.3: An example of a silicon nitride spectrum taken in a low residual stress area away from any indentations.

Point scans of the 1 kg indentation with a laser spot size of 1 μm were taken at various locations around the indentation e.g. at the residual indentation centre, indentation side slopes and in the region surrounding the indentation. Line maps were taken extending away from the indentation side and indentation corners. Area maps were also acquired at the crack tip of a radial cracks emanating from indentation corners. Examples of area and line map locations are given in Fig. 3.4. Maps were created from measuring the shift in Raman peaks located at approximately 861 cm^{-1} and 1044 cm^{-1} (which will be referred to as the S_1 and S_2 peaks respectively) relative to their peak position in the reference spectrum.

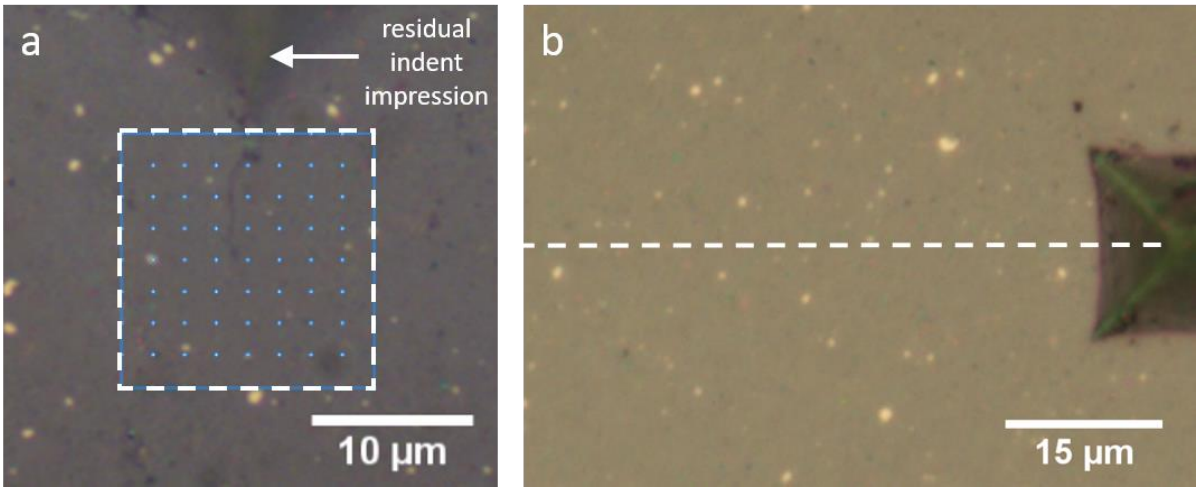

Figure 3.4: (a) The location of a Raman area map conducted over a radial crack tip from a 1 kg indentation. (b) An example of a line map extending away from a 1 kg indentation.

For longer acquisitions, a neon discharge lamp was used, incident to the sample surface, to use as a reference to correct against any thermal drift of the spectra. The neon peak positions that appear on the spectra are temperature-independent [2]–[4]. Therefore, if there is any change in peak position of the neon peaks in a spectrum acquired it is an indication of an instrumental effect caused by the expansion and contraction of the spectrometer grating due to temperature fluctuations. This thermal drift (if present) was then corrected for in all peaks by subtracting the difference between the measured neon peak position and the expected neon peak position.

After collection, raw data was baselined and peaks fitted using a combination of Lorentzian and Gaussian peak shapes (primary Lorentzian) in conjunction with a non-linear least squares curve fit method (carried out on LabSpec6 and OriginPro software).

3.6. Optical Profilometry

Optical profilometry for surface height and roughness measurements of samples was conducted using a Bruker Contour GT 3D optical microscope which utilises vertical scanning white light interferometry (VSWLI) to calculate changes in surface topography. A white light source is passed through a beam splitter where half of the light is directed towards the sample surface to be reflected, and the other half towards a reference mirror (Fig. 3.5). The two reflected beams then re-join and if their optical path difference is the same then an interference pattern is formed at the image plane – this indicates when the

sample surface is in focus. Displacement of the reference mirror through the vertical plane also causes the interference fringes to move relative to the image plane and with that comes an associated change in intensity. It is this change in intensity with incremental vertical displacement that is used to calculate the surface topography of a sample.

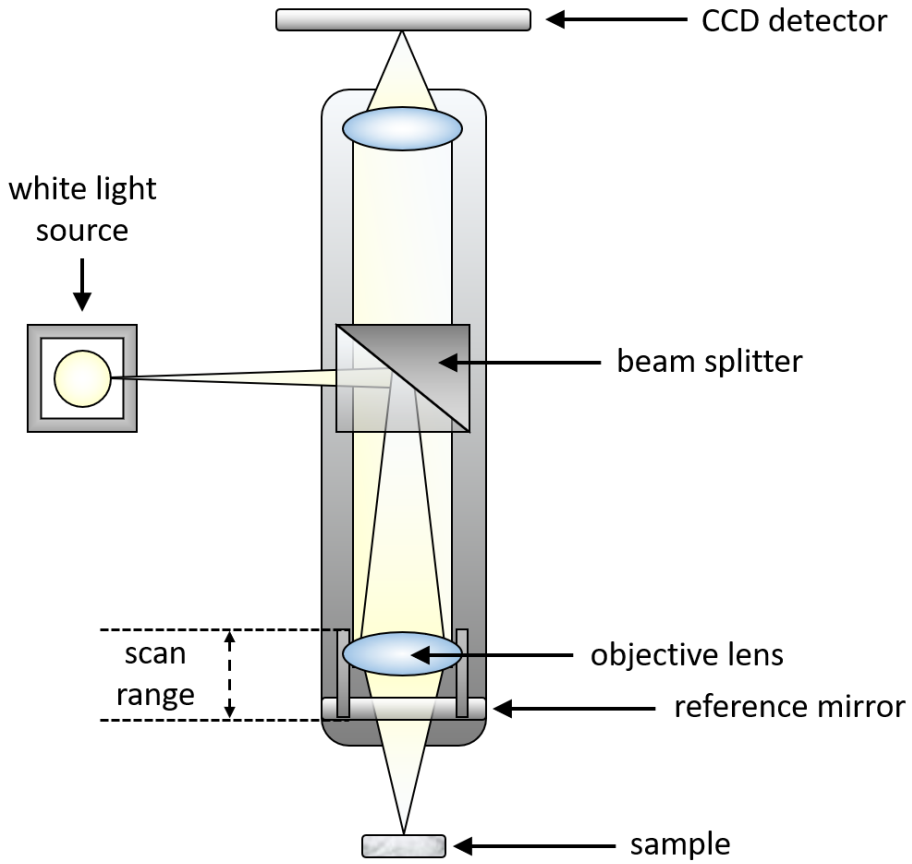

Figure 3.5: A schematic showing the components of a white light interferometry surface profiler.

Vickers indented samples with a range of applied loads from 0.5 kg – 5 kg were imaged using VSWLI mode. Indentations on samples were located using a 5× objective lens and the surface of the sample brought into the required focus by ensuring the intensity of the interference fringes were at a maximum. The intensity of the white light was then set to automatic – this ensures that the intensity of light is adjusted depending on the amount of reflected light that is being received and prevents saturation of the CCD detector or low signal. Two important parameters were then set: the *back-scan*, and the *length*, and they determined the vertical distance that the reference mirror scanned through. The back scan is how far above the focal plane the scanning should start at, and the length is how far below the focal plane it should continue before it stops, and should be set to be above and below the lowest and highest feature respectively. Both the back scan and length were

set to between 10-20 μm for indented samples. The scan was then started and upon completion a topographical map of the scanned surface was produced. The same process was then applied with the 20× and 50× objective lenses for higher magnification scans (each time the objective lens was changed the interference fringes had to be adjusted to maximum intensity).

This process was also utilised to obtain surface information about the ball-bearing component star features. However, because these features are located on a curved surface, a baselining function within the software (Vision64) was used to remove the underlying curve.

3.7. Scanning Electron Microscopy (SEM) Imaging

SEM imaging of samples was primarily carried out using an FEI Inspect F50 SEM equipped with a field emission gun (FEG) source. Prior to imaging, indented samples were attached to a 12.5 mm aluminium SEM stub using a carbon tab and the edges subsequently coated with silver paint to increase conductivity. In addition, a thin carbon coating ~ 15 nm thick was thermally evaporated (Edwards Coating System E305A) onto the sample surface to decrease surface charge build-up under electron beam irradiation - this is a problem when imaging highly insulating materials such as silicon nitride.

Images of 1 kg and 0.5 kg Vickers indented SNA and SNB samples were taken at a working distance of ~ 9.5 mm with a 20 kV accelerating voltage and a current of 1.6 nA. Both an Everhart-Thornley secondary electron detector (ETD) and a backscattered electron (BSE) detector were utilised: the ETD offers better topographical contrast, whereas the BSED gives more information on material phase. Beam dwell time was varied from 1 μs to 30 μs per line.

3.8. Focused Ion Beam (FIB) Tomography

3.8.1. FIB Tomography of Vickers Indentations

Vickers indented samples to be used for FIB tomography were mounted on a 12.5 mm diameter aluminium SEM stub using a carbon tab. The sample edges were coated with

conductive silver paint and a 30 nm layer of gold was thermally evaporated onto the surface (Emscope SC500) to both decrease charge build-up and reduce ion beam damage.

FIB tomography was conducted on a range of samples with indentation loads of 0.5 kg and 1 kg. The 1 kg indentations were the highest load investigated by FIB tomography because higher loads (e.g. 3 kg and 5 kg) would have required unfeasible milling times (> days). The FIB-SEM device used was an FEI Helios NanoLab G3 DualBeam system which consisted of a Ga^+ FIB beam and an attached high resolution FEG-SEM. Surface images of the samples were acquired using the Everhart-Thornley detector with an incident beam voltage of 5 kV.

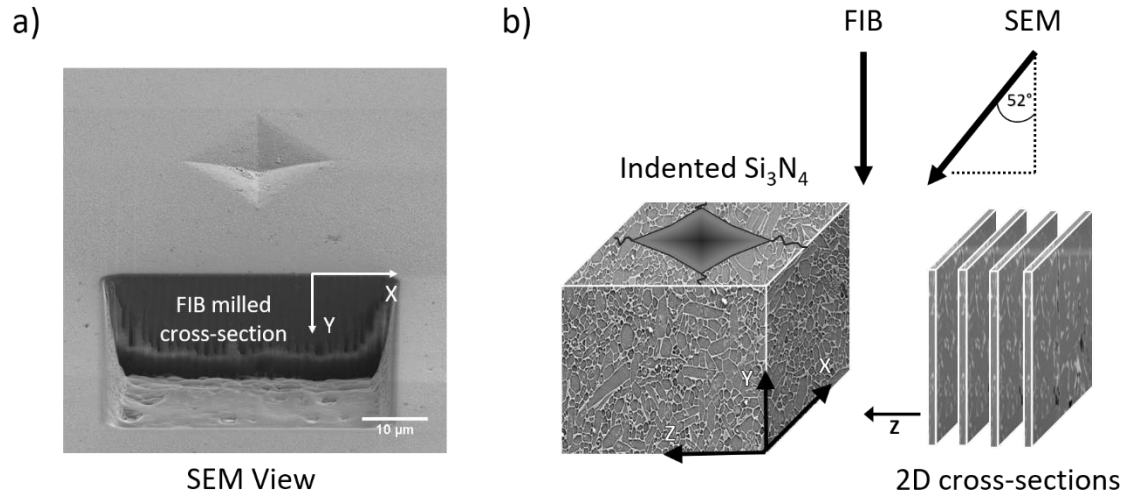

Figure 3.6: (a) An SEM with the 52° tilt showing a FIB milled cross-section in addition to the indentation on the surface. (b) A schematic of the FIB-SEM process through an indentation: The FIB is used to mill away slices of material, after each slice the newly revealed cross-section is imaged using the SEM that is angled such that the cross-section is in the path of the incident beam.

Most of indentations were milled towards the direction of the indentation corner as shown in Fig. 3.6. There were some indentations where milling was conducted in a differing orientation to the above, but these will be outlined in greater detail later, when discussing the associated results. The process described below is the one undertaken for a typical indentation FIB mill:

A sloped FIB trench with dimensions x = 40 µm, z = 35 µm and y-direction extending down to a maximum depth of 35 µm, was milled using the Ga^+ ion beam at a 65 nA current ~ 20 µm away from the indentation, so as not to interfere with the radial crack that extended from the indentation corner. The revealed cross-section was subsequently polished with an ion beam current of 21 nA and then 9.3 nA to make the microstructure more easily

observable. FEI Autoslice and View software was used to incrementally mill away slices of the material through the indentation sites. The ion beam current used for the slice milling was set at 9.3 nA; this current allows a sufficient volume of material to be sputtered in a reasonable timescale as well as providing a good enough polish to reveal microstructural features e.g. cracking and grain structure. Each slice had cross-section dimensions of x = 40 μm and y = 30 μm with a slice thickness of z = 750 nm; chosen both for time efficiency in addition to being slightly smaller than the average grain size of the material (~ 1 μm). The total volume milled away through each indentation was ~ 70,000 μm^3. After each slice was milled, SEM secondary electron images were taken of the revealed cross-sections at a tilt angle of 52°, again with a voltage of 5 kV. FIB ion-induced secondary electron images were also taken after each slice in order to realign the FIB beam with the trench; this drift correction (needed to compensate for sample charging) used a cross-fiducial that had been milled into the sample surface for alignment. A FIB mill of an indentation in silicon nitride typically produced ~ 80 cross-section slices with a total mill time of ~ 30 hours.

3.8.2. FIB Tomography of Star Features on Silicon Nitride Balls

The sample preparation for the star features was more complex than that of the artificially indented silicon nitride, the primary difference being is that the stars are located on a curved ball and not a flat surface. For FIB-SEM, the area to be milled has to be positioned as the highest point of the sample which is difficult to achieve when the feature size < 100 μm in diameter, in addition fixing a ball to an SEM stub whilst ensuring this is near impossible. To solve this problem, a custom aluminium SEM ball holder was made (Fig. 3.7). The ball-bearing for investigation was placed in the holder and the star feature located and positioned at the highest point using optical microscopy; the ball was secured in place by tightening the screws on the holder. Due to the larger sample size and morphology of the holder, extra steps were taken to decrease as much as possible charge build-up on the surface sample: copper tape was used to link the ball surface to the surrounding SEM holder and then the holder-ball combination underwent gold sputtering (~ 30 nm surface layer) to increase conductivity.

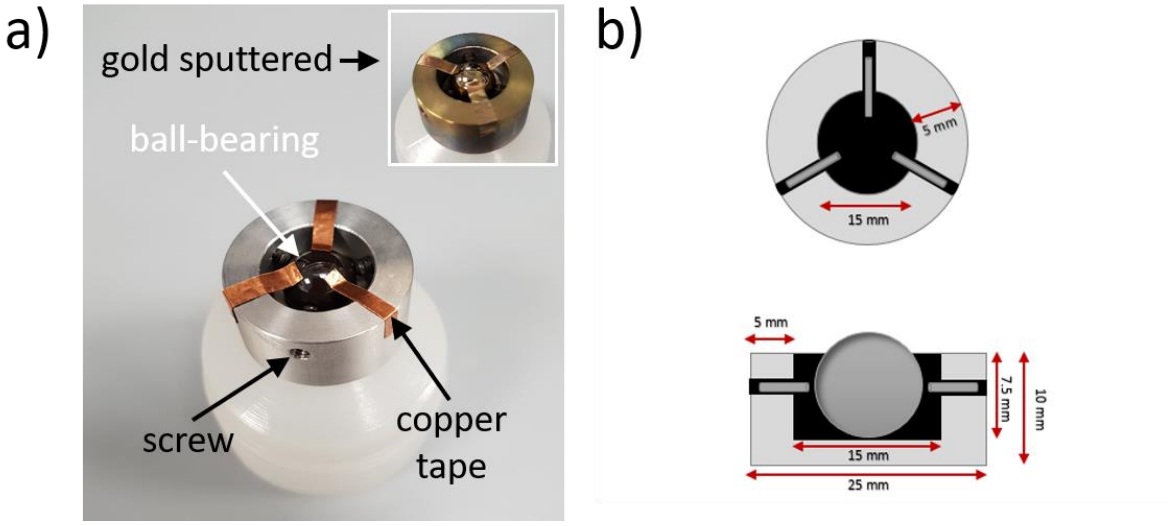

Figure 3.7: (a) The custom SEM holder with ball-bearing inserted and copper tape attached to bearing surface. Inset: The holder-bearing combination after gold sputtering. (b) A schematic of the SEM holder.

The knowledge gained from conducting milling on Vickers indentations was used in determining which parameters were appropriate for FIB tomography of the ball star features. The same basic process was kept the same, i.e. the milling of a large trench with 65 nA current followed by final polishing at 9.3 nA and subsequent slice increments of 750 nm. However, because of the size of the stars (some > 100 µm crack tip-to-tip) the slice dimensions were increased to x = 50 µm and y = 35 µm. Also, in some cases because of large feature size, the whole star feature was not milled through, only areas of specific interest (see Fig. 3.8). Again, FEI Autoslice and View software was used in conjunction with a cross fiducial for drift correction. Due to the increased slice volume in addition to the larger size of the star features (in comparison to the artificial indentations), the total milling time for a single star was ~ 35 – 40 hours.

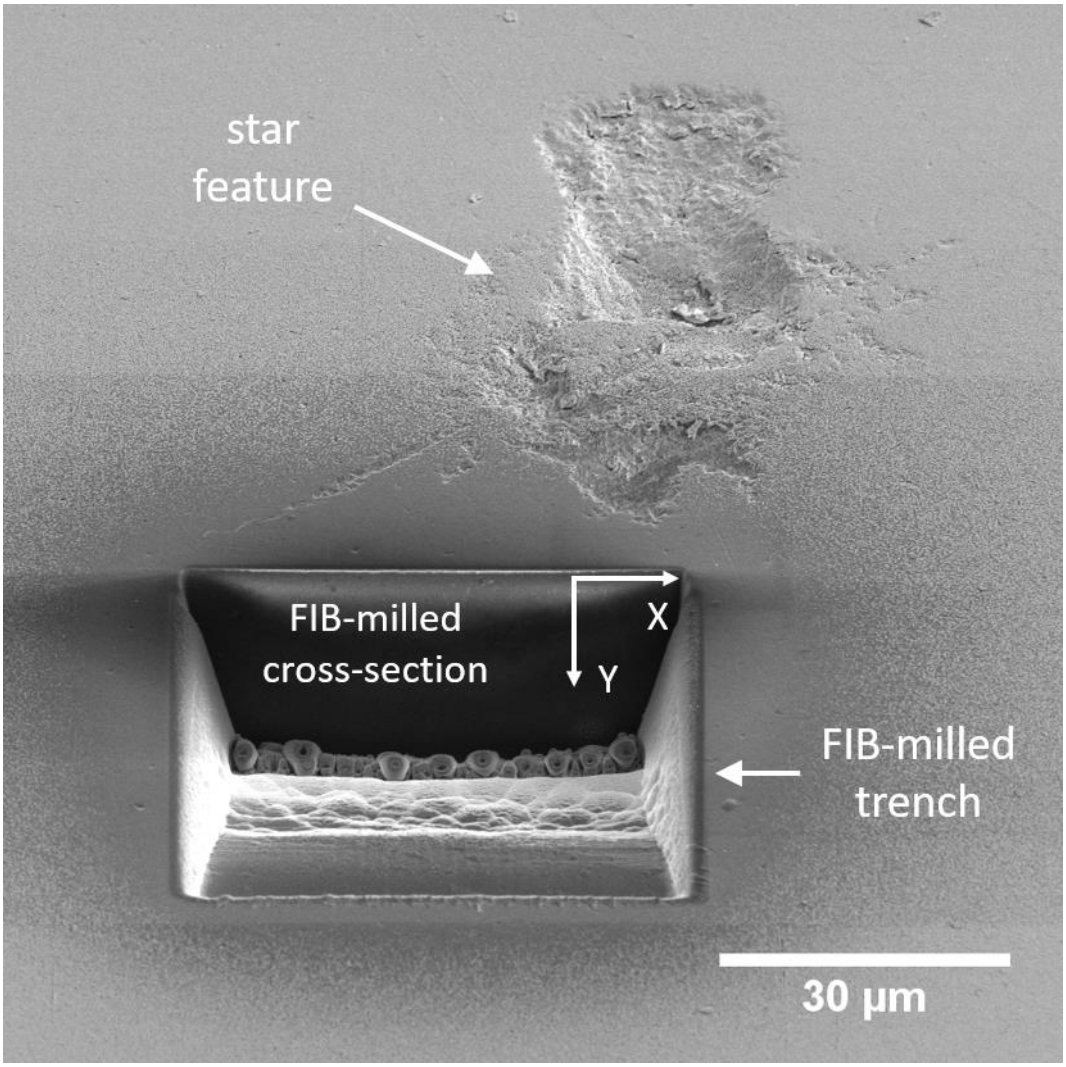

Figure 3.8: An SEM image at a 52° tilt angle of a star feature on the surface of a silicon nitride ball. As seen from the location of the initial trench, FIB tomography was not carried out for the whole sample.

3.8.3. IMOD 3D Reconstruction

The stack of parallel 2D images (slices) produced by Autoslice and View were aligned with each other using ImageJ software and underwent contrast adjustment in order to increase the visibility of cracking present on the cross-sections. The stack of images was then imported into IMOD software where cracking on each slice was identified and subsequently traced. The whole stack of slices was then reconstructed into a 3D crack map using a mesh formed from the traced cracks as an interpolation starting point.

3.9. Micro X-ray Computed Tomography (XCT)

3.9.1. Micro-XCT Sample Preparation

Micro-XCT was conducted on a 1 kg indented SND sample and a 5 kg indented SNA sample. For high resolution micro-XCT, the sample size had to be very small so that it could be located within the field of view of the chosen objective lens. Therefore, samples were indented and then cut down using a diamond wire saw (30 μm wire diameter) to dimensions 2 × 2 × 3 mm (SND) and 1.3 × 1.7 × 1.5 mm (SNA).

3.9.2. Micro-XCT 1 kg Indentation

The XCT device used for the SND sample was a Zeiss Xradia 510 Versa (Oxford University, Dr. Selim Barhli). The SND sample was attached to the head of a metal pin and placed inside the device chamber at a distance of 14 mm from the source and 46 mm from the detector (chosen to optimise FOV and signal intensity). A 4× objective lens was used in order to encompass the indented region of the sample within the field of view. At this magnification the smallest pixel size achievable was 0.78 μm. The sample was rotated through 360° and 1600 projections were taken with an exposure time of 45 seconds at an energy of 49 kV and current of 71 μA; the overall scan time was ~ 23 hours. An LE3 beam hardening filter was placed in front of the source to reduce the attenuation of low energy photons (that may not pass through the sample) from skewing the beam transmission function.

3.9.3. Micro-XCT of 5 kg Indentation

The XCT device used for phase contrast imaging of the SNA 5 kg indented sample was a Zeiss Xradia 400 Versa Bay (University of Manchester, Dr. Tristan Lowe). Because the sample was to undergo an area of interest scan to obtain higher resolution, it was attached to a metal stub and then a 1 mm polystyrene ball was placed adjacent to the side where the 5 kg indentations were located (Fig. 3.9); this meant the correct area could be located for analysis. The sample was then positioned 44 mm from the source and 11 mm from the

detector. A 20x objective lens was chosen which gave a pixel size of 0.7 μm and a LE3 beam hardening filter was added. The sample was again rotated through 360° but this time 1800 projections were taken with each with a 100 second exposure time at an energy and current of 95 kV and 108 μA respectively leading to an overall scan time of ~ 53 hours.

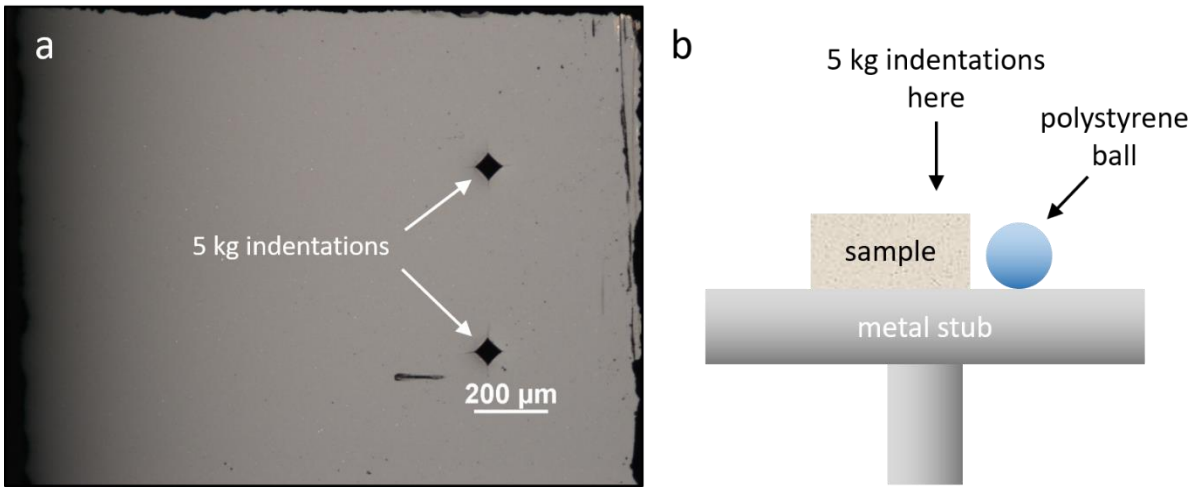

Figure 3.9: (a) Optical image showing the 5 kg Vickers indentations (arrowed) on the surface of the SNA tomography sample. (b) Sample and indentation position relative to the reference polystyrene ball.

3.9.4. Micro-XCT 5 kg Indentation With Penetrant

In order to increase the absorption coefficient of cracks, the 5 kg Vickers indented sample that had previously undergone micro-XCT phase contrast imaging was soaked for 24 hours in a zinc iodide solution that acted as a dye penetrant [5], [6] in preparation for absorption contrast imaging. The penetrant itself was made by mixing 50 g zinc iodide, 16 ml distilled water, 16 ml isopropyl and 0.2 ml Kodak photo-flo. The device used for XCT imaging was a Zeiss Xradia 410 Versa (Durham University, Dr. Katherine Dobson). The sample was glued to the tip of a cocktail stick and placed within the device at a distance of 48 mm from the source and 24 mm from the detector. A 10x objective lens was used giving a pixel size of 0.9 μm and an LE3 beam hardening filter added. This time 2500 projections were taken with an exposure time of 60 seconds at a voltage of 100 kV and current of 100 μA, resulting in an overall scan time of ~ 43 hours.

3.10. He and Ne Gas Field Ion Source (GFIS) Microscopy

Three samples Vickers indented with applied loads of 1 kg and 0.5 kg were prepared for characterisation by GFIS: Two SNA samples, one uncoated and one with a ~ 30 nm sputter coated gold layer (Emscope SC500), and a SND sample with a ~ 15 nm layer of thermally evaporated carbon (Edwards Coating System E305A). All samples were attached to 12.5 mm SEM stubs using a carbon tab.

GFIS imaging was carried out with a Zeiss ORION NanoFab device with switchable helium and neon gas ion sources and an attached electron flood gun for charge neutralisation. Vickers indentations on all samples were imaged with helium and neon FIB at a working distance of ~ 8.5 – 10.5 mm, and a voltage of 30 kV with beam currents of between 0.65 – 0.95 pA. For the uncoated SNA sample, the electron flood gun was utilised to counteract the build-up of positive surface charge from the He^+ and Ne^+ ions [7], [8]. The dwell time of the flood gun was varied from 0 – 1000 µs to observe the influence on image quality and the accelerating voltage was kept constant at 1000 eV. Images were taken in line scan mode and ISEs were detected with an ETD.

3.11. Summary

The experimental procedures described in detail here have been used for the characterisation of Vickers indentations and ball star features in the following investigation results chapters. Occasionally there have been deviations from the described methodologies, but where this is the case, the changes have been highlighted in the relevant chapter.

3.12. References

[1] J. Lankford, "Threshold microfracture during elastic-plastic indentation of ceramics," *J. Mater. Sci.*, vol. 16, no. 5, pp. 1177–1182, 1981.

[2] H. Ichimaru and G. Pezzotti, "Raman microprobe mapping of residual and bridging stress fields in AlN ceramics," *Mater. Sci. Eng. A*, vol. 326, pp. 261–269, 2002.

[3] G. Pezzotti, "In situ Study of Fracture Mechanisms in Advanced Ceramics using Fluorescence and Raman Microprobe Spectroscopy," *J. Ra*, vol. 875, no. May, pp. 867–875, 1999.

[4] S. Tochino and G. Pezzotti, “Micromechanical analysis of silicon nitride: A comparative study by fracture mechanics and Raman microprobe spectroscopy,” *J. Raman Spectrosc.*, vol. 33, no. 9, pp. 709–714, 2002.

[5] B. Yu, R. S. Bradley, C. Soutis, P. J. Hogg, and P. J. Withers, “2D and 3D imaging of fatigue failure mechanisms of 3D woven composites,” *Compos. Part A Appl. Sci. Manuf.*, vol. 77, pp. 37–49, 2015.

[6] B. Yu, R. S. Bradley, C. Soutis, and P. J. Withers, “A comparison of different approaches for imaging cracks in composites by X-ray microtomography,” *Philos. Trans. R. Soc. A Math. Phys. Eng. Sci.*, vol. 374, no. 2071, p. 20160037, 2016.

[7] G. Hlawacek, V. Veligura, R. van Gastel, and B. Poelsema, “Helium Ion Microscopy,” pp. 1–16, 2013.

[8] A. Belianinov, M. J. Burch, S. Kim, S. Tan, G. Hlawacek, and O. S. Ovchinnikova, “Noble gas ion beams in materials science for future applications and devices,” *MRS Bull.*, vol. 42, no. 9, pp. 660–666, 2017.

Chapter 4: Characterisation of Si_3N_4 Indentations via Microscopy, Micro-XCT and Raman Spectroscopy

4.1. Introduction

The aim of this chapter is two-fold: First, to characterise the surface structure of 1 kg and 0.5 kg Vickers indentations, as well as the associated cracking, on the SNA and SNB compositions of silicon nitride. Observations of the indentations have been carried out using high resolution scanning electron microscopy (SEM) as well as 3D optical surface profilometry to gain topographical information. In addition to this, surface residual stress analysis of indentations has been conducted using Raman spectroscopy. The second aim of the chapter is to investigate the sub-surface features of indentations on silicon nitride using non-destructive, high resolution x-ray computed tomography (micro-XCT) and to compare this with the destructive focused ion beam (FIB) tomography and sectioning via diamond lapping techniques utilised in Chapter 5 of this thesis.

4.2. Surface Analysis of Indentation Sites

4.2.1. SEM Observations

The residual indentation impressions and their associated cracking were imaged using SEM for 1 kg and 0.5 kg Vickers indentations on both SNA and SNB silicon nitride samples. Fig. 4.1(a, b) gives a comparison of a 1 kg SNB sample where an indent has been imaged using secondary electrons (SE) and backscattered electrons (BSE). Radial cracks can be seen emanating from each of the indentation corners and this was the case for all indentations imaged at both loads and compositions. This is because the indentation corners have the highest stress concentration, so it is where cracking initiates [1]. There are differences between the SE and BSE images of the indentation: the SE image offers more topographical contrast and hence offers more depth perception, such as at the residual indentation impression. In comparison, the BSEs give a clearer image of the microstructure, and the different phases, because the electron signal detected is a function of the average atomic number. For surface crack identification, it was found that the SE imaging is preferable because it was easier to locate their opening and closing than for

the BSE imaging where the relative contrast between the cracks and the surrounding material area was not as prominent. In addition to this, the cracks themselves appeared sharper because SEs give better edge contrast due to their shallower interaction volume.

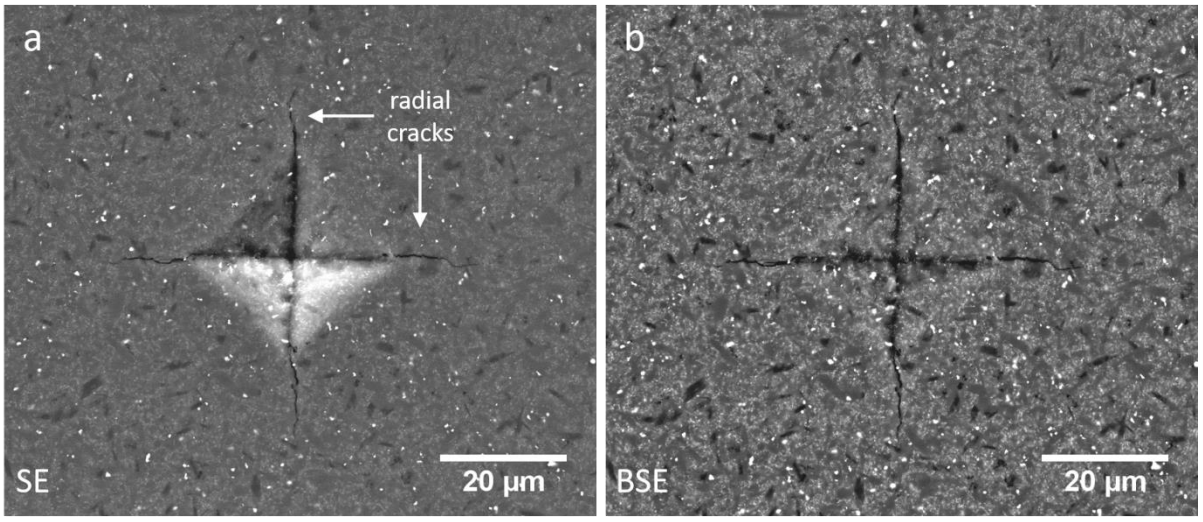

Figure 4.1: A 1 kg Vickers indentation on the SNB composition of silicon nitride imaged using (a) secondary electrons, and (b) backscattered electrons. Radial cracks are observed emanating from indentation corners (arrowed).

The indentation morphologies at the two chosen loads were similar, as seen in Fig. 4.2 which shows 1 kg and 0.5 kg indentations on the SNB composition. For the 1 kg indentations the average diagonal length of the indentions, 2a (refer to Fig. 4.3 in Chapter 2), was 34 ± 0.5 µm and 33 ± 0.5 µm for SNA and SNB respectively, whereas for the 0.5 kg indentations, 2a were measured at ~ 23 ± 0.5 µm for SNA and ~ 22 ± 0.5 µm for SNB. When the hardness was calculated (using Eq. 2.1 from Chapter 2), a lower value was found for the 0.5 kg indentations (for SNA, HV = 1650 ± 50 for 1 kg load in comparison to 1700 ± 50 for 0.5 kg load) implying that there is an indentation size effect present. The average radial crack length was measured to be ~ 12 µm for the 1 kg indentations for both compositions, and ~ 7 µm and ~ 6 µm for the SNA and SNB 0.5 kg indentations. The ratio of the surface radial tip to tip crack length, 2c, to the indentation diagonal length, 2a, was calculated at ~ 1.7 for the 1 kg indentations and ~ 1.6 for 0.5 kg indentations (both SNA and SNB had the same c/a ratios at the same loads). The c/a ratio is an important value as it can be used to predict the type of cracking regime that exists in the sub-surface, i.e. a half-penny crack regime of a Palmqvist regime [2]. As mentioned in Chapter 2, for silicon nitride, generally if the c/a ratio is less than 2, then a Palmqvist regime has typically been

found by serial sectioning using grinding methods [3], [4]. Therefore, for the 0.5 kg and 1 kg indentations investigated here, a Palmqvist regime is predicted.

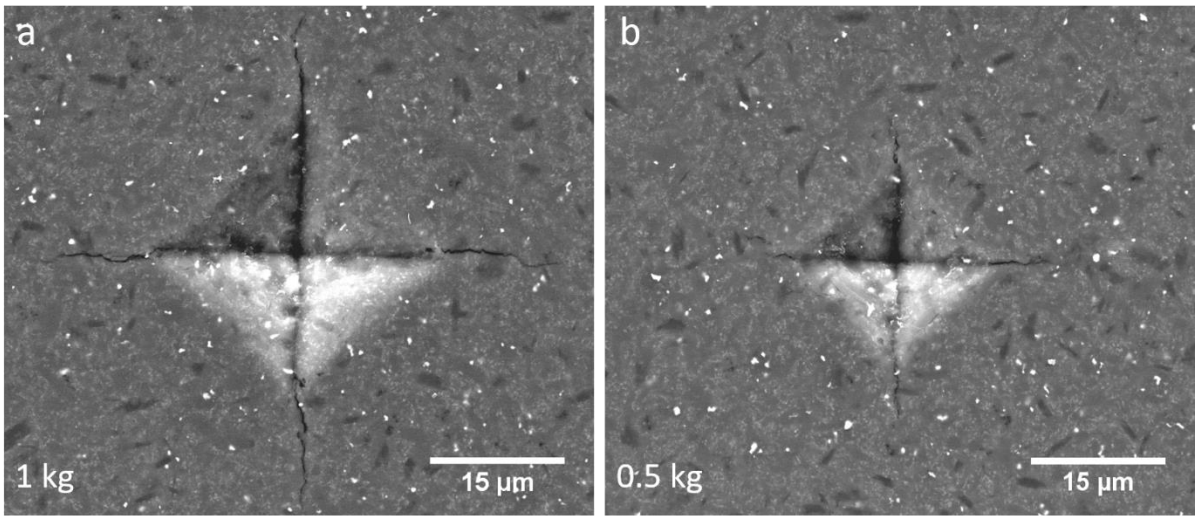

Figure 4.2: SEM images of (a) a 1 kg, and (b) a 0.5 kg indentation on the SNB composition of silicon nitride. Radial cracks are observed emanating from indentation corners at both loads.

Higher magnification images taken of the indentations revealed further microstructural damage. For instance, the 1 kg SNA indentation in Fig. 4.3 exhibited damage along the indentation edge in the form of micro-cracking and grain pull-out (inset). The micro-cracking is orientated parallel to the indentation edge, which would be expected to experience lower stress in comparison to the high concentration at the indentation corners. It is most likely formed as a result of volume displacement caused when the indenter tip presses in to the material surface compressing the central zone downwards [1], [5]. Since there are minimal slip systems in silicon nitride the extent of dislocation driven plastic deformation is limited and long range elastic compression can accommodate the downward displacement. As well as cracking at indentation edges, there may be an associated uplifted zone surrounding the residual indentation impression, but this not observed in the SEM images.

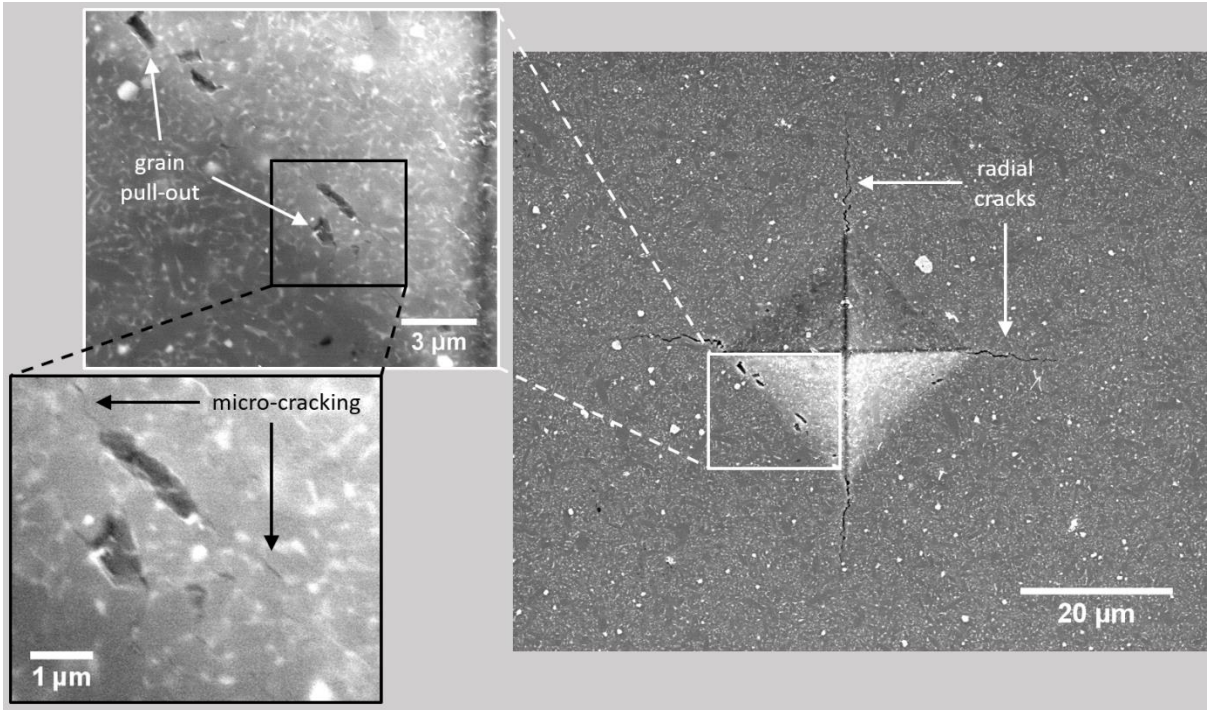

Figure 4.3: A 1 kg indentation on SNA showing radial cracking (arrowed). Inset: Along the indentation edge grain pull-out is observed as well as micro-cracking (arrowed).

The nature of the cracking associated with the indentations is illustrated further for SNA and SNB in Fig. 4.4 and Fig. 4.5 respectively. The radial cracks in SNA primarily adhered to an intergranular pathway as observed in Fig. 4.4(a) where the fracture traces along the side of an elongated ß-grain. Even at lower magnifications the jagged pathway of cracking implies intergranular paths as the preferred method of fracture. Where transgranular cracking was observed, it occurred where the crack front had contacted near-perpendicular to the grain edge (Fig. 4.4(b)). It was quite often the case that transgranular cracking preceded the crack tip or that the crack tip was located in contact with a grain. The morphology of the radial crack opening was particularly interesting in that there was no clear surface initiation point (which is expected at the corners for Vickers indentations [5]); at the indentation corner there were a number of narrow cracks that appear to diverge to form a single, wider radial crack as highlighted in Fig. 4.4(c). The primary branches of the radial cracks (in some cases there was a secondary radial) were observed to have a crack opening of approximately ~ 0.4 µm for the 1 kg indentations and ~ 0.2 µm for the 0.5 kg indentations and this progressively narrowed along the crack pathway until the tip (this was the same for radial cracks on the SNB composition).

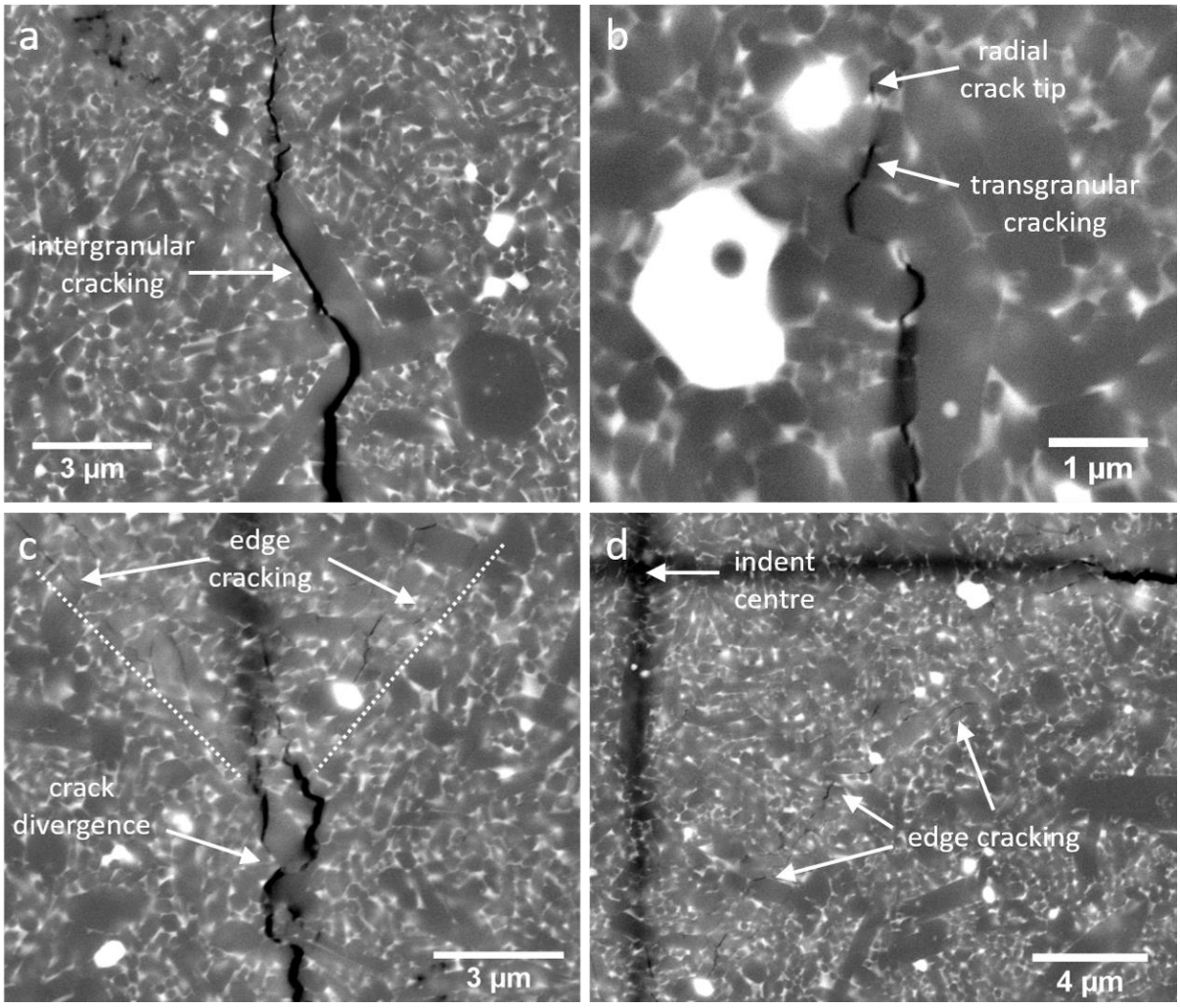

Figure 4.4: High magnification SEM BSE images of cracking on SNA indentations: (a) a radial crack showing an intergranular crack pathway. (b) a radial crack tip with transgranular cracking observed (arrowed). (c) an indentation corner (dashed line) showing crack divergence and edge cracking. (d) Cracking along the indentation edge.

The images in Fig. 4.5 are of cracking features that were observed on the indented SNB sample. Again, the cracking was primarily intergranular. The intergranular crack arrowed in Fig. 4.5(b) on a 0.5 kg indentation is an interesting example as the crack intersects the surface grain perpendicularly yet is still deflected along the grain edge. It may be that the reduced stress and crack velocity experienced by the 0.5 kg indentation radial cracks in comparison to the 1 kg indentions ones (due to a decrease in energy transferred from the indenter) means that the probability of transgranular cracking is reduced [6], although statistics for this have not been collected in this analysis. It is worth noting that the crack pathway may be determined by the easiest route on the sub-surface, but it is not possible to determine whether this is transgranular or intergranular from the surface. Edge cracking was observed in indentations such as that shown in Fig. 4.5(a).

Also shown is a large grain of ~ 7 μm in length (dashed line) that had multiple fracture branches within the grain itself (Fig. 4.5(a)). The location of the grain within the residual indentation impression and the multiple transgranular fractures across it suggest that cracking was formed as a result of direct contact with the indenter side upon loading. Micro-cracking at the indentation corner was observed to converge to form the radial crack (e.g. Fig. 4.4(c)). It is this micro-cracking that is the nucleation point from which radial cracks initiate [7]. Secondary radial cracking (Fig. 4.5(c)) was also seen in some indentations and occurred when the multiple micro-cracks located at the indentation corner did not converge to form a single radial crack. The secondary radial was always shorter and easily distinguishable from the primary radial. Occasionally surface radial cracks would show bifurcation and subsequent divergence around grains as shown in Fig. 4.5(d); this would be a location where grain pull-out is probable, and likely occurs sub-surface too.

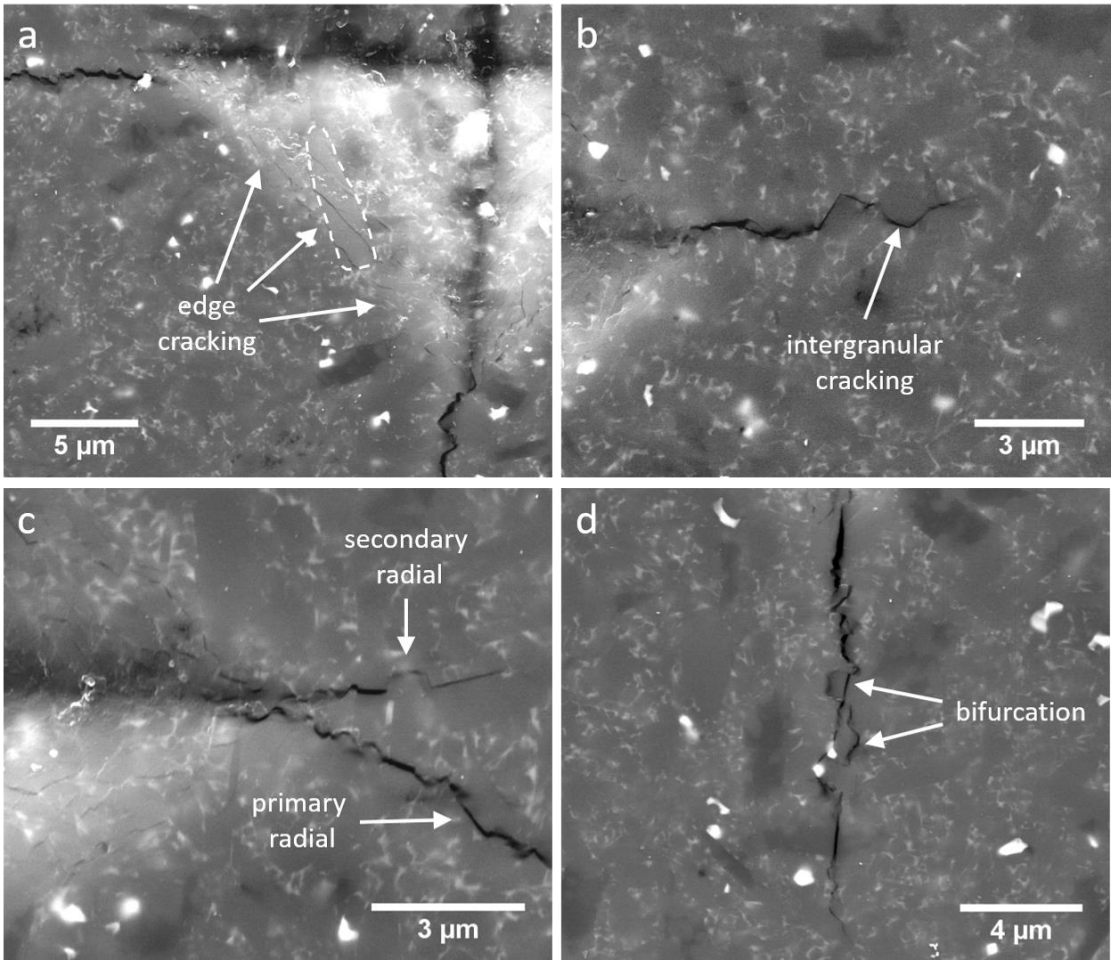

Figure 4.5: High magnification SEM images of cracking on SNB indentations: (a) Cracking along the indentation edge where a large grain (dashed line) has multiple fractures. (b) An intergranular fracture pathway observed in a radial crack. (c) Both a primary and a secondary radial crack emanating from an indentation corner. (d) Bifurcation around grains observed in a radial crack.

The SEM observations have revealed that the two primary compositions of silicon nitride investigated in this study, SNA and SNB, have similar cracking morphologies associated with Vickers indentations. They have the same c/a ratio for 1 kg and 0.5 kg indentations; both of which predict a sub-surface Palmqvist cracking regime [2], [4], [8]. The 0.5 kg and 1 kg indentations showed a similar morphology but a lower c/a ratio for the 0.5 kg indentation caused by a lower stress (crack velocity) as a result of the stress field extending out less, and hence a reduced crack length. The presence of micro-cracking, which occurs at the compressive-tensile stress boundary [9], along the indentation edges was observed in both loads but was more prominent in the 1 kg indentations. The primary fracture path exhibited by the radial cracks is intergranular. This is expected as the microstructure of bearings-grade silicon nitride is tailored for an increased fracture toughness via crack deflection and bridging caused by the presence of the high aspect ratio ß-grains [10]–[12]. No direct evidence of sub-surface lateral cracking was visible via SEM surface imaging, however the cracking observed around the indentation edges may partially be shallow lateral cracks intersecting with the surface. If that is the case, then these would be areas where material removal could occur in the form of flaking under rolling contact, although even micro-cracking can remove grains (as highlighted in Fig. 4.3).

4.2.2. 3D Optical Profilometry

Optical surface profilometry was used on the 1 kg and 0.5 kg SNA and SNB indentation to gain an insight into the topography of the residual indentation impressions and the surrounding region. Fig. 4.6 shows a contour map of the 1 kg SNA indentation (Fig. 4.6(a)) as well as a line plot taken across the indentation from one side to the other (Fig. 4.6(b)). The red regions on the contour map represent zones which have an increased uplift relative to the average level of surrounding material. This is primarily located surrounding the residual indentation impression, with uplift height measured at ~ 400 nm for the indentation in Fig. 4.6. In addition to this uplift, there is also a raised region surrounding the radial cracks emanating from the indentation corners (arrowed). The line plot gives an indication of the topographic profile across the indentation and shows that the uplift reaches a maximum at the very edge of the residual indentation impression and trails off to a zero gradient ~ 15 μm from the edge. The topography within the residual indentation impression is more difficult to establish as there are not as many data points

because the morphology of the indentation makes it hard for reflected laser light to be detected by the CCD. However, the central point of the impression is relatively flat (potentially due to indent diamond tip blunting), so a depth measurement can be acquired and was found to be ~ 3.5 µm for this indentation.

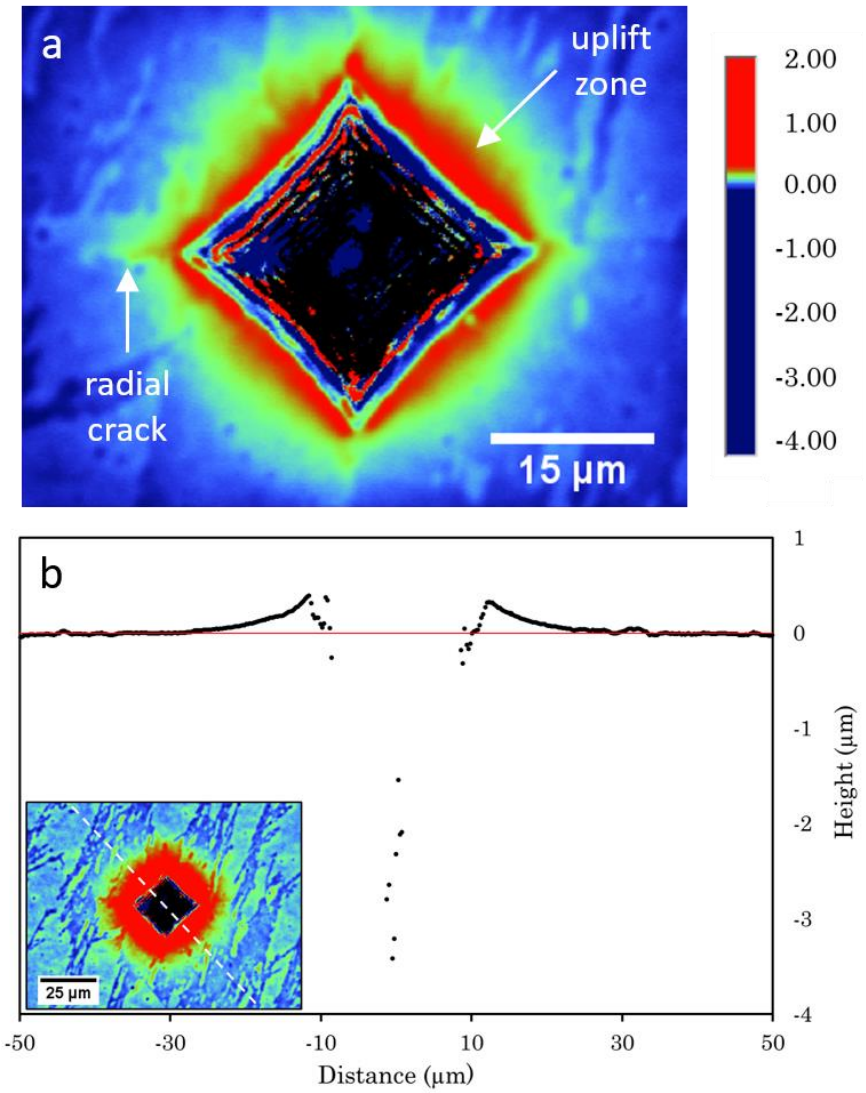

Figure 4.6: (a) A topographic contour plot of a 1 kg SNA indentation showing areas of uplift and depression. (b) A topographic line plot across the same 1 kg indentation. Inset shows a topographic contour plot overlaid with where the line plot was extracted.

The contour map and line plot of a 0.5 kg SNA indentation are given in Fig. 4.7. The overall morphology of the topography is similar to that of the 1 kg indentation with the uplifted zone surrounding the residual indentation impression. Again, the highest zone of uplift, with a height of ~ 250 nm (for the indentation in Fig. 4.7), was located at the region closest to the indentation edge. The line plot of surface height has the same profile as that of the 1 kg indentation, however, the distance at which the slope away from the

indentation edge falls to zero was measured at ~ 10 µm, compared to 15 µm in Fig. 4.6. The deepest recorded data point from the line plot for the 0.5 kg indentation was ~ 2 µm. It is important to note that the maximum recorded heights measured for both the 0.5 kg and 1 kg indentations were greater than the heights taken from the line profiles; this is because there can be localised peaks in height caused by grain pull-out or debris on the sample surface of the order of 1 – 2 µm (the grain size).

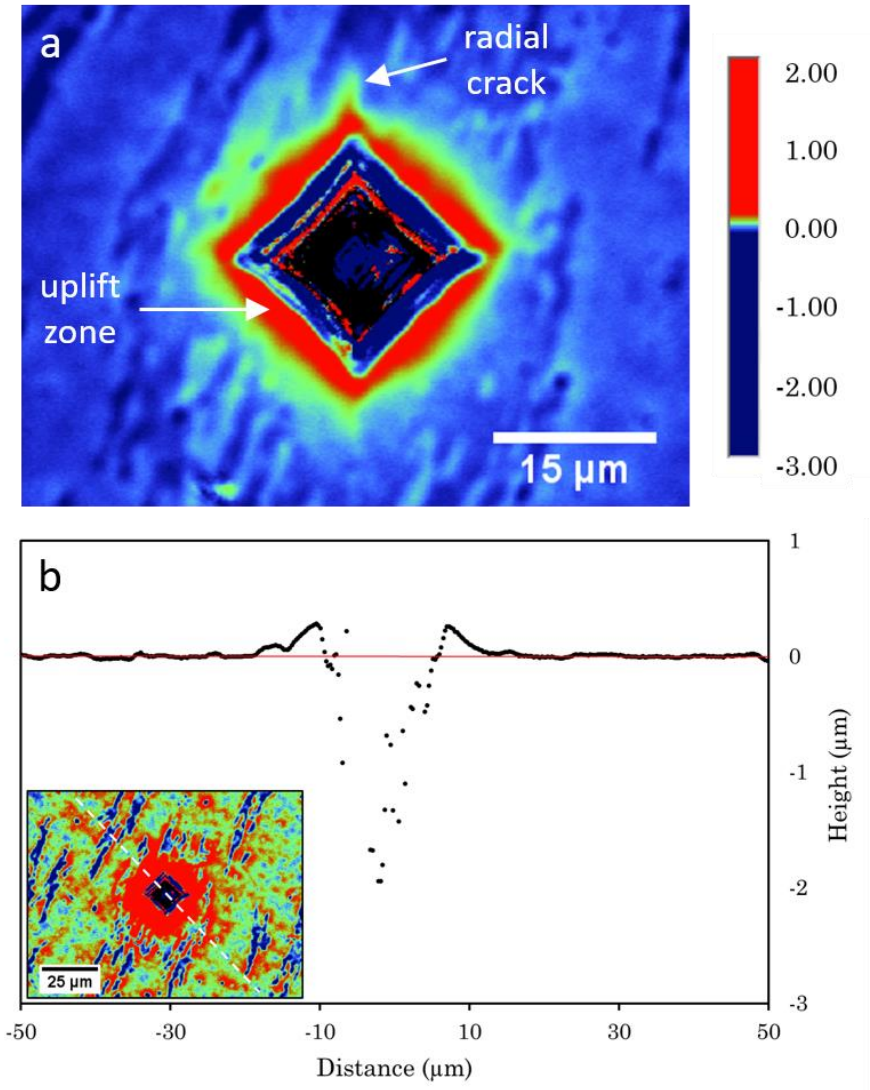

Figure 4.7: (a) A topographic contour plot of a 0.5 kg SNA indentation showing areas of uplift and depression. (b) A topographic line plot across the same 0.5 kg indentation. Inset shows a topographic contour plot overlaid with where the line plot was extracted.

The average depth and uplift of the SNA and SNB 1 kg and 0.5 kg indentations (three indentations at each load and composition) taken from line plot measurements are given in Table 4.1 below. They show similar average uplift for each load but slightly differing

residual indentation depths, however this may be due to a shortage of data points within the residual indentation impression in comparison to the surrounding area.

Composition	SNA		SNB	
Indentation	1 kg	0.5 kg	1 kg	0.5 kg
Uplift Height (µm)	0.38 ± 0.02	0.27 ± 0.03	0.38 ± 0.03	0.30 ± 0.04
Depth (µm)	3.4 ± 0.1	2.1 ± 0.1	3.3 ± 0.2	2.4 ± 0.1

Table 4.1: The average values for the uplift height and indentation depths on SNA and SNB.

The radial cracks emanating from the indentation corners also appeared to show some adjacent surface uplift. Fig. 4.8 is a line plot across a radial crack on a 1 kg SNA indentation. The uplift showed a peak between 150 – 200 nm and then a sharp drop off followed by smaller peak; this dip could be the radial crack opening.

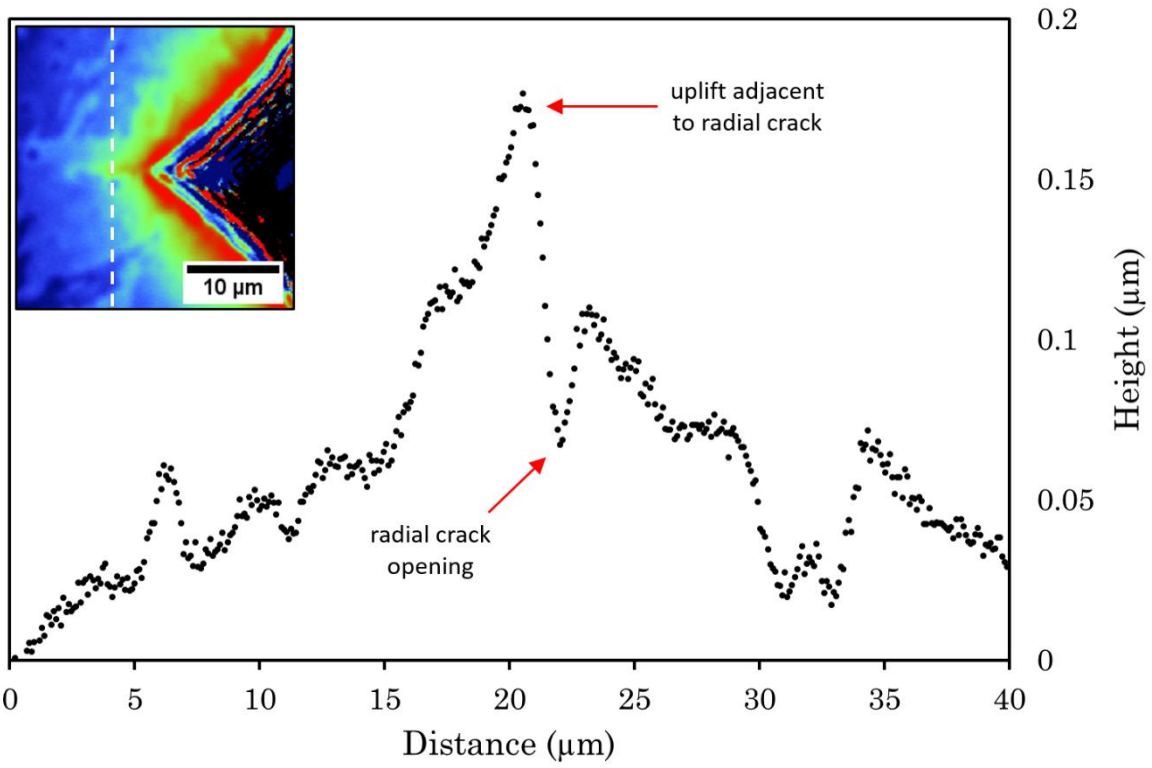

Figure 4.8: A topographic line plot across a radial crack emanating from a 1 kg indentation. Arrowed is the maximum area of uplift in addition to evidence for the radial crack opening.

The surface profiling using white light interferometry has revealed quantifiable topographical information about the indentation on silicon nitride that was not possible

with SEM imaging. The most significant finding was the presence of the uplifted zone surrounding residual indentation impressions which has importance for the tribological properties of the material. For instance, if an indentation was on the surface of a bearing then the uplifted zone would act as a first contact point for any rolling contact, which would increase the friction between the contacting surfaces potentially resulting in wear and material removal [13], [14]. In addition to this, the localised uplift observed at the edges of radial cracks may initiate further crack propagation under contact.

4.3. Raman Spectroscopy

To predict how micro-cracks might form and/or propagate under externally applied stresses it is also important to understand the residual stresses present in the material. Raman spectroscopy was used to characterize localised stress in regions surrounding a 1 kg indentation to ascertain which locations contain residual stress and the magnitude of this stress. Point scans, line scans, and area maps were performed on regions of interest by measuring the change in peak position of the stress dependent S_1 (861 cm^{-1}) and S_2 (1044 cm^{-1}) silicon nitride peaks as a function of location [15]. The S_1 peak has been found to have a greater stress dependency than the S_2 peak so is the primary peak used here, however, the S_2 peak has occasionally been used as a comparison.

4.3.1. Point Scans Surrounding Indentations

Point scans were performed at the following locations for a 1 kg indentation on SNA: at the centre of the residual indentation impression, on the impression slope, and over a radial crack. A scan was also taken at a representative parent material region far away from the indented area, the spectrum of which is given in Fig. 4.9 with the S_1 and S_2 peaks arrowed. The peak positions at the reference region for the S_1 and S_2 peaks were measured to be 860.9 ± 0.5 cm^{-1} and 1044.0 ± 0.4 cm^{-1}, this compares well with that published by Pezzotti et al [15]–[17]. Table 4.2 gives the peak positions and FWHM of the peaks of interest and the various locations.

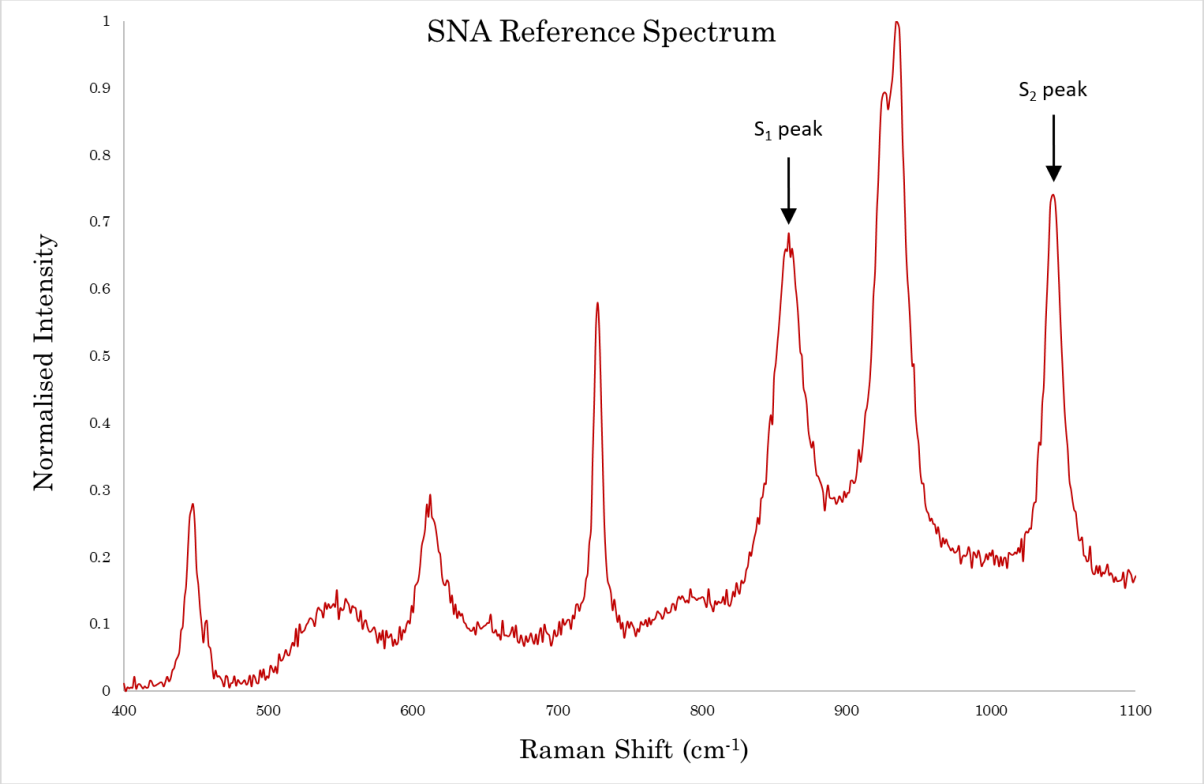

Figure 4.9: A Raman spectrum taken at the reference location using a 10 µm laser spot size on SNA silicon nitride. Arrowed are the S_1 and S_2 peaks.

	Peak Position		FWHM	
Peak	**S_1 (cm^{-1})**	**S_2 (cm^{-1})**	**S_1 (cm^{-1})**	**S_2 (cm^{-1})**
Parent Reference	860.9 ± 0.5	1044.0 ± 0.4	23 ± 2	26 ± 1
Centre of Indent	873 ± 1	1056 ± 1	50 ± 4	32 ± 6
Slope of Indent	871.4 ± 0.6	1058.0 ± 0.5	44 ± 2	73 ± 2
Radial Crack	861.7 ± 0.5	1044.6 ± 0.4	23 ± 1	26 ± 1

Table 4.2: The peak positions and full width at half maximum (FWHM) for the S1 and S2 at various locations in the SNA 1 kg indentation vicinity.

At the centre of the residual indentation impression there is a significant shift in the peak position for the S_1 peak from 860.9 ± 0.5 cm^{-1} measured at the zero-stress region to 873 ± 1 cm^{-1}; a similar shift is also observed for the S_2 peak. The point scan on the indentation slope showed a similar peak shift although not the same magnitude as at the centre. There was also a peak shift for the scan over a radial crack, but this was small in comparison to those taken within the residual indentation impression.

An increase in peak frequency position from the parent material reference value should equate to the presence of residual compressive stress, with the amount of increase giving

an indication to the magnitude of the compressive stress present [18]. The values of peak position obtained in Table 4.2 imply that there is a very high level of residual compressive stress present at the centre of the residual indentation impression as well as on the slope. These regions are where the indenter tip contacted the surface under the applied 1 kg load resulting in localised plastic deformation as the material is compressed, so the presence of high compressive stress at the centre correlates with the area which would have experienced the highest pressure under tip contact. However, the plastic deformation of the silicon nitride within the residual indentation impression causes damage to the crystal lattice structure which increases the FWHM of the peak whilst shifting it to a higher position, and is similar to what is seen in Raman peaks of glassy phases [19]. This phenomenon is highlighted in the relative differences between the FWHM of the S_1 peak at the centre of the indentation, and that at the reference region: 50 ± 4 cm^{-1} and 23 ± 2 cm^{-1} respectively. Therefore, Raman spectroscopy is not suitable to accurately measure residual stress levels in regions that have undergone significant plastic deformation because Raman emission relies on an intact lattice structure, but it can be used as an indication to which region have undergone plastic deformation; in this case, the volume of material within the residual indentation impression.

4.3.2. Line Scans of Indentations

Line scans of peak frequency position as a function of distance away from the indentation, as well as distance along a radial crack emanating from an indentation corner, were produced to investigate how the residual stress changes with distance. Fig. 4.10 shows the line scan for the S_1 peak starting from just inside the 1 kg indentation and extending out to 80 μm. There is a steep shift in peak position with distance from the indentation until ~ 30 μm out where the rate of change of the slope decreases. After ~ 60 μm the slope levels out to just below the reference value of ~ 861 cm^{-1} until the end of the line scan indicating the presence of long-distance residual tensile stress; this has been observed in a previous Raman study of indentations on silicon nitride [19]. The highest peak position of 876 cm^{-1} is located within the residual indentation impression, however the accuracy of this value is limited because, as mentioned previously, this is an area of plastic deformation, so the stress-peak position relationship is unknown.

From the peak frequency line scan in Fig. 4.10, the nature of the residual stress field around the residual indentation impression can be inferred in addition to its lateral

extent. There is a residual compressive stress present that decreases as a function of the distance from the indentation side up to ~ 60 μm (as mentioned above) where the residual stress approaches the reference value. This compressive stress surrounding the residual indentation impression is caused by the presence of the elastically deformed zone associated with the formation of the residual indentation impression [20], [21]. The change in rate of decrease of the compressive stress at ~ 30 μm may be indicative of a transition zone from a plastic and elastically deformed region to just an elastically deformed one; similar to that proposed by Pajares et al for the volume beneath an indentation [21], [22]. Although the compressive stress-distance relationship is not necessarily linear so a change in rate of the decrease in compressive stress may not be a related to a zone transition.

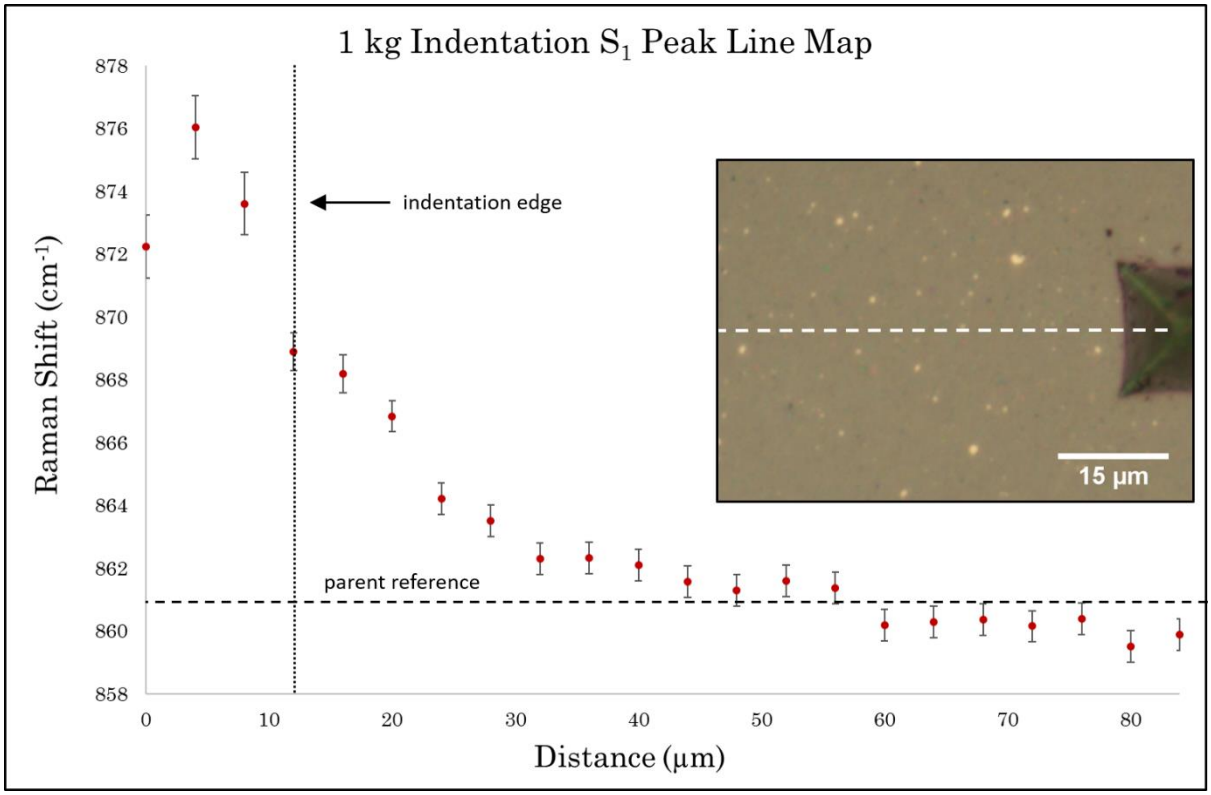

Figure 4.10: A scatter plot of S1 peak Raman shift as a function of distance from the 1 kg residual indentation impression. Inset is an optical image with the dashed line showing the location of the line scan.

The equation for piezospectroscopic residual stress calculations described in Equation 2.3. in Chapter 2.7. can be used to calculate the magnitude of the residual stress present from the peak position shifts measured. Unfortunately, the piezospectroscopic coefficient for

the silicon nitride compositions used in this project are not available. However, by taking values of Π from published literature, estimates of the residual stress here can be estimated. Here Π = -2.11 ± 0.15 cm^{-1} GPa^{-1} has been used for the S_1 peak position stress calculations [15]. From this it can be calculated that the residual compressive stress at the indentation edge (where S_1 = 869 ± 0.5 cm^{-1}) is ~ 3.8 ± 0.5 GPa.

A peak wavenumber line scan was also conducted outward from the indentation corner adjacent to the side of the radial crack pathway (Fig. 4.11). As in Fig. 4.10 of the line scan away from the indentation side, the peak position starts higher than that of the reference value, although for Fig. 4.11 the peak is lower than that in Fig. 4.10 with a value of 865.3 ± 0.5 cm^{-1} in comparison to 876 ± 1 cm^{-1} because the magnitude of plastic deformation is probably different. Again, like in Fig. 4.10, there is a decrease in peak position to around the parent material reference value, at ~ 10 μm out from the indentation impression however, this decrease continues past the reference value to ~ 13 μm where it begins to increase until reaching the reference value position again at ~ 20 μm.

The above is consistent with the surface residual compressive stress present at the indentation corner being less than that at the indentation side, and further out (~ 10 μm), the compressive stress changes to a residual tensile stress regime. This region of tensile stress from 10 μm to 20 μm can be explained in terms of the stress relief mechanism induced as a result of the indentation shape. The Vickers indenter faces push material perpendicular to the face planes causing a compressive stress, on unloading, tensile stress is induced at indentation corners at the boundary between the plastic and elastic deformation zones; if the magnitude of this tensile stress is greater than the material toughness then radial cracking is initiated [19], [21], [23]. The shift from residual compressive stress to tensile stress (peak position = 859.3 ± 0.5 cm^{-1}) correlates with the tip of the radial crack which has a measured length of ~ 10 μm. Again, using Eq. 2.3 this gives a residual surface tensile stress magnitude of σ = 0.8 ± 0.3 GPa. This tensile stress that continues beyond the crack tip is most likely acting to pull apart the crack faces and hence propagate the crack further, although no directional stress analysis was conducted here.

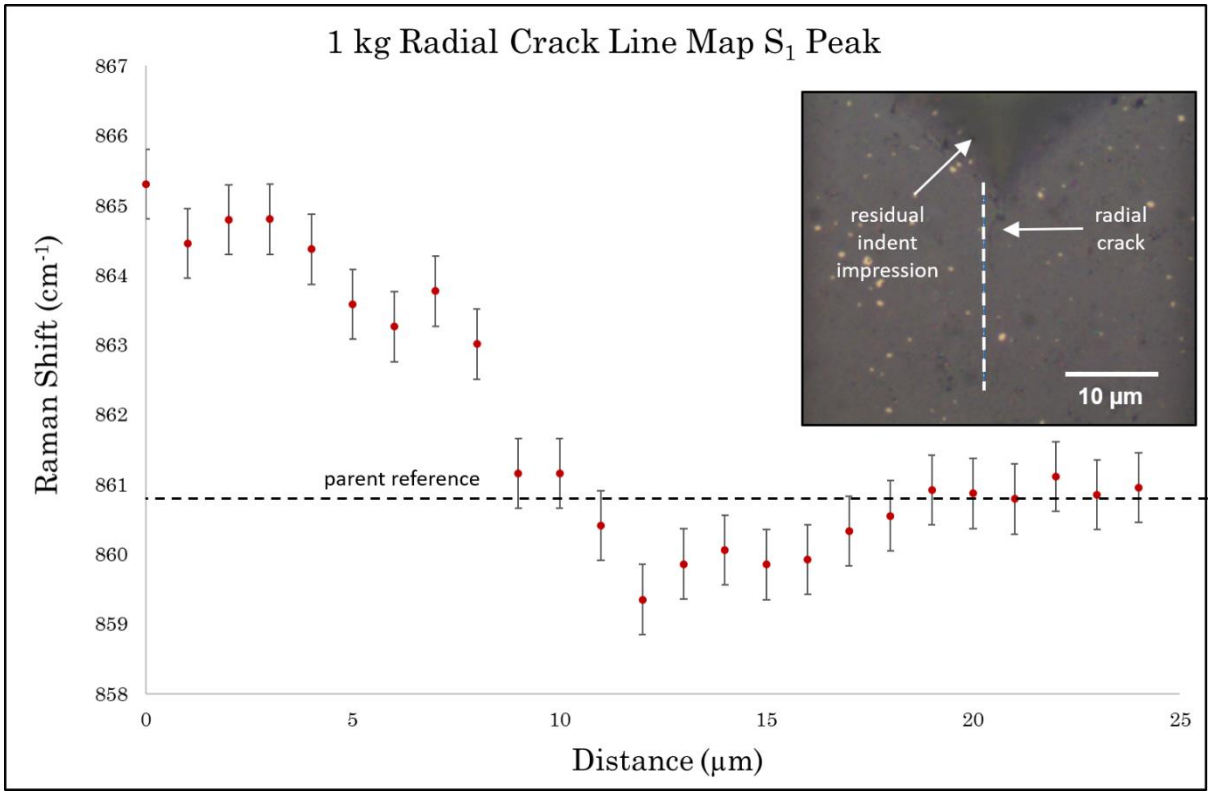

Figure 4.11: A scatter plot of S1 peak Raman shift as a function of distance from the corner of a 1 kg residual indentation impression extending outward along the side of a radial crack (arrowed). Inset is an optical image with the dashed line showing the location of the line scan.

4.3.3. Area Mapping of Radial Crack

A 15 × 15 μm area map of the peak positions was carried out around the same radial crack present emanating from the 1 kg indentation investigated via the line scan in Fig. 4.11 to further characterise the surrounding residual stress levels. The subsequent S_1 and S_2 peak position maps are given in Fig. 4.12(a, b); the location of the indentation mapped is shown in the Fig. 4.12(b) inset. Traced over the area maps is the location of the radial crack observed from optical imaging.

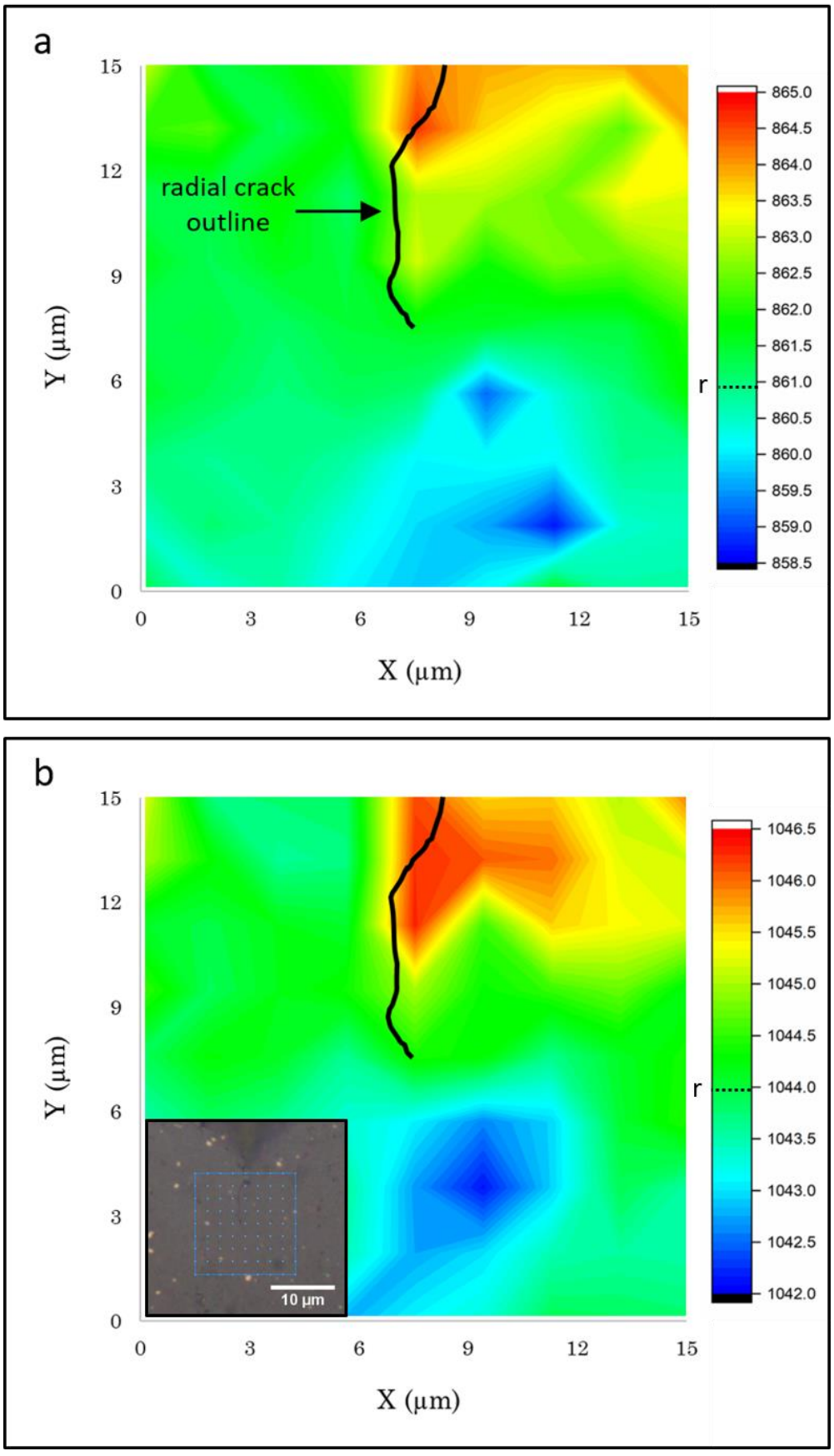

Figure 4.12: Area maps of the S1 (a) and S2 (b) peak positions in the vicinity of a radial crack emanating from a 1 kg indentation corner. The inset in (b) shows the mapped area (starting from the indentation corner).

An increase in peak position occurs surrounding the crack opening at the indentation with a maximum value of 864.6 ± 0.5 cm^{-1} which indicates an area of increased compressive stress calculated as σ = 1.9 ± 0.4 GPa. The peak position for both the S_1 and S_2 decreases past the parent reference value and into the tensile stress zone (the blue coloured region) just beyond the radial crack tip. The tensile stress zone may be expected to start directly after the crack tip but in Fig. 4.12 there is a 2 – 3 μm gap before it does; this is most likely due to an underestimate of the radial crack observed length from the limited optical resolution, i.e. the radial crack extends further than the trace shows. In addition, only the surface residual stress is being measured (and is an average over the sampled volume) so the location of stresses may differ to the sub-surface. The visible region of relatively high tensile stress shown on the area maps is ~ 6 × 6 μm which is a sizeable area relative to the crack size. The maximum S_1 peak position shift within this region (S_1 = 858.7 ± 0.5 cm^{-1}) equated to a average surface tensile stress of σ = 1 ± 0.3 GPa; this is within the uncertainty of that calculated for the tensile stress region plotted in Fig. 4.11. This compares well to previous Raman studies on indentation in silicon nitride where surface tensile stress at crack tips was found to be ~ 2.3 GPa for a 5 kg indentation [24] and 0.2 GPa for a 0.5 kg indentation [19], although the latter was for a Berkovich-shaped indenter tip not a Vickers tip. A study on residual stress at crack tips in silicon nitride formed by notch fracture found a tensile stress value of 0.5 GPa [15]. Under further applied external stress, i.e. in rolling contact, the magnitude and area of the tensile region would increase which may lead to further crack propagation [15].

4.4. Micro-XCT of Indentations for Sub-Surface Analysis

4.4.1. XCT of 1 kg Indentation

To examine sub-surface microstructural changes under the indentation zones, x-ray micro-computed tomography was carried out. A 1 kg indented SND sample was scanned using a Zeiss Xradia 510 Versa x-ray microscope with the parameters described in Chapter 3. The SND composition was chosen because it has a larger grain size than the other compositions, so it was thought that details of the microstructure could potentially be visible. The multiple 2D x-ray absorption projections produced by the XCT scan underwent 3D reconstruction and were subsequently converted into a stack of 2D tomographic slices an example of which is given in Fig. 4.13(a). In Fig. 4.13(b), within the red circle is what is thought to be the 1 kg indentation. It was difficult to locate and, as

can be seen, the morphology of the indentation was not resolvable which means the aim of resolving the sub-surface cracking was not achieved. The lack of resolution was most likely a combination of the small feature size of the 1 kg indention (crack width of ~ 0.4 μm), a lack of spatial resolution, and insufficiently long exposure time per projection resulting in a low signal-to-noise ration.

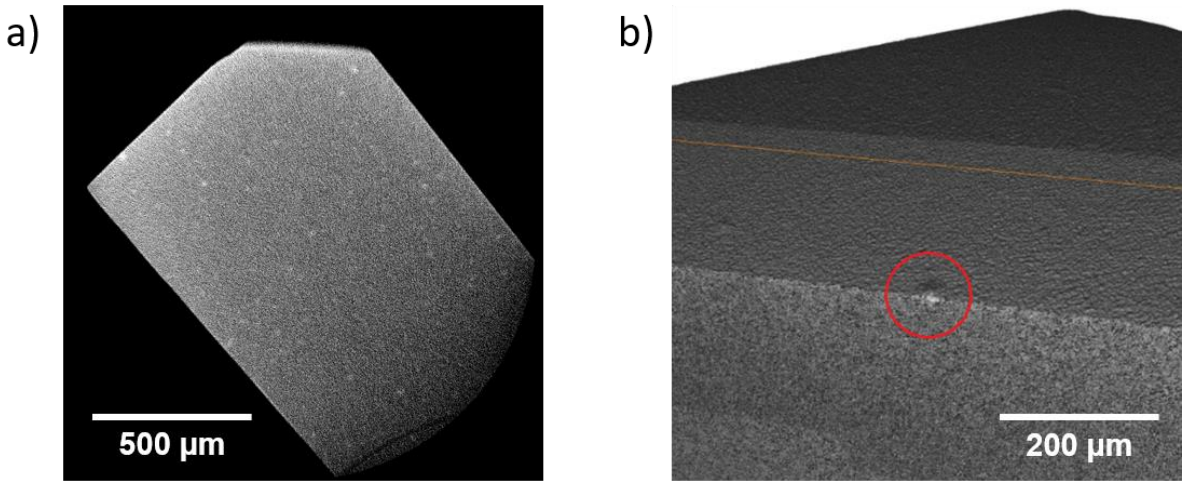

Figure 4.13: (a) An example of a 2D tomographic slice from the 1 kg SND indentation scanned with the XCT. (b) A 3D reconstruction of the projections highlighting what was thought to be the 1 kg indentation (red circle).

4.4.2. XCT of 5 kg Indentation

The 3D XCT reconstruction of the 1 kg indentation is clearly not of sufficiently high resolution enough to gain any useful information from about sub-surface cracking. Therefore, to improve the chance of resolving cracking, several parameters were changed: the indentation load was increased from 1 kg to 5 kg to increase the crack sizes and widths, the number of projections and their exposure time were also increased, and the sample was made smaller to fit in a smaller field of view hence allowing for increased spatial resolution (see Chapter 3: Materials and Methodology for exact parameters). For a 5 kg indentation, the typical diagonal size of an indentation impression was 75 μm, and the length of radial cracks ~ 35 μm. After scanning, the 1800 projections were tomographically reconstructed and subsequently converted in to a stack of 2D images representing the 3D reconstruction.

Unlike for the XCT scan on the 1 kg sample, the 5 kg indentations were easily located. However, although there were two 5 kg indentations on the sample, only one of them had

remained fully within the field of view during sample rotation. 2D tomographic slices of the indentation are shown in Fig. 4.14, the orientation of which are almost parallel to the sample surface. The residual indentation impression is visible as an area of darker contrast in comparison to the surrounding region which is lighter. This darker contrast is due to the different phases, i.e. the volume taken up by the residual indentation is composed of air whereas the sample itself is silicon nitride. The larger region of darker contrast that almost overlaps the indentation is the air above the sample surface and is visible because the tomography slicing was not carried out perfectly parallel with the sample surface (the sample was scanned with a slight tilt).

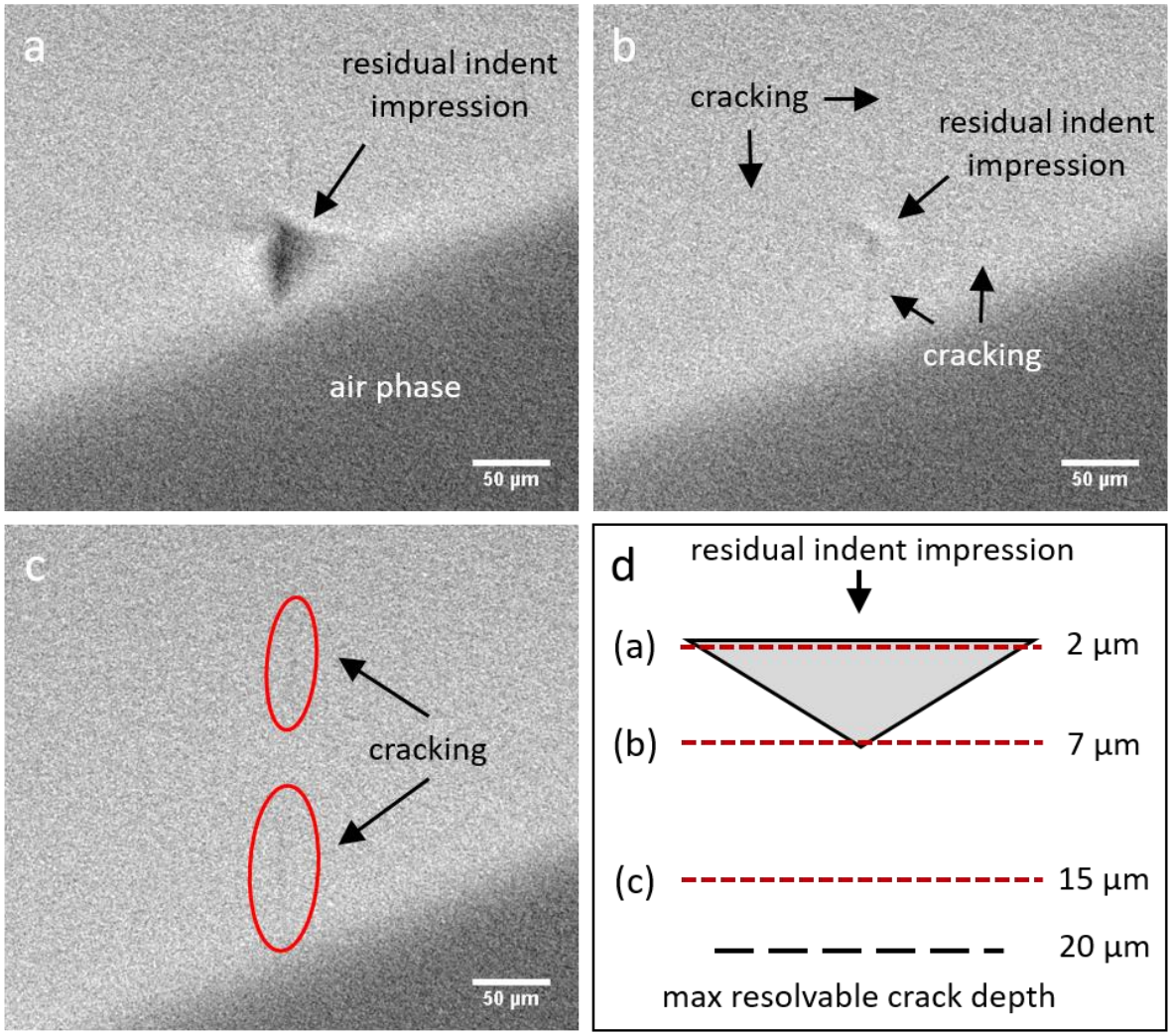

Figure 4.14: Tomographic slices parallel to the surface of the 5 kg indented silicon nitride sample at increasing depths showing: (a) the residual indentation impression. (b) the residual indentation impression and radial cracks. (c) the presence of radial cracks observed deeper than the residual indentation impression. (d) a schematic of the indentation showing the slice depths of (a)-(c).

Fig. 4.14(b) is a slice deeper into the sample surface where the residual indent impression is still visible. In addition, the presence of radial cracks is observed as darker contrast lines emanating from the indentation corners (arrowed). Although visible, they are difficult to observed because the width of the cracks (< 2 μm at widest point as measured from optical images) is of the order of the spatial separation of the pixels meaning there is only contrast differences (related to cracking) in single pixels. The measured greatest length of the radial cracks taken from the tomography slices is ~ 35 μm, this is understandably shorter than that measured optically (~ 40 μm) due to the difficulty in determining where the crack tips are in the tomography slices (decreased width near crack tips leads to decreased contrast in images). The presence of radial cracking (as in Fig. 4.14(c)) can be detected at z > 20 μm beneath the z ~ 7 μm depth of the residual indent impression, however their visibility decreases because of the decrease in crack width with depth.

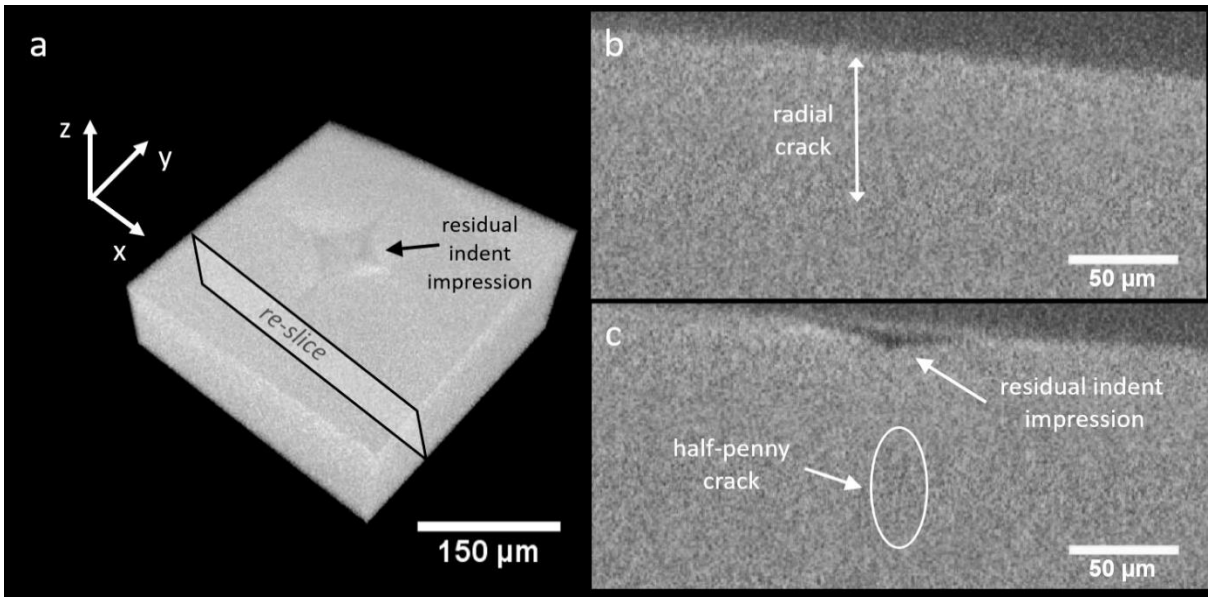

Figure 4.15: (a) A 3D reconstruction of the tomographic 2D slices showing the residual indentation impression as well as the new re-slice in the z-direction. (b) 2D slice showing the sub-surface of a radial crack. (c) 2D slice through the indentation centre where evidence of half-penny cracking was observed.

To gain an insight into the type of cracking regime beneath the indentation, as well as the depths of the cracks, the 2D tomographic slices were reconstructed into 3D again and then resliced in the z-direction given in Fig. 4.15(a), i.e. so that the 2D slice cross-sections are now perpendicular, not parallel, to the surface plane. Fig. 4.15(b) shows a cross-section intersecting one of the radial cracks and a sub-surface crack extending to 70 μm in depth is observed. The contrast grayscale has been adjusted to make the cracking as visible as

possible but even with this the lack of contrast with the surrounding area makes the crack difficult to observe. A cross-sectional slice through the centre of the residual indent impression (Fig. 4.15(c)) reveals faint cracking which is consistent with a half-penny cracking regime. This is to be expected for an indentation with a c/a ratio of > 2 (the c/a ratio was measured optically as ~ 2.3). In addition, the crack appears not to intersect with the surface and starts approximately 50 μm beneath the surface extending down a further 30 μm. This is likely due to the presence, directly beneath the residual indent impression, of a compressively stressed plastically deformed zone formed as a result of the indentation load on the surface. It is the high compressive stress that makes it hard for cracks to propagate into this region and hence the half-penny crack traces around it instead [25].

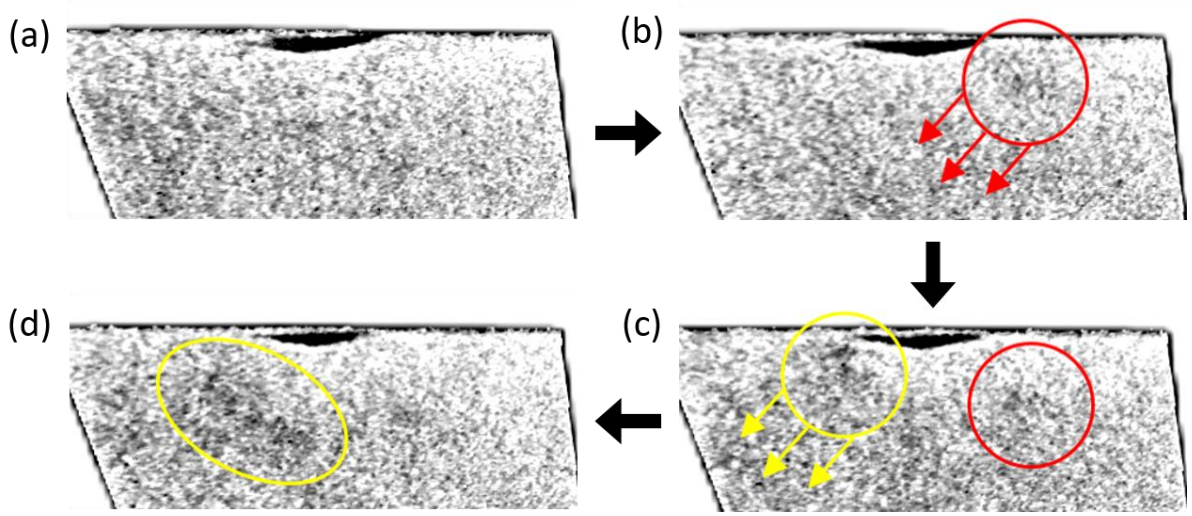

Figure 4.16: (a)-(d) are slices in the z-direction with a slice separation of ~ 4 μm. Evidence of half-penny cracking in the form of dark contrast regions shown within the red and yellow circled areas. The half-penny cracking is parallel to the 2D slice direction.

Evidence of half-penny cracking to a depth of ~ 90 μm was also observed as regions of darker contrast that appeared underneath the indentation as highlighted in the 2D slices given in Fig. 4.16. These regions are sections through the half-penny crack that is oriented nearly parallel to the tomographic slices (whereas the cracking shown in Fig. 4.15(b, c) is oriented perpendicular). The contrast change is difficult to see visually, but line scans across the region measuring change in grayscale value revealed that significant contrast change is present. Like Fig. 4.15, the half-penny cracking in Fig. 4.16 does not appear to be present in the region directly beneath the residual indentation, i.e. the plastically deformed, high compressive stress zone, however, the depth below the residual indentation impression at which the cracking is visible appears to be shallower than in Fig. 4.15, but this may be because of the different viewing orientation. No evidence of

lateral cracking was seen in the 2D tomographic slices which correlates with dark field images taken of this indentation prior to tomography (not shown here).

Although the cracking regime was determined for the 5 kg indentation, and half-penny cracks observed, the visibility of cracking was still low using the chosen micro-XCT system. This is primarily because of the crack widths being of the order of the spatial resolution of the device (~ 0.7 μm), but the crack contrast offered by imaging in propagation phase contrast mode may also be a factor. Increasing the spatial resolution by a meaningful amount was not possible due to the sample size and equipment available, however, increasing the crack contrast using a different imaging mode; absorption contrast, was attempted.

4.4.3. XCT of 5 kg Indentation with Dye Penetrant

The same 5 kg Vickers indented sample as above was soaked in a zinc iodide solution with the aim that the liquid would penetrate the cracks and provide x-ray attenuation much greater than that of air, hence increasing the crack contrast difference. Unfortunately, due to equipment unavailability, an alternative XCT device (Zeiss Xradia 410 Versa) was used with a slightly lower achievable spatial resolution of 0.9 μm. However, the greater field of view offered by the 10x objective lens (in comparison to the 20x lens used previously) meant that both indentations on the sample, not just one, were observed and tomographically reconstructed from the projections.

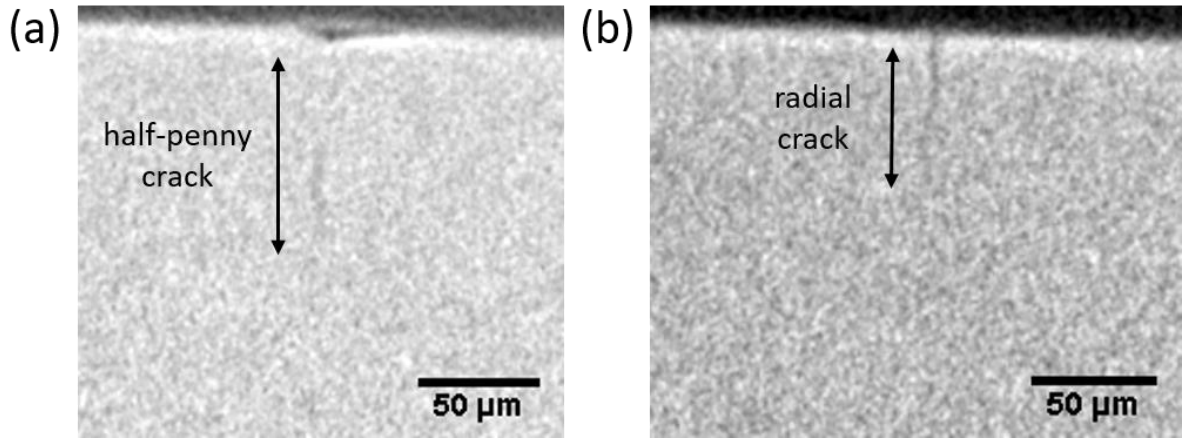

Figure 4.17: (a) A 2D tomographic slice through the centre of a 5 kg indentation with dye penetrant showing half-penny cracking. (b) a 2D tomographic slice through a radial crack.

Again, multiple 2D x-ray images of the area of interest containing each indentation were reconstructed and then re-sliced in the z-direction, so that the sub-surface nature of the cracks could be observed. For the first indentation (the same one that had been scanned previously, Fig. 4.15 and Fig. 4.16) cracking was still visible despite the lower resolution. Fig. 4.17 shows a slice through the residual indentation impression (a) and a slice through a radial crack emanating from the indentation corner (b). In Fig. 4.17(a), as in the previous scan, there is cracking present beneath the residual indentation impression implying a half-penny cracking regime. However, the visibility of the crack is greater than that of the previous scan due to it having a greater observable width because of the precipitated dye. In fact, the presence of cracking beneath the residual indentation impression was seen in more of the 2D slices than in the previous scan and increased width of the cracks (> 2 μm in some cases) was observed in both radial and half-penny cracks across many of the tomographic slices. The increased visibility of the cracks is a result of the presence of the zinc iodide penetrant within the cracks that leads to increased absorption contrast in comparison to the surrounding region. The penetrant may be responsible for the observed increase in width of the cracks as it penetrates not only the primary branch of the cracks but also any micro-cracking that may exist in the local area hence increasing the contrast enough for the voxels adjacent to the primary crack to also have a higher grayscale value in comparison to the surrounding silicon nitride.

The maximum observed depth of the half-penny crack was measured at ~ 90 μm but the starting depth was only measured to be ~ 30 μm from the surface plane in comparison to the ~ 50 μm of the previous scan, again, this is probably due to the increased crack visibility. The depth of half-penny cracking for both 5 kg indentations observed using micro-XCT correlate well with sectioning via manual grinding studies [8], [25] on multiple 5 kg Vickers indentations on silicon nitride of differing microstructures where half-penny cracking was found to start ~ 40 – 55 μm beneath the residual impression and extend down to between 60 – 95 μm. As in Fig. 4.16, half-penny cracking was observed as darker contrast regions with the maximum depth of the dark contrast being measured down to ~ 90 μm which correlates well with the half-penny crack depth measured for Fig. 4.16. These regions offered better contrast and were easier to observe than in the previous scan. The deepest radial crack, located at the corner of the indentation, was measured at ~ 70 μm which is the same as in the non-dye penetrated scan.

As mentioned, the second 5 kg indentation was also contained within the field of view of the objective lens, so this was analysed as well. It showed very similar characteristics to

the first indentation with radial and half-penny cracking being observed. Fig. 4.18 highlights the darker contrast regions indicative of half-penny cracking beneath the residual indentation impression sectioned nearly parallel to the crack orientations (like Fig. 4.16 does). Interestingly the depth of the half-penny cracking implied from the depth of the darker regions at was ~ 90 µm – the same as in the first indentation. However, the depth of the deepest cracking beneath the residual indentation impression was measured to be ~ 100 µm which was slightly deeper.

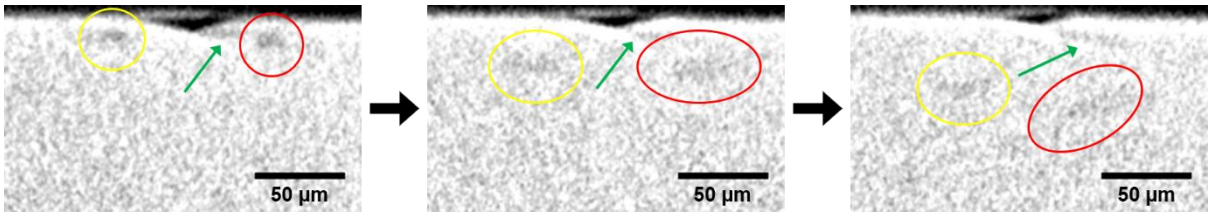

Figure 4.18: Darker contrast regions indicative of half-penny cracking observed in the second 5 kg indentation as well (highlighted within the red and yellow ovals). The green arrow points to observed lateral cracking.

The deepest radial crack (Fig. 4.19(a)) had a length of ~ 120 µm and, unlike in the first indentation, was angled 15 ° from perpendicular to the surface giving it a maximum depth of ~ 105 µm. This is greater than the deepest crack measured beneath the residual indentation impression (where the deepest cracking should reside for a half-penny crack regime), although this may be due to the cracking beneath the impression being narrower and hence less visible than the radial cracks.

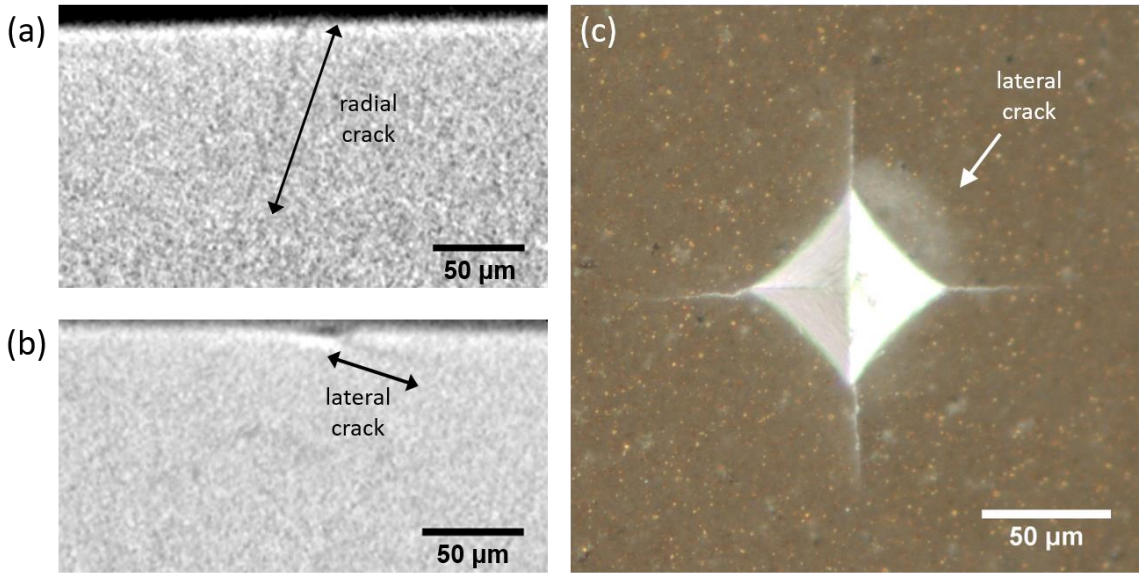

Figure 4.19: (a) A radial crack in the second indentation. (b) The presence of a lateral crack which was also observed in the dark field optical images (c) of the same indentation (arrowed).

One of the biggest differences between the two indentations scanned was the presence of lateral cracking in the second 5 kg indentation. This was observed prior to the scan in the dark field optical images and can be seen in Fig. 4.19(c) as a lighter contrast region extending outward from the indentation side. From the optical image the depth of the lateral crack beneath the surface cannot be determined, only the extension outward from the centre of the indentation, which was measured as ~ 50 μm. However, the lateral cracking was observed in the 2D tomography slices, one of which is shown in Fig. 4.19(b) and can also be seen in all the slices shown in Fig. 4.18 (arrowed). The lateral crack appears to start from the bottom of the residual indentation impression at a depth of ~ 7 μm and extend downwards at an angle of 20° from the surface to a maximum depth of ~ 12 μm. The extension of the lateral crack outward from the centre was measured at ~ 35 μm; this discrepancy with the optical measurement of ~ 50 μm is potentially due to a narrowing at the crack tip for which the tomography instrument used does not have a high enough resolution to resolve. Alternatively, the zinc iodide dye may not have penetrated the cracking fully meaning that the increased absorption contrast consequential from the dye was not present; this phenomenon is not limited to just the lateral cracking but is applicable to all the dye penetrated cracks.

As seen in the literature reviewed (Chapter 2), lateral cracking is one of the primary cracking modes associated with material removal in the form of flaking and spalling, particularly shallow laterals. Lateral cracking has been observed using manual grinding techniques beneath indentations of 5 kg applied load on silicon nitride in a previous study [25], and in indentations of a similar applied load in other ceramic materials [1], [23], [26]. Micro-XCT examination has shown that the lateral crack appears to initiate from the depth of the residual indentation impression, i.e. the zone of maximum compressive stress, and propagates outward. An important factor for material removal is the intersection of lateral cracking with the surface [13], [27] which is not observed here. However, under further applied pressure, such as that experienced by silicon nitride balls in operational conditions, the lateral cracking could propagate to the surface creating a leverage point for flaking [28]. The optical dark field image in Fig. 4.19(c) also shows that the lateral cracking may intersect with the radial cracking. This is not confirmed completely from the X-ray tomography slices, but it can be inferred from Fig. 4.18 that there is an intersection as lateral cracking is visible emanating from the bottom of the residual indent impression in the same slice that the darker regions associated with half-penny cracking are also present.

4.5. Summary

In this chapter, the surface damage around low applied load Vickers indentations have been characterised using a combination of SEM, 3D optical profilometry and Raman spectroscopy to reveal information about the indentation morphology, associated residual stress and cracks. The main findings from these investigations are as follows:

- Silicon nitride has a primarily intergranular fracture mode for both the SNA and SNB compositions.
- For both 0.5 kg and 1 kg indentations the measured c/a ratios predict a sub-surface Palmqvist cracking regime.
- The 3D optical profilometry revealed the presence of an uplift zone surrounding indentation edges which would be a wear initiation point in sliding contact.
- Raman spectroscopy revealed surface tensile stress of ~ 1 GPa at crack tips for 1 kg indentations as well as the presence of surface compressive stress out to a distance of ~ 50 μm from the residual indentation impression centre.

In addition to this, non-destructive micro-XCT has been utilised to investigate sub-surface indentation cracking. The resolution was not sufficient for use with 1 kg indentations, however micro-XCT was applied to indentations with an increased load of 5 kg with these findings:

- Sub-surface half-penny and radial cracking were better resolved once indentations were penetrated with zinc iodide solution to increase contrast.
- Lateral cracking observed using dark field optical microscopy could also be detected using XCT at a maximum depth of ~12 μm with reasonable correlation shown between the two methods.
- Half-penny cracking was observed to start ~ 30 μm beneath the residual impression indicating a volume in which cracking does not propagate – consistent with a compressive stress plastic deformation zone.

The SEM and 3D optical profilometry have both proved successful and will be applied to silicon nitride ball samples (Chapter 6), however, Raman spectroscopy is limited to flat surfaces so will not work on the curved ball surface. Unfortunately, due to insufficient resolution, the micro-XCT is also not applicable to investigating the star features on ball-bearing components samples which are of the size order of 1 kg

indentations, so alternative methods for sub-surface characterisation (i.e. FIB tomography, Chapter 5) need to be employed.

4.6. References

[1] R. Cook and G. Pharr, "Direct observation and analysis of indentation cracking in glasses and ceramics," *J. Am. Ceram. Soc.*, vol. 73, no. 4, pp. 787–817, 1990.

[2] K. Niihara, "A fracture mechanics analysis of indentation-induced Palmqvist crack in ceramics," *J. Mater. Sci. Lett.*, vol. 2, no. 5, pp. 221–223, 1983.

[3] K. Niihara, R. Morena, and D. P. H. Hasselman, "Evaluation of Klc of Brittle Solids By the Indentation Method With Low Crack To Indent Ratios," *J. Mater. Sci. Lett.*, vol. 1, pp. 13–16, 1982.

[4] X. Yang, X. Liu, Z. Huang, X. Yao, and G. Liu, "Vickers indentation crack analysis of solid-phase-sintered silicon carbide ceramics," *Ceram. Int.*, vol. 39, no. 1, pp. 841–845, 2013.

[5] Y. Tang, A. Yonezu, N. Ogasawara, N. Chiba, and X. Chen, "On radial crack and half-penny crack induced by Vickers indentation," *Proc. R. Soc. A Math. Phys. Eng. Sci.*, vol. 464, no. May, pp. 2967–2984, 2008.

[6] Y. Kadin, S. Strobl, C. Vieillard, P. Wijnbergen, and V. Ocelik, "In-situ observation of crack propagation in silicon nitride ceramics," *Procedia Struct. Integr.*, vol. 7, pp. 307–314, 2017.

[7] B. Lawn and R. Wilshaw, "Indentation Fracture: principles and applications," *J. Mater. Sci.*, vol. 10, pp. 1049–1081, 1975.

[8] H. Miyazaki, H. Hyuga, Y. I. Yoshizawa, K. Hirao, and T. Ohji, "Crack profiles under a Vickers indent in silicon nitride ceramics with various microstructures," *Ceram. Int.*, vol. 36, no. 1, pp. 173–179, 2010.

[9] S. S. Chiang, D. B. Marshall, and A. G. Evans, "The response of solids to elastic / plastic indentation. I. Stresses and residual stresses," *J. Appl. Phys.*, vol. 53, no. 1, pp. 298–311, 1982.

[10] B. T. Lee, B. D. Han, and H. D. Kim, "Comparison of fracture characteristic of silicon nitride ceramics with and without second crystalline phase," *Mater. Lett.*, vol. 58, no. 1–2, pp. 74–79, 2004.

[11] S. Ii, C. Iwamoto, K. Matsunaga, T. Yamamoto, and Y. Ikuhara, "Identification of crack path of inter- and transgranular fractures in sintered silicon nitride by in situ TEM," *J. Electron Microsc. (Tokyo).*, vol. 53, no. 2, pp. 121–127, 2004.

[12] S. Wei, L.W. Porz, Z. Xie, B. Liu, J. Chen, W. Xue, "Crack propagation in silicon nitride ceramics under various temperatures and grain boundary toughness," *Mater. Sci. Eng. A*, vol. 632, no. April, pp. 58–61, 2015.

[13] Y. Wang and M. Hadfield, "A study of line defect fatigue failure of ceramic rolling elements in rolling contact," *Wear*, vol. 253, no. 9–10, pp. 975–985, 2002.

[14] M. Hadfield and T. A. Stolarski, "Observations of delamination fatigue on pre-cracked ceramic elements in rolling contact," *Ceram. Int.*, vol. 21, no. 2, pp. 125–130, 1995.

[15] S. Tochino and G. Pezzotti, “Micromechanical analysis of silicon nitride: A comparative study by fracture mechanics and Raman microprobe spectroscopy,” *J. Raman Spectrosc.*, vol. 33, no. 9, pp. 709–714, 2002.

[16] G. Pezzotti, “In situ Study of Fracture Mechanisms in Advanced Ceramics using Fluorescence and Raman Microprobe Spectroscopy,” *J. Ra*, vol. 875, no. May, pp. 867–875, 1999.

[17] G. Pezzotti, H. Ichimaru, and L. P. Ferroni, “In Situ Measurement of Bridging Stresses in Toughened Silicon Nitride,” *J. Am. Ceram. Soc.*, vol. 56, pp. 1249–1256, 1999.

[18] V. Sergo, G. Pezzotti, G. Katagiri, N. Muraki, and T. Nishida, “Stress Dependence of the Raman Spectrum of ß-Silicon Nitride,” *Journal of the American Ceramic Society*, vol. 79, no. 3. pp. 781–784, 1996.

[19] N. Muraki, G. Katagiri, V. Sergo, and G. Pezzotti, “Mapping of residual stresses around an indentation in beta-Si3N4 using Raman spectroscopy,” *J. Mater. Sci.*, vol. 32, no. 2, pp. 5419–5423, 1997.

[20] C. Baudín, J. Gurauskis, A. J. Sánchez-Herencia, and V. M. Orera, “Indentation damage and residual stress field in alumina-Y2O3-stabilized zirconia composites,” *J. Am. Ceram. Soc.*, vol. 92, no. 1, pp. 152–160, 2009.

[21] A. Pajares, F. Guiberteau, R. W. Steinbrech, and A. Dominguez-Rodriguez, “Residual stresses around Vickers indents,” *Acta Metall. Mater.*, vol. 43, no. 10, pp. 3649–3659, 1995.

[22] A. Pajares, F. Guiberteau, F. L. Cumbrera, R. W. Steinbrech, and A. Dominguez-Rodriguez, “Analysis of kidney-shaped indentation cracks in 4Y-PSZ,” *Acta Mater.*, vol. 44, no. 11, pp. 4387–4394, 1996.

[23] J. J. Kruzic and R. O. Ritchie, “Determining the Toughness of Ceramics from Vickers Indentations Using the Crack-Opening Displacements : An Experimental Study,” *J. Am. Ceram. Soc.*, vol. 86, no. 8, pp. 1433–1436, 2003.

[24] G. Pezzotti, Y. Enomoto, W. Zhu, M. Boffelli, E. Marin, and B. J. McEntire, “Surface toughness of silicon nitride bioceramics: I, Raman spectroscopy-assisted micromechanics,” *J. Mech. Behav. Biomed. Mater.*, vol. 54, pp. 328–345, 2016.

[25] T. Lube, “Indentation crack profiles in silicon nitride,” *J. Eur. Ceram. Soc.*, vol. 21, pp. 211–218, 2001.

[26] D. B. Marshall, B. R. Lawn, and A. G. Evans, “Elastic/Plastic Indentation Damage in Ceramics,” *J. Am. Ceram. Soc.*, vol. 65, no. 11, pp. 561–566, 1982.

[27] Y. Wang and M. Hadfield, “A mechanism for nucleating secondary fractures near a pre-existing flaw subjected to contact loading,” *Wear*, vol. 254, no. 7–8, pp. 597–605, 2003.

[28] R. F. Cook and D. H. Roach, “The effect of lateral crack growth on the strength of contact flaws in brittle materials,” *J. Mater. Res.*, vol. 1, no. 4, pp. 589–600, 1986.

Chapter 5: FIB Tomography of Vickers Indentations on Silicon Nitride

5.1. Introduction

In this chapter, the sub-surface cracking that is located beneath 0.5 kg and 1 kg applied load Vickers indentations is mapped in three-dimensions using a FIB tomography sectioning technique. The aim is to characterise the crack morphology and regimes that exist in silicon nitride after indentation at low applied loads, to analyse how cracks might impact material removal in bearing components, but also to assess the effectiveness of FIB tomography for observing sub-surface cracking. In addition to this, a more conventional top-down sectioning method using incremental diamond polishing has also been utilised to further investigate 1 kg indentations as well as evaluate the effect the different sectioning techniques have on the observed crack morphology. Some of the investigations in this chapter have been published as "*3D characterisation of indentation induced sub-surface cracking in silicon nitride using FIB tomography"* in the Journal of the European Ceramic Society 39 (2019) 3620-3626 [1]. Permission for the use of copyrighted material has been obtained from the publisher Elsevier.

5.2. FIB Sectioning of Vickers Indentations

5.2.1. FIB Sectioning of a 1 kg SNA Indentation

A dual-beam FIB-SEM instrument was used to section through a 1 kg Vickers indentation on the SNA composition of silicon nitride as described in detail in Chapter 3. In total 77 incrementally FIB-milled slices were imaged using SEM to observe the sub-surface crack morphology. Secondary electron (SE) imaged cross-sections of the 1 kg SNA indentation with increasing proximity to the residual indentation centre are given in Fig. 5.1. For the cross-section shown in Fig. 5.1(a), a radial crack is observed extending to a depth of 20 µm beneath the surface intersection. A primarily intergranular fracture pathway is deduced from the jagged nature of the cracking and is consistent with the surface SEM observations of fracture made in Chapter 4. On approach to the indentation corner (Fig.

5.1(b)) a lateral crack (arrowed) appears branching from the initial radial crack at a depth of ~ 11 µm and extending downward an angle of 20° relative to the surface plane until intersection with the trench side-wall at 15 µm depth. In the subsequent cross-section (not shown), a further lateral appeared on the opposite side of the radial crack with the same starting depth (~ 11 µm), and it also emanated out to the trench side wall with an intersection depth of ~ 16 µm. Fig. 5.1(c) shows that as milling progresses past the indentation corner and further within the residual indentation impression, radial cracking is no longer observed, and only lateral cracking remains. Note that the lateral crack arrowed on the left-hand of Fig. 5.1(c) is a separate branch from that observed in Fig. 5.1(b). It was not always possible to observe the full extent of the lateral and radial cracking because they occasionally extended beyond the milled trench dimensions.

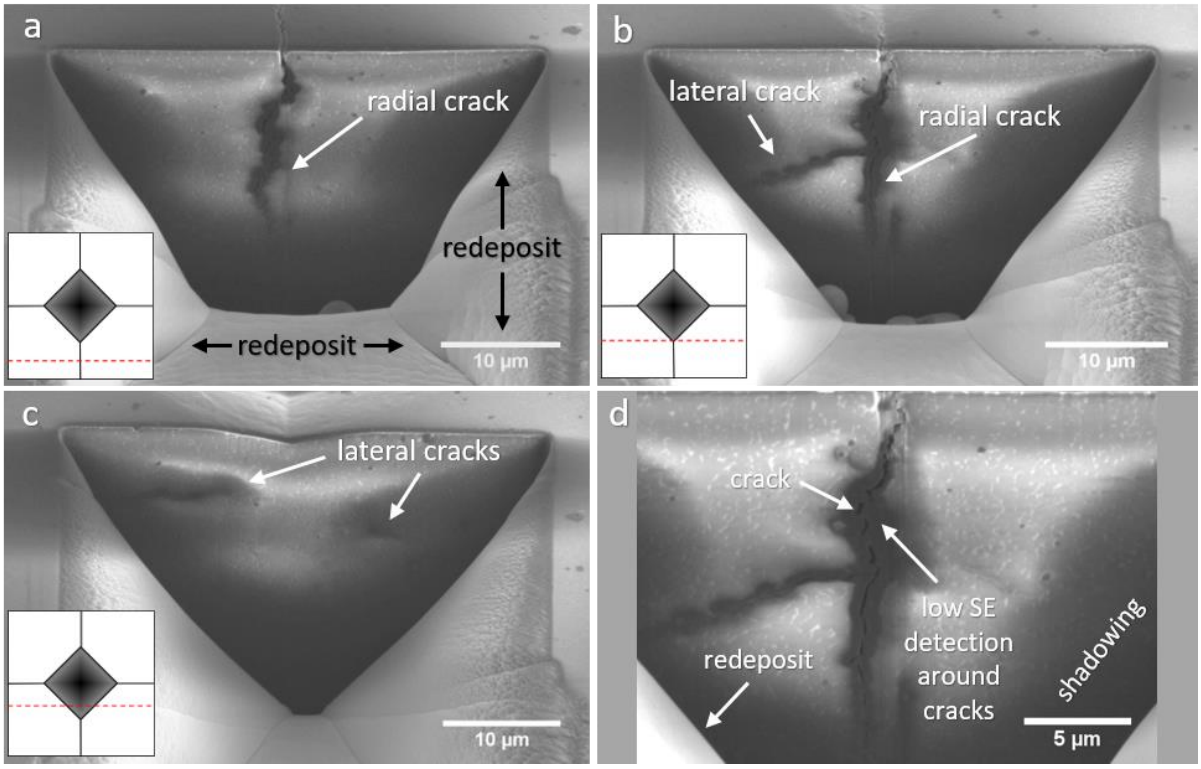

Figure 5.1: SEM imaged cross-sections of the 1 kg SNA FIB-milled indentation taken at a tilt angle of 52°. The inset schematics in the bottom left show the cross-section location in relation to the indentation: (a) FIB slice through the radial crack (arrowed) emanating from an indentation corner. (b) Slice taken at the indentation corner showing both lateral and radial cracking. (c) Approaching the indentation centre where lateral cracking is observed. (d) A close up of the cross-section in (b) strong variations in SE contrast is due to localized voltage contrast (charging) and beam shadowing caused by the trench walls.

As FIB sectioning reached the mid-point between the already FIB-milled indentation corner and the residual indentation centre, the lateral cracking seen in Fig. 5.1(c) was no longer observed. The cross-section given in Fig. 5.2, through the centre of the residual

indentation impression, shows the presence of a damaged zone consisting of interconnected micro-cracking that corresponds with one of the surface radial cracks (emanating from an indentation corner) located parallel to the sectioning direction. A similar zone was observed for the radial crack on the opposite side, however, the depth of these parallel-milled radial cracks is difficult to determine, since their width is of a similar dimension to that of the FIB slice thickness. Directly beneath the residual indentation impression centre, half-penny (or median-radial) cracking was observed (shown in the Fig. 5.2 inset); this crack did not intersect the surface like the radial cracks and instead was located at a start depth of ~ 20 μm beneath the residual indentation impression centre and extended to the bottom of the milled trench (~ 30 μm). Here, half-penny cracking has been defined as having no intersection with the surface plane, and extending beneath the residual indentation impression [2], [3].

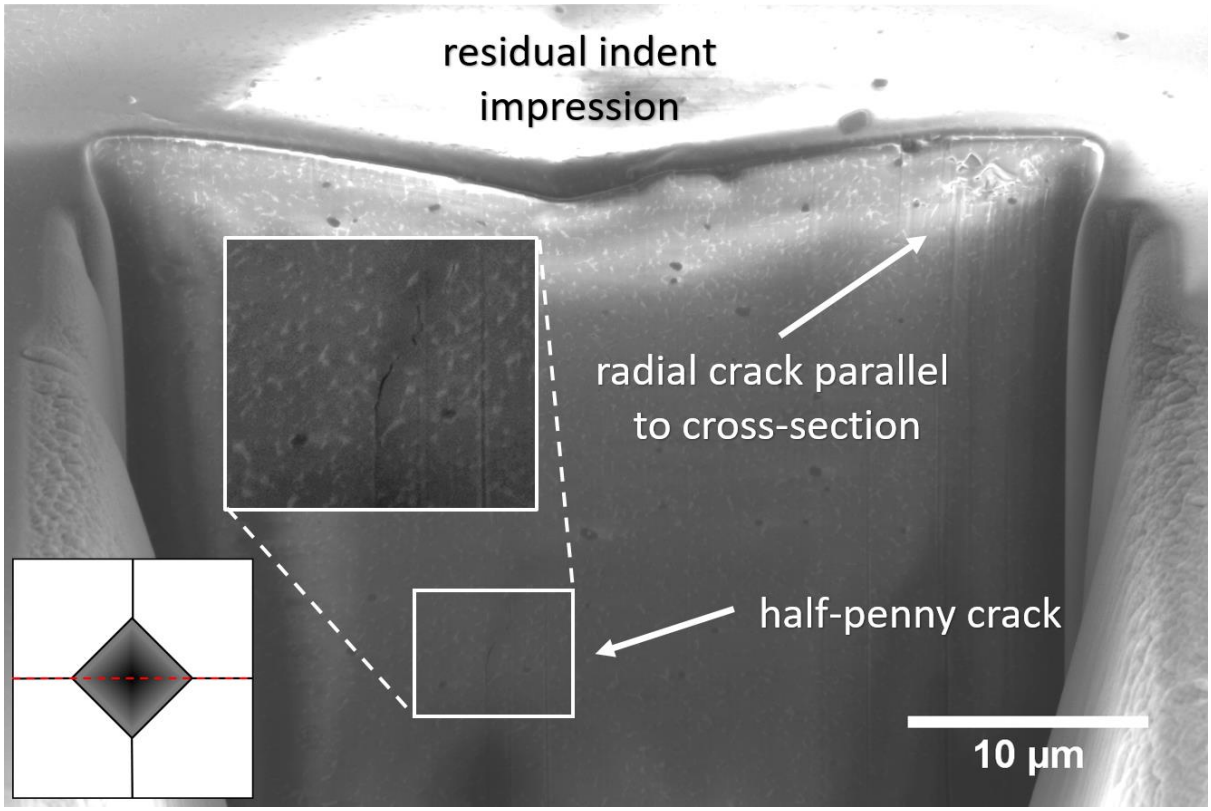

Figure 5.2: SEM imaged FIB cross-section through the centre of the 1 kg SNA indentation taken at a tilt angle of 52°. A radial crack occurring predominantly parallel to the milling direction and a central half-penny crack (magnified inset) are identified.

In the SEM images of the cross-sections shown in Fig. 5.1 and Fig. 5.2, as well as all subsequent cross-sectional images shown, there are a few FIB machining and SEM-induced phenomena which exist and have been highlighted in Fig. 5.1(a, d). For example, there is a build-up of material present (light contrast) at the bottom and on the side walls

of the FIB-milled trenches that is caused by the redeposition of sputtered silicon nitride (labelled in Fig. 5.1 (a)). There are problems associated with sputtered material in that it can not only obstruct the view of the milled cross-section, but there is also the potential for sputtered material to redeposit within cracks making them more difficult to observe [4]. Here, when the volume of built-up material became too great, the Ga^+ ion beam was used at a high current (21 nA) to sputter away the redeposited material. Another prominent SEM phenomenon is the variation in brightness across the face of the cross-sections as a result of differing SE emission. This is the result of localised electron charge build-up on the surface of the insulating silicon nitride (light contrast) that subsequently deflects incident electrons towards the detector. Unlike at the indented sample surface, there is no conductive gold-layer present on the cross-sections to assist electron flow away from the imaged surface (although implanted gallium adds some conductivity) [5]–[7]. The dark contrast in the vicinity of cracking indicates low SE detection relative to the surrounding region which may imply different topography (e.g. depression surrounding cracks) as SE contrast highlights topographical differences [8]. There is also a shadowing effect adjacent to the bottom and side of the trenches caused by the inhibition of SEs from reaching the detector due to the presence of the trench walls [9].

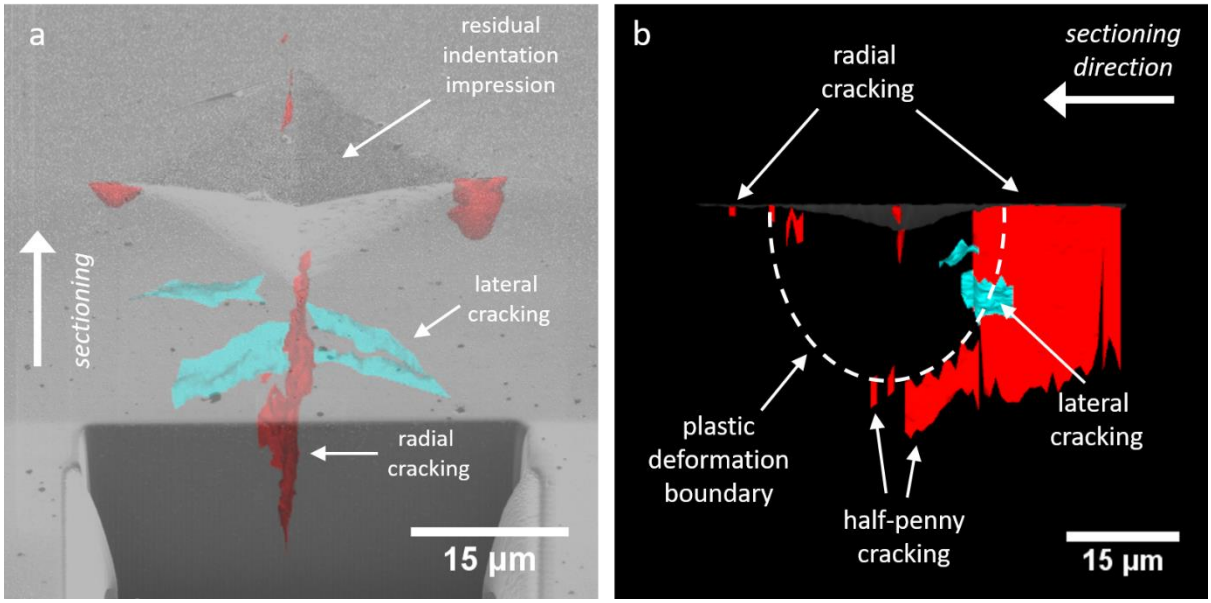

Figure 5.3: (a) A crack map created using IMOD overlaid onto an SEM image taken at a 52° tilt angle for the SNA 1 kg FIB milled indentation. (b) A side view schematic of the same IMOD crack map highlighting the different crack morphologies as well as the proposed extent of the plastic deformation region (dashed line). Lateral cracks are coloured blue and radial cracks red.

The SEM imaged FIB-milled cross-sections through the indentation were aligned and the identified cracks were traced and subsequently reconstructed into a 3D crack map using

IMOD software. Fig. 5.3(a) shows the 3D crack map overlaid onto an SEM image of the SNA 1 kg indentation with a 52° tilt angle, and Fig. 5.3(b) is a side profile of the 3D reconstruction with the differing crack morphologies highlighted. The lateral cracking is coloured blue and the radial (including half-penny) is coloured red. The presence of half-penny cracking beneath the indentation is evident in addition to lateral cracking that starts at the indentation corner and extends under the residual indentation impression. Under an applied load of 1 kg, and with a crack length (c) to indent half-diagonal (a) ratio (c/a ratio) of < 2 (measured for this indentation as ~ 1.7), a Palmqvist cracking regime, and not a half-penny regime, is generally expected for Vickers indentation [3], [10], [11]. Here, the crack density is seen to decrease significantly in the second half of the FIB indentation sectioning relative to the first half, with lateral cracking only identified in the first half. In addition, radial cracking observed in the second half was difficult to resolve and did not extend as deep within the sub-surface (< 5 μm depth). There also exists a region beneath the residual indentation impression (Fig. 5.3(b) outlined by the dashed line) where there is minimal cracking. This compressive stress zone will be discussed in further detail later on in the chapter.

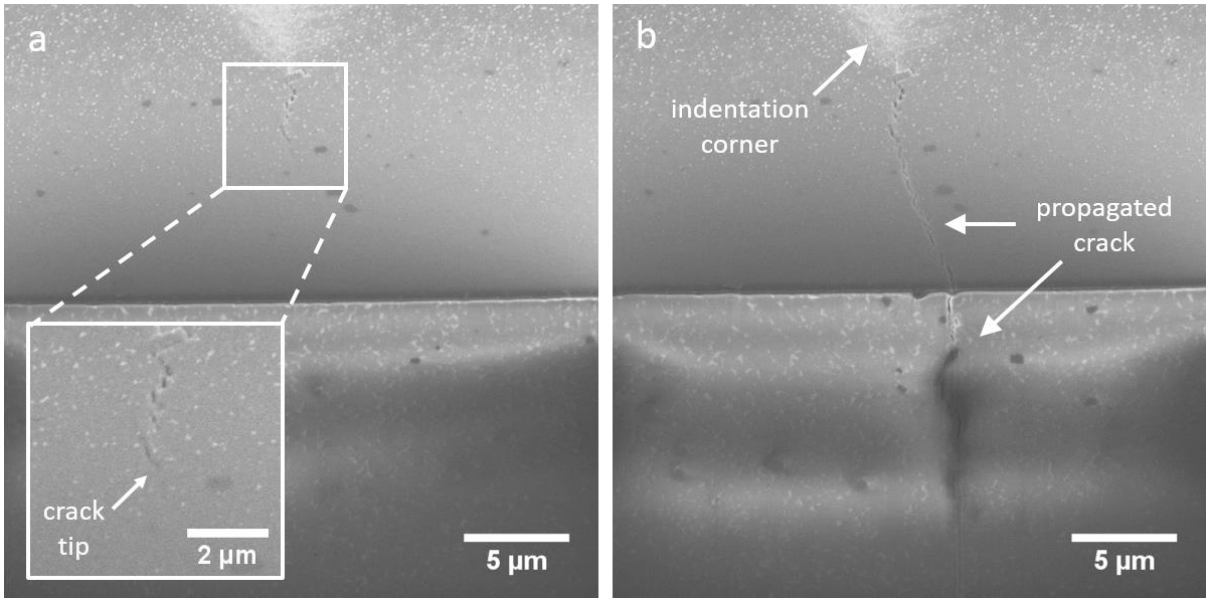

Figure 5.4: Two SEM images (tilt angle of 52°) taken before (a), and after (b), a FIB milling increment towards the indentation corner. The radial crack highlighted in the inset in (a) was observed to propagate towards the FIB milled trench as arrowed in (b).

During the FIB sectioning of the 1 kg SNA indentation, on approach to a surface radial crack, the radial crack was observed to suddenly propagate towards the FIB milled trench. Prior to propagation the radial crack, seen in Fig. 5.4(a), had a length of ~ 7 μm, however, after FIB milling the next cross-section for SEM imaging, the radial crack had extended

significantly by a further ~ 10 μm and intersected with the trench. In addition to the surface propagation, the radial crack was observed on milled cross-section (Fig. 5.4(b) where previously it had not been present. The opening of a new free surface (the cross-section) as a result of the FIB sectioning inevitably affects the local residual stress [12], [13]. In addition, the Raman spectroscopy mapping of radial cracks carried out in Chapter 4.3 revealed that there is significant surface tensile stress present at the crack tips. The combination of this tensile stress and the new free surface lead to crack propagation in the direction of least resistance. This has implication for the morphology of cracks observed on the FIB-milled cross-sections, i.e. is the morphology of the sub-surface cracking observed the same as it was prior to sectioning or is the sectioning process causing cracks to propagate further both on the surface and on the sub-surface. The propagation of the crack in Fig. 5.4 also gives an indication of residual stresses still present in the region surrounding the residual indentation after unloading of the indenter. If there was no tensile stress present around the crack tips then there would be no crack propagation towards the FIB milled trench.

5.2.2. Effect of Load and Material

The crack morphology observed using FIB sectioning and SEM imaging for the 1 kg indented SNA sample was compared to the cracking observed in a 1 kg indented SNB sample. The crack morphology exhibited by the 1 kg SNB sample was very similar to SNA with long range radial cracking and multiple branches of lateral cracking visible in the vicinity of the sectioned indentation corner at a maximum depth of ~ 17 μm and projecting at an angle of ~ 28° to the indented surface plane (laterals were observed on both sides of the radial crack). Again, half-penny cracking was observed directly beneath the residual indentation impression at a starting depth beneath the surface of ~ 23 μm extending down to ~ 30 μm. As for the SNA sample, cracking observed during sectioning of the second half of the indentation was greatly reduced relative to the first, with only radial cracking (and no lateral cracking) being visible, with these cracks having a lesser observed depth in addition to a reduced width.

In order to ascertain the role that the applied load has on the cracking regime present beneath indentations, the cracking observed for the 1 kg indentations was compared with that surrounding a lower applied load 0.5 kg indentation on the SNB composition. Multiple branches of lateral cracking were also observed in the SNB 0.5 kg sample on

approach to the indentation with the maximum depth measured to be ~ 9 μm which correlates with the reduced measured depth of the residual indentation impression. As for the 1 kg indentations, half-penny cracking was observed at a depth of ~ 14 μm below the residual indentation impression extending to a depth of ~ 20 μm. In the 0.5 kg indentation, no radial cracking at all was identified in the second half of the indentation. The depth of the residual indentation impressions measured for the 0.5 kg and 1 kg SNB sectioned indentations were ~ 2.6 μm and ~ 3.6 μm respectively; this compares well with the measurements (~ 2.4 μm and ~ 3.3 μm) made using the surface optical profilometry in Chapter 4.2.2..

5.2.3. Effect of FIB Sectioning Direction

The previous indentations discussed had all undergone FIB sectioning in the direction towards the indentation corner. To investigate the influence that the direction of FIB sectioning has on the observed cracking, another 1 kg indentation on SNB was sectioned parallel to, and moving towards, a side wall of the indentation. In SEM cross-section images, the two radial cracks emanating from the nearest two indentation corners were visible on the sub-surface, the orientation of which (upon 3D reconstruction) were expected to be 45° relative to the FIB sectioning plane. As milling approached the edge of the residual indentation impression, the radial cracks reduced in depth and interconnected with shallow lateral cracking as arrowed in Fig. 5.5. Shallow micro-cracking was also observed just beneath the surface. In addition, deeper lateral cracking was identified near the indentation edge with a maximum depth of ~ 14 μm; this was observed both sides of the radial cracks in a similar way to that seen in the 1 kg indentations that were sectioned towards the indentation corner. Beneath the indentation centre, evidence of half-penny cracking was also observed at a depth of ~ 16 μm.

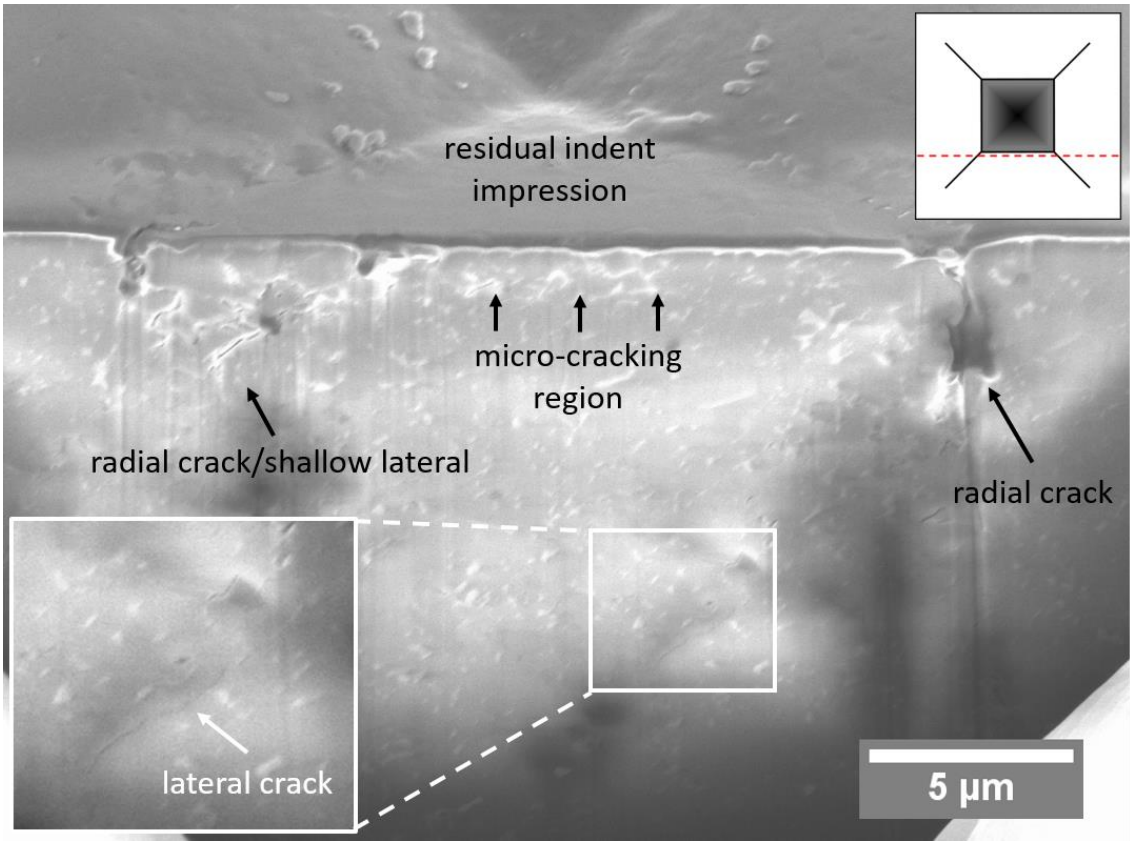

Figure 5.5: An SEM imaged (tilt angle of 52°) FIB cross-section located at the edge of the 1 kg SNB indentation where the FIB milling approach was towards the indentation side. Two radial cracks are visible in addition to sub-surface micro-cracking along the indentation edge, and deep lateral cracking.

5.3. 3D Crack Map Analysis of Indentations

As was done for the SNA 1 kg indented sample, 3D reconstructions were carried out for the 1 kg and 0.5 kg SNB indentations by using IMOD software to identify cracking on the SEM imaged FIB-milled cross-sections and produce sub-surface crack maps. The crack maps for the FIB-milled volumes beneath the 1 kg and 0.5 kg SNB indentations (where the sectioning direction was towards the indentation corner) are shown in Fig. 5.6 overlaid onto SEM images of the indentations at a tilt angle of 52°.

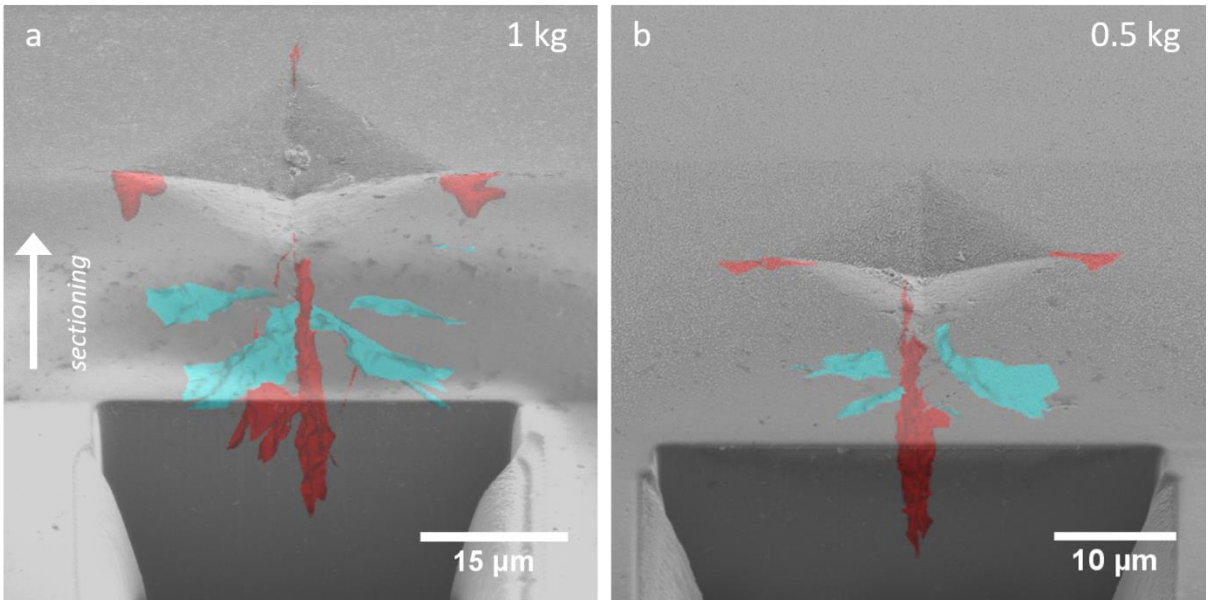

Figure 5.6: Crack maps created using IMOD overlaid onto SEM images taken at a 52° tilt angle for the SNB (a) 1 kg indentation and (b) 0.5 kg indentation. Lateral cracks are coloured blue and radial cracks red.

The sub-surface cracks for the 0.5 kg and 1 kg indentations shown in Fig. 5.6 exhibit a similar overall cracking structure, with an initial radial crack first identified followed by branching lateral cracking as the residual indentation impression corner is approached. Evidence of half-penny cracking was also observed in both loads as opposed to the Palmqvist morphology often predicted for Vickers indentations where the c/a ratio is < 2 [3], [11], [14]. The c/a ratios here were measured as ~ 1.7 and ~ 1.5 for the 1 kg and 0.5 kg indentations respectively so a half-penny cracking regime for the 1 kg indentation is not unexpected, however it is more of a surprise for the 0.5 kg indentation where half-penny cracking for a c/a ratio of 1.5 has not previously been observed. The lack of previous identification of half-penny cracking in Vickers indentations of lower loads may be due to the small crack width (which has only been observable here with the use of high resolution SEM) in addition to the limitations of the techniques used e.g. low resolution optical microscopy and damaging grinding methods [3], [15]. The geometry of the half-penny cracking observed in all FIB-milled indentations was vertically orientated along the principle stress axes, i.e. the indentation diagonals.

For all indentations, the crack density in the first half of the sectioned volume (i.e. the volume milled up until the indentation centre was reached) was greater than that in the second half with no laterals being identified in the second half for all loads, and no radials being observed for the 0.5 kg indentation. The observed change in measured crack density between the two halves of an indentation can be explained in terms of the localised

changes in residual stress as a result of the FIB sectioning process [4], [12], [13], [16]. The cracking originally formed as a stress relief mechanism to alleviate the highly compressive and tensile stressed regions induced as a result of plastic deformation formed beneath the residual indentation impression upon applying a load. During the incremental FIB sectioning of the indentation, as the central volume of plastic deformation is removed, the associated stresses (both tensile and compressive) are also systematically reduced which leads to closure of the remaining cracks, hence decreasing their width and making them difficult to resolve even under an electron beam.

One of the interesting features of the half-penny cracks is that they do not intersect with the surface plane in the indent centre (this is partly what defines them). This is because cracking does not preferentially propagate into the compressively stressed zone beneath the residual indentation impression due to the increased hardness and compressive stress present [15]. However, micro-cracking may still exist in this zone [17]. Instead, the crack pathways trace the region of tensile stress that surrounds the plastic deformation zone resulting in half-penny cracking. Therefore, the starting depth of the half-penny cracking can be used to indicate the volume beneath the residual indentation impression that the compressively stressed plastically deformed zone occupies by assuming this volume is a semi-ellipsoid the depth of which equates to the half-penny crack maximum depth beneath the centre of the residual impression, and the two elliptic radii are equal to half the indentation diagonal length. Fig. 5.7 gives side-on views of the IMOD crack map reconstructions for the SNB 1 kg and 0.5 kg indentations, and shown on the schematic of each indentation is an arc (dashed line) that encompasses the proposed volume of the plastically deformed compressive stress zone within which there is minimal cracking (this is also given on Fig. 5.3(b) for the 1 kg SNA sample). The depth of the semi-ellipsoids used for the SNB 1 kg and 0.5 kg indentations were ~ 14 μm and ~ 23 μm respectively (taken from the half-penny crack depth) which corresponds to volumes of ~ 3,000 μm^3 and ~ 11,000 μm^3. For the SNA 1 kg indentation the radius was ~ 20 μm and the volume ~ 9,500 μm^3. The smaller volume of the plastic deformation zone estimated for the SNA 1 kg indentation in comparison to the SNB 1 kg indentation is likely a result of the greater hardness and fracture toughness possessed by the SNA composition.

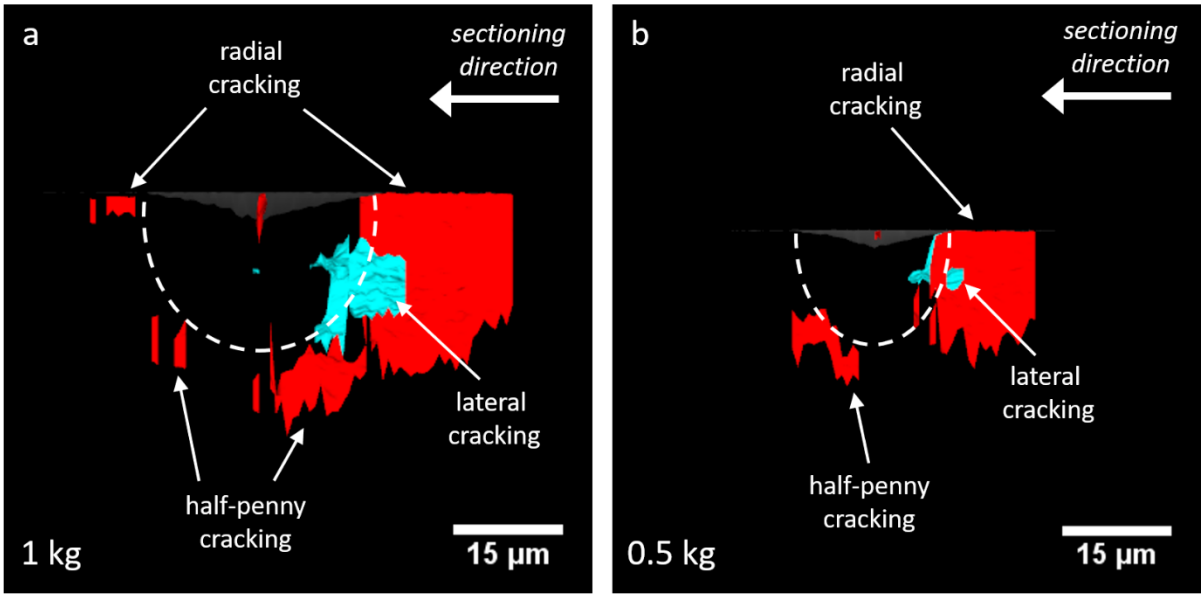

Figure 5.7: Side view schematics of the sub-surface IMOD crack maps for the SNB (a) 0.5 kg indentation, and (b) 1 kg indentation highlighting the location of the different crack morphologies (arrowed). Lateral and radial cracks are coloured blue and red respectively. The region of plastic deformation beneath each indentation is highlighted by the dashed semi-circle.

In previous investigations into sub-surface cracking on Vickers indented silicon nitride that utilised transverse serial sectioning via incremental polishing and flexure breaking [3], [15], lateral cracks were not observed at applied loads of 1 kg whereas in this study lateral cracking was observed in all four FIB-milled indentations, even with their different sectioning orientations, composition, and applied loads. This may be due to the higher spatial resolution method (SEM) used here in comparison to transverse and top-down serial sectioning polishing methods imaged by optical microscopy. However, a study using transverse serial section polishing methods [15] where SEM has been used in conjunction with dye penetrant to increase crack contrast (similar to the micro-XCT penetrant technique used in Chapter 4) lateral cracking was only observed for indentation loads > 3 kg, although this method relies on the assumption that the cracks have been fully saturated with dye. However, sub-surface lateral cracking in the vicinity of indentation corners for indentation loads of 0.5 kg and 1 kg indentation has been detected in SEM images of single FIB-milled cross-sections in other polycrystalline ceramics [18], [19]. Another explanation is that the sub-surface lateral cracks clearly observed here may be initiated, or further opened, by the localised residual stress changes associated with FIB sectioning. This has already been highlighted by the propagation of radial cracks towards the FIB-milled trench in addition to the closing of cracks that occur in the second half of indentation milling. Unlike in the radial crack propagation (as seen in Fig. 5.4),

the extent of FIB-induced lateral crack propagation, if any exists, is harder to observe because there is no significant intersection of the lateral cracking directly with the surface. Therefore, the degree to which the lateral cracking has been changed due to sectioning in comparison to the pre-sectioning morphology is difficult to determine. No time-dependent changes in sub-surface lateral crack geometries were observed here.

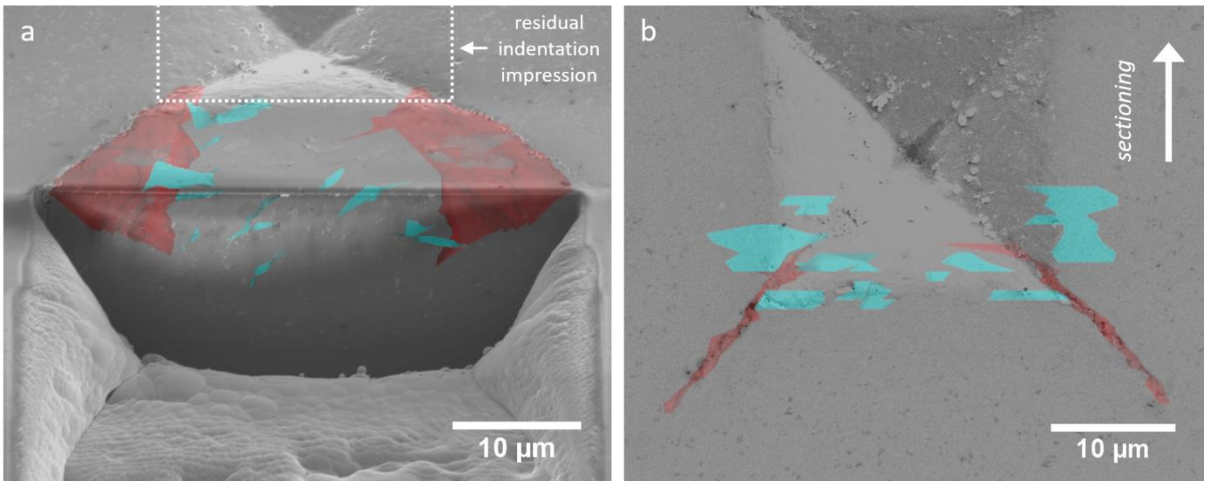

Figure 5.8: Crack maps made in IMOD overlaid onto SEM images for the 1 kg SNB indentation that was milled towards the indentation side. (a) 52° view of the indentation, the residual impression is outlined by the dotted line. (b) Top down view of the indentation. Lateral and radial cracks are coloured blue and red respectively.

Underneath the indentations, lateral cracks were observed at both shallow (< 5 µm) and deeper (> 5 µm) depths. The shallow laterals were observed to have a decreased crack width in comparison to the deeper laterals and tended to be either connected to radial cracks at the point they intersect the surface near the indentation corner (arrowed in Fig. 5.5) or related to near-surface micro-cracking resulting from the plastic deformation under the residual indentation impression. Under further applied pressure, these shallow lateral cracks would be particularly susceptible to material removal in the form of flaking or chipping, even more so if they intersect with the surface via radial cracks or micro-cracking [20], [21]. As for the deeper laterals which branched out from the primary radial cracks (e.g. Fig. 5.1(b)), they were not observed to have any direct intersections with the surface meaning they are less susceptible to material removal relative to shallow lateral cracks.

The depth of the deeper lateral cracks for SNB fits well with the prediction by Chiang et al [22] that the maximum tensile stress normal to the surface for a Vickers indented surface is at a depth less than half that of the maximum compressive stress depth from

the surface, i.e. the lateral crack starting depth to compressive stress zone depth is ~ 0.36 for the 0.5 kg indentation and ~ 0.40 for the 1 kg indentation. It must be noted however, that Chiang et al's analysis does not include the reduction in residual tensile stress associated with radial cracking. Similar ratios (< 0.5) were found in a study on higher load (> 3 kg) indentations on silicon nitride [15]. Analogous to the how it was proposed that the pathway of half-penny cracking borders the compressive-tensile stress boundary, the deep laterals are an indicator to the maximum depth of the compressive-tensile stress boundary. This correlates well with the decreased depth of deep laterals observed in the 0.5 kg indentation relative to the 1 kg indentations owing to a smaller compressively stressed volume.

Fig. 5.8 shows the 3D crack map of the SNB 1 kg indentation milled at a 45° angle to the indentation corner (parallel to the indentation side) and provides additional information regarding the relationship between the radial and lateral cracking in comparison to the other FIB-milled indentation because the sectioning encompasses two radial cracks. From Fig. 5.8 it can be seen that lateral cracking is present in between the two radial cracks indicating that these lateral cracks may connect adjacent radial on the sub-surface. If two adjacent radials are connected via deep lateral cracking, then the possibility of material removal under operational conditions increases as there are two intersections with the surface. However, the lateral cracks are at slightly differing depths and there is no full connection between the two adjacent radial cracks via a single lateral crack.

Deep lateral cracks have been found to propagate towards the surface plane under applied Hertzian contact pressure experienced by silicon nitride ball-bearings during service [23], [24]. Material removal initiated from deep laterals is more serious than shallow lateral cracks in terms of bearing failure because the volume of material detached would be greater than that for the shallow lateral cracking [20], [25]. The likelihood of material removal from lateral cracks is increased further when the 3D optical profilometry results from Chapter 4 are also taken in to account which showed an uplifted zone around the indentation edges. This is the same location where the laterals primarily reside and would be a primary pressure point in sliding contact. A schematic of how deep lateral cracking may lead to material removal is given in Fig. 5.9.

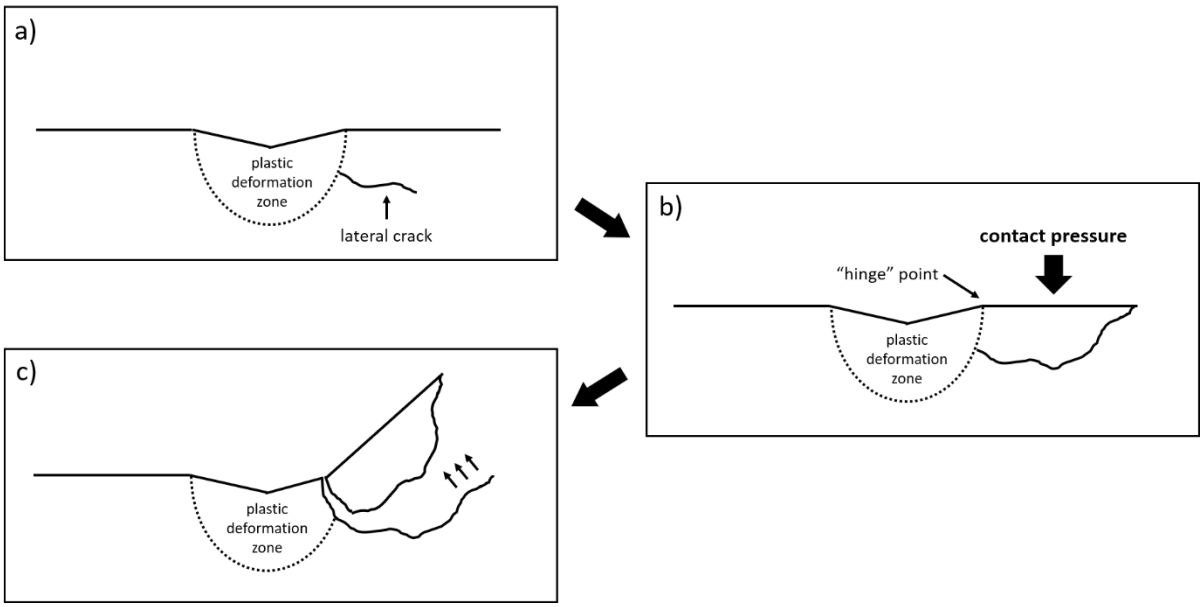

Figure 5.9: The process of potential material removal from deep lateral cracking: (a) Deep lateral cracks are located beneath the surface at the edge of the residual indentation impression. (b) Under applied contact pressure the lateral crack propagates and intersects with the surface creating a "hinge" point (as described by Cook and Roach [25]). (c) Sliding contact with the "hinge" leads to material removal along the lateral crack pathway.

The sequence in which cracking occurred during the indentation process is difficult to determine from the FIB tomography reconstructions. For Vickers indentations on ceramics, the radial/half-penny cracking has been observed to initiate on loading from flaws at the indentation corner [2], [26]. These subsequently experience further growth on unloading as the impression undergoes elastic rebound [27]. Half-penny cracking has been observed to form in ceramics [3], [26], [28] as two radial cracks propagate under the compressive zone (and changing from a Palmqvist morphology) to join beneath the indentation once a threshold load is reached, so this is likely the case for the indentations investigated here. It is suggested by Chiang et al [29] that this occurs because the driving force behind radial crack formation is stronger than that for median crack formation. Deep lateral cracks are considered to be formed on unloading as a result of high tensile unloading stresses and initiate from flaws at the tensile-compressive stress boundary [2], [30]. This correlates well with the location of lateral cracks observed via FIB tomography here where lateral cracking is limited by the aforementioned boundary. However, the radial/half-penny cracking does intersect with the deep lateral cracks (as seen in Fig. 5.1(b)), which indicates their presence influences the pathway of lateral crack propagation as proposed by Xie et al [18], [19] in a study on sub-surface cracking of SiAlON ceramics.

5.4. FIB Sectioning of a Radial Crack

In addition to the FIB tomography of whole indentation zones, FIB-sectioning of a single radial crack emanating from a 1 kg indentation on the SNC material was carried out to identify the radial crack morphology in greater detail. The milling plane was oriented almost parallel to the crack and the FIB-section thickness was reduced to 300 nm per slice (29 slices in total) in comparison to the 750 nm used for the other indentations. Fig. 5.10 shows SE images of successive FIB-milled sections taken at sectioning locations before, directly intersecting, and after the surface radial crack trace. In Fig. 5.10(a) a region of micro-cracking is observed on approach to the surface radial crack near the indentation corner. Directly intersecting the surface radial crack (Fig. 5.10(b)) there is a large damaged zone of interconnected cracking (highlighted by the dashed line) extending to a depth beneath the surface plane of ~ 4 μm and outward to the surface radial crack tip. This micro-cracking damaged zone also reached within the residual indentation impression just inside the indentation corner. In Fig. 5.10(c), the slice succeeding the surface radial crack trace, the micro-cracking damage zone can be seen to continue beneath the indentation corner, again to a depth of ~ 4 μm, and in addition, lateral cracking was also observed (arrowed) at a depth of ~ 3 μm.

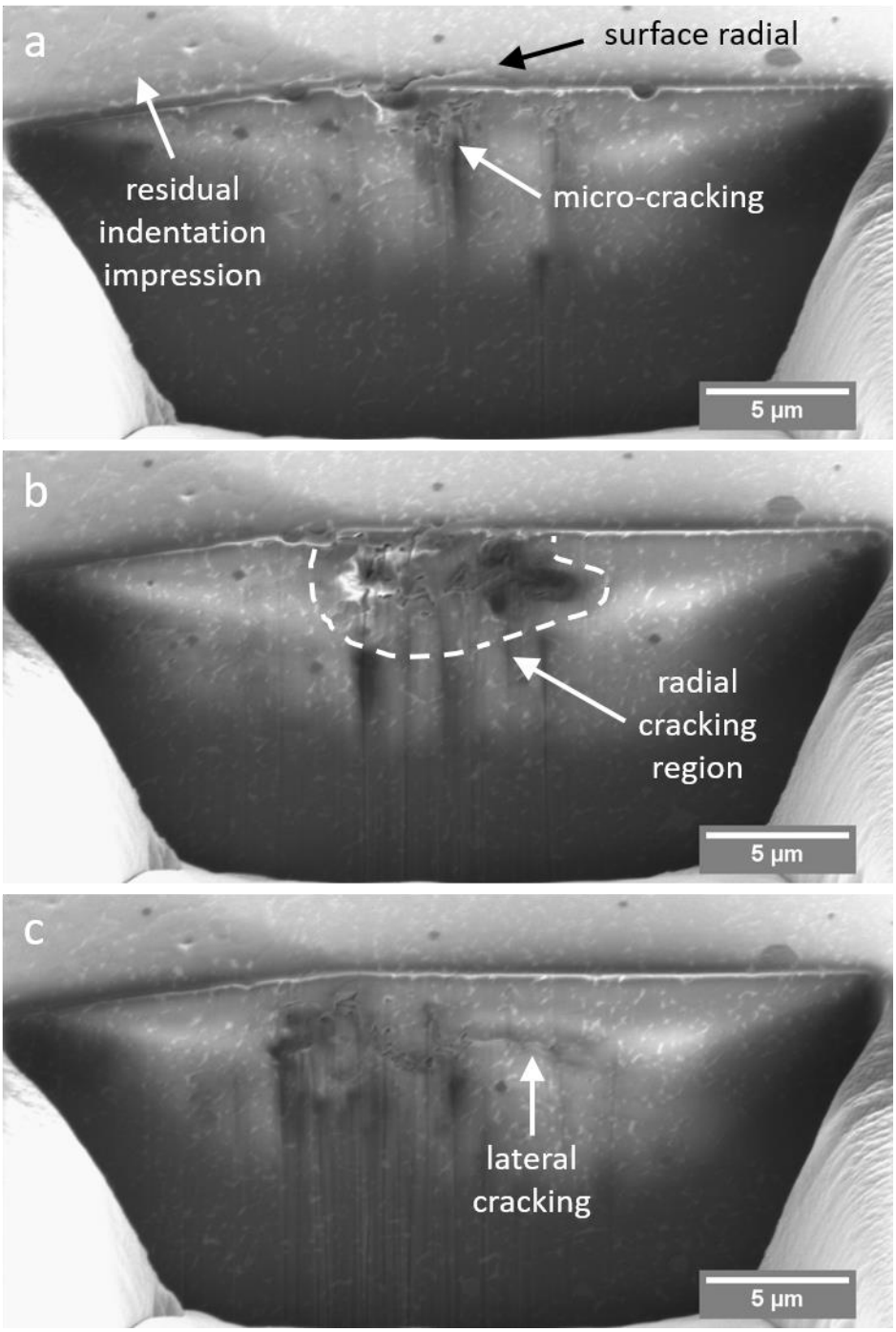

Figure 5.10: SEM images of three adjacent FIB milled slices (a)-(c) through a radial crack emanating from a 1 kg indentation on SNC composition. (a) Micro-cracking is visible sub-surface adjacent to the surface radial crack (arrowed). (b) Directly beneath the surface radial crack there is a significant damaged region (dashed outline). (c) After the surface radial crack has been milled through, lateral cracking (arrowed) is visible connected to the radial cracking region.

The 29 FIB slices from the sectioning of the radial crack were reconstructed into 3D using IMOD software and are shown in Fig. 5.11. The red cracking represents the damaged zone (highlighted in Fig. 5.10(b)) directly beneath the surface radial crack, and the blue is for lateral cracking. From Fig. 5.11(b) it can be seen that minimal lateral cracking is present

on approach towards the radial crack, however, in the close vicinity of the radial crack, there is a significant amount of lateral cracking the maximum depth of which was measured to be ~ 13 µm; a similar depth to deep lateral observed in the other indentations. Sub-surface lateral cracking was observed in the first few slices after the radial crack extended out to the radial crack tip. This was not seen in the previous FIB-sectioning of indentations, although the angle of this lateral cracking (arrowed) was particularly steep indicating that these laterals could be regarded as an extension of the radial crack instead of a branching lateral crack. Again, as with the other sectioned indentations, the lateral cracking does not extend far beneath the residual indentation impression.

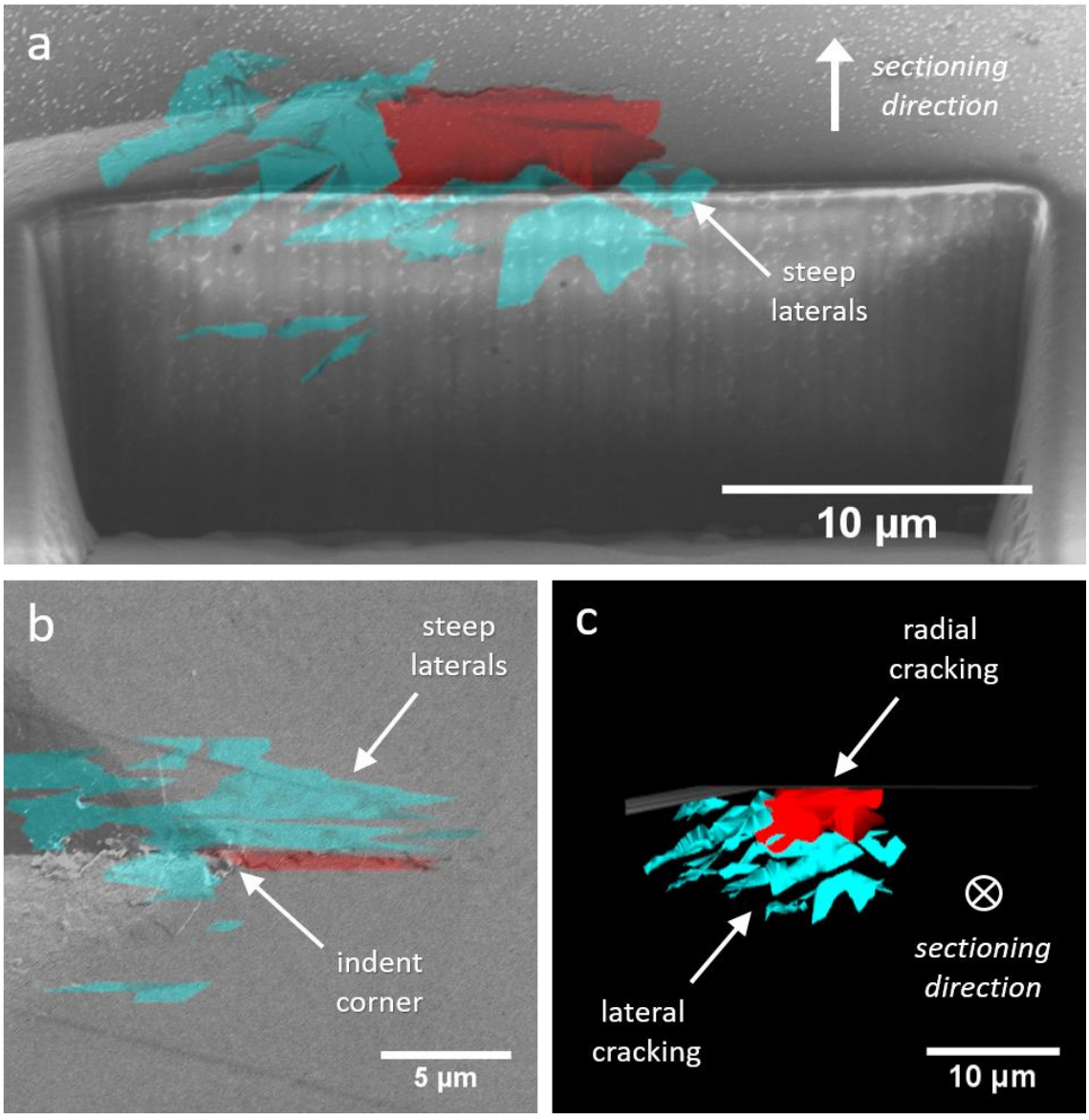

Figure 5.11: 3D Crack maps produced with IMOD of the radial crack on the 1 kg indented SNC sample: (a) Overlaid on to an SEM image of the radial crack at a 52° tilt angle. (b) Overlaid on to an SEM image with a top-down view of the surface radial crack. (c) A schematic showing a side view of the IMOD crack map.

The depth of this radial crack (i.e. the depth of the damaged zone beneath the surface radial crack) does not compare with that measured for the radial cracks in the SNA and SNB 1 kg indentations (Fig. 5.3 and Fig. 5.7) which is probably a combination of two things: firstly, the radial cracks in the other FIB-milled indentations, where the sectioning direction was perpendicular to the indentation corner, all propagated towards the FIB-milled trench causing crack opening and extension in surface length (extension of ~ 4 μm and ~ 8 μm for the SNB 1 kg and 0.5 kg indentation, and ~ 10 μm for the SNA 1 kg indentation) . Secondly, the milling plane here is parallel to the crack and therefore if the radial crack width decreases with depth then a single sectioning slice of 300 nm may remove much of the radial crack where the width is < 300 nm. Furthermore, the lateral crack density also appears to be lower before (in comparison to after) the radial crack had been milled away. This could be due to localised residual stress changes opening up the lateral cracks as a result of the removal of the radial crack, and is in agreement with the prediction by Xie et al [18] that the presence of radial cracking (which is formed prior to lateral cracking) influences the propagation of lateral cracks.

5.5. Top-Down Sectioning of Vickers Indentations

5.5.1. Sectioning of 1 kg Vickers Indentations

To compare the FIB sectioning methodology with more conventional methods, three additional 1 kg Vickers indentations on SNA composition were incrementally sectioned 'top-down' by serial polishing using diamond lapping paper and imaged optically to reveal the crack morphology as a function of depth. Bright field (BF) and dark field (DF) images of one of the 1 kg indentations on SNA prior to polishing are shown in Fig. 5.12(a). In both images, radial cracks can be seen emanating from the indentation corners with a measured outward extension of up to ~ 10 μm. No surface traces of lateral cracking were observed in any of the 1 kg indentations before polishing. After ten polishing increments (i.e. an estimated depth of ~ 4 μm as shown in Fig. 5.12(c)) the residual indentation impression, as well as the associated radial cracks were no longer observed in the bright field images of the 1 kg indentation. However, in the dark field images the radial cracking is still visible in addition to a surrounding 'border' region, where the edge of the residual indentation impression previously was. This DF contrast zone was observed in all the 1 kg indentation sectioning. The visibility of the indentation features in DF decreased with

increasing polishing depth. This is evident in the dark field image in Fig. 5.12(c), after the twentieth polishing increment (a depth of ~ 8 µm) the radial cracks and border region are difficult to resolve. The maximum depth at which any of the indentation features were resolvable using either dark or bright field optical microscopy was at the twenty-fourth increment (a depth of ~ 10 µm), after which there was no distinction between where the indentation previously was and the surrounding area. The radial cracking and border region were both still present at the maximum resolvable depth with the radial cracks being connected to the border region at all imaged depths.

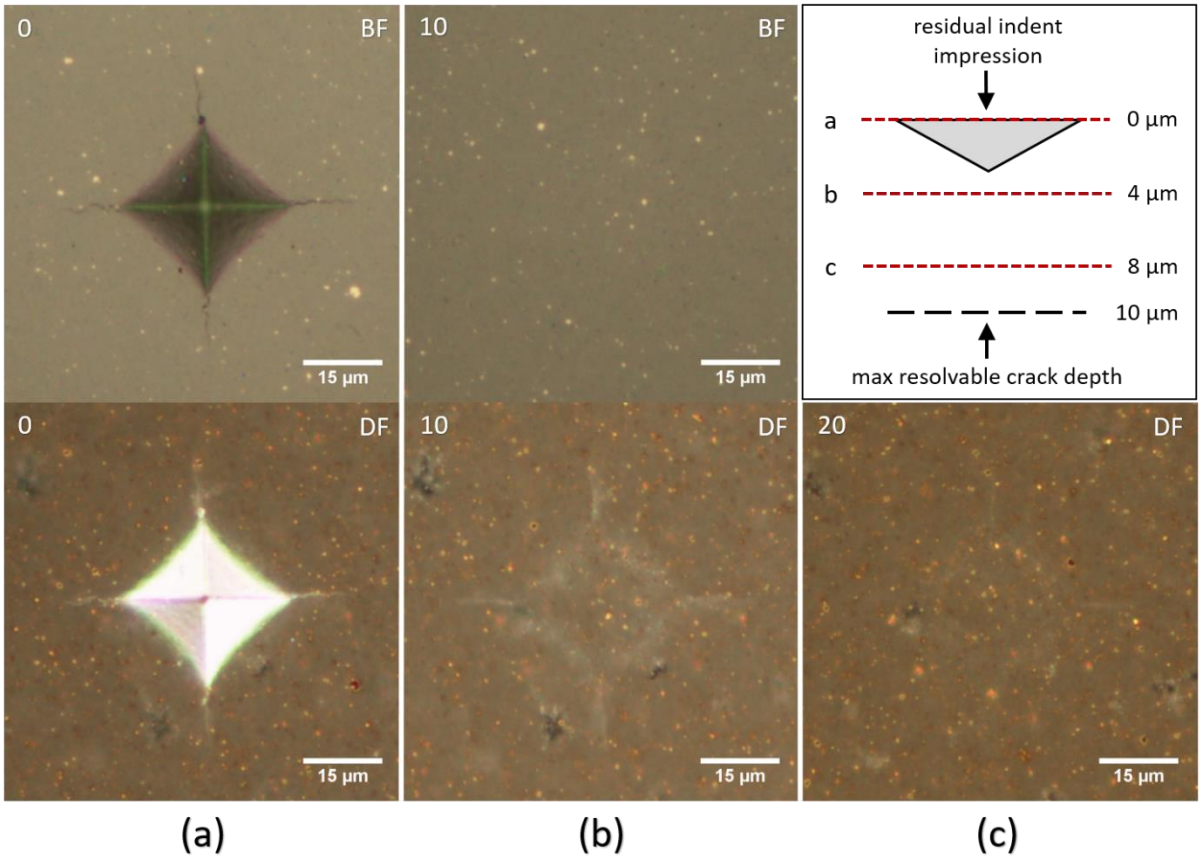

Figure 5.12: Optical images in both bright field (top) and dark field (bottom) mode showing one of the 1 kg SNA indentations (a) before polishing (b) after the tenth increment of polishing, and (c) a schematic of where each image is in location to depth (top), as well as the dark field image after the twentieth increment.

As evident in Fig. 5.12(b), dark field optical microscopy was more effective than standard bright field optical microscopy in detecting features i.e. radial cracks and the border region on the 1 kg indentations. The location of the border region correlates with the micro-cracking zone which is likely to cause significant light scattering from the high density of cracks and dislocations. During the incremental polishing of the 1 kg indentations, no clear evidence of lateral cracking was observed at any polishing depth. This may be

because lateral cracking was present within the border region/micro-cracking zone and hence was difficult to directly observe. The FIB sectioning investigations support this explanation where shallow lateral cracking was observed within regions of micro-cracking (Fig. 5.5). In addition, because laterals are often oriented at a shallow angle (0 - 28°) relative to the surface plane, it is likely that they were removed during polishing steps in between optical imaging as their crack width is of the same order as the depth of the material removed via polishing increments (in the same way that the radial crack sectioned parallel using FIB was only easily observable in one cross-section). The shallow angle of lateral cracks relative to radial cracks also means that their projected light scattering is also decreased hence making them more difficult to detect.

The attachment of the radial cracks with the border region at all polishing depths implies that the sub-surface cracking regime is half-penny in nature. In a Palmqvist regime it would be expected that radial cracks detach from the residual indentation corners at increasing depth, but this was not observed [31]. It is noted however, that radial cracking at increasing depths was more difficult to resolve meaning there is a limit to the observations that can be made in comparison to the FIB tomography. The decreasing crack visibility with depth for the optical microscopy is caused by the effective radial crack width (from which light scattering is sufficient to be detectable) decreasing below the spatial resolution of the optical microscope which needs crack openings (and the adjacent damaged zone) to be wide enough for light scattering to occur and subsequently be detected. Crack width decreases as a function of depth, however, a further decrease in crack width (and even crack closure) could have occurred as a result of the removal (via polishing) of the plastically deformed compressive stress volume that resides beneath the residual indentation impression. Surrounding this volume is a zone of tensile stress where radial cracks initiate to alleviate the built-up stress. The removal of the surface tensile stress zone, as well as the compressive zone encompassed within, means that the cracks are in a reduced stress environment and therefore can close [12], [13]. This may also be another explanation as to why sub-surface lateral cracks were not observed. There are parallels between this crack closure mechanism and that which causes the decrease in crack density in the second half of the FIB sectioned indentations discussed earlier in the chapter.

5.6. Discussion of 3D Characterisation Techniques

The FIB tomography method for characterising sub-surface cracking beneath the Vickers indentations on silicon nitride has proved to be very effective as illustrated by the detail in the IMOD 3D reconstructions of the crack maps produced (Figs. 5.3, 5.6, 5.7, 5.8 & 5.11) . Different crack types, sizes and orientations were able to be clearly resolved, and quantified, including radial, lateral and half-penny cracking. In addition to this, the high resolution of the SEM enabled new and greater understanding of the cracking regimes that exist beneath Vickers indentations performed at low loads (< 1 kg), i.e. the observation of half-penny and lateral cracking. Another advantage is that the spatial precision of the FIB allows for site-specific localised milling at high spatial resolution, meaning that specific features, e.g. an individual radial crack, could be investigated in detail. Relaxation of residual as a consequence of FIB sectioning was found to initiate changes in the crack morphology, both in the opening-up of cracks and their propagation (Fig. 5.4), but also in crack closure below the detection limit during the second half of indentation FIB-milling. This potentially means that the 3D cracking observed may not have been a true representation of the sub-surface cracking present prior to milling. However, similar cracking was observed for the 1 kg SNB indentation milled at a 45° angle (Fig. 5.8) despite the differing FIB sectioning approach directions, which suggests that the cracking morphology does not change a significant amount.

The top-down diamond polishing method in conjunction with dark field optical microscopy revealed useful information about the sub-surface nature of the indentations, including the presence of the micro-cracking region surrounding the residual indentation impression, as well as further evidence for the existence of a half-penny cracking regime. However, the limited resolution of optical microscopy, in addition to the uncertainty in depth measurements, means that sectioning via diamond polishing lacks the detail and precision offered by FIB tomography – aspects which will be of particular importance when investigating actual ball-bearing component star features (in Chapter 6), which are not reproducible like Vickers indentations. Both 3D sectioning methods utilised in this chapter are destructive methods and remove the investigated features but, as has been discussed in Chapter 4, the resolution of non-destructive micro-XCT is not sufficient for characterising the ball star features which are of a similar order in size to the 1 kg indentations studied here. Therefore, the 3D characterisation method which is most applicable to the star features, and will provide the most detailed analysis, is FIB tomography.

5.7. Summary

This chapter has focused on the 3D investigation of sub-surface cracks beneath 0.5 kg and 1 kg applied load Vickers indentations on silicon nitride using FIB tomography and top-down sectioning in conjunction with optical microscopy. The SEM images from the FIB tomography were used to successfully produce 3D crack maps, and the main findings from these were:

- For the first time, half-penny cracking, instead of the expected Palmqvist cracking regime, was observed in low applied load Vickers indentations (0.5 kg) with c/a ratio ~ 1.5.
- Half-penny cracking was also observed in all 1 kg indentations for both the SNA and SNB silicon nitride composition.
- Deep lateral cracking at depths of up to ~ 0.4× the compressive stress zone depth were observed near the indentation corners for all applied loads and compositions.
- The location of half-penny and lateral cracks can indicate the volume occupied by the plastically deformed compressive stress zone present beneath the residual indentation impression (~ 3,000 μm^3 and 11,000 μm^3 for the SNB 0.5 kg and 1 kg indentations respectively, and 9,500 μm^3 for the SNA 1 kg indentation).
- Lateral cracks were edged by micro-cracking and radial cracks, and were angled 0° - 25° relative to the surface plane.

The FIB sectioning process was also found to change the residual stress in the indentation area sometimes resulting in radial crack propagation towards the FIB-milled trench. This is in addition to a decrease in measured crack density in the second half of the milled indentations in comparison to the first half as a result of the removal of compressive and tensile stressed zones present beneath the residual indentation impression. For the top down sectioning using diamond polishing, the main findings were as follows:

- The presence of a micro-cracking border zone surrounding the residual indentation impression that remained even after the surface impression had been removed by polishing.
- Radial cracks were not seen to detach from the micro-cracking border with increasing depth of polishing, indicating a half-penny cracking regime.

Indentation features were only observable down to a depth of 10 μm for the top-down polishing method because of the low optical resolution and crack closure. The FIB tomography method for 3D crack characterisation was found to be superior due to the increased spatial and depth resolution, as well as the precision of 3D sectioning. In addition, the discovery of half-penny and lateral cracking in the 0.5 kg and 1 kg indentations using FIB tomography is of great importance in understanding cracking present in silicon nitride bearing component materials, as these are potential initiation point for material removal via spalling and flaking under operational conditions.

5.8. References

[1] A. Baggott, M. Mazaheri, and B. J. Inkson, "3D characterisation of indentation induced sub-surface cracking in silicon nitride using FIB tomography," *J. Eur. Ceram. Soc.*, vol. 39, no. 13, pp. 3620–3626, 2019.

[2] Y. Tang, A. Yonezu, N. Ogasawara, N. Chiba, and X. Chen, "On radial crack and half-penny crack induced by Vickers indentation," *Proc. R. Soc. A Math. Phys. Eng. Sci.*, vol. 464, no. May, pp. 2967–2984, 2008.

[3] H. Miyazaki, H. Hyuga, Y. I. Yoshizawa, K. Hirao, and T. Ohji, "Crack profiles under a Vickers indent in silicon nitride ceramics with various microstructures," *Ceram. Int.*, vol. 36, no. 1, pp. 173–179, 2010.

[4] F. Elfallagh and B. J. Inkson, "3D analysis of crack morphologies in silicate glass using FIB tomography," *J. Eur. Ceram. Soc.*, vol. 29, pp. 47–52, 2009.

[5] M. Schaffer, J. Wagner, B. Schaffer, M. Schmied, and H. Mulders, "Automated three-dimensional X-ray analysis using a dual-beam FIB," *Ultramicroscopy*, vol. 107, no. 8, pp. 587–597, 2007.

[6] N. Payraudeau, D. McGrouther, and K. U. O'Kelly, "Quantification of subsurface damage in a brittle insulating ceramic by three-dimensional focused ion beam tomography.," *Microsc. Microanal.*, vol. 17, no. 2, pp. 240–5, 2011.

[7] K. H. Kim, Z. Akase, T. Suzuki, and D. Shindo, "Charging Effects on SEM/SIM Contrast of Metal/Insulator System in Various Metallic Coating Conditions," *Mater. Trans.*, vol. 51, no. 6, pp. 1080–1083, 2010.

[8] H. Seiler, "Secondary electron emission in the scanning electron microscope," *J. Appl. Phys.*, vol. 54, no. 11, 1983.

[9] A. Zankel, J. Wagner, and P. Poelt, "Serial sectioning methods for 3D investigations in materials science," *Micron*, vol. 62, pp. 66–78, 2014.

[10] K. Niihara, "A fracture mechanics analysis of indentation-induced Palmqvist crack in ceramics," *J. Mater. Sci. Lett.*, vol. 2, no. 5, pp. 221–223, 1983.

[11] X. Yang, X. Liu, Z. Huang, X. Yao, and G. Liu, "Vickers indentation crack analysis of solid-phase-sintered silicon carbide ceramics," *Ceram. Int.*, vol. 39, no. 1, pp. 841–

845, 2013.

[12] B. J. Inkson, D. Leclere, F. Elfallagh, and B. Derby, "The effect of focused ion beam machining on residual stress and crack morphologies in alumina," *J. Phys. Conf. Ser.*, vol. 26, no. 1, pp. 219–222, 2006.

[13] F. Elfallagh and B. J. Inkson, "Evolution of residual stress and crack morphologies during 3D FIB tomographic analysis of alumina.," *J. Microsc.*, vol. 230, no. Pt 2, pp. 240–51, 2008.

[14] K. Niihara, R. Morena, and D. P. H. Hasselman, "Evaluation of Klc of Brittle Solids By the Indentation Method With Low Crack To Indent Ratios," *J. Mater. Sci. Lett.*, vol. 1, pp. 13–16, 1982.

[15] T. Lube, "Indentation crack profiles in silicon nitride," *J. Eur. Ceram. Soc.*, vol. 21, pp. 211–218, 2001.

[16] F. Elfallagh, "3D analysis of indentation damage by FIB tomography and TEM," University of Sheffield, 2008.

[17] H. Z. Wu, S. G. Roberts, G. Möbus, and B. J. Inkson, "Subsurface damage analysis by TEM and 3D FIB crack mapping in alumina and alumina/5vol.%SiC nanocomposites," *Acta Mater.*, vol. 51, no. 1, pp. 149–163, 2003.

[18] Z. H. Xie, P. R. Munroe, R. J. Moon, and M. Hoffman, "Characterization of surface contact-induced fracture in ceramics using a focused ion beam miller," *Wear*, vol. 255, no. 1–6, pp. 651–656, 2003.

[19] Z. H. Xie, M. Hoffman, R. J. Moon, P. R. Munroe, and Y. B. Cheng, "Subsurface Indentation Damage and Mechanical Characterization of α-Sialon Ceramics," *J. Am. Ceram. Soc.*, vol. 87, no. 11, pp. 2114–2124, 2004.

[20] M. Hadfield and T. A. Stolarski, "Observations of delamination fatigue on pre-cracked ceramic elements in rolling contact," *Ceram. Int.*, vol. 21, no. 2, pp. 125–130, 1995.

[21] Y. Wang and M. Hadfield, "A mechanism for nucleating secondary fractures near a pre-existing flaw subjected to contact loading," *Wear*, vol. 254, no. 7–8, pp. 597–605, 2003.

[22] S. S. Chiang, D. B. Marshall, and A. G. Evans, "The response of solids to elastic / plastic indentation. I. Stresses and residual stresses," *J. Appl. Phys.*, vol. 53, no. 1, pp. 298–311, 1982.

[23] Y. Wang and M. Hadfield, "Failure modes of ceramic rolling elements with surface crack defects," *Wear*, vol. 256, no. 1–2, pp. 208–219, 2004.

[24] Y. Wang and M. Hadfield, "A study of line defect fatigue failure of ceramic rolling elements in rolling contact," *Wear*, vol. 253, no. 9–10, pp. 975–985, 2002.

[25] R. F. Cook and D. H. Roach, "The effect of lateral crack growth on the strength of contact flaws in brittle materials," *J. Mater. Res.*, vol. 1, no. 4, pp. 589–600, 1986.

[26] R. Cook and G. Pharr, "Direct observation and analysis of indentation cracking in glasses and ceramics," *J. Am. Ceram. Soc.*, vol. 73, no. 4, pp. 787–817, 1990.

[27] J. Alcalá, A. C. Barone, and M. Anglada, "Influence of plastic hardening on surface deformation modes around Vickers and spherical indents," *Acta Mater.*, vol. 48, no. 13, pp. 3451–3464, 2000.

[28] A. Pajares, F. Guiberteau, F. L. Cumbrera, R. W. Steinbrech, and A. Dominguez-Rodriguez, "Analysis of kidney-shaped indentation cracks in 4Y-PSZ," *Acta Mater.*, vol. 44, no. 11, pp. 4387–4394, 1996.

[29] S. . Chiang, D. . Marshall, and A. G. Evans, "The response of solids to elastic / plastic indentation . I . Stresses and residual stresses," *J. Appl. Phys.*, vol. 53, no. 1, pp. 298–311, 1982.

[30] J. T. Hagan and M. V. Swain, "The origin of median and lateral cracks around plastic indents in brittle materials," *J. Phys. D Appl. Phys.*, vol. 11, no. 15, pp. 2091–2102, 1978.

[31] Husni, M. Rizal, M. Aziz, and M. Wahyu, "Ceramic tools insert assesment based on vickers indentation methodology," *IOP Conf. Ser. Mater. Sci. Eng.*, vol. 352, no. 1, pp. 0–8, 2018.

Chapter 6: FIB Tomography of Star Features on Silicon Nitride Balls

6.1. Introduction

The purpose of this chapter is to utilise the FIB tomography technique that was successfully used on Vickers indentations on silicon nitride in Chapter 5 and apply it to star features on silicon nitride balls where the features have been formed under actual processing conditions, not artificially. The FIB tomography determination of the sub-surface crack morphology, in conjunction with 3D optical profilometry, should give an insight into how the star features may further evolve in service and reduce ball-bearing performance.

6.2. Surface Morphology of Star Features

The star shaped indent-like features that are found on silicon nitride balls have varying morphologies dependent on how they were originally formed, in addition to what tribological processes they have been subject to since formation. Optical images of a variety of the stars are shown in (at the top of) Fig. 6.1. It can be seen that some stars have a central indentation surrounded by associated cracking, often with some missing material, whilst there are also stars which exhibit no indention as such, just a central zone surrounded by cracking. Therefore, for the following FIB tomography investigations, the stars have been grouped into two types: those where there is no indentation present and cracking is primarily radial, and those where there is a central indentation and/or lateral and radial cracking – these will be referred to as Morphology 1 (M1) and Morphology 2 (M2) stars respectively. Schematics of the two types of star morphology and their keys features, along with examples, are given in Fig. 6.1(a & b). In this chapter, a total of five stars have been serial-sectioned using FIB tomography; three M1 stars, and two M2 stars.

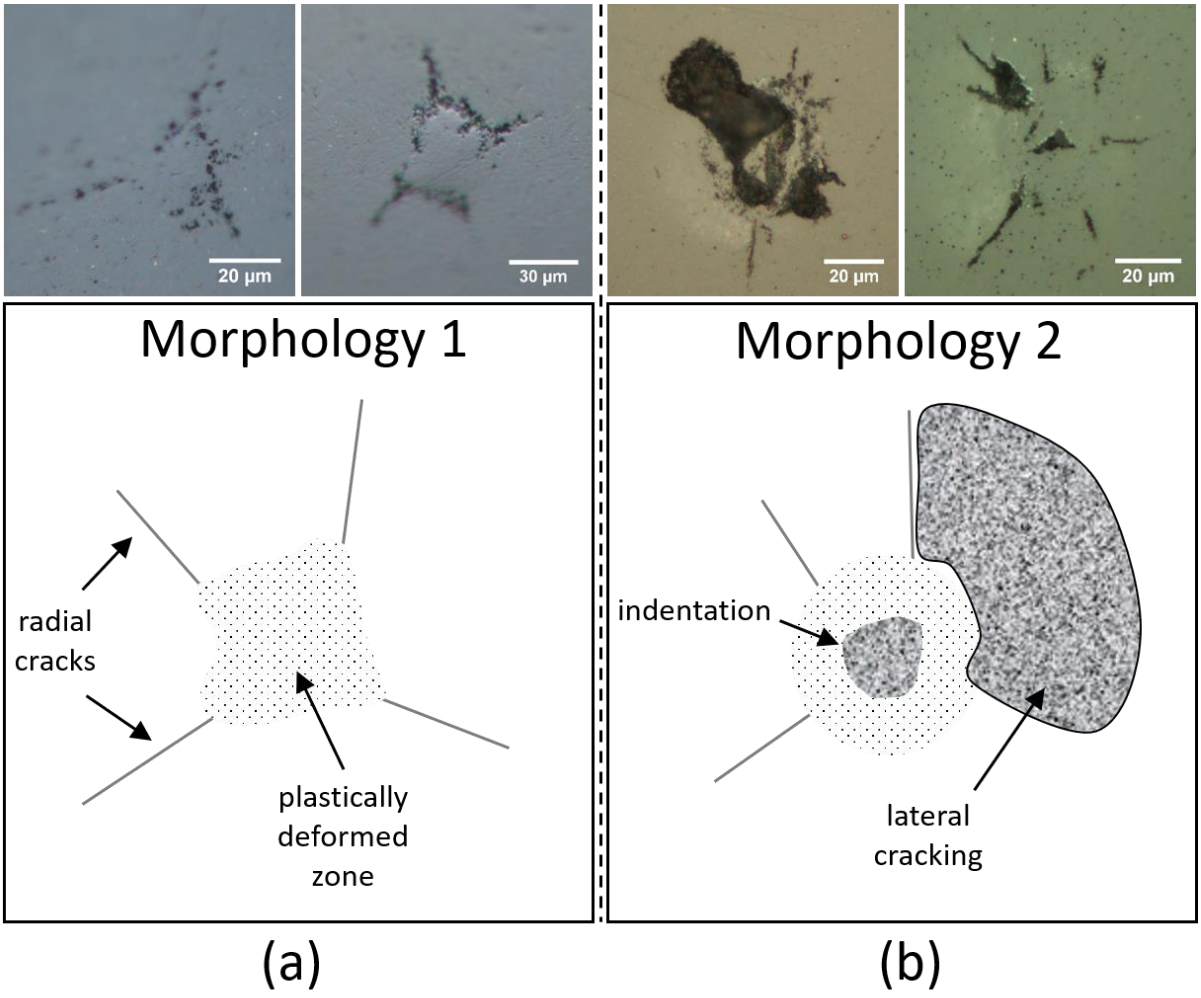

Figure 6.1: Schematics of (a) Morphology 1 star features and (b) Morphology 2 star features showing common features of both. Optical images of examples of each type of star are given above the respective star schematic.

6.3. Surface Characterisation of Morphology 1 Stars

6.3.1. Optical and UV Imaging of M1 Stars

The three M1 stars investigated were chosen based on their appearance when viewed under optical microscopy as well as previously taken images using UV fluorescence microscopy conducted by the project industrial sponsor. These stars will be referred to as SNA-1, SNA-2 and SNB-3 in reference to their composition, i.e. the SNA and SNB silicon nitride compositions investigated in the previous chapters. Fluorescence imaging was carried out by soaking the balls in a fluorescent penetrant (and subsequently rinsing excess penetrant off the surface) with the aim that the central region and any associated cracking is saturated with the penetrant. Incident UV light then excites the penetrant

causing it to fluoresce in the visible spectrum. The emitted light can reach the surface as the silicon nitride medium allows transmission down to a certain depth (~ tens of microns) hence revealing the location of sub-surface features, e.g. cracks. N.B. All UV fluorescence images used in this chapter were collected by the industrial sponsor and have been used to assist in sample selection and methodology comparison.

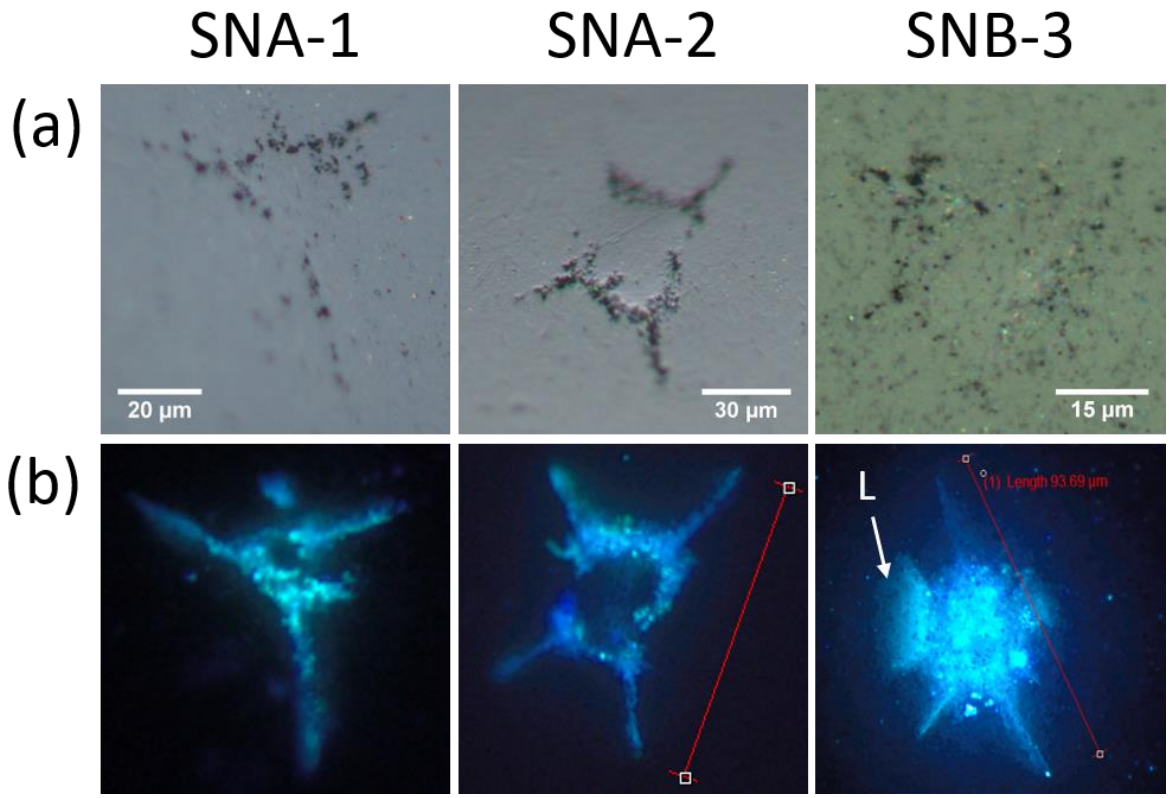

Figure 6.2: Bright field optical (a) and UV fluorescence images (b) of the three Morphology 1 type stars chosen for investigation: referred to here as SNA-1, SNA-2, and SNB-3. On the SNB-3 UV fluorescence image, the lateral crack has been labelled L (arrowed). The UV fluorescence images used in (b) have been used and edited with permission from the industrial sponsor.

Optical images of the three M1 stars as well as the associated UV fluorescence images are given in Fig. 6.2. The optical images are slightly out of focus in some regions because of the curvature on the ball surface. SNA-1 and SNA-2 show quite similar features in that they both have a central zone with no cracking, outlined by a darker contrast region with emanating surface radial cracks. SNA-2 in particular has a very similar morphology to the polished-down 1 kg SNA indentations investigated in Chapter 5; this is likely indicative that the M1 stars have undergone material removal after indentation, leading to the current observed morphology with no central indentation present. The UV fluorescence images correlate well with the optical images, although the projected length of radial cracks does appear longer in the UV images. For SNA-1, UV emission is present

within the central zone, indicating that dye penetration and thus (likely) cracking extends beneath this region. The regions bordering the central zone also exhibit strong UV emission implying they have a morphology which allows for a high level of penetrant saturation; probably micro-cracking. SNB-3 is slightly different in comparison to SNA-1 and SNA-2 in that the UV fluorescence reveals information about the sub-surface microstructure that is not apparent in the surface optical images. For instance, there appears to be the presence of a lateral crack in the UV images (arrowed L) that from the surface would appear to be two radial cracks. There are also radial cracks emanating from the central zone which are not resolved in the optical images but are observed in the UV images. In addition, a high level of UV emission is present in the central region of SNB-3. The crack tip to crack tip length, i.e. the distance between the two furthest apart radial crack tips, was measured for each of the stars (from the UV fluorescence images) and found to be 85 μm, 99 μm and 94 μm for the SNA-1, SNA-2 and SNB-3 star features respectively. This is large compared to the 1 kg indentations where tip-to-tip distance is ~ 45 μm (Chapter 4 and 5).

6.3.2. 3D Optical Profilometry of M1 Stars

As in the Chapter 4 investigations of the Vickers indentations, 3D optical profilometry has been used here to map the surface topography of the SNA-1 and SNB-3 M1 stars (the SNA-2 star was not available for profilometry).

In Fig. 6.3 a line plot across the central zone of the SNA-1 star feature is given as well as the topographical profilometry map (inset). In the map, red regions represent raised zones, and blue regions depressed zones (relative to the average surface height). The central zone is raised in comparison to the surrounding region. The areas where radial cracking was observed in the optical and UV fluorescence images (Fig. 6.2) exhibit localised surface depression (arrowed). From the line plot, the uplift at the centre (Fig. 6.3, arrowed) is ~ 0.15 μm and does not show a gradual slope to the maximum, i.e. the uplift zone protrudes from the surface. The uplift zone appears to be contained within the border region observed in the optical and UV fluorescence images of the star and is consistent with compressive stress relief.

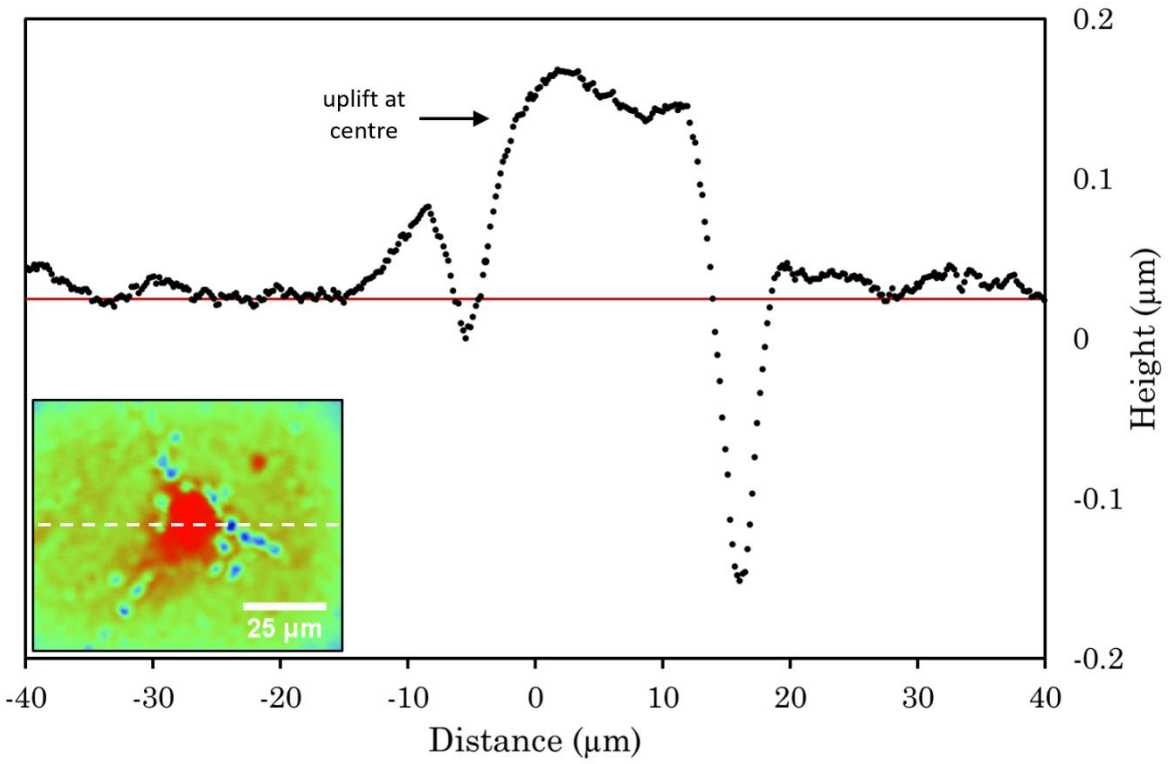

Figure 6.3: A topographic line plot across the SNA-1 star showing an uplift zone at the centre. Inset is the height profile of the star where red and blue regions are above and below the average surface height respectively.

An optical profilometry line plot and topographic map are also given for the SNB-3 star in Fig. 6.4. The topographic profile is similar to that of the SNA-1 star with the central area being raised relative to the surrounding region. The maximum uplift across the line plot is ~ 0.2 µm with the central uplift zone again exhibiting a steep gradient. As with the optical image of SNB-3, radial cracking is not well resolved in the optical profilometry indicating that the laser spot size is of the order of the crack width (~ 1 µm). This means that small surface height changes within the laser analysed volume will not be collected.

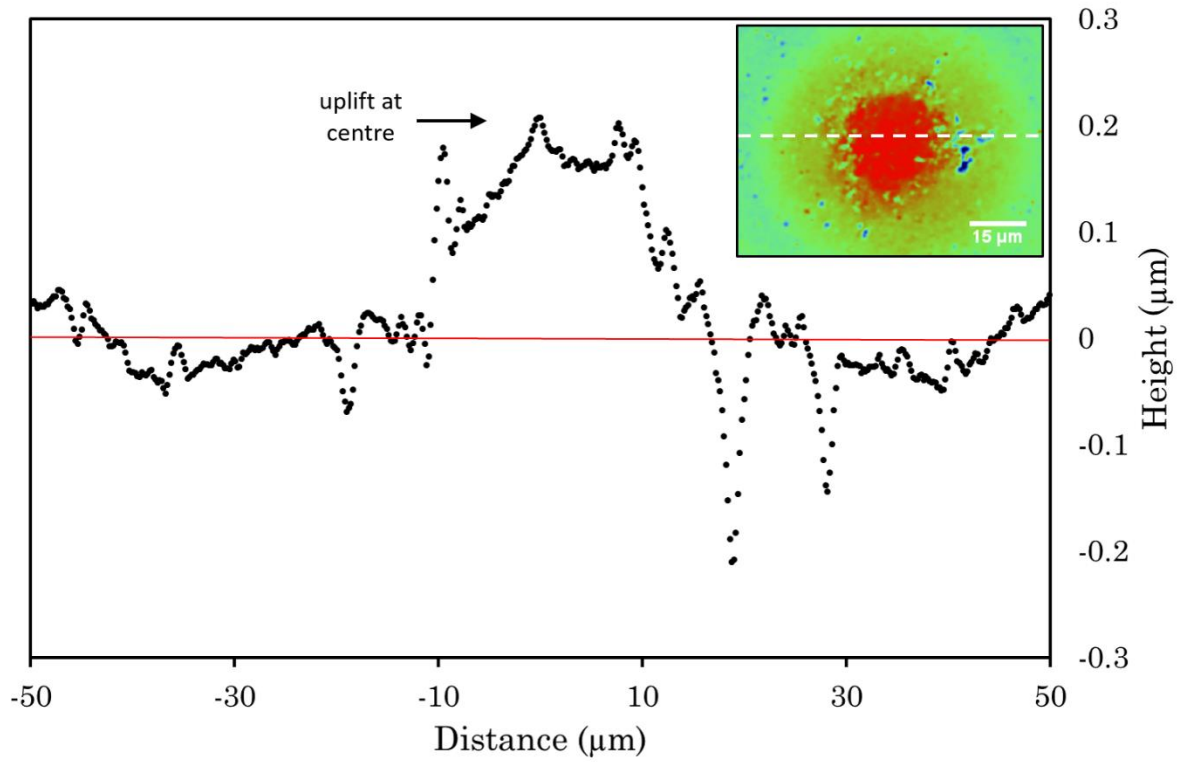

Figure 6.4: A topographic line plot across the SNB-3 star showing an uplift zone at the centre. Inset is the height profile of the star where red and blue regions are above and below the average surface height respectively.

For the sake of comparison, Fig. 6.5 shows topographic profiles of a 5 kg Vickers indentation that has had the residual indentation impression polished away using diamond lapping paper (Fig. 6.5(a)), and a 5 kg Vickers indentation that has not undergone any polishing (Fig. 6.5(b)). The topographic morphology of the polished indentation shown in Fig. 6.5 (a) is similar to that of the M1 stars with the central region of uplift bordered by the surface cracking. This could imply that the formation process for M1 stars is of the same nature, i.e. an original indentation with associated cracking that has undergone subsequent material removal leaving behind a uplifted zone caused by material relaxation as the high compressive stress plastic deformation region beneath the indentation is removed [1]. It also suggests that Vickers indentation, as a method for reproduction of star features formed during manufacturing and service of silicon nitride ball-bearings, is a suitable technique. The topography of the 5kg Vickers indentations (Fig. 6.5(b)) is more comparable to the M2 stars, so will be discussed later in reference to them.

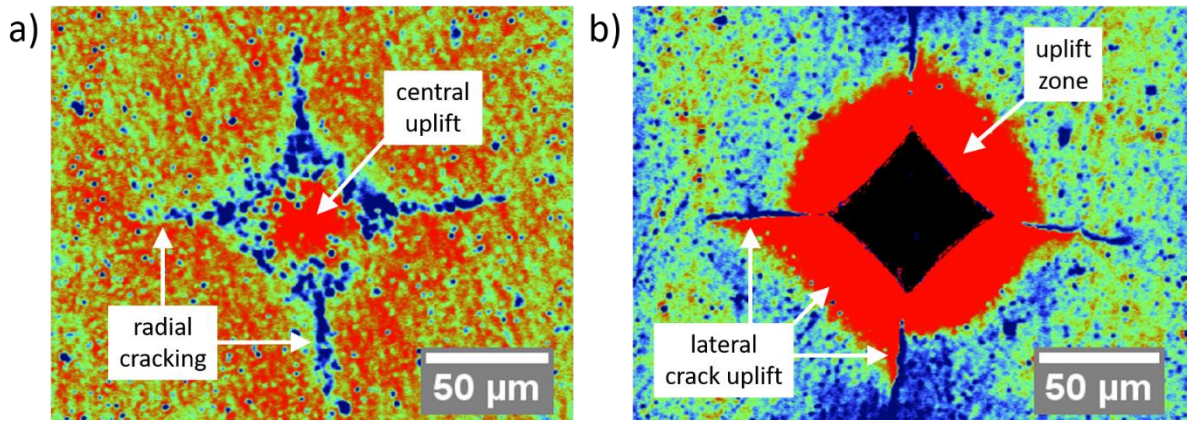

Figure 6.5: Topographic optical profiles of: (a) A 5 kg Vickers indentation on the SNA composition of silicon nitride that has undergone diamond lapping to remove the residual indentation impression. An area of material uplift at the centre is arrowed. (b) a 5 kg Vickers indentation showing uplift from lateral cracking (arrowed).

6.4. FIB Tomography of Morphology 1 Stars

The FIB-sectioning method utilised on the M1 star features was very similar to that used on the Vickers indentations in Chapter 5. However, as the M1 stars are asymmetric and occupy a larger area than the indentations, the parameters used for FIB-sectioning, i.e. the depth and width of the milled volume, were adjusted for each sample. Images of the surfaces of the stars observed through SEM have been taken at the same orientation as the optical and UV fluorescence images to aid comparison.

6.4.1. FIB-Sectioning of SNA-1

For the SNA-1 star, FIB-sectioning was started ~ 20 µm from the longest radial crack tip and proceeded in the direction of the central zone (Fig. 6.6(a)). On approach, the radial crack was not observed to propagate towards the trench as seen in the FIB-milling of whole Vickers indentations (Chapter 5). As milling reached the tip of the surface radial crack (with the surface crack trace perpendicular to the mill plane), it appeared on the FIB-milled cross-section emanating downward at an angle of 68 ° from the surface plane. The maximum depth of the radial crack was not measurable as it extended to depth beyond the milled trench depth of ~ 40 µm. At ~ 25 µm along the surface radial crack (Fig. 6.6(b)), the sub-surface radial crack detached from the surface and instead was observed at a depth of ~ 19 µm beneath the surface extending down to the trench bottom in a now half-penny crack morphology (Fig. 6.6(b)). This continued up until the central zone was

reached where the half-penny crack view on the cross-section was observed to separate in to two cracks as seen in Fig. 6.6(c) with the left-hand crack further separating from the primary half-penny crack on approach to the middle of the central zone. The primary half-penny crack was then observed to disappear, but an additional radial crack appeared to the right of the trench and, near the end of the central zone, potentially connected with a lateral crack that was located centrally on the cross-section at a depth of ~ 14 µm (Fig. 6.6(d)); although the radial crack was difficult to resolve at this point. Also, at the same location, steep lateral cracking with an angle of 40° to the surface plane was observed at a maximum depth of ~ 10 µm emanating towards the trench side-wall. The majority of cracking observed on the sub-surface via SEM imaging of the FIB-milled cross-sections correlated well with cracking observed on the surface plane (Fig. 6.2).

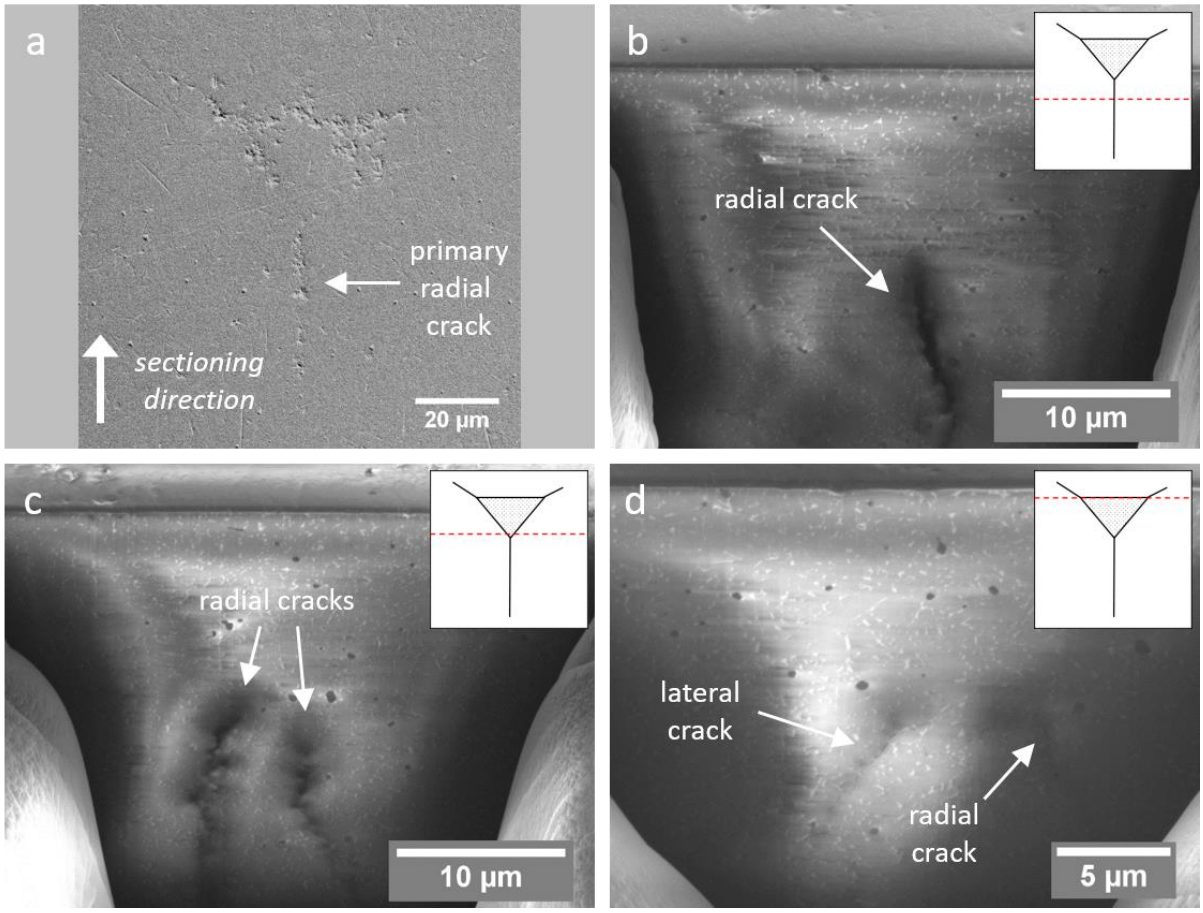

Figure 6.6: (a) An SEM image of the SNA-1 star giving the direction of FIB-sectioning. SEM imaged FIB-milled cross-sections (with the SEM at a tilt angle of 52°) at various locations through the sectioning process of SNA-1 are given in (b)-(d). The insets are top-down schematics of the stars with the red dashed line showing the location of the SEM cross-section image relative to the star. Cracks of interest have been arrowed.

6.4.2. FIB-Sectioning of SNA-2

In a similar way to SNA-1, the FIB-sectioning of SNA-2, shown in Fig. 6.7(a), started away from the tip of the longest radial crack and headed inward towards the central zone. After the first FIB-milled increment, the surface radial crack was observed to propagate and/or open a distance of ~ 13 μm towards the trench and appeared on the sub-surface cross-section. As FIB-sectioning approached the corner of the central region, a lateral crack was observed (Fig. 6.7(b)) to branch from near the top of the radial crack emanating outward to the trench wall at an angle of 35° and a maximum depth of ~ 15 μm. Further into the central zone, the lateral crack and the radial crack disconnected from the surface with the lateral crack extending further to the left and becoming almost parallel to the surface at a maximum depth of ~ 18 μm; the radial crack was now observed to begin ~ 13 μm beneath the surface as seen in Fig. 6.7(c), therefore making it a half-penny crack. As sectioning continued towards the centre of the star, the lateral cracking dissipated and the half-penny crack separated in to two half-penny cracks (Fig. 6.7(d)) in a similar way to Fig. 6.6(c) for SNA-1. It is important to note that cracks appearing to separate when viewed on the SEM imaged cross-section does not indicate that this was the sequence of cracking, i.e. one crack formed and then subsequently split in to two cracks. It may be that two separate cracks propagated into the centre from different directions and then converged. The furthest right half-penny crack progressively moved further right and intersected with the top-right surface radial crack seen in Fig. 6.7(a), with the left half-penny crack dissipating upon reaching the far-end of the central zone without re-joining with the surface. The deepest half-penny crack observed started at a depth of ~ 40 μm and extended down to the trench bottom at ~ 48 μm. Radial cracking that intersected the surface appeared as FIB-milling reached the surface radial crack near the top of Fig. 6.7(a), although it had a decreased crack width in comparison to the radial crack observed previously in the sectioning process. Regions of shallow micro-cracking (< 5 μm depth) were observed on the sub-surface as the pitted regions bordering the central zone were milled through. These were significantly more prominent for SNA-2 in comparison to SNA-1 where minimal micro-cracking was observed.

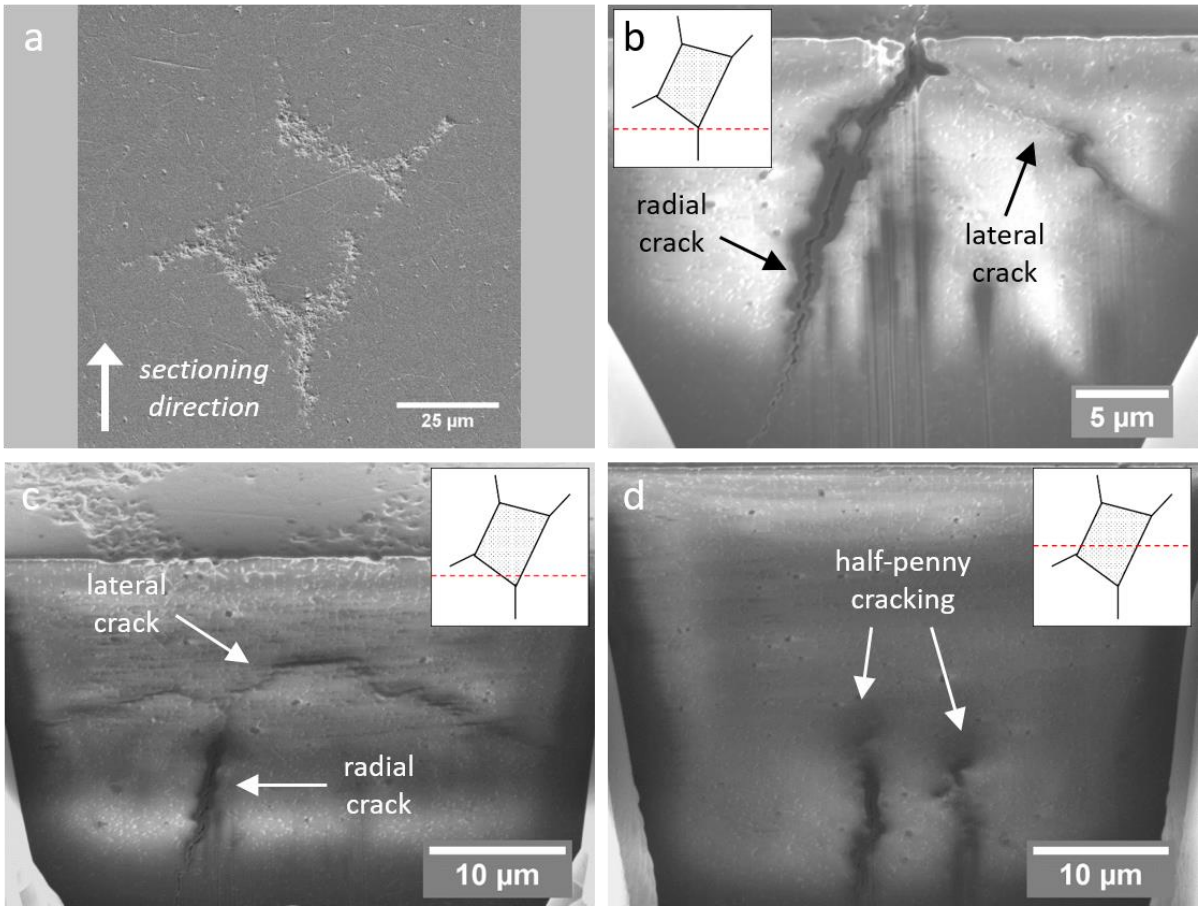

Figure 6.7: (a) An SEM image of the SNA-2 star giving the direction of FIB-sectioning. Images (b)-(d) are SEM images of the FIB-milled cross-sections at different locations through SNA-2: (b) On approach to the central zone corner showing a lateral crack branching from a radial crack (arrowed). (c) Located just within the central zone where the radial cracking has disconnected from the surface and lateral cracking extended. (d) Half-way through the central region two half-penny cracks are observed. Again, the insets are schematics of the star with the red dashed line showing the location of the SEM cross-section image relative to the star.

6.4.3. FIB-Sectioning of SNB-3

The SNB-3 sample is different to the previous M1 stars in that the UV fluorescence image of it in Fig. 6.2(b) shows that there is lateral cracking beneath the surface, so this will be a point of interest in the FIB-sectioning. In addition to this, in the SEM image of the star shown in Fig. 6.8(a), the cracking was difficult to resolve except at high magnifications and even then, the crack widths were small. Therefore, ensuring the correct orientation of the star to line up with the area of interest (in this case the lateral cracking) was non-trivial.

FIB-sectioning of SNB-3 was carried out towards the tip of a narrow radial crack (as illustrated in the insets in Fig. 6.8). As the radial crack was reached, a shallow radial crack was observed on the FIB-milled cross-section at a maximum depth of ~ 12 µm.

However, this crack soon disappeared, and the radial crack seen in Fig. 6.8(b) appeared to the left of the cross-section as FIB-sectioning reached a second surface radial crack. As milling progressed through the central zone, the radial crack moved across the sub-surface to the right (arrowed) and subsequently detached from the surface to become a half-penny crack which started ~ 15 μm beneath the surface and extended downward to ~ 37 μm at its deepest point. It continued to progress towards the right and re-attached to the surface plane where a surface radial crack was observed (the furthest right crack illustrated in Fig. 6.8 insets and in the UV image of SNB-3). At the location where the UV fluorescence image revealed the likely presence of lateral cracking, a lateral crack with narrow crack width of < 150 nm was observed intersecting with the surface and extending out to the trench wall with an angle of ~ 30° and maximum depth ~ 9 μm. Shallow sub-surface micro-cracking was also observed in the region surrounding the lateral crack. The lateral cracking remained visible on the sub-surface until FIB-sectioning reached the end of the central zone. Although in the UV image of SNA-3 a radial crack was observed emanating from the end of the central zone, no evidence of this was observed with the resolution used on the sub-surface when this area was FIB-milled.

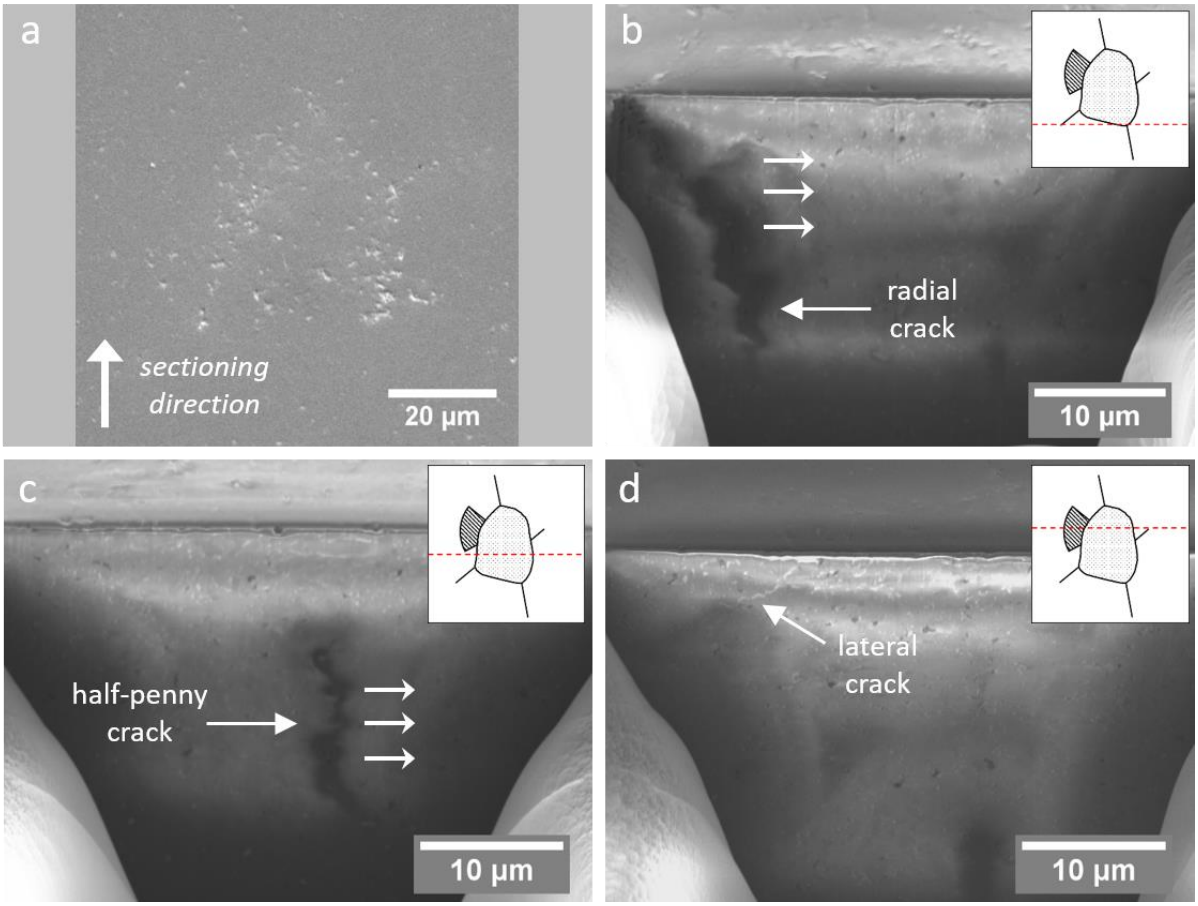

Figure 6.8: (a) An SEM image of the SNB-3 star giving the direction of FIB-sectioning. Images (b)-(d) are SEM images of the FIB-milled cross-sections at different locations through SNB-3: (b) On approach to the central zone corner the left-hand surface radial appeared in the sub-surface and gradually moved right (arrows give movement direction). (c) The radial crack in (b) disconnected from the surface and became a half-penny crack. (d) Lateral cracking (arrowed) was observed when sectioning through the region where lateral cracking was seen in the UV images. In the inset schematics, lateral cracking observed in the UV images is illustrated with the dashed pattern.

6.5. Surface Characterisation of Morphology 2 Stars

6.5.1. Optical and UV Imaging of M2 Stars

The M2 star features are different in morphology to the M1 features investigated above as they have regions of missing material which may indicate they have undergone different tribological processes to M1 stars. The two M2 stars chosen for investigation, labelled here as SNA-4 and SNA-5, are shown in Fig. 6.9 which gives optical bright and dark field images (Fig. 6.9(a & b)) of the stars as well as the UV fluorescence images (Fig. 6.9(c)).

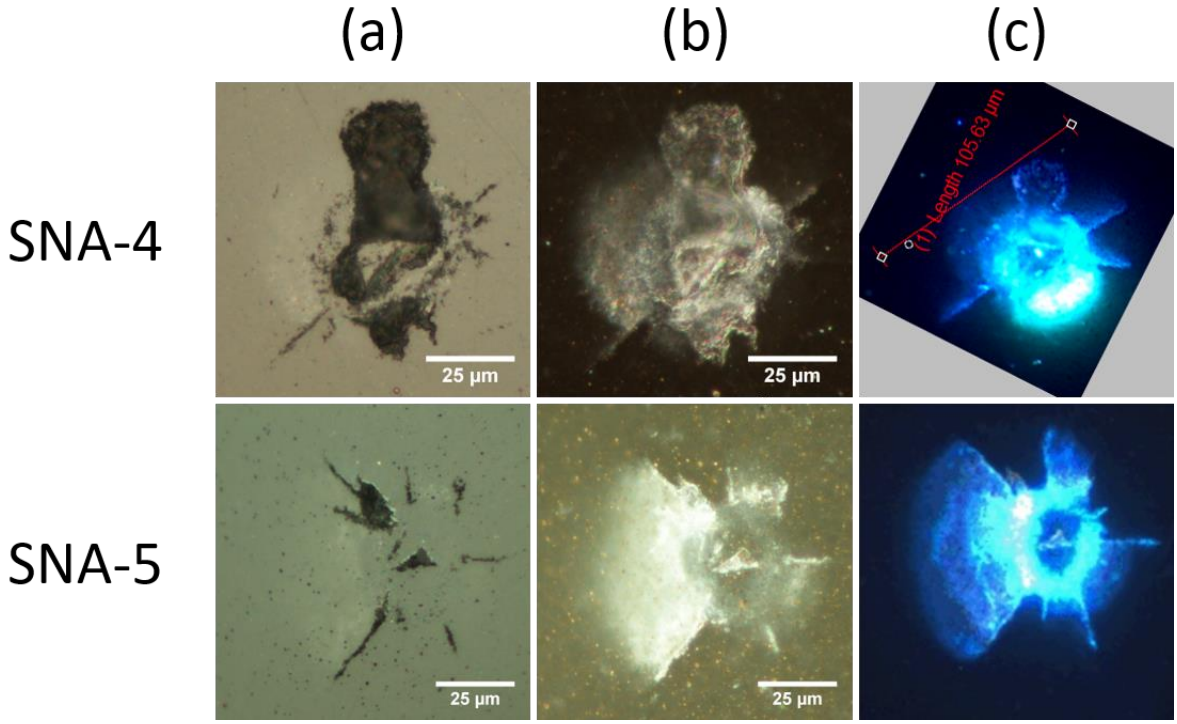

Figure 6.9: (a), (b), and (c) give optical bright field, dark field and UV fluorescence optical images respectively of the Morphology 2 type stars SNA-4 and SNA-5. The UV fluorescence images used in (b) have been used and edited with permission from the industrial sponsor.

There is a large region of spalling present at the top of the SNA-4 star in addition to further regions of missing material near the centre (darker contrast, Fig. 6.9). From the bright field image, it is hard to determine if lateral cracking is present, however, in the dark field and UV fluorescence images a large lateral crack is observed to the left of the star extending outward to a distance of ~ 37 µm and ~ 45 µm from the centre respectively. Adjacent to the lateral crack at the bottom left of all the images is a radial crack emanating from the central zone at a 45° angle relative to the image orientation; the lateral crack does not appear to extend out to the tip of this radial crack. The SNA-5 star is similar to the SNA-4 star as it also has a lateral crack (left) extending outward from the central region (to ~ 58 µm) which was only observable under dark field and UV fluorescence microscopy. However, the lateral crack on the SNA-5 star is located between two surface radial cracks, and the lateral cracking extends out to the tips of both radial cracks. The central zone is unique relative to the other star features imaged in that it shows a small triangular-shaped region of removed material in the middle surrounded by a relatively non-damaged zone from which all observed cracking emanates.

6.5.2. 3D Optical Profilometry of M2 Stars

Topographic line plots of the M2 star features SNA-4 and SNA-5, as well as their topographic profiles (inset) are given in Fig. 6.10 and Fig. 6.11 respectively. The SNA-4 star line profile is similar to that of the Vickers indentation investigated in Chapter 4 (and that shown in Fig. 6.5(b)) with the central indentation zone surrounded by a region of uplift. The measurements across the line plot show the maximum uplift to be ~ 0.8 µm adjacent to the central impression with the height decreasing with distance from the centre. The deepest point measured in the central impression across the line plot was ~ 4.5 µm deep. No uplift or depression relative to the surrounding regions was seen where the lateral crack (approximate location labelled in the inset) was observed via the dark field/UV fluorescence imaging.

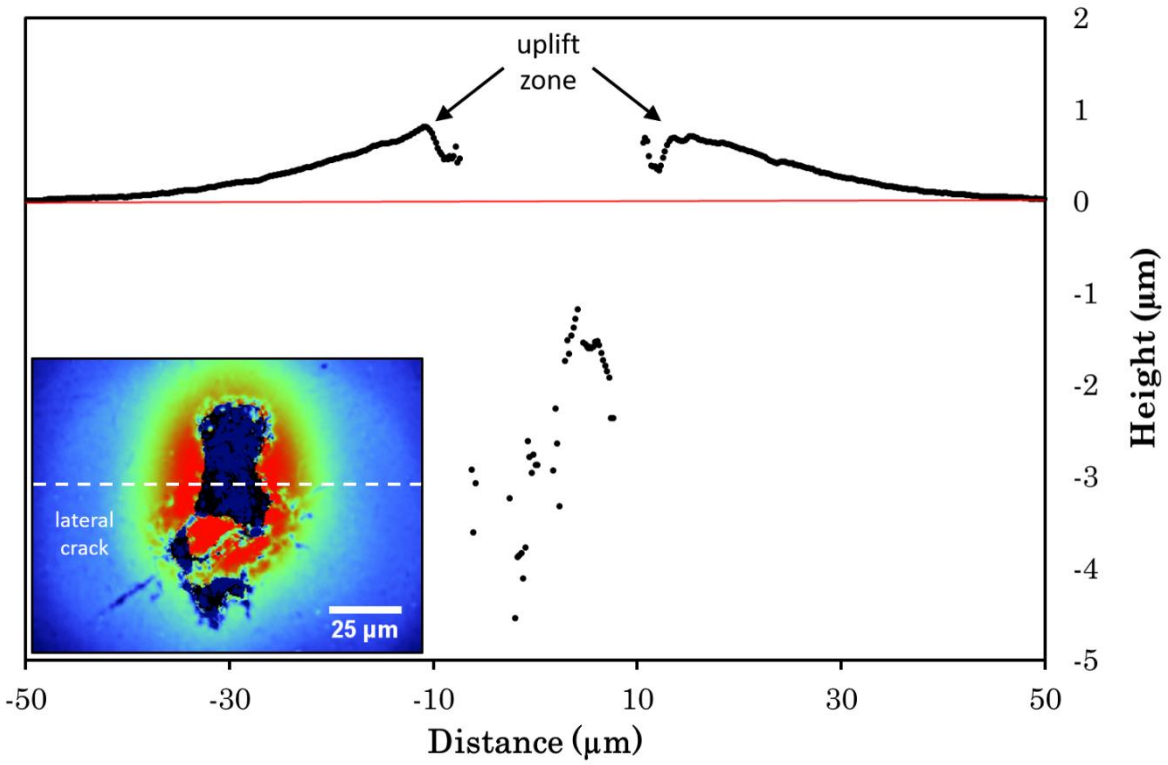

Figure 6.10: A topographic line plot across the SNA-4 star showing a central depression surrounded by an uplift zone. Inset is the height profile of the star where red and blue regions are above and below the average surface height respectively. The region where the lateral cracking was observed in the dark field images is labelled.

The SNA-5 topographic profile (Fig. 6.11 inset) shows an uplift area in the central zone with a slight depression which was measured at ~ 0.2 µm deep where the central impression is. An important feature to note is the presence of raised zones (arrowed) that are located on just one side of the surface cracks and then drop off on the adjacent side;

these had an associated uplift of ~ 0.2 μm. This is also seen in the line plot (arrowed) where the uplift increases to ~ 0.5 μm adjacent to the central zone and sharply drops back down to ~ 0.1 μm beneath the surface height. From the dark field/UV fluorescence images it is known that there is a lateral crack to the left of these raised zones adjacent to the surface cracking, however, the raised zones supply further evidence of this as lateral cracks often cause material displacement in the surface plane [2]. These raised zones were also seen to be present around the lateral crack on the 5 kg Vickers indentation shown in Fig. 6.5(b). The central region surrounded by the surface cracking generally had an uplift of ~ 0.1 – 0.2 μm.

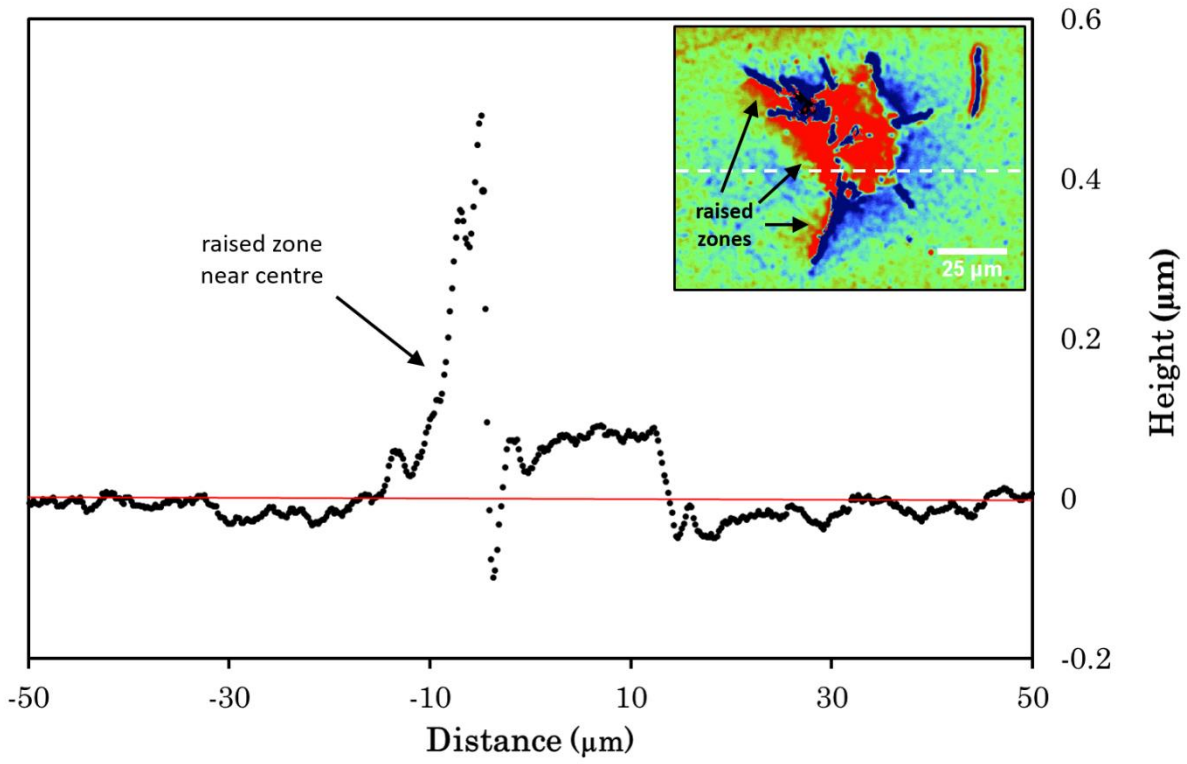

Figure 6.11: A topographic line plot across the SNA-5 star showing an uplift zone at the centre. Inset is the height profile of the star where red and blue regions are above and below the average surface height respectively. Raised zones at the edge of where lateral cracking was observed in the dark field image are arrowed.

All four of the stars analysed using the optical profilometry have exhibited regions of uplift (relative to the surrounding topography) primarily in the central zone, with the exception of SNA-4 where uplift was observed surrounding a central indentation. Ball-bearings are required to have a high surface smoothness so deviations from this will inevitably affect the tribological properties and hence their efficiency during service. Additionally, it is important in how the stars could evolve further due to their

topographical profile, particularly for the M2 stars which exhibited a greater magnitude of uplift in addition to lateral cracking. For example, under contact pressure during service, the uplift zones may be the first point of contact, such as in SNA-5 where there is uplift associated with the lateral cracking. Studies on similar zones by Hadfield and Wang found that, under high contact pressure, flaking of the lateral cracking region may be possible [3]–[5].

6.6. FIB Tomography of Morphology 2 Stars

For the two M2 stars, FIB-sectioning was only undertaken in the regions surrounding the large lateral cracks, not through the whole of the star like in the M1 star features. This was for two reasons: Firstly, the M2 stars cover a larger area than the M1 stars making it impractical to FIB-mill the whole star due to both the time required (the sectioning time for each M1 star was already > 4 days) and additional complications such as significant material redeposition. Secondly, as discussed in Chapter 2, lateral cracking are potential initiation points for material removal via spalling, so it is important that they are investigated in great detail, to ensure that the majority of the lateral crack is encompassed within the FIB sectioning.

6.6.1. FIB-Sectioning of SNA-4

The priority of the FIB-sectioning of SNA-4 was to mill through the large lateral crack visible to the left in the UV fluorescence and dark field optical images in Fig. 6.9. A schematic of the FIB-milled trench width and location relative to the star is given as the black dashed line in the insets of Fig. 6.12. The sectioning direction (shown in Fig. 6.12(a)) was at a 45° angle towards the radial crack adjacent to the lateral crack. Sub-surface radial cracking appeared as FIB-sectioning reached the tip of the surface radial crack; there was no propagation of the surface radial crack towards the trench. As FIB-milling progressed, the radial crack moved along the cross-section to the right and lateral cracking appeared to the right of the trench (Fig. 6.12(b)). This lateral cracking had a depth of ~ 10 μm and split in to two branches to intersect the surface at a location where surface cracking was observed, and at a region where there was missing material. On approach to the region where the extensive lateral cracking was observed in the dark field/UV images, lateral cracking appeared emanating from the sub-surface radial crack

at a depth of ~ 3 μm near-parallel to the surface plane as seen in Fig. 6.12(c). The sub-surface radial disconnected from the surface as the associated surface radial was milled through and was no longer observed soon after. The large lateral was observed throughout the whole sectioning and reached a maximum depth of ~ 10 μm, and it was also observed to intersect with the surface at a region where there had been significant material removal. On milling through the spalled area, significant zones of shallow micro-cracking were observed just below the spalled region. In addition to the large lateral crack, several smaller lateral cracks were also observed to the right-hand side of the milled cross-section, one of which is arrowed in Fig. 6.12(d). These smaller laterals were located adjacent to areas where material had been removed and were observed at depths of up to ~ 15 μm.

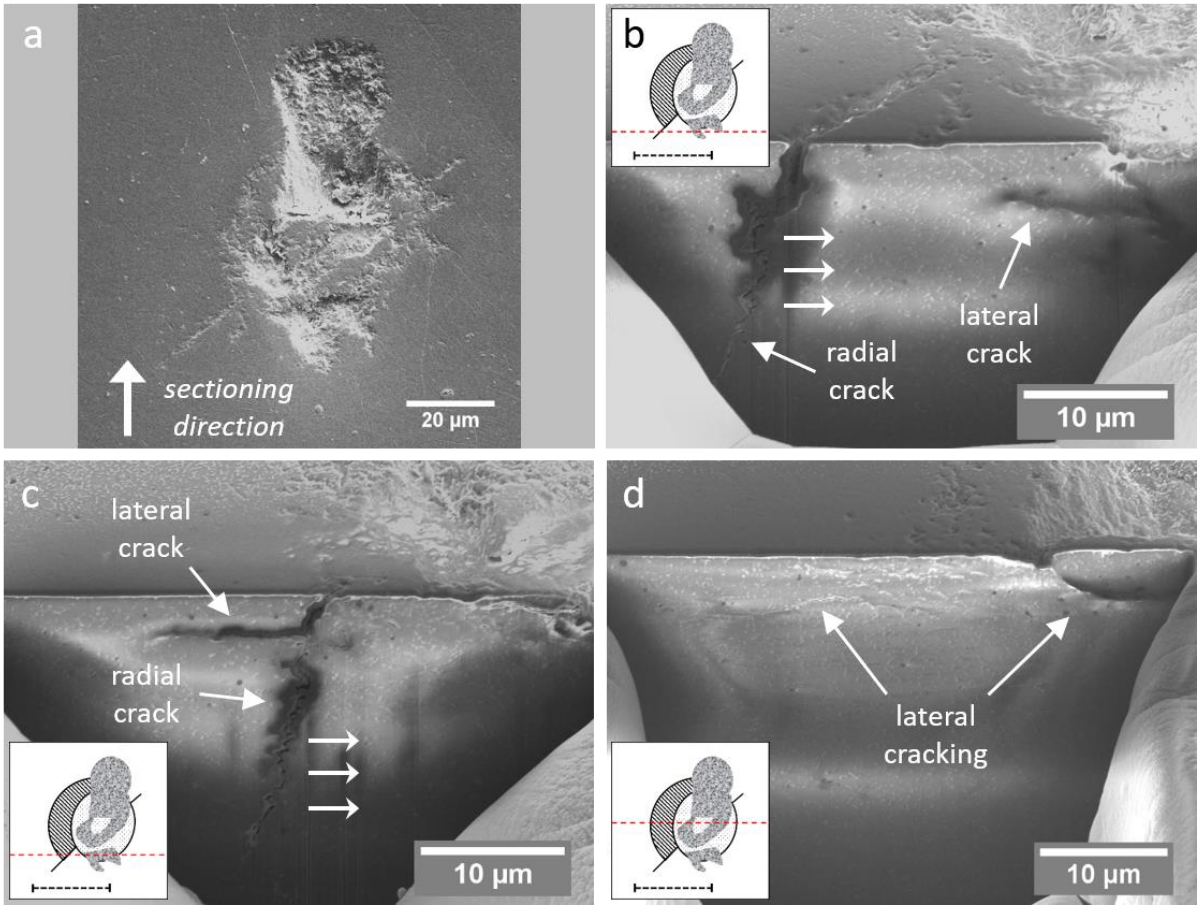

Figure 6.12: (a) An SEM image of the SNA-4 star giving the direction of FIB-sectioning. Images (b)-(d) are SEM images of the FIB-milled cross-sections at different locations through SNA-4: (b) Radial cracking correlated with the surface radial (arrows give movement direction) and lateral cracking was observed adjacent to a region of missing material. (c) The primary lateral crack appeared connected to the radial crack. (d). Again, lateral cracking was observed adjacent to a region of missing material (right arrow). In the inset schematics, areas of material removal are represented by the anisotropic black and white pattern, and the black dashed line (bottom) gives the width of the FIB-milled trench.

6.6.2. FIB-Sectioning of SNA-5

The FIB-sectioning of SNA-5 was conducted in a similar way to SNA-4 in that the priority was to investigate the large lateral crack observed emanating from the left-hand side of the central zone as seen in the dark field and UV images (Fig. 6.9). However, for the sectioning, the FIB-milled trench was moved further to the left to ensure that the tips of the lateral cracking were observed on the sub-surface cross-section. This is because in the previous mill of SNA-4, the large lateral crack tip nearly extended out of the trench wall, and if it had done so, the distance of the lateral crack from the centre of the star, an important dimension, could not have been accurately determined.

Unlike in SNA-4, the surface SEM images of SNA-5 gave an indication that lateral cracking was present beneath the surface. Fig. 6.13(b) is a high magnification image of the arrowed crack (L) in Fig. 6.13(a) taken at a tilt angle of 52°, i.e. the same angle used for imaging the FIB-milled cross-sections. At this angle, the crack opening would not be expected to be observable if it was a radial crack, however, here the crack opening and a ridge-like feature are visible - which implies that the crack is intersecting the surface at a shallow angle; a characteristic of lateral cracking. During the FIB-sectioning, the lateral cracking was observed on the sub-surface with a downward angle of 30° at the point at which sectioning reached the tip of the surface crack. As milling progressed, the lateral crack extended out further from the trench wall and was observed to reach a maximum depth of ~ 14 μm at the maximum outward extension (Fig. 6.13(c)). In Fig. 6.13(d) an additional lateral (top) crack is observed branching from the primary lateral (bottom) crack extending towards the surface. The appearance of this secondary lateral crack correlated with the sectioning of a small surface crack (as illustrated in the inset). This secondary lateral crack disappeared shortly after and the primary lateral crack was then seen to decrease in length and depth until it was no longer visible on approach to the uppermost surface crack seen in Fig. 6.13(a). Minimal micro-cracking was observed for the SNA-5 star, this is likely due to the localised nature of the FIB-sectioning, i.e. away from the star central zone.

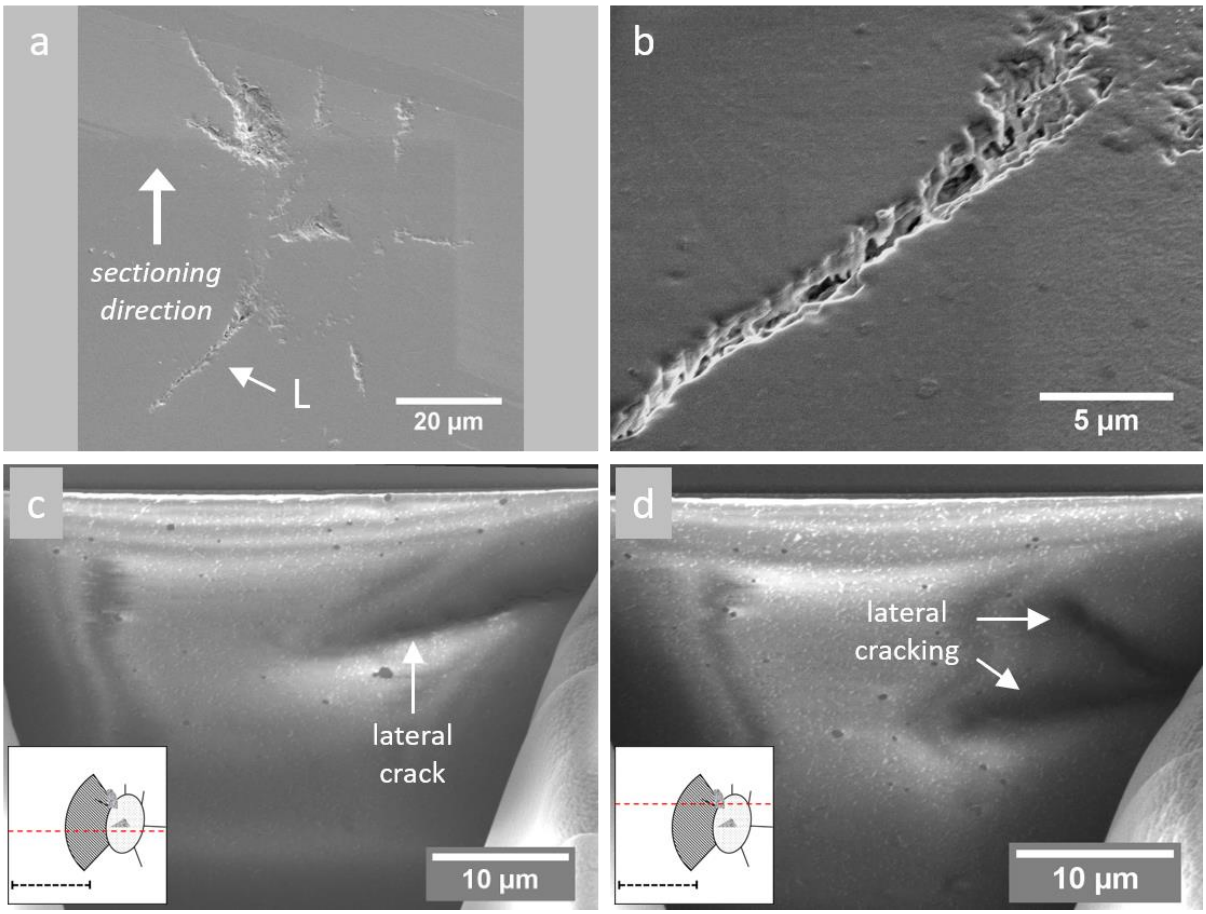

Figure 6.13: (a) An SEM image of the SNA-5 star giving the direction of FIB-sectioning and the location of the edge of lateral crack, L. (b) A higher magnification image of the lateral crack, L, taken at a tilt angle of 52°. The morphology of the crack opening gives an indication of its lateral nature. (c) 2D FIB-cross-section showing the primary lateral crack at the mid-point of the sectioning (arrowed). (d) Appearance of a second lateral branching from the primary lateral as sectioning passed through a surface radial.

6.7. 3D Analysis and Discussion of Morphology 1 Stars

As with the Vickers indentations in Chapter 5, the 2D cross-sections obtained using the FIB-SEM microscope were collated together and cracking visible on the milled cross-sections was traced using the IMOD software. These were then used to produce a 3D tomographic reconstruction of the cracking occurring sub-surface of the Morphology 1 stars using meshing tools within the software.

6.7.1. SNA-1 3D Crack Reconstruction

In Fig. 6.14 (a) the 3D reconstruction of the SNA-1 star feature is shown overlaid onto an SEM image of the surface of the star at a tilt angle of 52°; the inset has the reconstruction

on a top-down image of the star. It can be seen that the sub-surface cracking correlates closely to the observed surface cracking with the border regions surrounding the central zone having cracks directly beneath (the blue cracking). The primary radial crack (red) also follows the location of the surface cracking but, as can be seen from Fig. 6.14(b) (which shows a side view of the 3D reconstruction), disconnects from the surface and continues beneath the central plastic deformation zone where it dissipates. There are similarities with this cracking and the half-penny cracking observed in the Vickers indentations, although the cracking here does not have the same symmetry to it, i.e. it does not appear to re-connect to the surface after the plastic deformation zone. However, the steep lateral cracks arrowed in Fig. 6.14 do get nearer to intersecting the surface and may be connected with the primary radial crack (as it appears so on the surface). Again, as with the Vickers indentations, the region represented by the dashed arc in Fig. 6.14(a)) into which minimal cracking enters (due to increased compressive stress), can be used to estimate the volume of the compressively stressed zone [1]. The volume was approximated to be ~ 3,500 μm^3 (in the same way as for the indentations in Chapter 5), by assuming the compressively stressed zone has the geometry of a semi-ellipsoid. The maximum diameter of the compressively stressed central zone measured from the surface SEM images was ~ 25 µm, but the diameter of the compressively stressed central zone measured from the crack maps, i.e. the diameter of the dashed arc, was ~ 45 µm.

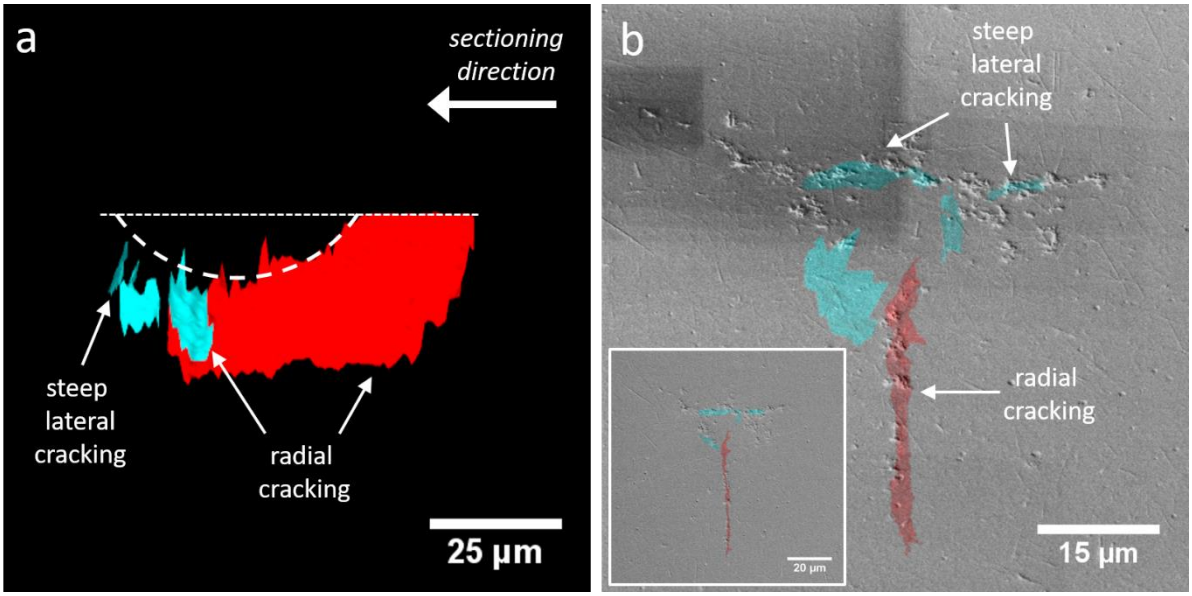

Figure 6.14: The 3D reconstruction of SNA-1: (a) A side view of the reconstruction, the dotted line gives the location of the surface plane and the dashed line is the proposed region of compressive stress. (b) The 3D reconstruction overlaid on to an SEM image of SNA-1 at a tilt angle of 52°: the inset gives a top-down view of the reconstruction on an SEM image. Lateral and radial cracks are arrowed. The primary radial crack is coloured red and additional cracking is coloured blue.

The lateral cracks shown in Fig. 6.14 can be seen to have a steep angle relative to surface plane and do not extend a significant distance outward from the star; they may be better described as an amalgam of radial and lateral cracking, in particular when compared to the lateral cracking observed in the 3D crack maps of the Vickers indentations (Chapter 5). Lateral cracking is often an initiation point for material removal so the lack of prominence in SNA-1 may imply that under rolling contact similar features may be resistant to further material removal. However, as has been discussed in Chapter 2.3.3., even line features (radial cracks) have been found to be initiation points for further cracking as secondary lateral cracks branch from the initial radial crack and subsequently intersect with the surface leading to spalling [5]–[7].

6.7.2. SNA-2 3D Crack Reconstruction

The 3D reconstruction of the cracks visible in the SNA-2 FIB-sectioning is given in Fig. 6.15, and the cracks are again shown overlaid onto SEM images at 52° (a) and top-down (b), in addition to the side view (c). As has been mentioned before, the SNA-2 star showed similarities in its surface features to a Vickers indentation, i.e. the central plastic deformation zone with four radials emanating out from the corners. This similarity appears to have continued to the sub-surface morphology of cracking regime with half-penny cracking observed (arrowed in Fig. 6.15(b & c)) beneath the plastic deformation zone and lateral cracking (arrowed) appearing near the border of this zone. However, the half-penny cracking does not exhibit the same symmetry as the Vickers indentations sectioned and instead intersects the surface at both the radial crack opposite the first radial crack sectioned, and at the radial crack in the top right corner of Fig. 6.15(b). Again, the half-penny cracking (maximum initiation depth of ~ 40 μm) traces the transition zone between tensile stress, where the cracking occurs, and the compressively stressed zone (dashed line Fig. 6.15(c)). By using this information, the volume of the compressively stressed plastic deformation zone was calculated as ~ 22,000 μm^3.

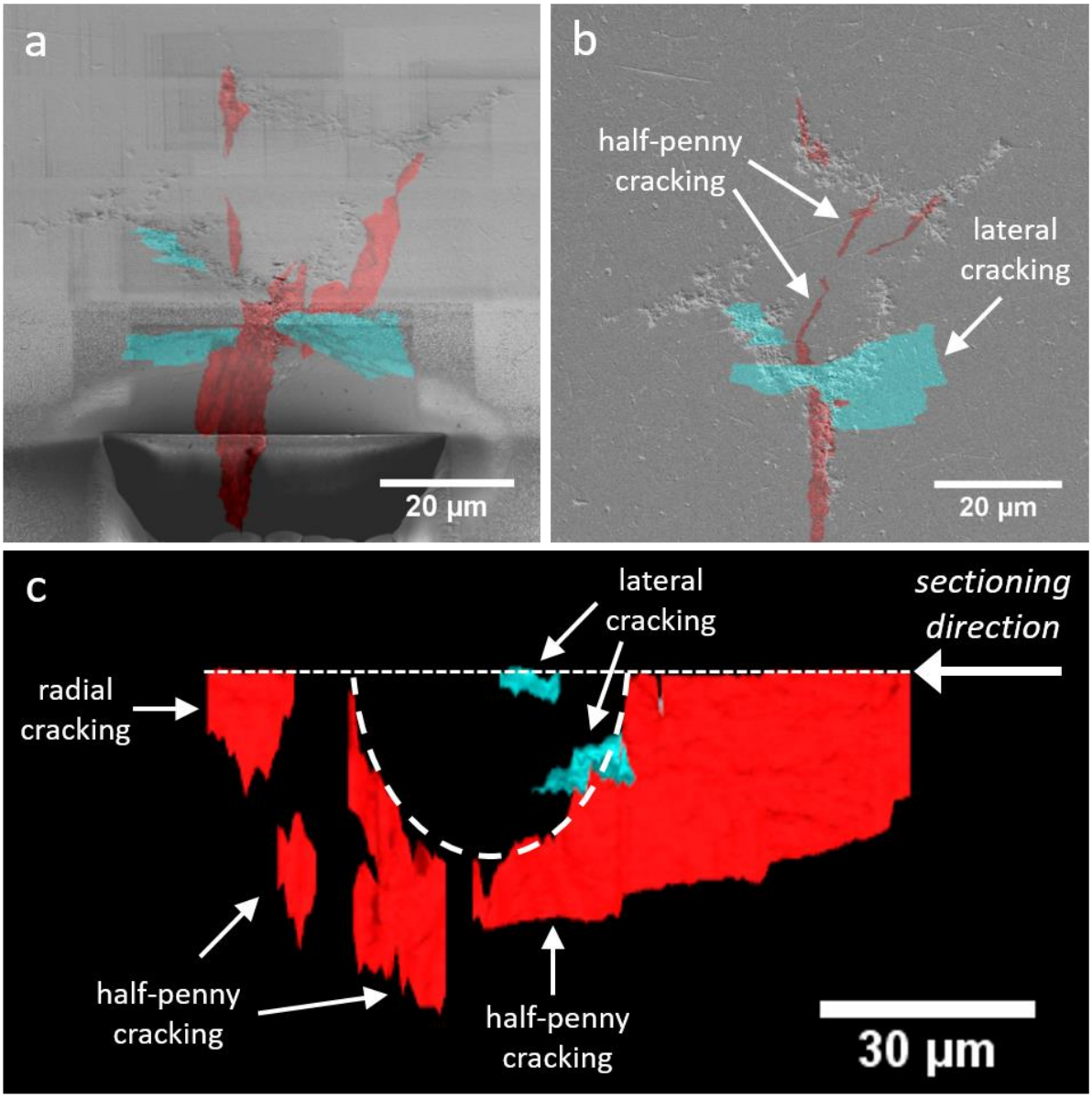

Figure 6.15: The 3D reconstruction of SNA-2: (a) Overlaid onto an SEM image at a tilt angle of 52°. (b) A top-down view of the reconstruction (on an SEM image of SNA-2) showing the location of half-penny and lateral cracking (arrowed). (c) A side view of the reconstruction showing the region of high compressive stress (dashed line) and the identified crack morphologies (arrowed).

The lateral cracking in SNA-2 is near parallel to the surface and occurs at a maximum depth of ~ 19 µm. As is clear in Fig. 6.15(c), there is also shallower lateral cracking which was located underneath a region of micro-cracking on the surface. Interestingly, and unlike in SNA-1, none of the lateral cracking observed via the FIB-sectioning was visible in the UV fluorescence images of SNA-2. This may be due to the FIB-related phenomena discussed previously [8]–[10] such as the change in residual stress caused by the opening of a new free surface which leads to crack closing/opening, or it could be poor/incomplete

saturation of the cracks (especially lateral cracking which has no visible intersections with the surface here) with the fluorescence dye [11]. Alternatively, it could be that the lateral crack depth is greater than the optical attenuation of the fluorescence through the silicon nitride so the light emission does not reach the surface and is hence not detected; this could also explain the absence of the half-penny cracking in the UV fluorescence image. The presence of the lateral cracks is a concern for how the star could evolve when put under localised applied pressure, even more so because there was no indication of their existence from the surface images. Shallow lateral cracking observed here could undergo spalling, but it is the deeper lateral cracking in combination with the half-penny cracking surrounding the plastic deformation zone which would contribute to significant material removal in operational conditions, even if the deep lateral currently have no intersection with the surface plane [5], [6].

6.7.3. SNB-3 3D Crack Reconstruction

The SNB-3 star was different to the other Morphology 1 stars investigated in that lateral cracking was observed in the UV fluorescence image of the star. Fig. 6.16 shows the 3D reconstruction of the FIB-sectioning in various formats, as well as the UV fluorescence image (Fig. 6.16(c)) in order to compare the cracking observed using the two methods. The half-penny cracking observed and arrowed in Fig. 6.16(b & d) is of interest as it was not related to the first radial crack that was sectioned through, i.e. R_1 in Fig. 6.16. In fact, the first radial crack (R_1) can be seen from Fig. 6.10(b) to be shallow (~ 12 μm) and of minimal length in comparison to the half-penny crack that was angled ~ 35° relative to the FIB-sectioned trench. The radial crack opposite the first radial crack (top of Fig. 6.16(c) labelled R_2) was not observed during the FIB-sectioning; this was probably due to crack closure as a result of the FIB-sectioning of the compressive/tensile stressed plastic deformation zone (as observed for the second-half of Vickers indentations in Chapter 5). The half-penny crack, as with the other M1 stars, was not observed in the UV fluorescence images, however, its location is represented in Fig. 6.16(c) with the dashed line. The compressively stressed zone here has been estimated to have a volume of ~ 8,000 μm^3 (maximum depth of ~ 15 μm). Only a single lateral crack was observed for SNB-3 and has been labelled L in Fig. 6.10. When comparing the lateral crack in Fig. 6.16(c & d) it can be seen that its location showed good correlation between the UV fluorescence and FIB-sectioning methods. A decrease in fluorescence brightness of the lateral crack with

increasing distance from the star centre also matches up with an increase in lateral crack depth with distance from the star centre. However, the full extension outward of the lateral crack for FIB-sectioning was obstructed by the FIB trench wall.

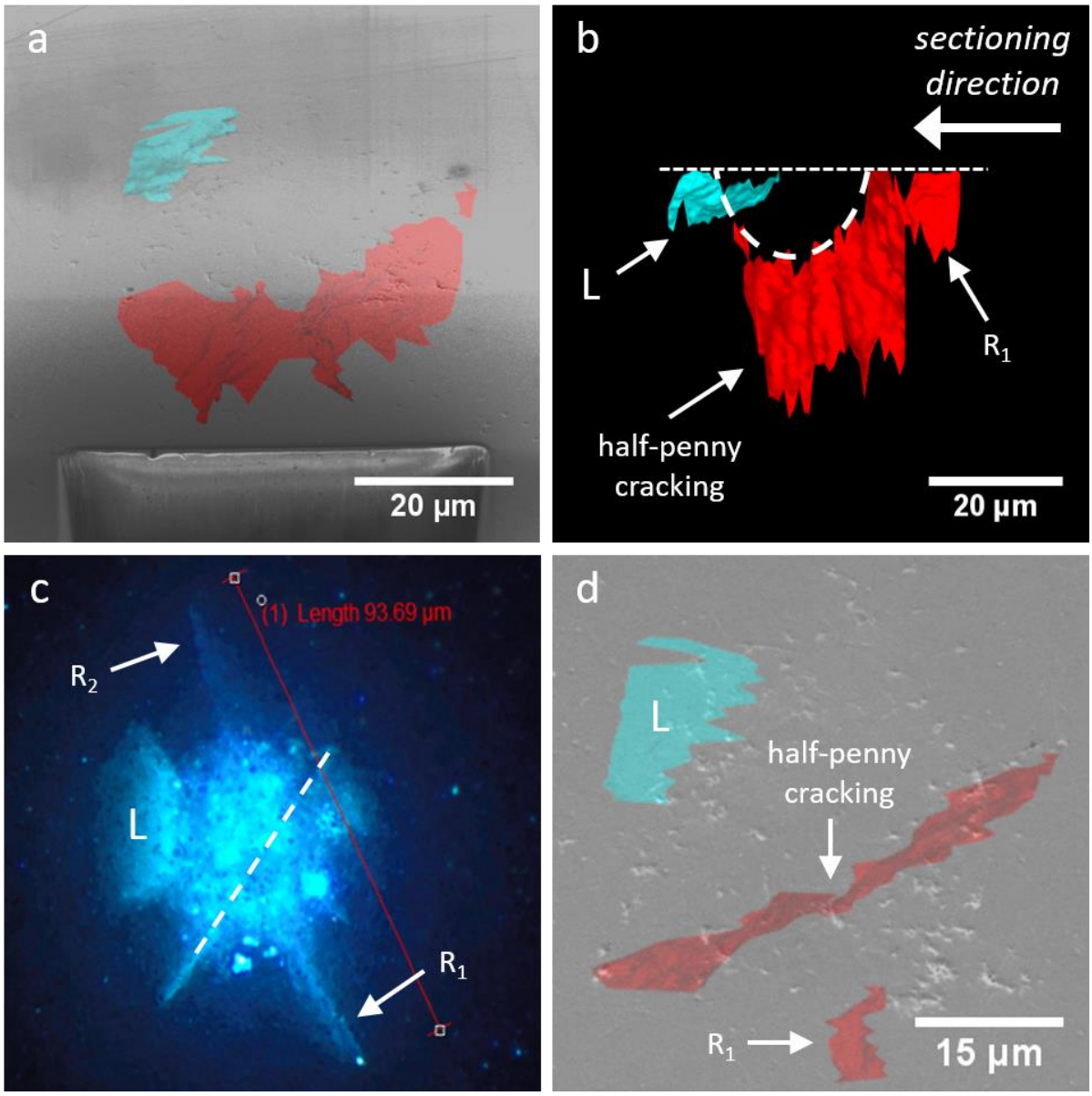

Figure 6.16: The 3D reconstruction of SNB-3: (a) Overlaid onto an SEM image at a tilt angle of 52°. (b) A side view of the reconstruction with the lateral crack seen on the UV image labelled, L. Half-penny and radial cracking (R_1) has also been arrowed with the proposed plastic deformation region outlined by the dashed line. (c) The UV fluorescence image of the star with the cracking observed during FIB-milling labelled: the dashed line shows the location of the half-penny crack, the lateral crack is again labelled L, the radial cracking (R_1 and R_2) is arrowed. (d) A top-down view of the reconstruction with the observed cracks labelled in the same way they were in (c) so that a comparison can be made. The UV fluorescence image used in (c) has been used and edited with permission from the industrial sponsor.

6.8. 3D Analysis and Discussion of Morphology 2 Stars

The priority with the Morphology 2 star features was to map the largest lateral cracks that were observed in the UV fluorescence images. Since the Morphology 2 stars (and the lateral cracks) were large in comparison to the Morphology 1 stars and Vickers indentations, only regions of interest were FIB-sectioned and hence only regions of interest have been reconstructed in to 3D crack maps using IMOD software.

6.8.1. SNA-4 3D Crack Reconstruction

The 3D reconstructions of the SNA-4 star cracks are shown in Fig. 6.17(a, b, c) along with the dark field image showing the lateral crack of interest. One of the particularly interesting aspects of the SNA-4 star is the way the primary radial crack appears to connect with the primary lateral cracking, yet the lateral cracking does not extend out to the tip of the radial crack as frequently seen in Vickers indentations of high load. Although not fully sectioned, the primary radial crack does again extend beneath the plastic deformation zone implying a half-penny cracking regime is present. The lateral cracking to the right in Fig. 6.17(a) was located adjacent to areas where material had been removed but beneath material that was still present (also visible in Fig. 6.17(c)). This is important as the lateral cracking was of the same depth as the spalling, indicating that the spalling probably initiated from the same lateral cracking. Furthermore, it is most likely that all the lateral cracking observed in the 3D crack map of SNA-4 is part of a single lateral crack that has been bisected upon material removal. Fig. 6.17(c & d) show a top-down comparison of the lateral cracks in the FIB reconstruction and the optical dark field image with the distance from the centre of the star to the lateral crack tip labelled C. These distances were measured at ~ 43 μm and ~ 37 μm respectively (for the UV fluorescence image it was ~ 45 μm). The discrepancy in the measured values of C could be a result of the tip of the lateral crack extending out beyond the trench wall in the FIB-sectioning meaning the full length was not observed.

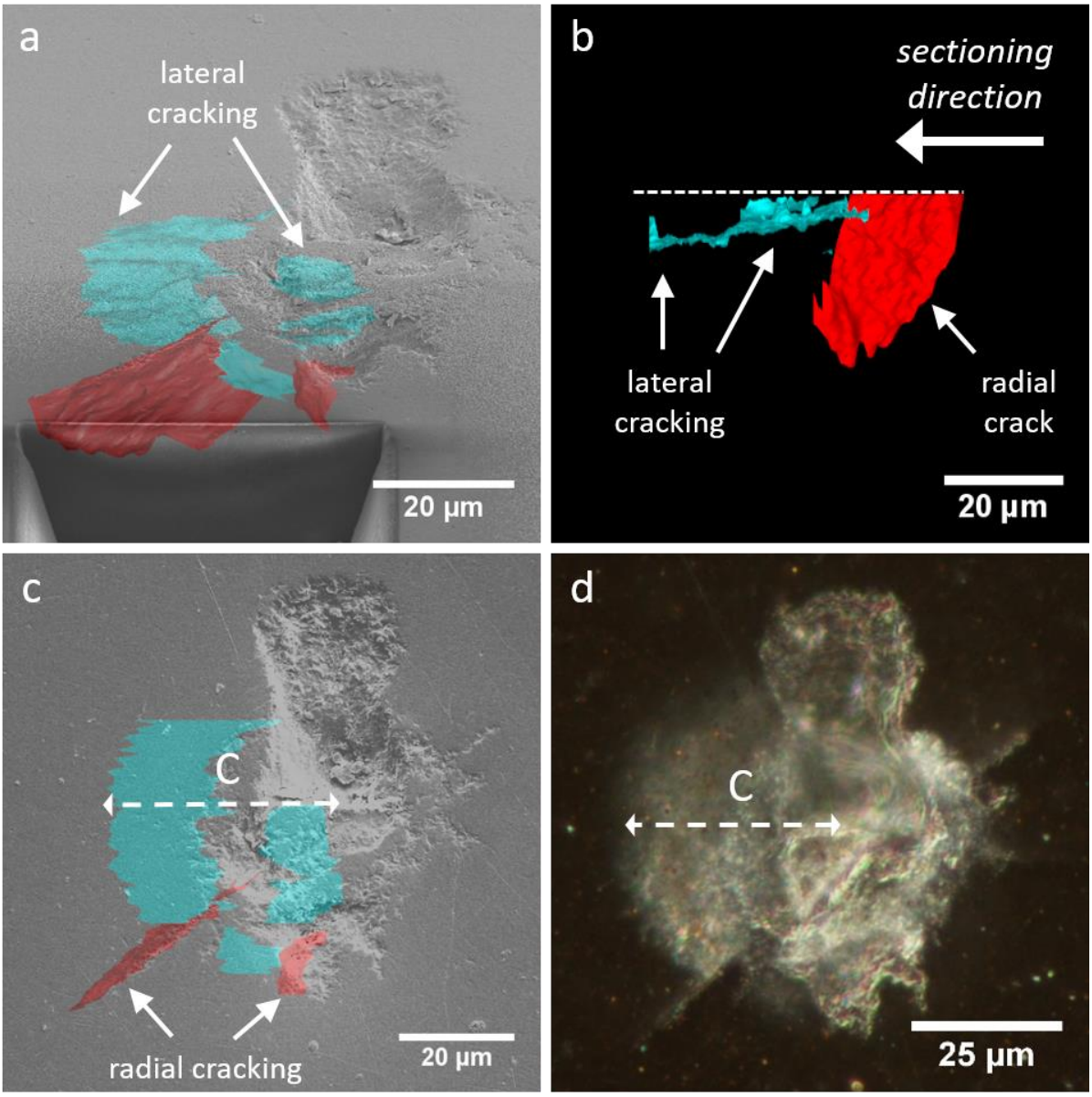

Figure 6.17: The 3D reconstruction of SNA-4: (a) Overlaid onto an SEM image at a tilt angle of 52° with lateral cracking arrowed. The radial cracking is coloured red and the lateral cracking is coloured blue. (b) A side view of the reconstruction with the lateral cracking and radial cracking arrowed. (c) Top-down view of the reconstruction overlaid onto an SEM image; C is the distance between the centre of the star and the lateral crack tip. (d) A dark field optical image of the star where the lateral cracking is visible, again, C is labelled.

6.8.2. SNA-5 3D Crack Reconstruction

In SNA-5 only the lateral crack (and none of the central plastic deformation zone/indentation) was FIB-sectioned to ensure that the lateral crack tips were visible, unlike for SNA-4. In Fig. 6.18 two lateral cracks are visible; the primary lateral crack with a maximum depth of ~ 14 µm and a secondary branching lateral crack which extends slightly towards the surface. Unlike in SNA-4, there was no radial cracking connected to

the lateral crack, and the primary lateral crack intersected with the surface plane at the first surface crack milled through. In addition, the concave shape of the lateral crack (Fig. 6.18(a)) suggests it would have mostly likely intersected again with the surface crack at the top of Fig. 6.18(a) as the lateral cracking can be seen to be extending towards the surface again in Fig. 6.18(b), but the surface cracking in question was not sectioned. Lateral cracking that intersects with the surface, as is the case with the primary lateral crack here, is a prime location for material removal via spalling when under rolling contact. The secondary lateral crack which was extending towards the surface could also intersect and make it more susceptible to spalling.

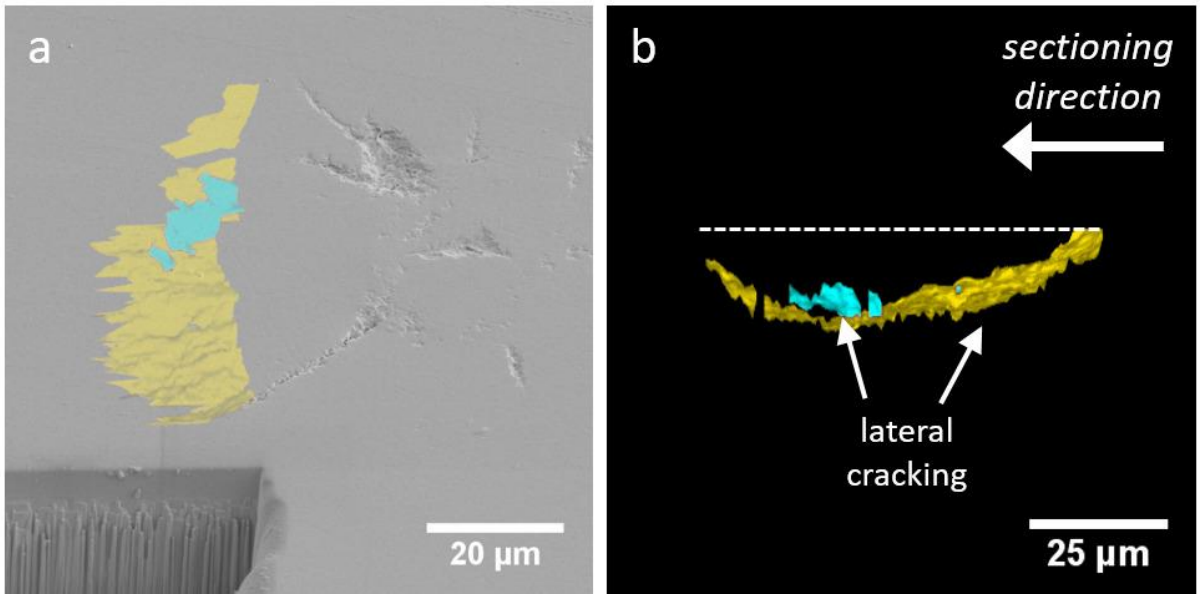

Figure 6.18: The 3D reconstruction of SNA-5: (a) Overlaid onto an SEM image at a tilt angle of 52°. (b) A side view of the reconstruction with the lateral cracking labelled. The primary lateral crack is coloured yellow and additional lateral cracks are coloured blue.

Fig. 6.19 gives a comparison between the FIB reconstruction, optical dark field, and the UV fluorescence images of SNA-5, with the lateral crack tip to star centre distance labelled C, as in Fig. 6.17. The distance, C, for each was measured as 58 µm, 55 µm and 58 µm respectively so the UV fluorescence image and the FIB-sectioning image correlate excellently with each other. This correlation also implies that the length of the lateral cracking has not been affected significantly by the FIB-sectioning process. Also, in Fig. 6.19(a & c) the two lateral cracks observed have been labelled L_1 and L_2 with L_2 in the UV fluorescence image appearing visible by the change in brightness of the fluorescence emission as a result of L_2 being shallower than L_1. L_2 probably relates to the adjacent surface crack observed in Fig. 6.19(a). The C value measured from L_2 in both images was

46 µm, again, showing good agreement between the UV fluorescence and FIB tomography methods.

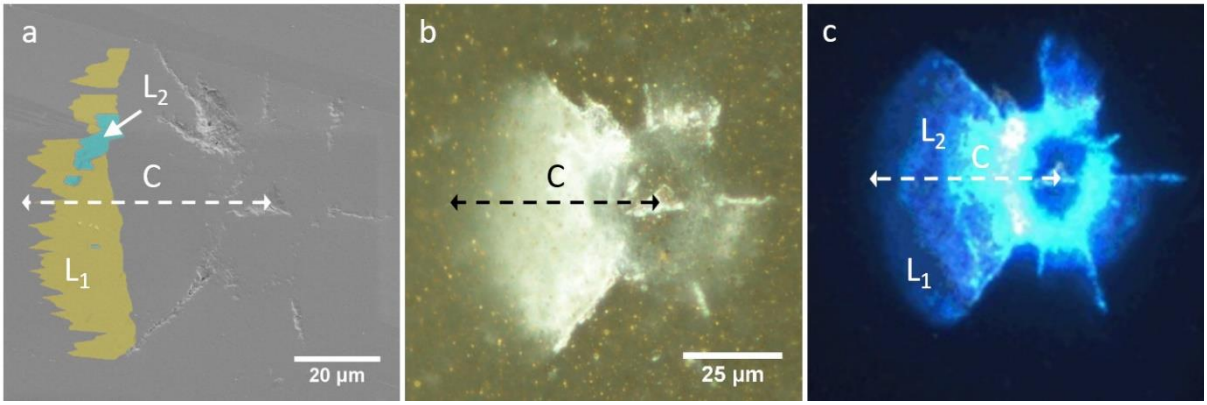

Figure 6.19: A comparison of the lateral cracks as obtained from the 3D reconstruction (a), the dark field optical imaging (b), and the UV fluorescence imaging (c). C is the measured distance from the centre of the star to the primary lateral crack tip. The L_1 and L_2 labels in (a) and (c) highlight the two different lateral cracks observed in the images.

6.9. Discussion of FIB Tomography of Star Features

6.9.1. Star Feature Formation and Evolution

The M1 and M2 stars are formed as a result of diamond particles under load indenting the ball surface during the lapping process in manufacturing (see Chapter 2 for details) [12], [13]. Therefore, their initial geometry (directly after indentation) is determined by multiple factors, e.g. size and shape of the diamond particle, angle and load of diamond indentation. As has been discussed in Chapter 2, these stars can be modelled like artificial indentations, so it can be expected that they have a similar morphology, i.e. a central indentation with associated cracking, and a sub-surface compressive stress zone [14]. However, the processes that follow the initial formation of the stars determines their current state, and hence their morphology observed here can be used to indicate what wear processes they have likely undergone. For instance, the schematic in Fig. 6.20 shows how the morphology of the indentation may change under wear either via further diamond lapping or wear during service. Fig. 6.20(a) shows the star prior to any additional wear; the presence of the compressive stress zone beneath will likely cause uplift even after indentation as stress relaxation occurs (there will also be uplift associated with the downward displacement of material caused by the indentation) [1]. After further lapping (Fig. 6.20(b)), displaced material surrounding the star will be removed along with any uplift leaving a reduced depth indentation and a surrounding central region bordered by

surface micro-cracking, e.g. like SNA-5 (Fig. 6.9). However, as is seen in the optical surface profilometry of SNA-5 (Fig. 6.11) there is still uplift in the central region implying the compressive stress zone beneath the indentation is still of sufficient magnitude for stress relaxation to be induced. Fig. 6.20(a & b) are representative of the processes undertaken by the M2 stars. Removal of the central indentation impression completely, as for all M1 stars, does not necessarily mean that the compressive stress region has been fully removed (Fig. 6.20(c)). Therefore, stress relaxation and resulting uplift can still occur; this explains the central uplift observed in the optical surface profilometry of the M1 stars and has been observed before in polishing studies of indentation by Lube [1]. The magnitude of uplift may also be indicative of the size of the compressively stressed volume.

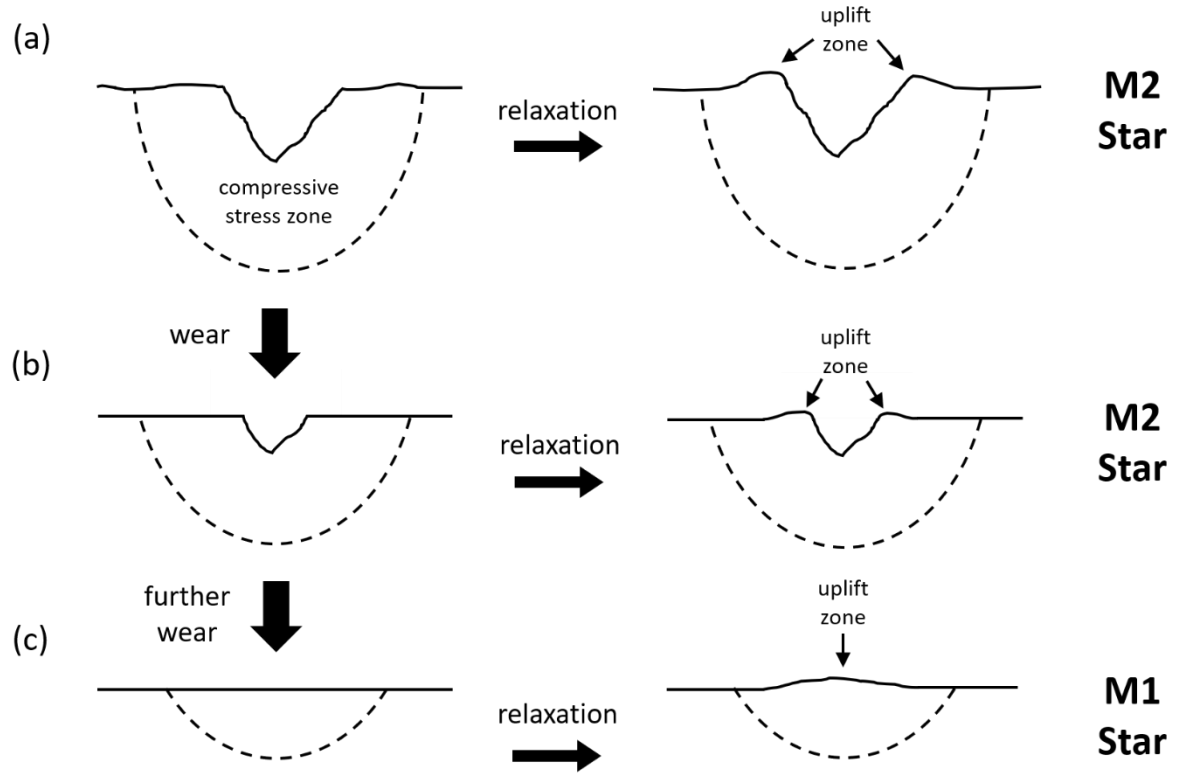

Figure 6.20: A schematic showing how star features may change with subsequent surface material removal via lapping or in service: (a) the star prior to any material removal, and (b) after some material removal. (a) and (b) represent the process undertaken by the M2 stars. (c) After the indentation impression has been fully removed, uplift can still occur if the compressive stress zone (dashed line) still exists.

The M1 stars sectioned using FIB tomography were all found to have half-penny cracking that extended beneath the plastically deformed central zone that was observed in the surface optical and SEM imaging. This is important because the half-penny cracking itself was not observed in either the surface imaging or the UV fluorescence imaging. As

mentioned previously, half-penny cracking traces around the tensile stress-compressive stress zone boundary so can be used as an indicator for the volume of this zone. From this, the star with the largest compressively stressed zone was calculated to be SNA-2. The volume of this zone does have implications for how the stars may behave under applied cyclic contact pressure, such as that during service. If significant volumes of tensile/compressive stress do exist (as observed here) then further crack propagation is possible with external changes in stress, particularly for silicon nitride where crack tips have a high stress intensity factor [15], [16]. This was observed during FIB-sectioning of SNA-2, with the primary radial crack propagating suddenly towards the milled trench as a result of the change in residual stress initiated by the FIB-milling [10], but not in SNA-1 and SNB-3, indicating that stars with a lower volume compressively stressed zone are less susceptible to further crack propagation. The perpendicular orientation of half-penny and radial cracking relative to the surface does mean that they are less likely to undergo material removal processes associated with lateral cracking (such as flaking and spalling), however, in studies by Yang and Hadfield [3], [6] of bearings under Hertzian contact pressures, radial cracking was observed to initiate secondary lateral cracks that intersect with the surface and lead to subsequent spalling.

The lateral cracking observed in SNA-2 and SNB-3 is of greater concern in relation to flaking or spalling, and the associated effect that might have on the performance of the component. In fact, on the M2 SNA-4 star, spalling is visible which potentially initiated from the lateral cracking identified. Lateral cracking that has an intersection with the surface, such as in SNB-3, are even more susceptible to material removal as the surface intersection would tend to act as compliant hinge [17]. Although, even lateral cracks with no surface contact may propagate towards the surface under applied pressure, this is more likely to occur for shallower lateral cracks.

The large M2 stars were only partially FIB-sectioned so it is not known what cracking systems (i.e. half-penny) are present beneath the central zone, and hence the extent of the compressively stressed plastic deformation zone cannot be estimated. However, the radial crack observed in SNA-4 does show some evidence that half-penny cracking may be present as it disconnects from the surface plane. This radial crack was observed to have a connection to the primary lateral crack indicating that the presence of the radial crack may influence the formation of the lateral crack [18], [19]. The lateral cracking in SNA-4 reveals information regarding the material detachment processes that could occur in these stars if lateral cracking is present. This is because the depth of much of the lateral

cracking was approximately the same depth as the spalled zone as measured using the optical profilometry (~ 5 μm) implying that the spalled zone was once part of the same lateral crack branch. The observation of some lateral cracks intersecting with the surface also suggests that further material removal would be likely under high rolling contact pressure (as the intersection would act as a hinge) and poor lubrication. Delamination and spalling of surface-intersecting lateral cracks on silicon nitride bearings has been observed previously by Hadfield and Stolarski [14].

When compared to the depth of half-penny cracking and radial cracking observed in the M1 stars (and in SNA-4), the depth of the lateral cracks can be considered quite shallow (e.g. in SNA-2, a depth of 19 μm for the primary lateral crack, but 30 μm for the half-penny crack). As mentioned previously, shallow lateral cracks are more likely to intersect the surface (potentially leading to spalling), and this is seen in SNA-5. The size of the lateral cracks beneath the sub-surface of the M2 stars as well as their relatively shallow depth means that wear during service could lead to large volumes of material being removed, more so than that of the M1 stars where lateral cracking was not as severe which may be due to lateral cracks having been removed by subsequent polishing after formation. This is further supported by the surface profilometry of the two types of star feature which showed that M2 stars exhibit significantly more uplift material than the M1 stars and in locations surrounding the lateral cracking – again, important when operational conditions are considered (since uplift zones act as first points of contact). It could therefore be proposed that the M2 stars in general are more likely to undergo material removal processes in service than the M1 stars. Studies on rolling contact induced indentations have shown that the risk of spalling and further crack propagation can be enhanced when considering lubrication [20]–[22]. Lubricant can become trapped within indentation pits and the resulting hydraulic pressure can cause increased tensile stresses at pit corners which can initiate cracking [20]. For the star features examined here (where sub-surface cracking is already present), lubricant driven crack propagation may be a concern, particularly for lateral cracking where the hydraulic pressure may cause propagation to the surface leading to spalling.

For Vickers indentation of ceramics, it is generally proposed that radial cracks/half-penny cracks form on loading and then lateral cracking initiates on unloading from flaws at the tensile-compressive stress boundary as a consequence of high tensile unloading stresses [1], [23], [24]. Therefore, the crack formation process for the star features is likely to be similar because the sub-surface crack morphology observed for the features is also similar,

i.e. half-penny cracking bordering the tensile-compressive stress zone, and shallower lateral cracking. Any micro-cracking present in the M1 stars was typically observed at a shallow depth, just beneath the central indentation impression bordering the central plastic deformation zone and where lateral cracking intersected with the surface (e.g. in SNA-2 and SNB-3). For SNA-4, micro-cracking was significant at locations below spalled material and near lateral cracking. The location of micro-cracking in the vicinity of lateral cracks may indicate that micro-cracks are the flaws from which lateral cracks present in the star features initiate.

From the information gained about star features via FIB tomography, it may be possible to estimate an equivalent Vickers indentation load. This might however be challenging for the M1 stars in particular, where the original indentation impression is no longer present. The depth of lateral cracking for the M2 stars is similar to that for the 1 kg Vickers indentations observed in Chapter 5 where lateral cracking ranged from 15 – 17 μm in depth, however the size of the observed surface central plastic deformation zone suggests the star features may be more comparable to a higher load Vickers indentation. In fact, the size of the surface central plastic deformation zone is similar for M1 and M2 stars (maximum diameter range between 38 – 42 μm with the exception of SNA-1 where the diameter is ~ 24 μm) indicating they were formed under similar load, correlating with a Vickers indentation applied load of ~ 3 kg (from measuring the diameter of the residual indentation impression of the Vickers indentation). Given this approximation, it may be possible to determine the stage of lapping at which the stars are most likely to be formed, as from the top-down polishing investigations in Chapter 5 it was observed that the central plastic deformation diameter does not decrease significantly with depth. However, the estimated volume of the sub-surface compressively stressed zone calculated for the M1 star features varies significantly from star to star. SNA-1 and SNB-3 have estimated compressively stressed zone volumes (3,500 μm^3 and 8,000 μm^3) that equate to the volumes calculated in Chapter 5 for 0.5 kg and 1 kg Vickers indentations (3,000 μm^3 and 9,500 μm^3 respectively). The compressively stressed volume of the SNA-2 star (22,000 μm^3) is significantly larger than for the other M1 stars, especially considering the maximum diameter (~ 42 μm) of its surface central zone is comparable to the other stars. This could indicate that less of the star has been removed by subsequent lapping (e.g. Fig. 6.20) in comparison to the other M1 stars.

The mechanical properties of silicon nitride mean that diamond lapping is currently the only suitable way to polish such ceramic ball components, although if the stars are formed

at an earlier stage in the lapping process then staged lapping with successively smaller diamond grit size may decrease their severity. The depth of the initial star indentation will be the determining factor on how effective this is. Tribo-chemical polishing of silicon nitride has been put forward as a method for removing processing indents/pits but it is currently not utilised in large scale manufacturing as the process by which it occurs is not well understood [13], [25], [26].

6.9.2. FIB Tomography for Star Feature Analysis

The FIB tomography method for the 3D characterisation of the silicon nitride ball star features has provided information about their sub-surface cracking morphology not attainable in such high resolution through other methods, e.g. micro-XCT and sectioning via polishing [2], [27], [28]. Half-penny and lateral cracking was visible that could not be seen in UV fluorescence images – potentially due to their depth being too great for attenuation through the silicon nitride, or because the cracks were not saturated fully by the dye. However, the UV fluorescence images did reveal the majority of lateral cracking (which assisted in deciding the direction and location of FIB-sectioning), the surface length of which correlated well with what was observed using the SEM. However, the FIB tomography revealed depth, orientation and morphology information (for the radial and half-penny cracks as well) not possible using UV fluorescence imaging alone. In addition to this, the presence and extent of the compressively stressed plastic deformation zone was able to be estimated from the FIB tomography reconstructions.

There are still problems associated with the FIB tomography technique which have become further apparent in these investigations. For instance, it is still fundamentally a destructive process which leads to several issues: firstly, once a star has undergone FIB-sectioning further analysis is not possible. Secondly, as has been discussed, the removal of material changes the local residual stress potentially resulting in crack opening/closing (as in the propagation of the radial crack in the SNA-2 star). This may mean that the FIB tomography observed sub-surface cracking is not the same as that which was present prior to FIB-sectioning [8], [10], [29]. Lateral cracking dimensions (extension from star centre) measured from FIB tomography did not seem to vary significantly when compared to surface measurements taken from the UV fluorescence images.

The limited sputtering rate of the Ga^+ FIB means that sectioning of volumes greater than ~ 100,000 μm^3 becomes time consuming (and costly) – each star feature here took > 4 days

to section, however, xenon-based FIB devices have been developed recently which have a significantly increased sputter yield of 300% in some materials [30] and could be used in future analyses. Another problem associated with the FIB-sectioning here was the redeposition of the sputtered material on the surrounding regions; this not only obstructs the view of the milled cross-section and hence limits crack observations, but it also adds an additional step to the sectioning process as it must be sputter removed when the build-up becomes too great. However, despite these drawbacks, FIB tomography has been successful here in characterising the sub-surface cracking present beneath star features located on silicon nitride balls.

6.10. Summary

In this chapter, the FIB tomography technique has for the first time been used to characterise processing generated microscale star features on silicon nitride balls in three dimensions. Optical profilometry has also been used to gain topographical information. Two types of star feature have been investigated: Morphology 1 which have no central indentation present and exhibit primarily radial cracking, and Morphology 2, which have regions of missing material in addition to significant lateral cracking. The main findings for Morphology 1 stars are as follows:

- FIB tomography revealed half-penny and lateral cracking that could not be observed in UV fluorescence images.
- All Morphology 1 stars exhibited half-penny cracking that extended beneath the central compressive stress zone – with a max depth of 40 μm in the SNA-2 star.
- Half-penny crack shape and location can give an indication of the volume of the compressive stress plastic deformation zone underneath the star features.
- Surface profilometry showed slight uplift zones for Morphology 1 stars near the central region.

And for the Morphology 2 star features:

- Large lateral cracks were found to have depths of up to ~ 15 μm.
- Lateral cracking intersected the surface plane at locations where surface cracking was observed.
- Lateral cracking in the SNA-4 star sample were located at the same depth as spalling (~ 5 μm).

- The dimensions of the lateral cracks extending from the centre of the star were found to correlate well with the UV fluorescence images.
- Surface profilometry showed significant uplift zones in regions adjacent to lateral cracking and areas of material removal.

From the surface profilometry and FIB tomography results, it is likely that Morphology 1 stars are an evolution of the Morphology 2 type stars, that have undergone further lapping and hence the central indentation impression has been removed, and lateral cracking reduced.

Here, FIB tomography has revealed information about sub-surface crack networks in star features that has previously been unattainable. The discovery of the depth of lateral cracking beneath these star features, and that they intersect the surface, shows that they could be susceptible to material removal via flaking and spalling during service; this would inevitably affect the performance of the component. The potential impact of these stars is further contributed to by the uplift associated with them, and in particular that which is present around lateral cracking and spalled material in the Morphology 2 stars. For these reasons it is proposed that star features of the Morphology 2 type are of greater concern, although the radial and half-penny cracks in Morphology 1 star features have the potential to evolve lateral cracks under high external applied pressure.

6.11. References

[1] T. Lube, "Indentation crack profiles in silicon nitride," *J. Eur. Ceram. Soc.*, vol. 21, pp. 211–218, 2001.

[2] Y. Vertyagina, M. Mostafavi, C. Reinhard, R. Atwood, and T. J. Marrow, "In situ quantitative three-dimensional characterisation of sub-indentation cracking in polycrystalline alumina," *J. Eur. Ceram. Soc.*, vol. 34, no. 12, pp. 3127–3132, 2014.

[3] Y. Wang and M. Hadfield, "Failure modes of ceramic rolling elements with surface crack defects," *Wear*, vol. 256, no. 1–2, pp. 208–219, 2004.

[4] W. Wang, M. Hadfield, and A. A. Wereszczak, "Surface strength of silicon nitride in relation to rolling contact performance measured on ball-on-rod and modified four-ball tests," *Tribol. Int.*, vol. 43, no. 1–2, pp. 423–432, 2010.

[5] Y. Wang and M. Hadfield, "A mechanism for nucleating secondary fractures near a pre-existing flaw subjected to contact loading," *Wear*, vol. 254, no. 7–8, pp. 597–605, 2003.

[6] Y. Wang and M. Hadfield, "A study of line defect fatigue failure of ceramic rolling elements in rolling contact," *Wear*, vol. 253, no. 9–10, pp. 975–985, 2002.

[7] Z. Yu and S. Boseck, “Scanning Acoustic Microscopy and Its Applications to Material Characterization,” *Rev. Mod. Phys.*, vol. 67, no. 4, pp. 863–891, 1995.

[8] B. J. Inkson, D. Leclere, F. Elfallagh, and B. Derby, “The effect of focused ion beam machining on residual stress and crack morphologies in alumina,” *J. Phys. Conf. Ser.*, vol. 26, no. 1, pp. 219–222, 2006.

[9] F. Elfallagh and B. J. Inkson, “3D analysis of crack morphologies in silicate glass using FIB tomography,” *J. Eur. Ceram. Soc.*, vol. 29, pp. 47–52, 2009.

[10] F. Elfallagh and B. J. Inkson, “Evolution of residual stress and crack morphologies during 3D FIB tomographic analysis of alumina.,” *J. Microsc.*, vol. 230, no. Pt 2, pp. 240–51, 2008.

[11] B. Yu, R. S. Bradley, C. Soutis, P. J. Hogg, and P. J. Withers, “2D and 3D imaging of fatigue failure mechanisms of 3D woven composites,” *Compos. Part A Appl. Sci. Manuf.*, vol. 77, pp. 37–49, 2015.

[12] R. Komanduri, Z.B. Hou, N Umehara, M. Raghunandan, “A ‘gentle’ method for finishing Si3N4balls for hybrid bearing applications,” *Tribol. Lett.*, vol. 7, no. 1, pp. 39–49, 1999.

[13] W. Maw, F. Stevens, S. C. Langford, and J. T. Dickinson, “Single asperity tribochemical wear of silicon nitride studied by atomic force microscopy,” *J. Appl. Phys.*, vol. 92, no. 9, pp. 5103–5109, 2002.

[14] M. Hadfield and T. A. Stolarski, “Observations of delamination fatigue on pre-cracked ceramic elements in rolling contact,” *Ceram. Int.*, vol. 21, no. 2, pp. 125–130, 1995.

[15] L. Wang, R. Snidle, and L. Gu, “Rolling Contact Silicon Nitride Bearing Technology: a Review of Recent Research,” *Wear*, vol. 246, no. 1–2, pp. 159–173, 2000.

[16] N. K. Arakere, S. Pattabhiraman, G. Levesque, and N. H. Kim, “Uncertainty analysis for rolling contact fatigue failure probability of silicon nitride ball bearings,” *Int. J. Solids Struct.*, vol. 47, no. 18–19, pp. 2543–2553, 2010.

[17] R. F. Cook and D. H. Roach, “The effect of lateral crack growth on the strength of contact flaws in brittle materials,” *J. Mater. Res.*, vol. 1, no. 4, pp. 589–600, 1986.

[18] Z. H. Xie, P. R. Munroe, R. J. Moon, and M. Hoffman, “Characterization of surface contact-induced fracture in ceramics using a focused ion beam miller,” *Wear*, vol. 255, no. 1–6, pp. 651–656, 2003.

[19] Z. H. Xie, M. Hoffman, R. J. Moon, P. R. Munroe, and Y. B. Cheng, “Subsurface Indentation Damage and Mechanical Characterization of α-Sialon Ceramics,” *J. Am. Ceram. Soc.*, vol. 87, no. 11, pp. 2114–2124, 2004.

[20] J. Lai, Y. Kadin, and C. Vieillard, “Characterization and modelling of the degradation of silicon nitride balls with surface missing-material defects under lubricated rolling contact conditions,” *Wear*, vol. 398–399, no. March, pp. 146–157, 2018.

[21] R. Raga, I. Khader, C. Zdeněk, and A. Kailer, “Experimental and numerical investigation of crack initiation and propagation in silicon nitride ceramic under rolling and cyclic contact,” *J. Phys. Conf. Ser.*, vol. 843, no. 1, 2017.

[22] R. Raga, I. Khader, Z. Chlup, and A. Kailer, “Damage initiation and evolution in

silicon nitride under non-conforming lubricated hybrid rolling contact," *Wear*, vol. 360–361, pp. 147–159, 2016.

[23] J. T. Hagan and M. V. Swain, "The origin of median and lateral cracks around plastic indents in brittle materials," *J. Phys. D Appl. Phys.*, vol. 11, no. 15, pp. 2091–2102, 1978.

[24] Y. Tang, A. Yonezu, N. Ogasawara, N. Chiba, and X. Chen, "On radial crack and half-penny crack induced by Vickers indentation," *Proc. R. Soc. A Math. Phys. Eng. Sci.*, vol. 464, no. May, pp. 2967–2984, 2008.

[25] R. C. Dante and C. K. Kajdas, "A review and a fundamental theory of silicon nitride tribochemistry," *Wear*, vol. 288, pp. 27–38, 2012.

[26] S. R. Hah, C. B. Burk, and T. E. Fischer, "Surface Quality of Tribochemically Polished Silicon Nitride," *J. Electrochem. Soc.*, vol. 146, no. 4, pp. 1505–1509, 1999.

[27] B. Karunamurthy, M. Hadfield, C. Vieillard, G. E. Morales-Espejel, and Z. Khan, "Cavitation and rolling wear in silicon nitride," *Ceram. Int.*, vol. 36, no. 4, pp. 1373–1381, 2010.

[28] H. Miyazaki, H. Hyuga, Y. I. Yoshizawa, K. Hirao, and T. Ohji, "Crack profiles under a Vickers indent in silicon nitride ceramics with various microstructures," *Ceram. Int.*, vol. 36, no. 1, pp. 173–179, 2010.

[29] F. Elfallagh, "3D analysis of indentation damage by FIB tomography and TEM," University of Sheffield, 2008.

[30] T. L. Burnett, R. Kelley, B. Winiarski, L. Contreras, M. Daly, "Large volume serial section tomography by Xe Plasma FIB dual beam microscopy," *Ultramicroscopy*, vol. 161, pp. 119–129, 2016.

Chapter 7: He and Ne FIB Imaging of Vickers Indentations on Silicon Nitride

7.1. Introduction

In this chapter, a recently developed focused ion beam (FIB) microscope that uses helium (sometimes referred to as helium ion microscopy, or HIM, for short) and neon gas field ion sources (GFIS) instead of the conventional gallium source has been used to image Vickers indentations, and associated surface cracking, on silicon nitride. The purpose of this is to investigate the suitability of GFIS for imaging non-conductive samples, and cracking features, by using the attached electron flood gun to neutralise charge. As it has been seen in previous chapters, in order to image non-conductive samples under a conventional gallium FIB or electron microscopy, a conductive coating of gold or carbon is required to avoid charging effects, whereas no coating is required if an electron flood gun is used. Therefore, the imaging of uncoated, gold coated, and carbon coated samples with both the neon beam and the helium beam has been compared. Some of the investigations in this chapter have been published as "*A comparison of He and Ne FIB imaging of cracks in microindented silicon nitride"* in Materials Characterization 141 (2018) 362-369 [1]. Permission for the use of copyrighted material has been obtained from the publisher Elselvier.

7.2. He and Ne Beam Imaging of Uncoated Si_3N_4

7.2.1. Comparison of He and Ne Imaging

Uncoated silicon nitride SNA composition samples Vickers indented with loads of 1 kg were imaged with both the neon and helium beam with the use of an electron flood gun for charge neutralisation. Images were formed using the ion-induced secondary electrons (ISE) detected using an Everhart-Thornley detector (ETD).

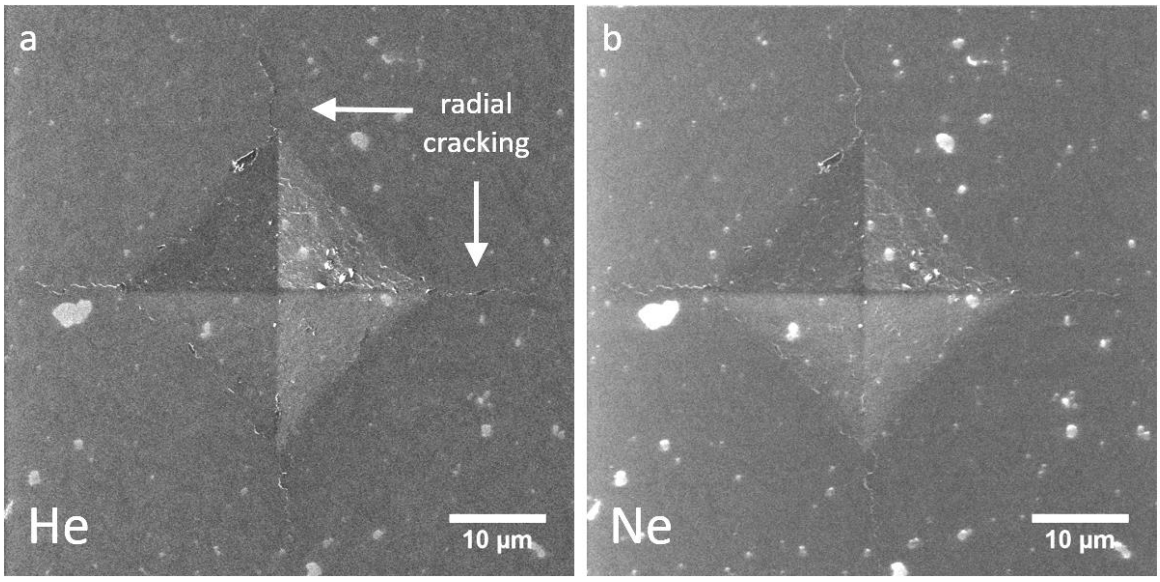

Figure 7.1: GFIS ion-induced secondary electron images of a 1 kg indentation on SNA taken using the (a) He beam, and (b) the Ne beam.

Fig. 7.1 shows a 1 kg indentation imaged with the helium (Fig. 7.1(a)) and the neon beam (Fig. 7.1(b)). The residual indentation impression can be seen under both beams and is distinguishable from the surrounding region. Radial cracks (arrowed) are also resolved emanating from the indentation corners. In both images there are small regions of light contrast (arrowed), implying greater ISE emission, which are most likely the glassy intergranular phase. In the Ne-ISE image these regions appear to be slightly more prominent in comparison to the He-ISE image. Overall however, at this magnification the images appear to be almost identical.

In Fig. 7.2(a) which shows a higher magnification He-ISE image of an indentation corner, radial cracking is observed emanating with a jagged pathway implying intergranular cracking. Cracking consistent with the intersection of lateral cracks with the surface (arrowed) is also observed to be present along the inside edge of the residual indentation impression. Again, regions of the glassy intergranular phase are visible because of the higher ISE emission but at this magnification the α and ß grain microstructures are not distinguishable. In the He-ISE images of the indentation, there appeared to be no localised build-up of charge that would be expected if imaging an uncoated insulating sample with an electron microscope. Fig. 7.2(b) is an Ne-ISE image of a radial crack, a section of which had previously been imaged with the helium beam (He-ISE image is given in the inset). The section which had undergone previous imaging appears to be a lighter contrast than the surrounding region which may indicate charge build-up induced by prior

irradiation with the He beam, although ion surface charging normally exhibits a darker contrast. It may be that the He beam has sputtered away surface material, however, this is unlikely as silicon nitride has a high hardness and He ions have a low mass (i.e. a low sputter yield). Alternatively, contaminants within the microscope vacuum chamber, such as hydrocarbons, can be directed towards the material surface (by the ion beam) and sputter away material, or they can be deposited on to the surface in a similar way to carbon deposition; both of which could cause a lighter contrast region.

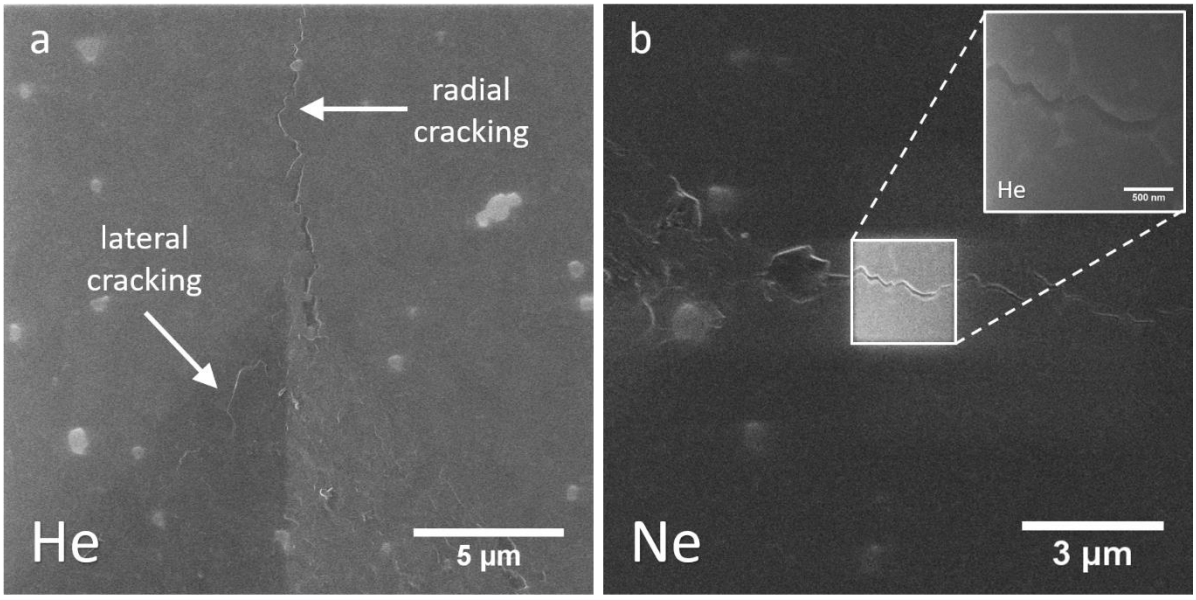

Figure 7.2: (a) A He beam image of a 1 kg indentation corner showing radial cracking in addition to lateral cracking (arrowed) within the residual indentation impression. (b) A Ne beam image of a radial crack emanating from an indentation corner highlighting how previous imaging of an area with the He beam (inset) affects the Ne beam image contrast.

Higher magnification He-ISE images of radial cracks are given in Fig. 7.3(a & c) with Ne-ISE images for comparison shown in Fig. 7.3(b & d). The crack edges in both Fig. 7.3(a & b) show lighter contrast known as 'edge contrast' due to enhanced secondary electron (SE) escape at edges inclined to the incident ion beam. For both the He-ISE and Ne-ISE images this appears to be more prominent on just one edge of the cracking which is consistent with a change in topography, i.e. a raised region, in comparison to the surrounding area. There is likely edge contrast on both sides, but the position of the detector within the microscope chamber will have some influence the collected ISEs. The reduced edge contrast for the He-ISE images in comparisons to Ne-ISE images (in Fig. 7.3) may be due to a difference in absolute contrast of the two beams. Within the He-ISE image there is also a small, lighter contrast zone (Fig. 7.3(a) arrowed) overlapping the crack opening of approximately ~ 500 nm in diameter which does not appear in the Ne-ISE image. It could

potentially be a region of charge build-up, alternatively it could be a grain (given the shape) or the intergranular phase exhibiting a phenomenon known as 'channelling contrast' [2], [3]. Channelling contrast is a change in the ISE signal that is dependent on the crystal orientation of the grain which in turn influences how deep within a sample an incident ion (in this case a He ion) can travel. The ion-grain interaction will be different depending on the type of ion and therefore the ISE emission will differ, hence why this region may be only observed in the He-ISE image and not the Ne-ISE image [4]. The Ne-ISE image does however show the intergranular phase (arrowed) whereas in the He-ISE image it is not distinguishable.

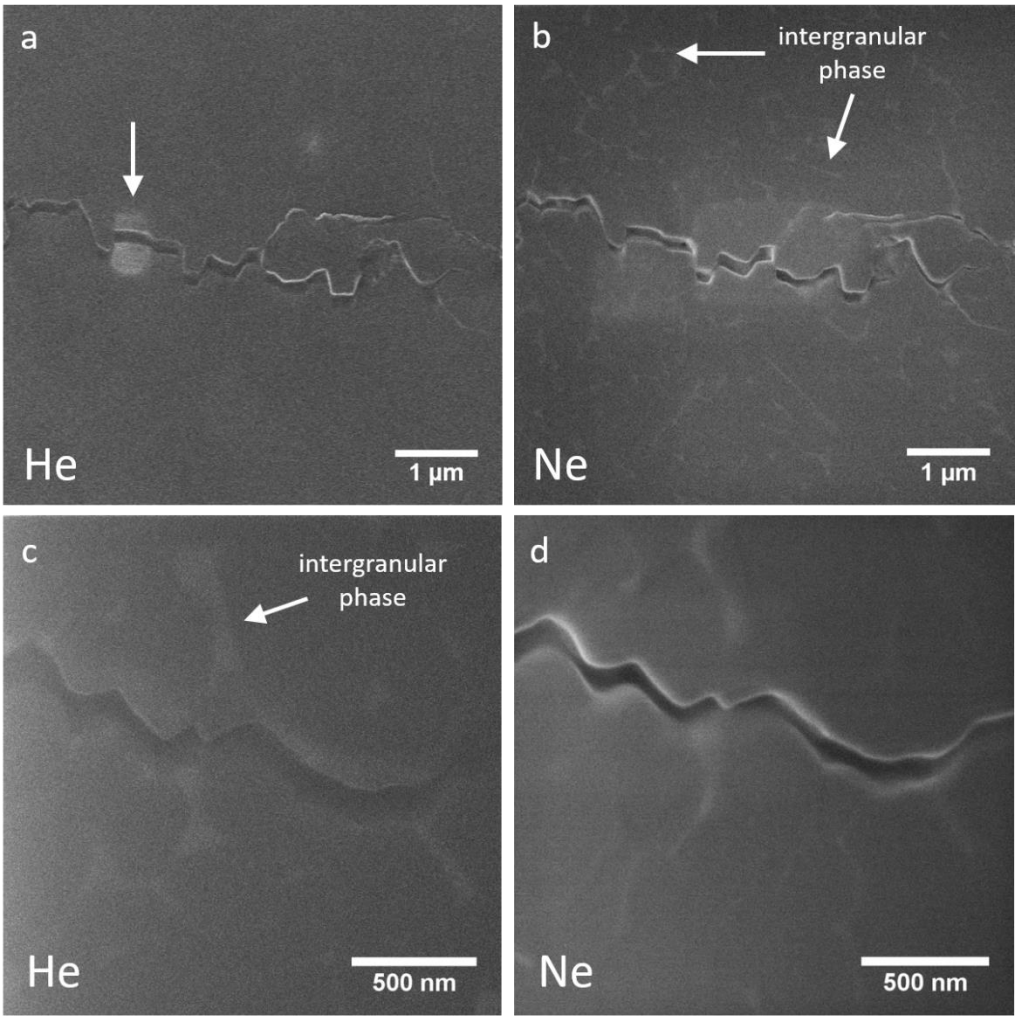

Figure 7.3: (a) and (c) show high magnification He-ISE images of sections of radial cracks with (b) and (d) being the same sections but imaged with Ne-ISE. The intergranular phase has been arrowed.

Figs. 3(c & d) are higher magnification images of a radial crack and here the intergranular phase is visible in both the Ne-ISE and He-ISE image (arrowed). The edge contrast exhibited on the crack edges by the Ne-ISE image is significantly greater than that of the He-ISE, where it is less obvious. This may be because the heavier Ne^{+} ions have a larger

interaction volume and shallower penetration depth than the He^+ ions and therefore produce more ISE emission from near the surface [5], [6]. In a similar way, the difference in phase contrast between the He-ISE and Ne-ISE images may be caused by the formation mechanism of the SEs. The He beam diverges slowly (due to low nuclear stopping power) upon contact with the sample and the ISEs produced only arise from the point at which the beam enters the sample, whereas for the Ne beam (which has a higher nuclear stopping power) ISEs can be produced at locations where backscattered ions escape the sample and where sputtering of atoms occurs. This leads to a higher ISE yield but lower spatial resolution for the Ne beam.

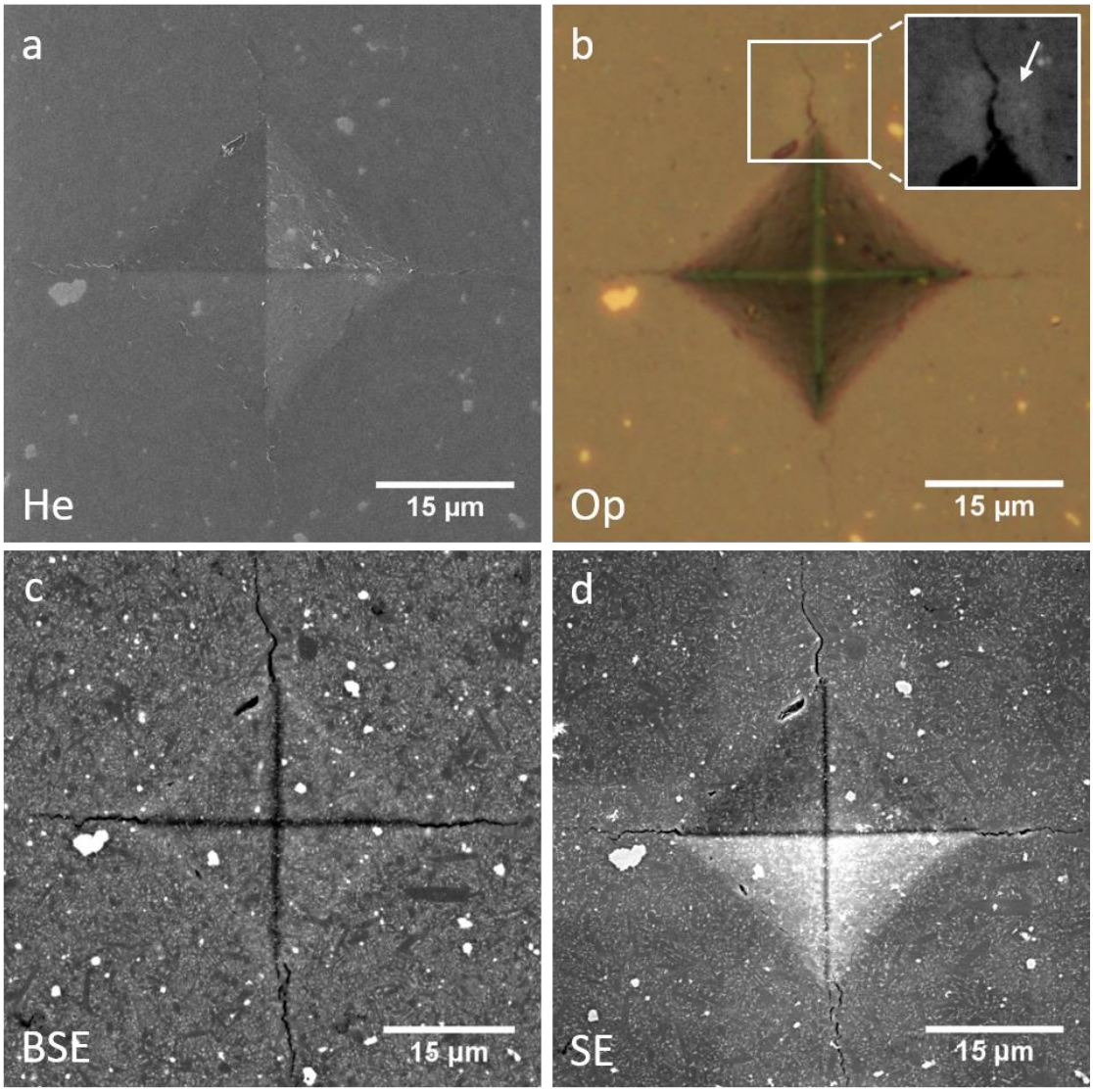

Figure 7.4: A comparison of techniques for imaging of a 1 kg indentation on silicon nitride: (a) Using He-ISE with flood gun, (b) Optical bright field, (c) SEM BSE with carbon coating and (d) SEM SE with carbon coating. A lighter contrast region believed to be caused by previous ion beam sputtering is arrowed in the inset of (b).

For the sake of comparison, Fig. 7.4 shows a 1 kg indentation that has been imaged with He-ISE (Fig. 7.4(a)), and the same indentation also imaged optically (Fig. 7.4(b)), and then with a surface carbon layer sputtered and imaged under an SEM (Fig. 7.4(c & d)) using backscattered secondary electrons (BSE) and secondary electrons (SE). Interestingly the optical image, which was taken after He and Ne beam imaging, has a region (arrowed Fig. 7.4(b) inset) which is of a slightly lighter contrast than the surrounding area. If this were under an SEM microscope then this lighter contrast region may be attributed to surface charge build-up, however, optical microscopy does not detect charging artefacts meaning it must be caused by a physical change to the silicon nitride surface, i.e. sputtering of material by the incident ions or contaminant deposition. Mostly likely the neon ions were responsible for the damage as they have a higher sputtering rate than helium ions. Damage via sputtering is important to take in to consideration when imaging even hard materials with GFIS microscopy as it can alter the surface contrast.

When the He-ISE image of the indentation in Fig. 7.4 is compared to both the SEM images after carbon coating (Fig. 7.4 (c) and (d)) it can be seen that the contrast between the granular and intergranular glassy phase is superior in the SEM images. This is particularly evident for the BSE image (Fig. 7.4(c)) where the contrast is dependent on material Z number, however, He-ISE does offer better topographical contrast similar to that of the SE image. The cracking is also better resolved in the SEM images, although it is important to remember that the sample was carbon coated prior to SEM imaging to reduce charging Without the carbon layer, SEM imaging of such an insulating sample would be almost impossible. Also, some ceramic samples may not be suitable for the application of a conductive coating if further surface analysis is required in which the carbon surface layer could interfere with data capture, e.g. Raman spectroscopy or EDX. In such cases, the use of GFIS microscopy in conjunction with an electron flood gun for high resolution imaging would be advantageous.

7.2.2. Influence of Flood Gun Dwell Time

As has been mentioned previously, the build-up of surface charge normally associated with the charged particle imaging of insulating materials, has been neutralised here using an electron flood gun – the negatively charged electrons couple with the positively charged He and Ne ions. The number of electrons incident on a specimen is dependent not only on the accelerating voltage but also the dwell time of the incident beam. In the He-ISE

images of an indentation corner in Fig. 7.5, the accelerating voltage has been kept constant (at 1000 eV) and the electron flood gun dwell time has been varied from 0 – 1000 μs to ascertain the influence it has on the He-ISE image obtained.

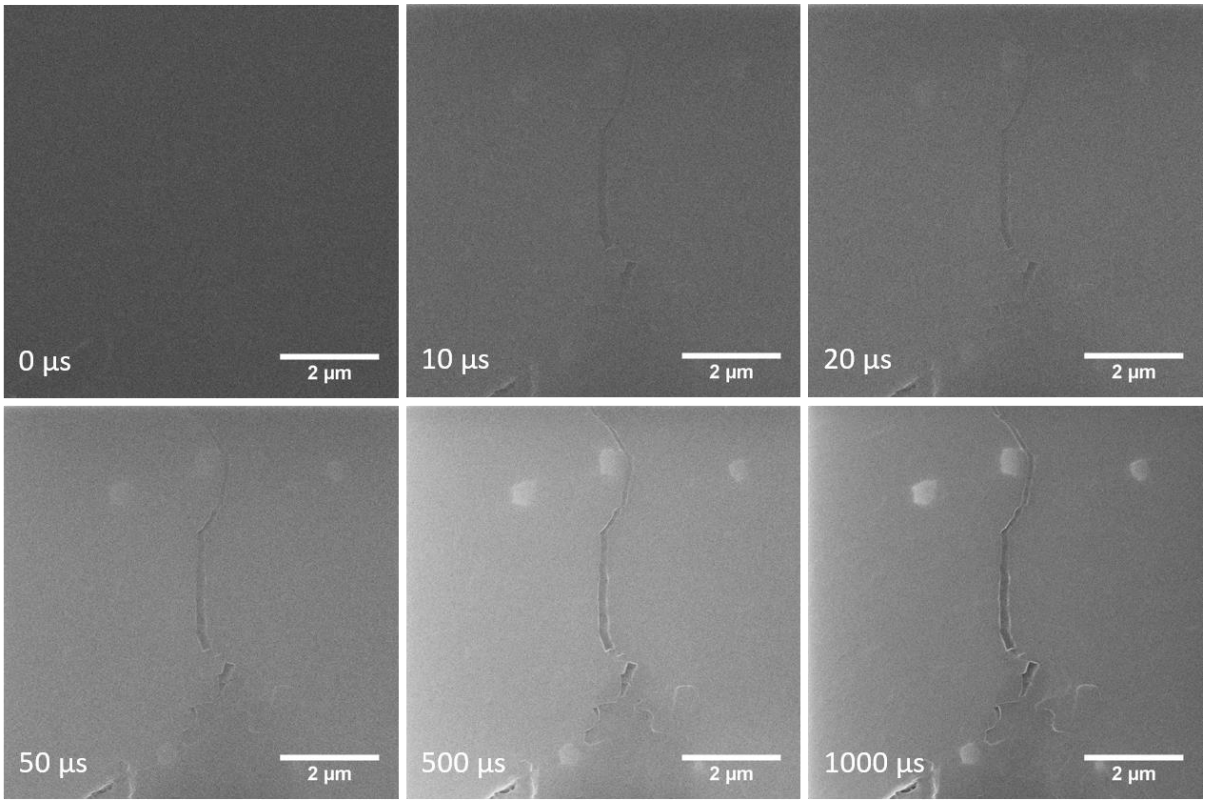

Figure 7.5: A montage of He-ISE images of a radial crack emanating from an indentation highlight how the electron flood gun dwell time (bottom left of images) has an influence on the image.

At 0 μs dwell time, i.e. no incident electrons, the image is dark and features of the indentation corner are not visible. This indicates that there is very low ISE emission most likely due to the build-up of surface positive charge as well as implantation into the surface of He^+ ions that inhibit secondary electron motion to the surface. As the dwell time is increased, even by 10 μs increments, the influence of the electron flood gun on the image is made more apparent by the appearance of the indentation corner and the emanating radial crack. The visibility of lighter contrast regions (similar to that discussed in reference to Fig. 7.3(a)) also increases as dwell time increases, as well as an increase in the observed edge contrast of the radial cracking. Features are also better resolved with higher dwell times, although after increasing beyond 1000 μs the observed difference was negligible. It can be seen from Fig. 7.5 that in the imaging of the uncoated sample, the use of electron flood gun is very effective for charge neutralisation. The charging associated with the use of the helium beam is primarily positive as the He ions are

positively charged. The high level of ISE emission from the helium-sample interaction also leaves the surface positively charged, and beam currents for GFIS microscopy are relatively low compared with SEM, meaning that positive charge build up is a gradual process [7], [8]. These phenomena combined make charge neutralisation with an electron flood gun an effective methodology.

Although increasing the dwell time of the electron flood does have a positive effect on the quality of the image produced as the local positive charge is neutralised, it increases the overall time required to take an image by more than just the sum of the increased dwell time. When using line scan mode (used here, and explained in Chapter 3) in conjunction with an electron flood gun the process is particularly time consuming as, for every line scan; the He beam is turned on, then blanked, whilst the electron flood gun is turned on, which is then itself blanked, and the He beam turned back on [9]–[11]. This can lead to single imaging times of the order of tens of minutes for electron flood gun dwell times of ~ 1000 μm.

7.3. He and Ne Beam Imaging of Gold-Coated Si_3N_4

Often, when imaging insulating samples under SEM or conventional Ga-FIB, localised charging is reduced (and hence image quality enhanced) by the use of a conductive coating. In Fig. 7.6, He-ISE images of two sections of the same radial crack emanating from the corner of a 1 kg Vickers indentation are shown, where the surface conductivity has been increased via the application of a ~ 30 nm gold surface coating. As with the uncoated sample, the surface radial crack here has a jagged morphology indicative of an intergranular pathway. The radial crack shows good edge contrast although the edges were observed to have a slight roughening effect due to the gold coating aggregating in to nanoscale 'islands'. Crack branching was occasionally observed around 200 – 400 nm features thought to be grains as arrowed in Fig. 7.6(b). The location of the radial crack tip was hard to define as it merged with nano-cracking present in the gold sputtered layer. Individual silicon nitride grains and the intergranular phase were not visible in the He-ISE images, primarily because of the absorption of the He-ISE (from the silicon nitride) by the gold coated layer.

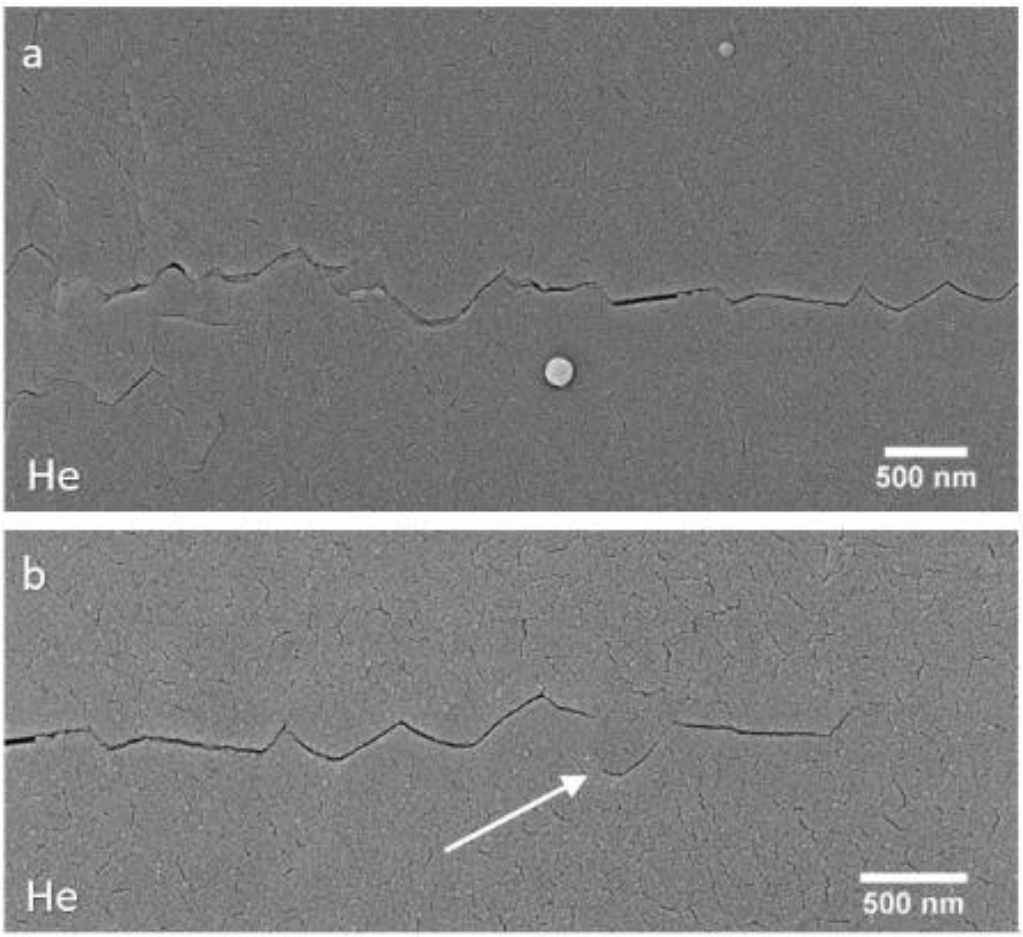

Figure 7.6: He-ISE imaging of a radial crack extending from a 1 kg indentation on gold-coated SNA silicon nitride. (a) Radial crack propagating from the indentation corner on left. (b) Branching of radial (arrowed) near to crack tip (on right).

In Fig. 7.7 the same section of radial crack imaged in Fig. 7.6 by He-ISE is shown but this time Ne-ISE imaging was used. As in the He-ISE image, the surface conductive gold layer also inhibits the detection of Ne-ISEs from the granular and intergranular glassy phase. Occasionally during Ne beam imaging, horizontal line scans which form the secondary electron image would exhibit varying intensity. This is actually a device effect and caused by variable incident neon beam intensity due to current fluctuations associated with the trimer tip [12], [13] (as discussed in Chapter 2). For the magnification used in Figs. 6 and 7, there is minimal difference in the resolution for the radial crack observed with He-ISE and Ne-ISE imaging.

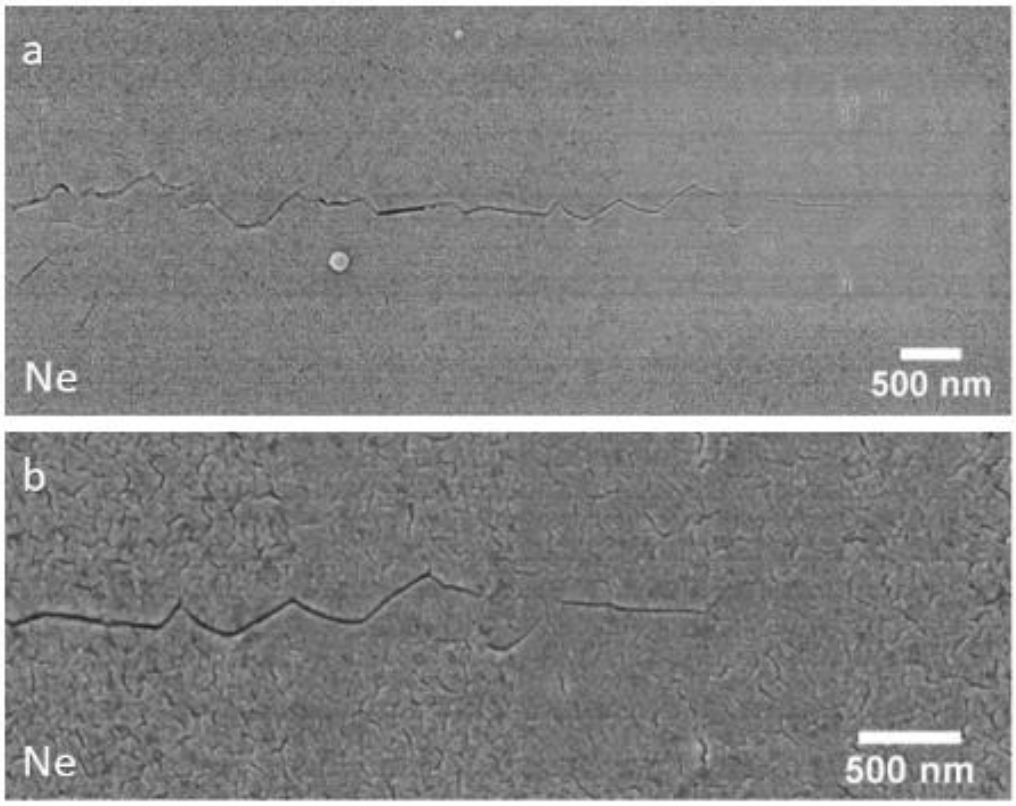

Figure 7.7: Ne-ISE imaging of a radial crack extending from a 1 kg indentation on gold-coated SNA silicon nitride. (a) Radial crack propagating from the indentation corner on left. (b) Radial crack undergoing bifurcation around a grain.

A section of the sputtered gold layer has been imaged at higher magnification with both He-ISE and Ne-ISE, and is shown in Fig. 7.8. At this magnification the differences between the imaging beams become more noticeable. For instance, in Fig. 7.8(a), the topographical contrast of the sputtered gold layer is more prominent due to the higher point resolution offered by the He-ISE imaging. As mentioned before, He-ISEs are primarily formed near the beam point of entry at the sample surface which is why it has better topographical contrast [6]. In addition, gold nano-islands with a diameter of ~ 20 nm are easily resolved in the He-ISE image but are less easily defined in the Ne-ISE image (Fig. 7.8(b)). The nano-cracks observed in the gold coating also have sharper edge definition in the He-ISE images; however, the Ne-ISE images show greater relative contrast between the nano-cracks (dark) and the gold edges (light). The nano-cracking exhibited in the gold coating is hard to distinguish from fine cracking induced by the micro-indentation as well as cracking at the radial crack tip. Therefore, using a gold coating to increase surface conductivity is probably not suitable for the imaging of micro/nanoscale cracks with He and Ne ion beams.

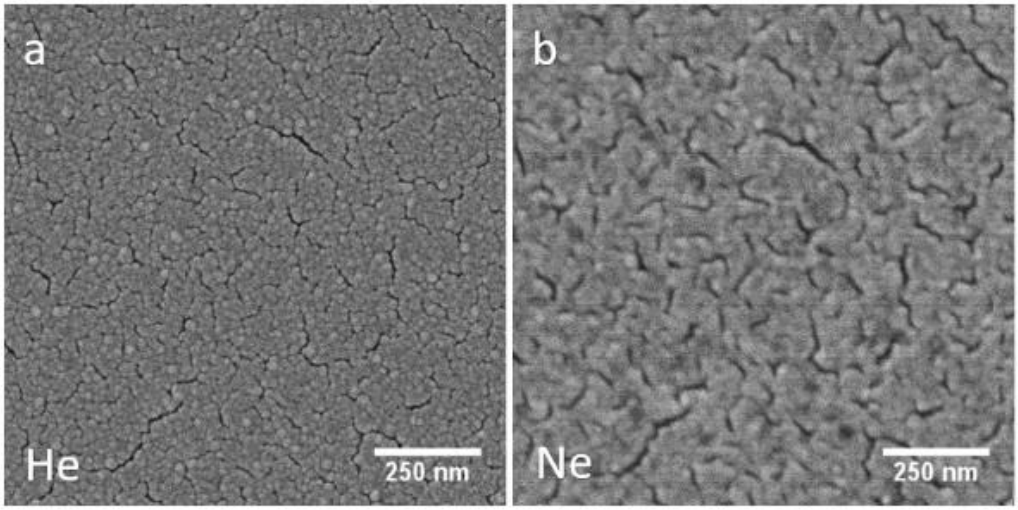

Figure 7.8: Region of gold coated SNA sequentially imaged with (a) He-ISE and (b) Ne-ISE.

7.4. He and Ne Beam Imaging of Carbon-Coated Si_3N_4

An often-used effective alternative to gold coating for increasing surface conductivity is sputtered carbon. It has been used here to investigate its efficacy for improving the imaging by He-ISE and Ne-ISE of the indentation induced cracking in silicon nitride. In Fig. 7.9(a & b) a comparison is given between He-ISE and Ne-ISE images taken sequentially of a section of radial crack emanating from a 0.5 kg indentation on the SND composition of silicon nitride. The sample has had a ~ 15 nm layer of carbon sputtered on the surface. Unlike in the gold coated samples, the conductive carbon coating here is thin enough that the differing contrast between the intergranular phase and the grains is visible as with the uncoated samples. Although the carbon layer is only half the thickness of the gold layer used on the SNA sample, the effect of thickness is small compared to the ISE attenuation length which is inversely proportional to the density of the coating. For carbon this is ~2 g/cm^3 and for gold is ~20g/cm^3 [14], [15] so ISEs from the substrate are absorbed rapidly by gold. In addition to this, gold has a higher ISE yield than carbon [16]. In both the He-ISE (Fig. 7.9(a)) and Ne-ISE (Fig. 7.9(b)) images the silicon nitride grains and the intergranular glassy phase are clearly distinguishable from each other. This contrast was not observed in the gold coated SNA sample where the phase contrast was poor.

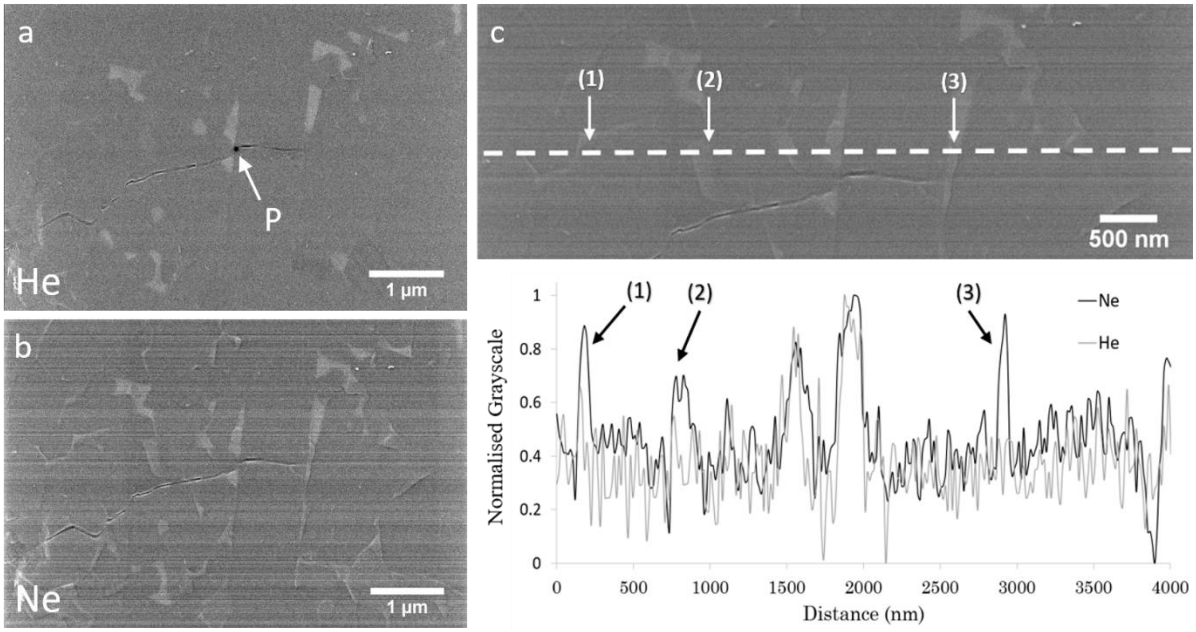

Figure 7.9: A section of a radial crack extending from a 0.5 kg indentation in carbon coated SND silicon nitride. (a) Image taken using He-ISE. (b) Image taken using Ne-ISE. (c) A normalized line profile along a section of the sample highlighting the difference in contrast grayscale values between the He and Ne images. Additional Ne peaks and their corresponding image location are labelled (1), (2), and (3).

In the Ne-ISE image, the delineation of the silicon nitride grains by the intergranular phase shows a greater contrast when compared to the He-ISE image. This has been highlighted in Fig. 7.9(c) which gives a line profile across the same location for the He-ISE image in comparison to the Ne-ISE image; additional peaks (labelled 1, 2, and 3) in the grayscale value were measured for the Ne-ISE image. It is important to note that scanning the carbon coating with the incident Ne beam may cause the sputtering away of the surface carbon more so than that of the He beam due to the increase mass of the Ne ions. However, under the experimental conditions used here, no noticeable changes in contrast, or appearance of localised surface charging, were observed.

The radial cracking shown in Fig. 7.9(a) has a singular faceted pathway which has propagated predominantly along grain boundaries. This again indicates a primarily intergranular cracking regime, although the radial crack did transition to a transgranular regime upon intersection with a large (> 4 μm long) silicon nitride grain preceding the crack tip. The crack opening was easily measurable in both the He-ISE and Ne-ISE imaging due to good crack edge contrast and found to be ~ 40 nm wide. In the He-ISE image given in Fig. 7.9(a), at the transition to transgranular cracking, a circular zone (labelled P) of depleted secondary electron emission (darker contrast) of diameter < 100

nm is visible. Similar features have been observed along crack pathways in the other GFIS images taken of the carbon coated SND sample, an example of which is given in Fig. 7.10 of a radial crack extending from a 1 kg indentation. It was often the case that localized zones of depleted SE emission in the He-ISE image (Fig. 7.10(a)) would correlate positionally with depleted SE emission in the Ne-ISE image (Fig. 7.10(b)). Typical characteristics of these depleted SE zones are that they are always located at crack edges and can extend to be within the crack gap and across the adjacent surface plane.

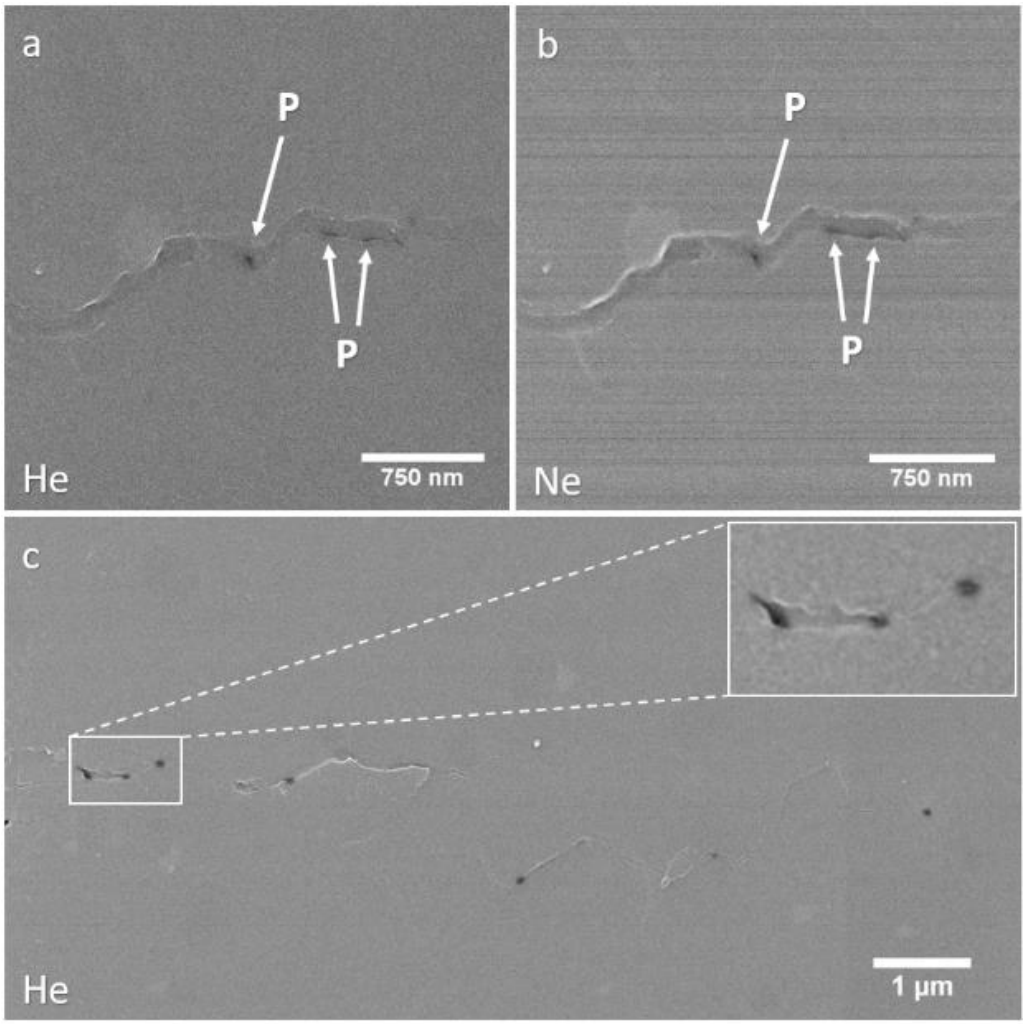

Figure 7.10: A section of a radial crack extending from a 1 kg indentation in carbon coated SND silicon nitride, exhibiting local zones of depleted ISE signal, P. (a) He-ISE image. (b) Ne-ISE image of same crack in (a). (c) He-ISE image showing a distribution of features, P, along the crack path.

The SE depletion zones observed in the GFIS imaging of the cracking on the carbon-coated silicon nitride may have origins in several mechanisms such as the local porosity, charging influences, and SE signal shadowing. However, the depletion of the SE signal in these zones is significantly higher than can be attributed to local loss of signal caused by the

existence of the cracking, or shadowing of SE signal reaching the detector by crack edges; both of which generate the standard type of contrast seen along most of the crack paths, and unlike the localised nature observed in the highlighted zones. Higher magnification He-ISE images of the depleted SE zones are given in Fig. 7.11. The radial crack in Fig. 7.11(a) shows cracking with the typical dark contrast within the crack gap (arrowed) with the brighter edge contrast, in addition to the strong local 'hotspot' of depleted SE signal (dashed arrow, labelled P). These hotspots typically have a lateral extensions of ± 50 nm from the crack edge (Fig. 7.11(b & c)).

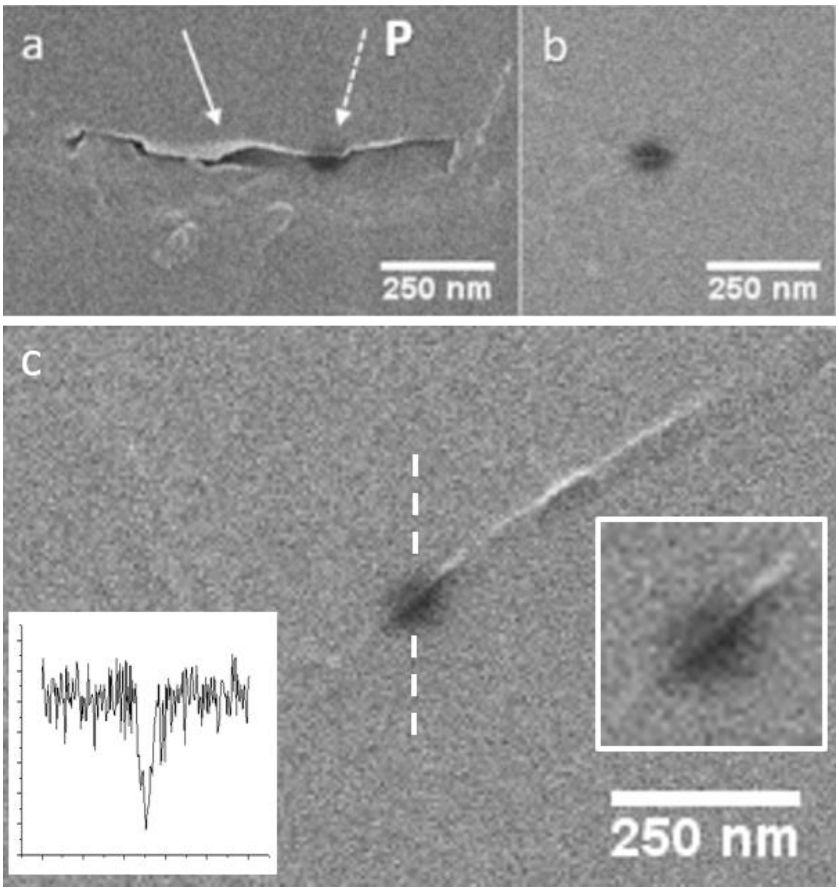

Figure 7.11: He-ISE images of charging hotspots on carbon coated SND. (a) Silicon nitride crack (block arrow) with ~100 nm zone, P, of local charging (dashed arrow) (b) ~100 nm diameter ISE depletion zone of a charging hotspot. (c) Hotspot with inset grayscale line scan and close-up.

The depleted SE emission hotspots have characteristics of a highly localised charging effect. Incident positively charged helium and neon ions build up in the silicon nitride sample under the incident beam. Although a carbon coating has been used to increase the flow of charged particles away from the imaged area, it is highly likely that sections of the cracks do not receive sufficient coating to neutralise local charge, and/or are not connected electrically to the surface coating. In addition, the spherical morphology of the hotspots

(Fig. 7.11(c)) is indicative of an electric field centred on a highly localised charge concentration. For example, highly concentrated localised charge and the associated electric field could arise from a very sharp point on a fracture surface or accumulate on a small electrically isolated section of fracture material. The formation of charge hotspots along the crack pathways will therefore depend on several factors such as the distribution of carbon coating, local crack geometry, and the parameters of the incident positive ion irradiation (e.g. current, dwell time, accelerating voltage). The inherent differences between helium and neon ions has led to the formation of the different ISE images observed for the same silicon nitride sample due to their differing mechanisms for ISE generation and emission, ion propagation, and ion irradiation [5], [6], [17].

7.5. Summary

This chapter has investigated the suitability of using GFIS microscopy, specifically helium and neon sources, for the imaging of insulating ceramics. Although GFIS microscopy has not been utilised in this way previously, it is of interest as gas ion beams have differing surface interactions and hence imaging characteristics when compared to SEM. Here, micro-indented silicon nitride and the associated cracking has been imaged with both helium and neon beam ion induced secondary electrons. Silicon nitride samples were imaged under three conditions: uncoated with the utilisation of an electron flood gun for charge neutralisation, with a conductive surface gold layer, and finally with a sputtered surface carbon layer. For the uncoated sample, the main findings are as follows:

- For the first time, an uncoated non-conductive ceramic, silicon nitride, was successfully imaged with a helium and neon GFIS in conjunction with an electron flood gun for charge neutralisation.
- Crack pathways and phase differences were observable in He-ISE and Ne-ISE images of indentations, with the Ne-ISE showing better phase contrast and crack edge contrast.
- Increasing the electron flood gun dwell time for He-ISE images was found to improve image clarity and contrast but at the cost of time efficiency.

The main findings for the gold and carbon coated silicon nitride samples are the following:

- The surface gold coating hid the silicon nitride microstructure as ISEs are inhibited from escape, however, this was not the case for the carbon coated sample where microstructure phase contrast was observed.
- High magnification imaging of nano-islands on the gold coating revealed that He-ISE provides high resolution and better topographical imaging than Ne-ISE.
- In the gold coated sample, indentation induced fine micro-cracking and radial crack tips in the silicon nitride substrate were not distinguishable from cracking in the gold coating.
- For the carbon coated sample, delineation of the granular and intergranular glassy phase showed greater contrast in Ne-ISE imaging.
- Under both Ne-ISE and He-ISE imaging, the presence of ~ 100 nm diameter 'hotspots' of depleted ISE emission were present on crack pathways on the carbon coated sample, consistent with the existence of highly localised electric fields.

The use of helium and neon GFIS microscopy with an electron flood gun for charge neutralisation is an effective high resolution alternative to SEM for imaging insulating ceramics. It is particularly advantageous if the application of a conductive surface coating is not suitable, such as when subsequent chemical analysis is required. With greater understanding of the ion-sample interactions and contrast mechanisms, it is expected that the use of GFIS for imaging non-conductive samples will become increasingly prominent.

7.6. References

[1] A. Baggott, M. Mazaheri, Y. Zhou, H. Zhang, and B. J. Inkson, "A comparison of He and Ne FIB imaging of cracks in microindented silicon nitride," *Mater. Charact.*, vol. 141, pp. 362–369, 2018.

[2] K. Ohya, "Simulation of channeling contrast in scanning ion microscope images," *AIP Adv.*, vol. 8, no. 1, 2018.

[3] L. A. Giannuzzi and J. . Michael, "Comparison of Channeling Contrast between Ion and Electron Images," *Microsc. Microanal.*, vol. 19, pp. 344–349, 2013.

[4] D. C. Bell, "Contrast mechanisms and image formation in helium ion microscopy.," *Microsc. Microanal.*, vol. 15, no. 2, pp. 147–153, 2009.

[5] F. H. M. Rahman, S. McVey, L. Farkas, J. A. Notte, S. Tan, and R. H. Livengood, "The prospects of a subnanometer focused neon ion beam," *Scanning*, vol. 34, no. 2, pp. 129–134, 2012.

[6] J. a. Notte, "Charged Particle Microscopy: Why Mass Matters," *Micros. Today*, vol. 20, no. 05, pp. 16–22, 2012.

[7] R. Hill and F. H. M. Rahman, “Advances in helium ion microscopy,” *Nucl. Instrum. Methods Phys. Res., Sect. A*, vol. 645, no. 1, pp. 96–101, 2011.

[8] M. S. Joens, C. Huynh, J.M. Kasuboski, D. Ferranti, “Helium Ion Microscopy (HIM) for the imaging of biological samples at sub-nanometer resolution.,” *Sci. Rep.*, vol. 3, p. 3514, 2013.

[9] L. Scipioni, C. A. Sanford, J. Notte, B. Thompson, and S. McVey, “Understanding imaging modes in the helium ion microscope,” *J. Vac. Sci. Technol. B Microelectron. Nanom. Struct.*, vol. 27, no. 6, p. 3250, 2009.

[10] J. Notte, B. Ward, N. Economou, R. Hill, “An introduction to the helium ion microscope,” *AIP Conf. Proc.*, vol. 931, no. 2007, pp. 489–496, 2007.

[11] D. Cohen-tanugi and N. Yao, “Superior imaging resolution in scanning helium-ion microscopy : A look at beam- sample interactions Superior imaging resolution in scanning helium-ion microscopy : A look at beam-sample interactions,” *J. Appl. Phys.*, vol. 104, no. 6, pp. 063504-063504-7, 2008.

[12] R. H. Livengood, S. Tan, R. Hallstein, J. Notte, S. McVey, and F. H. M. Faridur Rahman, “The neon gas field ion source - A first characterization of neon nanomachining properties,” *Nucl. Instrum. Methods Phys. Res., Sect. A*, vol. 645, no. 1, pp. 136–140, 2011.

[13] R. Urban, J. Pitters, S. Matsubara, and R. Wolkow, “Neon Gas Field Ion Source : Trimer and Single Atom Tip Comparison,” vol. 18, no. Suppl 2, pp. 822–823, 2012.

[14] K. Kanaya and H. Kawakatsu, “Secondary electron emission due to primary and backscattered,” *J. Appl. Phys.*, vol. 5, no. 1957, 1972.

[15] D. C. Joy, “A model for calculating secondary and backscattered electron yields,” *J. Microsc.*, vol. 147, no. 1, pp. 51–64, 1987.

[16] R. Ramachandra, B. Griffin, and D. C. Joy, “A model of secondary electron imaging in the helium ion scanning microscope,” *Ultramicroscopy*, vol. 109, no. 6, pp. 748–757, 2009.

[17] G. Hlawacek, V. Veligura, R. van Gastel, and B. Poelsema, “Helium Ion Microscopy,” pp. 1–16, 2013.

Chapter 8: Conclusion and Recommendations for Future Work

8.1. Conclusions

This thesis project has successfully characterised both the surface and sub-surface nature of microscale pit features, so called stars, located on the surface of silicon nitride balls for bearing applications with a view to predicting how they may evolve in operation conditions. Investigations were carried out on artificial star features, in the form of Vickers indentations, in order to ascertain which characterisation methodologies were most effective and applicable for ball star feature analysis. The techniques primarily chosen for use with the star features were FIB tomography, high resolution SEM, and optical surface profilometry. Additional valuable information was revealed about the ball star features from the studies on indentations using other techniques, e.g. Raman spectroscopy and manual serial grinding. A new gas field ion source FIB technique was also investigated for its suitability for imaging surface damage on non-conductive ceramics.

Surface characterisations of 0.5 kg and 1 kg Vickers indentations with SEM revealed silicon nitride primarily exhibits an intergranular fracture mode, with Raman spectroscopy investigations showing tensile stresses of up to 1 GPa at radial crack tips. High tensile stress at crack tips implies significant stresses are also present at the residual indent impression. The residual compressive stress zone for 1 kg indentations was found to extend out ~ 50 μm laterally from the residual indentation impression centre. Optical surface profilometry also showed an uplifted zone of ~ 0.4 μm in height surrounding indentation edges extending out to a lateral distance of ~ 10 μm for 1 kg applied loads. Imaging of Vickers indentations on silicon nitride with helium and neon ion beams, in conjunction with an electron flood gun, allowed for the characterisation of the microstructure and cracking without the need for a conductive surface coating. This is important as it allows for the imaging of insulating samples without prior preparation and does not restrict subsequent further surface analysis. Neon beam ISE imaging exhibited better edge contrast, but lower resolution, than helium beam ISE imaging. The presence of depleted regions of secondary electron emission were observed along crack pathways for carbon-coated silicon nitride; these were thought to be caused by highly localised charging hotspots.

The sub-surface characterisation of Vickers indentations was investigated using micro-XCT, FIB tomography and top-down manual grinding. Micro-XCT, although having the advantage of being non-destructive, was not of sufficient resolution for resolving sub-surface cracking on 1 kg indentations so was not subsequently utilised on the ball-bearing component star features. However, it was found that when used on 5 kg indentations, cracks were identified, and their visibility could be increased using a zinc iodide penetrant to increase absorption contrast.

The FIB tomography investigations proved to be very successful with evidence of half-penny cracking for 1 kg indentation loads and, for the first time in a polycrystalline ceramic, unexpected half-penny cracking was also found for indentations of lower loads (0.5 kg with a c/a ratio ~ 1.5). In addition, FIB tomography revealed deep lateral cracks interconnecting with radial cracking surrounding the residual indentation impression for both loads; this has not been observed before for such low indentation loads in silicon nitride using alternative methods, and has only been observed once previously using FIB tomography on a related ceramic material [1]. The half-penny and deep lateral cracks appear to originate at the region where the severe plastic deformation compressive zone transitions via the micro-cracking zone to the tensile stress zone, and hence the cracking can be used to approximate the volume of the central plastic deformation compressive zone.

The discovery of half-penny and lateral cracking in Vickers indentations of a low load and with c/a ratios as low as 1.5, contrary to the established predictions, has implications for how the c/a ratio is used in the evaluation of sub-surface cracking regimes. Their location and morphology also allude to how cracking systems in silicon nitride may further evolve under operational conditions. The use of FIB tomography for 3D characterisation of indentation features proved to more effective than both micro-XCT and the top-down manual grinding methods. However, there are still problems associated with it, such as the induced change in residual stress [2], [3] that can cause crack opening/closure as observed here. The sudden propagation of cracking whilst FIB milling does indicate relatively high local residual stress levels present within the indentation region.

The characterisation of the star features on silicon nitride balls via FIB tomography revealed half-penny and lateral cracking that was not observable using a conventional UV fluorescence imaging technique. For Morphology 1 stars (i.e. those without a central residual impression), half-penny cracking was found to have an initiation depth of up to ~ 40 μm and, as with the Vickers indentations, indicates the volume of the compressively

stressed plastic deformation zone located beneath the central indent. In Morphology 2 stars, lateral cracking was observed at a maximum depth of ~ 15 μm and often correlated with surface cracking. Lateral cracking for one star feature was also found to be located at the same depth as a spalling crater giving direct evidence that lateral cracking can intersect with the surface plane and lead to subsequent material removal [4]–[6]. Surface profilometry of both types of star features showed uplift zones, but the uplift was of greater magnitude for Morphology 2 stars, especially around lateral cracking.

The original aims of this project; to characterise both the surface and sub-surface nature of star features on silicon nitride ball-bearing components to predict how they may evolve, whilst finding sufficient methods to do so, have been achieved. FIB tomography in particular has been found to be a very effective technique for 3D sub-surface crack characterisation and has revealed new information about star features on silicon nitride not previously attained through any other method. The type and morphology of sub-surface cracking present in these stars, as well as their surface topography, shows that they could be susceptible to material removal in the form of spalling, flaking and chipping when in service; for a component which relies on minimal friction for optimal performance, material loss and subsequent topography change is extremely detrimental.

8.2. Recommendations for Future Work

There are many directions that future work relating to this project could take both in terms of development of methodologies used, and in the further characterisations of star-like features. Detailed below are some ideas with potential for future study specific to the star features:

- Now that the sub-surface cracking morphology of indentations on silicon nitride has been characterised, a suggested next step would be to indent the surface of a ball sample with the same applied load as used here (0.5 kg and 1 kg). The ball-bearing could then be wear tested under a 4-ball rolling contact testing system and the indentation observed at incremental time periods [7]. This would give an insight in to how the sub-surface cracking identified previously actually evolves in operation conditions.
- An alternative to the above would be to model the effect of changes in the external environment on the indentations using finite element modelling (FEM) processes.

For instance, since crack dimensions as well as stresses present at crack tips are now known, FEM could be used to change variables such as external Hertzian contact pressure and contact location to analyse how cracking may propagate [8]. This could also be applied to the star features, not just the indentations, however, their asymmetric nature would make them more difficult to model.

- One assumption of using Vickers indentation to replicate star features is that sharp-point contact is perpendicular to the surface plane which is probably not true for most cases. Therefore, it would be of interest to vary the angle of contact for Vickers indentation, and subsequently use FIB tomography, to see the influence that contact angle has on the surface and sub-surface cracking systems.
- As discussed previously, the FIB process can potentially cause modification of the morphology of the sub-surface cracking due to residual stress changes, which means that the 3D crack reconstruction gained from FIB tomography differs to that which existed prior to milling. It would be beneficial to be able to characterise the sub-surface prior to milling, but as it has been seen, non-destructive methods such a laboratory micro-XCT do not currently provide sufficient resolution (although synchrotron analysis may offer an improvement.). However, a recently developed FIB device that uses a xenon (Xe) plasma source [9], [10] has a sputter rate of ~ 300% greater than that of a gallium source device allowing for greater volumes to be analysed in the same amount of time. Therefore, a larger load indentation (such as the 5 kg one investigated in this project) could be imaged using micro-XCT and then the same indentation could be subject to FIB tomography via Xe-FIB. The sub-surface cracking observed in both methods could then be compared to see how the FIB milling process has affected the cracking regime.

The characterisation techniques and methodologies developed here also have wider implications to material science in general. Here are some of the recommendations and implications that have stemmed from this project:

- The 3D characterisation of ceramic materials via FIB tomography is still difficult in comparison to that of metals, mainly due to surface charge having an impact on milling precision as well as image contrast. In FIB tomography of metals, long duration mills can be automated because there is minimal beam drift, whereas this is not possible when milling ceramics, and instead manual intervention is required in between milling slices – a time consuming process. Therefore, it is recommended

that more research is conducted in to charge neutralisation methods in FIB milling of ceramics. As has been seen in Chapter 7, utilising an electron flood gun when imaging with a GFIS means that ceramics can already be imaged without a conductive coating, so milling would be an appropriate next step.

- As mentioned above, Chapter 7 involved the first ever imaging of a ceramic using a GFIS device. This is of particular interest in the wider material science area as non-conductive material was imaged without a conductive coating, meaning more detailed topographical information was obtained and further surface analysis using other methods was possible afterward (as no coating was present on the surface). In addition, due to the high resolution of helium microscopy, this may have applications in the surface imaging of non-conductive materials (without a coating) where the aim is to image features of nanoscale dimensions, such as in lithium-ion battery research and grain boundary analysis of ceramics with sub-micron grain size.
- The use of 3D optical profilometry in this project proved highly successful and analysing the topography of the defects, but in addition, it also revealed information about the crack morphology beneath, i.e. the surface uplift surrounding a region where a lateral crack was subsequently observed via FIB tomography. Surface uplift can also be observed with SEM, but the advantaged of the profilometry technique is that it does not require a vacuum or timely sample preparation, making it a quick process. There is currently not much in the literature about the effectiveness of profilometry in identifying sub-surface defects (not just in ceramics, but in any material) and due to the success here, it is an area that warrants further research.

8.3. References

[1] Z. H. Xie, P. R. Munroe, R. J. Moon, and M. Hoffman, "Characterization of surface contact-induced fracture in ceramics using a focused ion beam miller," *Wear*, vol. 255, no. 1–6, pp. 651–656, 2003.

[2] F. Elfallagh and B. J. Inkson, "Evolution of residual stress and crack morphologies during 3D FIB tomographic analysis of alumina.," *J. Microsc.*, vol. 230, no. Pt 2, pp. 240–51, 2008.

[3] B. J. Inkson, D. Leclere, F. Elfallagh, and B. Derby, "The effect of focused ion beam machining on residual stress and crack morphologies in alumina," *J. Phys. Conf. Ser.*, vol. 26, no. 1, pp. 219–222, 2006.

[4] R. F. Cook and D. H. Roach, "The effect of lateral crack growth on the strength of contact flaws in brittle materials," *J. Mater. Res.*, vol. 1, no. 4, pp. 589–600, 1986.

[5] Y. Wang and M. Hadfield, “Failure modes of ceramic rolling elements with surface crack defects,” *Wear*, vol. 256, no. 1–2, pp. 208–219, 2004.

[6] Y. Wang and M. Hadfield, “A mechanism for nucleating secondary fractures near a pre-existing flaw subjected to contact loading,” *Wear*, vol. 254, no. 7–8, pp. 597–605, 2003.

[7] Y. Wang and M. Hadfield, “A study of line defect fatigue failure of ceramic rolling elements in rolling contact,” *Wear*, vol. 253, no. 9–10, pp. 975–985, 2002.

[8] Y. Tang, A. Yonezu, N. Ogasawara, N. Chiba, and X. Chen, “On radial crack and half-penny crack induced by Vickers indentation,” *Proc. R. Soc. A Math. Phys. Eng. Sci.*, vol. 464, no. May, pp. 2967–2984, 2008.

[9] T. L. Burnett, R. Kelley, B. Winiarski, L. Contreras, M. Daly, “Large volume serial section tomography by Xe Plasma FIB dual beam microscopy,” *Ultramicroscopy*, vol. 161, pp. 119–129, 2016.

[10] R. Young, C. Rue, S. Randolph, C. Chandler, “A Comparison of Xenon Plasma FIB Technology with Conventional Gallium LMIS FIB: Imaging, Milling, and Gas-Assisted Applications,” *Microsc. Microanal.*, vol. 17, no. S2, pp. 652–653, 2011.